Tin dioxide supported catalysts for wet lean methane combustion

by

Roshni Sajiv Kumar

A thesis submitted in partial fulfillment of the requirements for the degree of

Doctor of Philosophy

in

Chemical Engineering

Department of Chemical and Materials Engineering
University of Alberta

Abstract

Owing to the factors of low cost, abundance and lower emissions from natural gas as compared to diesel and gasoline, there has been a surged interest in utilizing natural gas for transportation purposes. Though it is known for natural gas to burn in a clean manner with considerably fewer greenhouse gases (GHGs) and near-zero particulate matter, methane itself has a greenhouse gas potential that exceeds CO_2 by 23 times. Hence, its release from natural gas vehicles (NGVs) exhaust into the atmosphere needs to be averted. The presence of catalytic converters in the NGV exhaust could result in an abatement of methane emissions, however, it faces several challenges. The exhaust stream from a lean-burn natural gas vehicle (NGV) typically has a maximum temperature of about 550 ˚C, a low concentration of methane (500 – 1000 ppmv) and a large amount of water vapour (around 15 % by volume) which is a major cause of Pd catalyst deactivation. Such conditions pose significant challenges in the development of a small-footprint catalytic converter to mitigate methane emissions. Thus, the need to develop a stable combustion catalyst for mobile applications is of paramount importance.

The ability to overcome the negative effects of water is highly dependent on the catalyst formulation including the choice of the support material. In an attempt to develop stable combustion catalysts, water-resistant Pt was first incorporated into the catalyst formulation. To further enhance the resistance to deactivation, SnO_2 was employed as a support material due to its known ability to serve as a sink to the hydroxyls. The kinetics of methane combustion was investigated on the 1 wt.% Pd/SnO_2 and 1 wt.% (1:1 Pd:Pt molar ratio) Pd-Pt/SnO_2 catalysts for a lean-burn wet feed and compared against similar catalyst formulations deposited on the conventional γ-Al_2O_3 support. It was demonstrated that Pt addition to Pd provided stable

conversions with Pd-Pt/SnO_2 catalyst demonstrating the least deactivation during hydrothermal ageing. Both SnO_2 and γ-Al_2O_3-supported Pd-Pt catalysts demonstrated -1 order to water and reduced activation energies of 134 kJ mol^{-1}, proposing the choice of support was inconsequential with Pt addition from the viewpoint of the activation energy. The Pd/SnO_2 catalyst on the other hand reported a partial -0.11 order to water. A rate law was suggested with two active sites, one affected by H_2O with -1 order and activation energy of 158 kJ mol^{-1} (similar to that of the Pd/γ-Al_2O_3 catalyst), and the other unaffected by water with an activation energy of 108 ± 7 kJ mol^{-1}.

To further enhance the stability and activity of the Pd-Pt/SnO_2 catalyst, cobalt was chosen as a promoter as CoO_x has been demonstrated to participate in wet methane combustion. To the best of our knowledge, kinetic studies nor detailed investigations on such a catalyst combination have not been reported in the literature. Therefore, as a first step, a systematic study to optimize the promoter loading on the 1 wt.% Pd-Pt/SnO_2 was conducted. Hydrothermal stability tests revealed that the 10 wt.% Co-promoted Pd-Pt/SnO_2 catalyst exhibited enhanced stability and catalytic activity even at 400 ˚C. Kinetic investigations on the Co-promoted catalyst revealed that the catalyst reported a partial -0.37 order to water, which is the same as for the Pd/SnO_2 catalyst. Utilizing an additive rate model (like that of the Pd/SnO_2 catalyst), the site unaffected by water reported an apparent activation energy of 89 ± 9 kJ mol^{-1}. While SnO_2 dictated the kinetics in terms of activation energy, higher water tolerance on the Co-promoted catalyst could be attributed to synergistic interactions between the various components resulting in the presence of different active sites (or) components on the surface.

In terms of turnover frequency, the Pd-Pt/10Co_3O_4/SnO_2 catalyst surpassed all the catalyst formulations under consideration. Reaction rates normalized per catalyst mass at 500 ˚C and 10

vol% added water were found in the order of Pd/γ-Al_2O_3(“x”) < Pd-Pt/γ-Al_2O_3 (1.5x) < Pd-Pt/SnO_2 (1.6x) < Pd-Pt/10Co/SnO_2 (14x), consequently suggesting that the utilization of the Pd-Pt/10Co/SnO_2 catalyst could result in smaller catalytic converter volumes.

Preface

Chapter 1 of the thesis has been published as: R. Sajiv Kumar, R.E. Hayes, N. Semagina, "Effect of support on Pd-catalyzed methane-lean combustion in the presence of water: review", *Catalysis Today* 2021, **382**, 82–95. The paper is re-printed with the permission from Elsevier B.V. and of the co-authors. The manuscript contains a literature review pertaining to the present research study. Dr. Natalia Semagina proposed the concept for the review article. Manuscript draft preparation and writing were conducted by the author. Dr. Natalia Semagina and Dr. Robert E. Hayes provided feedback and comments as well as revisions for the manuscript. Section 1.3. and Section 1.10. are not a part of the published article and have been additionally added to provide a brief literature review on the performance of Pd-Pt catalyst formulations and on the effect of promoter addition for Pd-based catalytic lean-burn methane combustion, respectively. Similarly, sections 1.14., 1.15., 1.16., and 1.17. are not a part of the published article and have been incorporated to elaborate the research objective, research plan and thesis outline.

Chapter 2 of the thesis contains the catalyst synthesis procedure and methodology used for conducting the experiments. The chapter also delves into the differential equations utilized for the kinetic modeling studies in MATLAB as well as provides a brief explanation of the characterization techniques utilized in this thesis.

Chapter 3 of the thesis has been published as: R. Sajiv Kumar, R.E. Hayes, N. Semagina, "Pd and Pd-Pt catalysts supported on SnO_2 and γ-Al_2O_3: Kinetic studies of wet lean methane combustion", *Chemical Engineering Science* 2023, **269** : 118488. The paper is re-printed with the permission from Elsevier Ltd. and of the co-authors. The reaction setup for methane combustion was originally designed and built by Dr. Long Wu and Dr. Robert E. Hayes. The lab view program to communicate with the reaction setup was written by Les Dean. Conceptualization of the research idea and research methodology was proposed by Dr. Natalia Semagina and Dr. Robert E. Hayes. XRD characterization was performed by Rebecca Funk at the Earth and Atmospheric Sciences Department, University of Alberta. TEM-EDX characterization was performed by Haoyang (Emmett) Yu at nanoFAB, University of Alberta. All syntheses, reaction tests, data collection, interpretation and analyses of experimental results and other characterizations were performed by the author. The author drafted and implemented the MATLAB code for the nonlinear optimization and also performed the numerical analyses in this work. Manuscript draft preparation and writing were conducted by the author. Dr. Natalia Semagina and Dr. Robert E. Hayes provided discussions and feedback on the experimental results as well as comments and revisions for the manuscript.

Chapter 4 of the thesis has been published as: R. Sajiv Kumar, R. E. Hayes, N. Semagina, "Kinetic investigation of the promoting effect of cobalt on Pd-Pt/SnO_2 catalyzed wet methane combustion", *Applied Catalysis A: General* 2023, **666** : 119416. The paper is re-printed with the permission from Elsevier B. V. and of the co-authors. The reaction setup for methane combustion was originally designed and built by Dr. Long Wu and Dr. Robert E. Hayes. The lab view program to communicate with the reaction setup was written by Les Dean. Conceptualization of the research idea and research methodology was proposed by Dr. Natalia Semagina and Dr. Robert E. Hayes. XRD characterization was performed by Rebecca Funk at the Earth and Atmospheric Sciences Department, University of Alberta. TEM-EDX characterization was performed by Dr. Xuehai (Mike) Tan at nanoFAB, University of Alberta. TPD characterization was performed by Dr. Jing Shen, Department of Chemical and Materials Engineering, University of Alberta. All syntheses, reaction tests, data collection, interpretation and analyses of experimental results and other characterizations were performed by the author. The author drafted and implemented the MATLAB code for the nonlinear optimization and also performed the numerical analyses in this work. Manuscript draft preparation and writing were conducted by the author. Dr. Natalia Semagina and Dr. Robert E. Hayes provided discussions and feedback on the experimental results as well as comments and revisions for the manuscript.

The research project of the present thesis is funded by the Natural Sciences and Engineering Research Council of Canada (NSERC), Discovery grant program.

Dedication

This thesis is dedicated to my beloved parents, my father **Sajiv Kumar,** and my mother **Leena**; for their endless love, support, and encouragement.

Acknowledgements

I would like to take the opportunity to thank several individuals, without whose support and guidance, the completion of this dissertation would never have been possible.

I gratefully acknowledge the financial support from Natural Sciences and Engineering Research Council of Canada (NSERC), Discovery grant program, that enabled me to carry out my research.

I would like to express my sincere gratitude to my supervisors, Dr. Natalia Semagina and Dr. Robert E. Hayes (Department of Chemical and Materials Engineering at the University of Alberta):

Dr. Natalia Semagina,

For her incredible support, her immense patience, insights and for trusting and guiding me to grow as an independent researcher. Her mentorship helped me in every step of this journey and her positive attitude helped me stay motivated and inspired. I could have not imagined a better advisor and mentor for my Ph.D. journey.

Dr. Robert E. Hayes,

For his patience, his enthusiasm, and for sharing his invaluable expertise. With his extensive knowledge in the combustion field, I could not have asked for a better mentor to guide me on the same. I am thankful for his priceless insights and mentorship that were instrumental in this work.

I would also like to express my gratitude to:

My Ph.D. candidacy examination committee: Dr. Anastasia Elias (Exam Chair, Department of Chemical and Materials Engineering, University of Alberta), Dr. Natalia Semagina (Supervisor), Dr. Robert E. Hayes (Supervisor), Dr. Samir H. Mushrif (Supervisory committee, Department of Chemical and Materials Engineering, University of Alberta), Dr. Arvind Rajendran (Examiner, Department of Chemical and Materials Engineering, University of Alberta) and Dr. Hongbo Zeng (Examiner, Department of Chemical and Materials Engineering, University of Alberta) for their questions, suggestions and assistance in the early stages of my research.

My Ph.D. defense examination committee: Dr. Jing Liu (Exam Chair, Department of Chemical and Materials Engineering, University of Alberta), Dr. Natalia Semagina (Supervisor), Dr.

Robert E. Hayes (Supervisor), Dr. Samir H. Mushrif (Supervisory committee, Department of Chemical and Materials Engineering, University of Alberta), Dr. Arno De Klerk (Examiner, Department of Chemical and Materials Engineering, University of Alberta) and Dr. Kevin J. Smith (External examiner, Department of Chemical and Biological Engineering, University of British Columbia) for their valuable questions and comments on the thesis.

Dr. Jing Shen for her friendship and support. I cannot imagine my Ph.D. life without her constant guidance and valuable comments throughout the execution of my project. I would also like to thank Dr. Jing Shen for performing the TPD characterization and for assisting with the CO chemisorption characterization. My lab mates: Himanshi, for her friendship and for always being supportive and cheerful, and Amir Rouhi for always coming to my help in the lab when I requested him.

Dr. Nancy Zhang, Dr. Nastaran Yousefi, and Les Dean, for their continuous help and maintenance of the lab equipment. Haoyang (Emmett) Yu and Dr. Xuehai (Mike) Tan at Characterization group nanoFAB, University of Alberta for performing the HR-TEM analysis of my catalyst samples. Rebecca Funk at the Earth and Atmospheric Sciences Department, University of Alberta, for performing the XRD characterization of my catalyst samples.

Lily Laser, Marcy Doyle, Kevin Heidebrecht, and all other staff at the Department of Chemical and Material Engineering, University of Alberta, for their help and support. A very special thanks to Dr. James Sawada (Department of Chemical and Material Engineering, University of Alberta) for all his invaluable insights and expertise, his support, his guidance and for helping me immensely improve my presentation and writing skills.

I am highly indebted and grateful to my parents (Sajiv Kumar and Leena), my grandparents (P.R. Dasan and Suriyakumari), my sisters (Rajeswari and Renuka), my brother-in-law (Vivek), my adorable nephew (Rishab) and my partner (Matthew) for constantly supporting me throughout this journey and providing me with encouragement and positivity through my toughest moments.

Last but not the least, my dearest and closet friends Pooja and Yogashree, for constantly supporting me and being there for me whenever I needed them. A special mention to my amazing friends S. Kanthaan, Siddharth, Saravanan, Aravind, Ramakrishna, Anikesh, Rishiekesh, Raviraju, and Ravikiran for all their friendship, support, and encouragement throughout this journey.

Table of Contents

List of Tables

List of Figures

List of Symbol

A_c	Catalyst bed cross-sectional area (m^2)
b	Bed dilution factor by volume (-)
C_M	Methane concentration (mol/m^3)
C_{M0}	Initial methane concentration (mol/m^3)
C_{aq}	Water concentration (mol/m^3)
C_{WP}	Weisz-Prater number (-)
d_p	Catalyst particle diameter (m)
d_{pore}	Pore diameter (m)
D_{AB}	Bulk diffusivity (m^2/s)
D_K	Knudsen diffusivity (m^2/s)
D_{eff}	Effective diffusivity (m^2/s)
D_{pore}	Diffusivity in pore (m^2/s)
Ea	Observed activation energy (kJ/mol)
F_{M0}	Initial methane flow rate (mol/s)
F_{aq0}	Initial water flow rate (mol/s)
h	Heat transfer coefficient ($kJ/(m^2.s.K)$)
H_{rxn}	Heat of reaction (kJ/mol)
k'	Reaction rate constant (units vary)
k_c	Mass transfer coefficient (m/s)
k_t	Thermal conductivity ($kW/(m \cdot K)$)
k_{eff}	Effective thermal conductivity ($kW/(m \cdot K)$)
L_b	Catalyst bed length (m)
M_A	Methane molecular mass (kg/mol)
M_B	Air molecular mass (kg/mol)
n	Reaction order with respect to water (-)
Nu	Nusselt number (-)
N_{Pe}	Peclet number (-)
$^{N}Pe_{min}$	Minimum Peclet number (-)

Pr	Prandtl number (-)
P	Pressure (Pa)
P_i	Reaction pressure (atm)
Q	Correct volumetric flow rate (m^3/s)
Q_0	Initial volumetric flow rate (m^3/s)
$(-r_M)$	Reaction rate ($mol/(kg_{cat}.s)$)
R_{gas}	Universal gas constant (kJ/(mol.K))
R	Catalyst particle radius (m)
Re_p	Particle Reynolds number (-)
S_{BET}	Catalyst BET surface area (m^2/g)
Sc	Schmidt number (-)
Sh	Sherwood number (-)
T	Temperature (K)
T_i	Reaction temperature (K)
u	Free stream velocity (m/s)
W	Catalyst mass (kg_{cat})
X_M	Fractional methane conversion (%)

Greek Letters

β	Prater number (-)
ΔT_{max}	Maximum internal temperature rise (K)
μ	Dynamic viscosity (Ns/m^2)
ρ_g	Gas density (kg/m^3)
ρ_b	Bed density (kg/m^3)
ρ_c	Catalyst density (kg/m^3)
$(\sum \nu_i)_A$	Sum of the diffusion volume for air in Fuller equation (-)
$(\sum \nu_i)_B$	Sum of the diffusion volume for methane in Fuller equation (-)
ϕ_p	Particle porosity (-)

τ	Tortuosity (-)
ε	Catalyst bed porosity (-)
η	Internal effectiveness factor (-)
ϕ	Thiele modulus (-)

List of Abbreviations

a.u.	Arbitrary unit
aq.	Water
Al_2O_3	Alumina
BET	Brunauer-Emmett-Teller
CH_4	Methane
CO_2	Carbon dioxide
CO	Carbon monoxide
Co_3O_4	Cobalt Oxide
DFT	Density Functional Theory
DRIFT	Diffuse Reflectance Fourier Transform Infrared
EDX	Energy Dispersive X-ray
FID	Flame Ionization Detector
FTIR	Fourier Transform Infrared
GC	Gas chromatography
GHSV	Gas Hourly Space Velocity
GHG	Green House Gas
GWP	Global Warming Potential
H_2O	Water
IE	Ignition-Extinction
M	Methane
NGV	Natural Gas Vehicle
NMR	Nuclear Magnetic Resonance
NP	Nanoparticle

NW	Nanowires
O_2	Oxygen
PGM	Platinum Group Metal
S	Support material
SEM	Scanning Electron Microscopy
SMSI	Strong Metal Support Interaction
SnO_2	Tin dioxide
TEM	Transmission Electron Microscopy
TEOOS	Triethoxy(octyl)silane
TPR	Temperature Programmed Reduction
TPO	Temperature Programmed Oxidation
TPD	Temperature Programmed Desorption
TCD	Thermal Conductivity Detector
TOF	Turnover Frequency
XAS	X-ray Absorption
XANES	X-ray Absorption Near-Edge Structure
XPS	X-ray Photon Spectroscopy
XRD	X-ray Diffraction

Chapter 1: Effect of support on PGM-catalyzed methane-lean combustion in the presence of water[1]

1.1. Introduction

The worldwide energy demand continues to grow at a rapid pace, owing to increasing populations, as well as the desire of many countries to develop and improve their standard of living. Hence, a low cost and readily available supply of energy is essential to ensure the smooth functioning of many parts of the world [1]. Natural gas, a hydrocarbon gas mixture, which is primarily composed of methane (CH_4), is an abundant energy source with worldwide reserves estimated at over 193.9 trillion m^3. It is widely utilized as a fuel for heating, power generation and, more recently, for transportation purposes [2]. Methane has the highest H/C ratio of any hydrocarbon and produces the lowest amount of CO_2 per unit of energy, at about 55 g/MJ as compared to about 70 g/MJ for dodecane [3]. Typical pipeline-quality natural gas has low amounts of sulphur and nitrogen impurities and has a high-octane number [4]. Furthermore, natural gas burns cleanly with near-zero emissions of particulate matter and low emissions of CO and NO_X even when the combustion gases are not pre-mixed, compared to the more traditional fuels [5].

---

[1] **Chapter 1** of the thesis has been published as: R. Sajiv Kumar, R.E. Hayes, N. Semagina, "Effect of support on Pd-catalyzed methane-lean combustion in the presence of water: review", *Catalysis Today* 2021, **382**, 82–95. Section 1.3. and Section 1.10. are not a part of the published article and have been additionally added to provide a brief literature review on the performance of Pd-Pt catalyst formulations and on the effect of promoter addition for Pd-based catalytic lean-burn methane combustion, respectively. Similarly, sections 1.14., 1.15., 1.16., and 1.17. are not a part of the published article and have been incorporated to elaborate the research objective, research plan and thesis outline. Manuscript draft preparation and writing were conducted by the author. The paper was re-printed with permission from Reference [6] Copyright © 2021 Elsevier B. V. and of the co-authors.

For these reasons, the use of natural gas vehicles (NGVs) has been increasing markedly in recent years. Whilst emissions of many toxic species are low, incomplete combustion in a NGV can lead to significant emissions of methane which, while non-toxic, is nonetheless a potent greenhouse gas (GHG) with a global warming potential (GWP) more than 23 times that of CO_2 [7]. GWP is defined as a measure of how much energy the emissions of 1 ton of a gas will absorb over a given period of time, relative to the emissions of 1 ton of carbon dioxide [8]. Thus, the GWP of 1 kg methane would be equivalent to 23 kg of CO_2. Elimination of methane in the exhaust of NGVs can best be achieved by oxidation using a catalytic converter [9].

Homogeneous combustion of methane requires relatively high temperatures, of the order of 1500 to 2000 ˚C and has a strict range of flammability limits. The exhaust stream from a lean burn NGV typically has a maximum temperature of about 550 ˚C and a low concentration of methane (500 – 1000 ppmv). For these reasons, catalytic combustion is required [10]–[13]. A major issue with the catalytic combustion of methane in the exhaust is the presence of a large amount of water vapour (around 15 % by volume) which is a major cause of catalyst deactivation**.** Catalyst deactivation in this context accounts for the drop in conversion with time on stream as compared to that of the fresh catalyst. Therefore, the main objectives of catalyst developers for this application are to reduce the susceptibility of the catalyst to the effects of water and to have a relatively high low-temperature activity.

A catalytic converter for an NGV is required to have a high catalytic activity because the unit must have a small footprint. As a general rule of thumb, the total converter volume should not exceed twice the displacement of the engine, and smaller is always better. The most effective metals proposed for this application are the platinum group metals (PGMs), with Pd, Pt and Rh being common [14]. Among the PGMs, it has been found that palladium (Pd) based catalysts are highly efficient under lean-burn conditions [21], [22], as these catalytic materials have exhibited the highest activity. However, despite their promising initial high activity, Pd catalysts are found to deactivate under exhaust condition [14]–[21], particularly due to the presence of water vapour in the exhaust, as illustrated in Figure 1.1 [22]. It is believed that the activity of Pd catalysts deteriorate at temperatures below 450 ˚C due to the formation of inactive $Pd(OH)_2$ which in turn hinders the oxygen mobility and exchange and the involved metal-support interactions, resulting in inhibition of the combustion reaction [23]. Typically, γ-Al_2O_3 support is used in conventional catalyst formulations for Pd deposition, which are further physically mixed with CeO_2-based powders for the washcoat preparation.

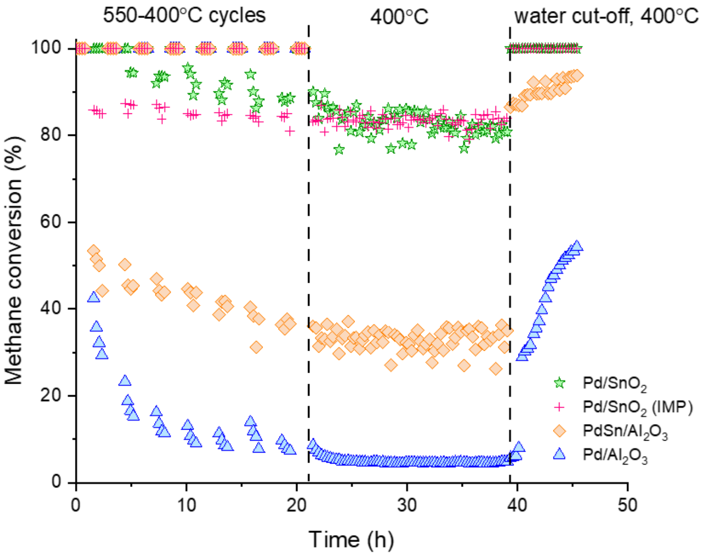

Figure 1. 1. Hydrothermal ageing (HTA) tests with 5 vol% water with periodical cycling of temperatures to study the trend of deactivation [24]. *Reproduced (adapted) with permission from* [24]. *Copyright © 2019 Wiley-VCH Verlag GmbH & Co. KGaA, Weinheim*

The role of supports in heterogeneous catalysis can hardly be overrated. They stabilize active metal nanoparticles against agglomeration and contribute to their size control via support's surface area, its surface chemistry, and pore structure. Only because of the existence of the supports, high metal dispersion can be maintained even in high-temperature applications, which implies the practical feasibility of catalytic processes in relatively small reactor volumes. Other, no less significant, roles of support may include the creation of new active sites on the metal-support interface, charge transfer, donation of lattice oxygen in oxidations, and other phenomena which are often referred to as (strong) metal-support interactions (SMSIs) [25], [26]. The main focus of this review is to summarize published studies and hypotheses up to date on how different supports can affect PGM catalyst activity and stability in wet lean methane combustion, as related to their application in NGVs. A review on the deactivation of Pd catalysts by water during methane combustion was published in 2015 by Gholami et al. [27]; since then, multiple mechanistic studies both on the water and support effects were reported and are reviewed here. We hope that this summary may prove itself useful in directing researchers' efforts to understand negative water effects in methane combustion and how they can be counteracted by a rational choice of support, and, ultimately, to develop efficient small-footprint converters to mitigate natural gas emissions.

1.2. State-of-the-art catalytic cycle of Pd-catalyzed wet methane combustion

Before exploring the support effect in mitigating the negative effects of water, it is essential to recognize the intermediates formed in the absence and presence of water. Recent investigations involving density functional theory (DFT) were conducted by Stotz et al. [28] to understand the mechanism of methane oxidation over the PdO(101) (Figure 1.2). Two active sites were recognized, namely, the coordinatively unsaturated (cus) Pd_{cus} and O_{cus} sites. The mechanism involved a C_1-pathway comprising various carbonaceous CH_xO_y intermediates combined with the formation of lattice oxygen vacancy via a Mars-van Krevelen mechanism. A total of 23 surface intermediates had been identified and considered, of which 15 surface species were related to Pd_{cus}-sites and 8 surfaces species were associated with O_{cus}-sites. Based on the C_1 scheme, it was analyzed that the reaction followed a particular pathway in the temperature range of 200-400 ˚C at dry conditions: $CH_4(g) \rightarrow CH_3\text{-}Pd \rightarrow CH_2OH\text{-}Pd \rightarrow CH_2O\text{-}Pd \rightarrow CHO\text{-}Pd \rightarrow CO\text{-}Pd \rightarrow CO\text{-}O \rightarrow CO_2(g)$, where the activation of methane mainly occurred at the Pd_{cus}-O_{cus} sites. In the case of the wet feed (12 vol% H_2O at 300 – 550 ˚C), the pathway follows an alternate sequence as delineated in Figure 1.2: $CH_4(g) \rightarrow CH_3\text{-}Pd \rightarrow CH_2\text{-}Pd \rightarrow CH_2O\text{-}Pd \rightarrow CHO\text{-}Pd \rightarrow CO\text{-}Pd \rightarrow CO\text{-}O \rightarrow CO_2(g)$. The major difference arises in the fact that hydroxyl-methyl intermediates are not produced, and methylene groups intercede the reaction sequence at high temperatures, and this could be attributed to the inhibition effect as depicted by the $(H_2O)Pd_{(cus)}$ coverage [28]. Based on the proposed mechanism, it is evident that hydroxyls are formed as an intermediate, which decomposes at temperatures above 450 ˚C. Pd reoxidation with an external oxygen source (gaseous O_2 in Figure 1.2) is another obvious requirement for the cycle to complete. No support effects were incorporated in the simulation, although one may speculate that if support affects the oxygen exchange or water retention, the reaction rates are to be affected.

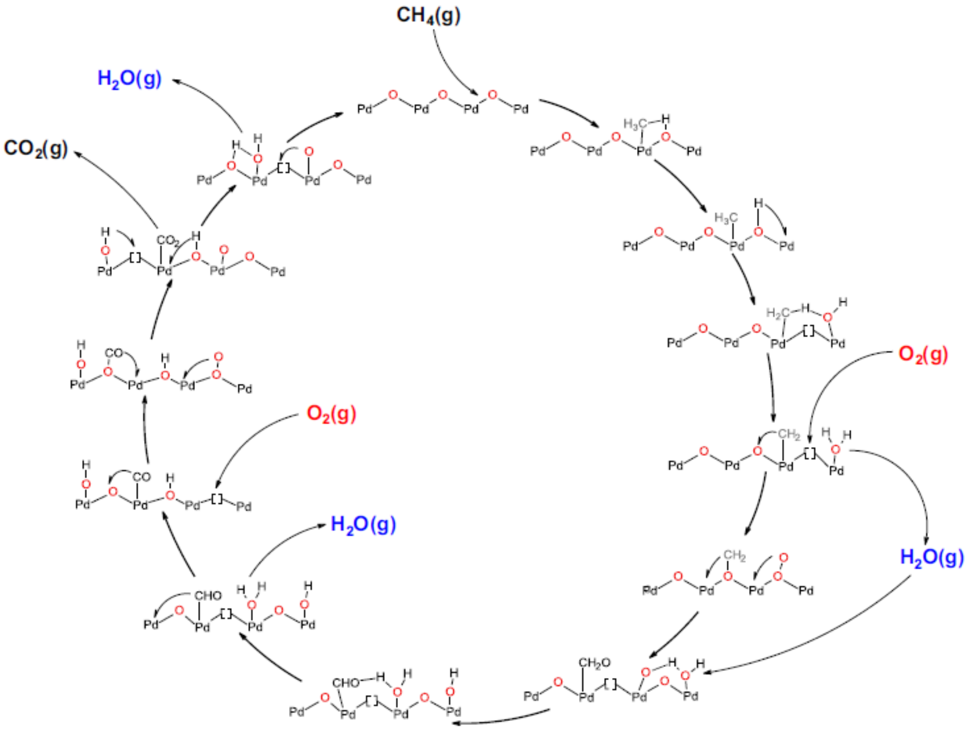

Figure 1. 2. Catalytic cycle for CH_4 oxidation under wet conditions [28]. *Reproduced with permission from* [28]. *Copyright © 2019, Elsevier*

It is crucial to note here that the mechanism of methane activation over the metallic Pd, PdO, and Pd surface saturated with chemisorbed oxygen (O*) could have various possible pathways [29], [30]. A widely believed hypothesis for methane combustion occurring over palladium-based catalysts is via the Mars-van Krevelen redox-type mechanism [31]. The mechanism demonstrates a reaction in which the metal oxide catalyst provides its oxygen during the reaction, following which the reduced metal oxide is re-oxidized by the gas phase oxygen [31]. Following this hypothesis, a study on the kinetics of methane combustion at low temperatures characterized by the Mars-van Krevelen mechanism detected the involvement of methane activation on site pairs comprising of Pd which functions as an oxygen vacancy and PdO_x that serves as a source for the oxygen atoms [32]. Methane was found to be dissociatively adsorbed on metallic Pd thereby producing H and CH_x species, while the oxidation occurred on the adjacent PdO [33], [34]. A study by Chin et al. [29] demonstrated that the first C-H bond activation of methane was found to occur via oxidative addition, H-atom abstraction, and σ-bond metathesis pathways on metal atom pairs (*-*), oxygen atom pairs (O*-O*) and Pd cation lattice oxygen pairs (Pd^{2+}-O^{2-}), respectively [30]. It was also proven that PdO had the lowest activation barrier (Pd^0: 84 kJ mol^{-1} [35], O*-saturated Pd^0: 158 kJ mol^{-1} [29], and PdO: 61 kJ mol^{-1} [29]) among the three species that were studied. It is also known for Pd catalysts to transition from metallic Pd to the PdO phase, however, this process could be kinetically limited due to reduced oxygen diffusion into Pd^0 at lower temperatures and the formation of a strongly bound oxygen passivation layer at high temperatures [36], [37]. However, there is a dearth of studies dedicated to comprehending the transient phases encountered and thus the most active Pd phases for such applications are still debatable [37]–[40].

1.3. Performance of Pd-Pt catalysts in wet methane combustion

Addition of Pt to Pd-based catalysts has shown to improve catalytic activity and stability, particularly under wet feed conditions. Nomura et al. [41] demonstrated that when Pt was added to the Pd catalyst formulation, it helped reduce the inhibition effect of water. The authors proposed that the improved water resistance could be attributed to synergistic interactions between Pd and Pt [41][20]Narui et al. [20] proposed that improved dispersions owing to the inclusion of Pt to the conventional Pd/γ-Al_2O_3 catalyst, resulted in improved wet methane combustion catalytic activity. While the particle size on the Pd/γ-Al_2O_3 catalyst increased from 8 to 11 nm upon long term exposure to the feed stream at 350 ˚C, significant increase in the particle size could not be observed on the bimetallic catalyst [20]. Similar conclusions were proposed by Yamamoto et al. [42] wherein by means of X-ray Diffraction (XRD) analysis it was demonstrated that the crystallite size grew faster on the Pd catalyst that the Pd-Pt catalyst supported on γ-Al_2O_3. The studies also demonstrated that the Pd-Pt/γ-Al_2O_3 catalyst demonstrated the most stable and longer lasting catalytic activity in comparison to the monometallic catalyst. Lean burn methane combustion studies by Lapisardi et al. [43] on the bimetallic Pd-Pt catalyst demonstrated that under dry feed conditions, the conversions over the Pd and Pd-Pt catalysts supported on Al_2O_3 were in the same range, while under wet feed conditions the bimetallic catalyst provided enhanced performance. Employing Temperature Programmed Oxidation (TPO) studies, the authors confirmed that Pt affected the formation and decomposition of PdO, suggesting some interactions between Pt and Pd that could contribute to the improved catalytic performance [43]. In a study by Datye and coworkers [44], the formation of metallic Pd-Pt alloy structures had been observed, where mobile Pt species were being trapped by PdO when aged in air, resulting in enhanced sintering resistance, and improved catalytic performance.[44][23]

Nassiri et al. [23] proposed that in the presence of water, the support surface could be considered oxygen deficient, thereby preventing Pt from being poisoned by oxygen and enabling Pt to catalyze methane. The amount of Pt included in the catalyst formulation is known to affect the Pd catalyst performance for wet methane combustion. Experimental studies by Persson et al. [45] and Watanabe et al. [46] demonstrated that the bimetallic Pt-Pd catalytic systems with a higher 2:1 and 1:1 Pt:Pd molar ratio offered enhanced catalytic activities in the presence of water. The studies demonstrated that the presence of alloyed Pd-Pt structures in contact with the PdO phase contributed to the enhanced catalytic activity and stability. Studies by Goodman et al. [47] and Karinshak et al. [48] depicted that while the Pd/Al_2O_3 catalyst activity suffered dramatically in the presence of water, the Pt incorporated catalysts remained unaffected by water due to the formation of PdO/Pd-Pt aggregates that could exhibit Pd-like activity. Wet methane combustion studies by Nassiri et al. [49] proposed that the 1:1 Pd:Pt catalyst provided the most stable conversions under lean-burn wet feed condition methane combustion studies. The authors proposed that transformation of the Pd core – Pt shell nanoparticles into alloyed structures contributed to the enhanced catalytic stability. Despite the presence of steam, it was proposed that Pt vaporization and subsequent encapsulation by PdO nanoparticles could also have occurred at temperatures below 550 ˚C resulting in the stable catalytic performance [49]. Studies on commercial Pd and Pd-Pt (4:1) catalysts by Abbasi et al. [50] under dry and wet methane combustion demonstrated that both catalysts lost a large portion of their initial upon exposure to 5 vol% water. However, upon stopping the flow of water to the catalysts, the bimetallic catalyst as opposed to the monometallic catalyst was able to recover a significant portion of its initial activity [50].

Kinetic studies under wet feed conditions by Yang et al. [51] reported activation energies of 127 kJ mol^{-1} and 58 kJ mol^{-1} for the 1Pd and 1Pd-1Pt on Al_2O_3, respectively. These studies also demonstrated that inclusion of Pt to the catalyst formulation had resulted in a reduction of the methane combustion activation barrier. The bimetallic catalyst also reported an improved water tolerance with an order of -0.23 to water as compared to the reaction order of -1 to water on the Pd catalyst. The authors proposed that though water occupied the sites on the Pd-Pt surface, the Pt-Pd core-shell structures imparted water resistance to the catalytic system compared to the reference PdO structure [51]. Wet methane combustion studies under 4.2 vol.% water by Goodman et al. [47] illustrated that addition of Pt to Pd-based catalyst as well as the Pt:Pd ratio altered the observed activation energies. The 4:1 Pt:Pd catalyst reported the lowest activation energy at 60 kJ mol^{-1}, compared to the Pd/γ-Al_2O_3 catalyst with an observed activation energy of 180 kJ mol^{-1} [47].

Though the above-stated studies indicate that the addition of Pt can improve the catalytic performance, there is a lack of a unified consensus on the beneficial effects of adding Pt to the catalyst formulation in the literature. Lean methane combustion studies by Nassiri et al. [52] on γ-Al_2O_3 supported Pd and Pd-Pt catalysts in the absence of water revealed that Pt inhibited the formation of active PdO thereby resulting in a retarded methane oxidation rate. On the contrary, the monometallic Pd catalyst was oxidized completely in the temperature range under study and provided an enhanced performance [52]. In another study by Kinnunen et al. [53], Pt addition affected the catalytic performances of the fresh and the air aged catalyst in a contrasting manner. While the latter catalyst exhibited an improved low-temperature methane combustion activity, the former did not exhibit such a trend, which could be attributed to the difference in the ratio of Pd and PdO on the catalyst surface in the presence of Pt. These studies further emphasized the importance of the catalyst formulation parameters, as well as the ratio of Pd to Pt that would be critical in determining the optimal methane combustion activity [53]. While under wet feed conditions, Pt inclusion helped in the reduction of activation barrier, similar conclusions could not be reported under the dry feed conditions. Investigations by Nie et al. [54] and Goodman et al. [47] illustrated that with an increase in the Pt-Pd ratio, the rate constants and the consequent reported reaction rates under dry feed conditions decreased due to the presence of a larger amount of inactive Pt on the surface, thereby preventing the formation of active PdO on the catalyst surface. Taking these studies into consideration, the addition of Pt to the catalytic system favors its application to provide enhanced stability and improved catalytic activity under wet feed conditions as opposed to the dry feed conditions. While under dry feed conditions Pt is less active than Pd and could prevent Pd from being oxidized, supported Pd-Pt catalysts exhibited improved water tolerance possibly due to Pd stabilizing Pt through strong interactions between

PdO and the support. Thus, it is crucial to understand support and active PdO interactions, which could alter the performance of PGM based methane combustion catalysts.

1.4. Pioneering studies of water and support effects in methane combustion

Back in 1972, Cullis et al. [55] initiated investigations to explore the effects of water on the methane combustion reaction, when a drop in the reaction rate on Pd/Al_2O_3 catalyst was attributed to an increase in water vapour concentration. Based on the sole recognizable product that had an inhibiting effect, it was proposed that the active sites were blocked due to the formation of $Pd(OH)_2$ on the PdO surface and that rate of catalyst deactivation was dependent on the ability of the support to retain water [55]. Similar investigations were carried out by Ribeiro, et al. [56] on Pd/Al_2O_3 and Pd/ZrO_2 catalysts. The results demonstrated that the reaction order was -1 for water when it was present in concentrations between 3 to 15 vol% at temperatures below 450 ˚C. The authors also proposed that the strong water inhibition effect observed could be due to the formation of $Pd(OH)_2$ at the PdO surface, thereby inhibiting methane from approaching the active sites [56].

Burch et al. [15] illustrated that for methane combustion experiments on 4 wt% Pd/Al_2O_3 catalyst carried out in the presence of 2.7 vol% water, the inhibitory effect of water was only present up to about 450 ˚C. The stated temperature was significantly critical, as below 450 ˚C, water was found to bind more actively to the catalytic surface as compared to CO_2 and desorbed from the catalytic surface at a slower rate. At 450 ˚C, the delay in desorption observed between CO_2 and H_2O was found to disappear, and they were found to desorb from the surface at about equal rates [15]. These studies suggested that the formation of inactive $Pd(OH)_2$ could have been one of the major deactivating factors and that the Al_2O_3 support contributed to stabilizing the $Pd(OH)_2$ formed, due to its ability to retain water [15].

A significant breakthrough in understanding water effects and the role of support in wet methane combustion can be attributed to L. Pfefferle and colleagues. In their earliest study, they related the partially reversible deactivation effect to the accumulation of hydroxyl groups on the support, which interfered with the oxygen transfer process [57]. A methane combustion study under 3.45

vol% wet feed conditions illustrated that the inhibitory effect of water was found to be stronger at lower temperatures on Al_2O_3 and ZrO_2 supported Pd catalysts. They proposed that the reaction proceeded in two regimes: (1) at temperatures below 450 ˚C, water desorption becomes the RDS, and the reaction order for water was -1, and (2) at temperatures above 450 ˚C, methane activation was found to be the RDS and the reaction order for water was 0 [57]. For 3 wt% Pd/ZrO_2 catalyst under both dry and 3.45 vol% wet feed conditions, water inhibition was reported to depend on the (temperature-dependent) kinetics of equilibration of the water adsorption-desorption processes [58].

This discovery prompted a further investigation to understand the role of support in the combustion process and the associated oxygen mobility on the support which could potentially play a crucial role in the catalyst activity. Isotopically labelled pulse experiments with ^{18}O were conducted at 425 ˚C on unsupported PdO and 3 wt% Pd/ZrO_2 under 2.45 vol% wet feed conditions [59]. The isotopic exchange of oxygen between the catalyst surface and the gas phase was hampered during methane oxidation over the oxidized Pd catalyst, which was postulated to be the effect of water blocking the oxygen exchange mechanism. The authors proposed that at the PdO surface, oxygen from the gas phase could be dissociated on the oxygen vacancy sites; when the vacancies were blocked by water, the surface became inactive, and the oxygen uptake from the gas phase could have been limited by the desorption of water molecules. Additional investigation of the oxygen exchange between Pd and Al_2O_3 support, as well as between Pd and ZrO_2 support [60], demonstrated that the exchange between the gas phase and PdO was much faster than the exchange between PdO and the support or between the support and the gas phase (Figure 1.3 [60]). [60]

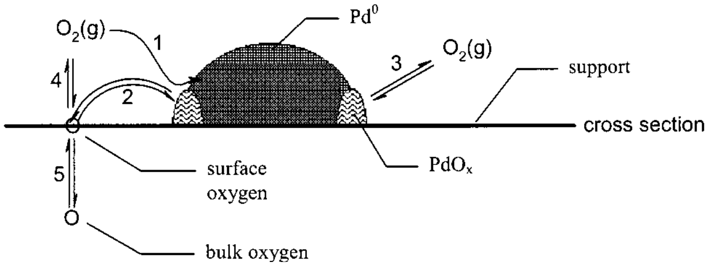

Figure 1. 3. Oxygen exchange process between the PdO phase and support [60]. *Reproduced with permission from* [60]. *Copyright © 2002, American Chemical Society*

Ciuparu et al. postulated that the metallic particle takes up oxygen from the gas phase and catalyzes to form a new PdO phase at the active metal-support interface, following which there is an oxygen exchange between the newly produced PdO_x phase and the support as well as between the PdO_x phase and the gas phase. Eventually, there occurs an oxygen exchange between the gas-phase oxygen and the surface [60].

Similar isotopic oxygen studies with $^{18}O_2$ on 3 wt% $PdO/Al_2{}^{16}O_3$ and 3 wt% $PdO/Mg^{16}O$ demonstrated that ^{18}O appeared more rapidly in the products from the $Mg^{16}O$ supported catalyst in comparison to the $Al_2{}^{16}O_3$ supported catalyst. [17] The percentage of ^{16}O appearing in the product gases was about 4% in the case of the $Pd/Al_2{}^{16}O_3$ indicating evidence that lattice oxygen from the support contributed to the reaction products and possible oxygen exchange between PdO and the support surface [17]. The authors elucidated that oxygen exchange with the support bulk was expected to be slow and negligible as the binding energies in the metal oxide supports were very strong. Utilizing flame photometry, the Al−O binding energy was determined to be around 485 kJ/mol, while the Mg−O binding energy was calculated to be around 377 kJ/mol [61] as depicted in Table 1.1 [17]. When Pd was added to Al_2O_3 and MgO, the Arrhenius plot evaluation demonstrated that the activation energy for oxygen exchange was further diminished to 27 and 39 kJ/mol, respectively [62], [63]. It was proposed that the lower activation energy associated with Pd, could be due to O_2 dissociation on Pd, which facilitated oxygen exchange with the support [17].

Table 1. 1. Data on binding energies of Al-O and Mg-O and activation energies for oxygen exchange on the surface of Al_2O_3 and MgO [17]. *Reproduced with permission from* [17].*Copyright © 2012, American Chemical Society*

	Al-O	**Mg-O**
Binding energy	485 kJ/mol	377 kJ/mol
Activation energy for oxygen exchange	125 kJ/mol	166 kJ/mol
Activation energy for oxygen exchange after the addition of Pd/PdO (in the absence of methane)	27 kJ/mol	39 kJ/mol

To determine hydroxyl accumulation on the catalyst surface, initial investigations were carried out by Ciuparu et al. [64] employing Diffuse Reflectance Fourier Transform Infrared (DR-FTIR) spectroscopy. When the methane combustion reaction was carried out under 3 vol% wet feed conditions on 3.5 wt% Pd/γ-Al_2O_3 catalyst, three absorption bands were observed centered at 3780, 3725 and 3678 cm^{-1}, which were attributed to the hydroxyl groups on the PdO surface or on sites at the alumina–PdO interface [64]. Later, Gao et al. [65] performed FTIR spectroscopy studies on 2 wt% Pd/Al_2O_3 catalyst under 10 vol% wet feed conditions and observed a broad peak at 3445 cm^{-1}, which was attributed to the stretching vibration of H-bonded hydroxyl groups on Al_2O_3. Thermogravimetric (TG) experiments for the combustion reaction under wet feed conditions for 4 hours showed a slight weight loss at 220 ºC, which was attributed to the decomposition of $Pd(OH)_2$ [65]. Another recent operando DRIFT spectroscopy study of Pd/Al_2O_3 catalysts in dry and wet methane combustion provided a detailed account of a variety of OH groups on the catalyst surface [66].

FTIR spectroscopy studies by Schwartz et al. [67] for the combustion reaction at 325 ˚C illustrated that the methane conversions for the MgO, Al_2O_3 and TiO_2 supported catalysts were observed to be in the same range (13%, 16% and 21% respectively), while in the case of the MCM-41 supported catalyst, it was significantly lower at about 4% due to greater accumulation of hydroxyls on the support, as compared to the other metal oxide supports. As per Figure 1.4.a, the hydroxyl region in the FTIR spectra extends from around 3200−3800 cm^{-1}, which corresponds to weakly H-bonded surface hydroxyls bonded to the support, while in the case of MCM-41 only a single distinguishable peak appeared at 3734 cm^{-1}, corresponding to MCM-41 silanol peak at 325 ˚C. It had also been observed that the rate of deactivation depended on the support material. The Pd/Al_2O_3 and Pd/MgO catalyst illustrated unique patterns of short-term deactivation, while the PdO/TiO_2 and PdO/MCM-41 did not exhibit any deactivation within the 20-minute time frame as depicted in Figure 1.4.b. It was postulated that due to the high surface area of MCM-41 (at about 1,113 m^2/g), the hydroxyl accumulation per unit surface area for PdO/MCM-41 was correspondingly lower than the hydroxyl accumulation per unit surface area on the other catalysts. This could have accounted for the relatively slow rate of hydroxyl desorption from the PdO/MCM-41 catalyst, thereby providing lower methane conversions [67]. It is important to acknowledge that from FTIR spectra, it is not practically possible to distinguish hydroxyl groups from $Pd(OH)_2$ and those from the support.

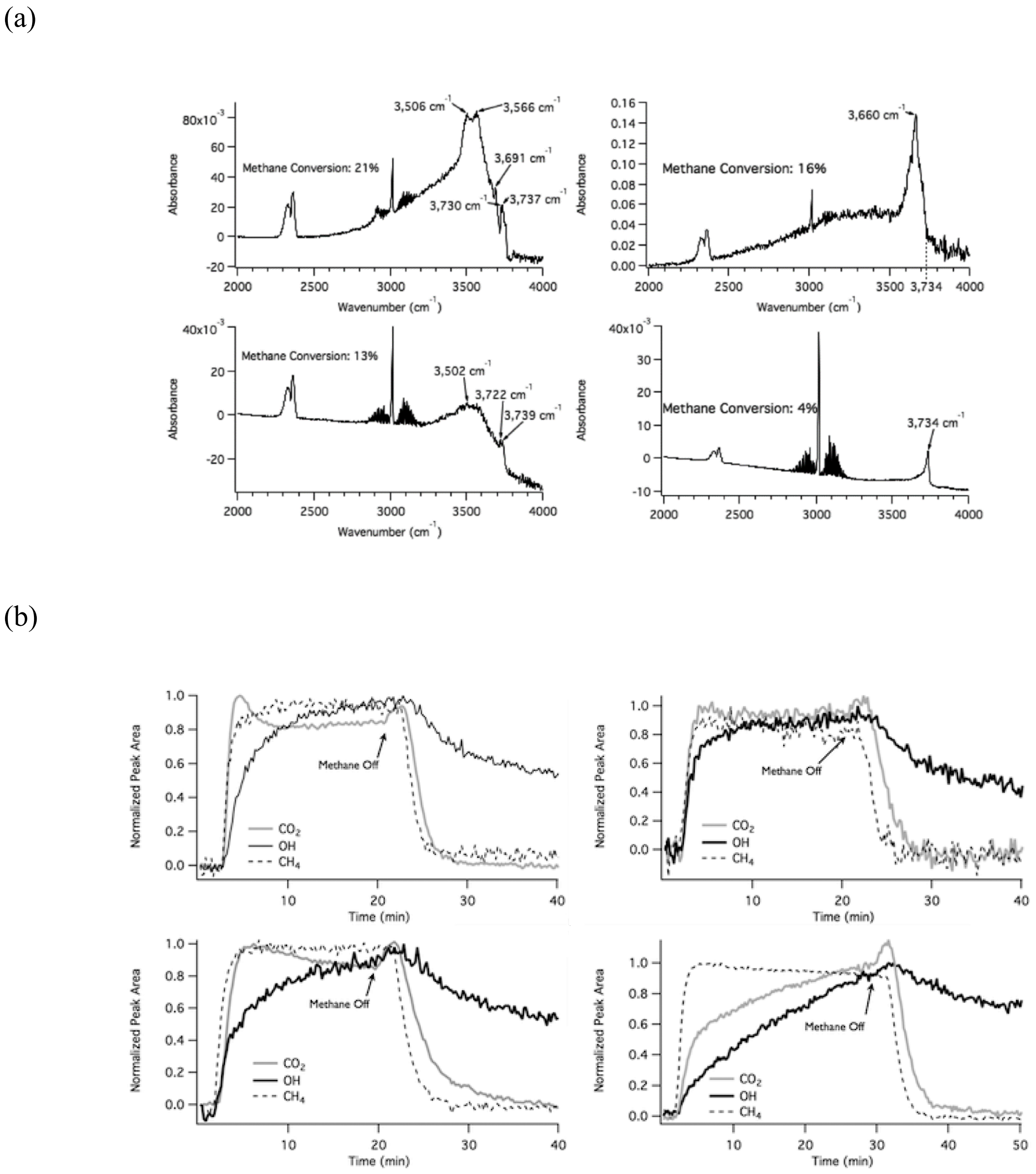

Figure 1. 4. (a) FTIR spectra during methane combustion at 325 ˚C over 3 wt % PdO/Al$_2$O$_3$ (top left), 3 wt % PdO/TiO$_2$ (top right), 3 wt % PdO/MgO (bottom left), and 3 wt % PdO/MCM-41 (bottom right); (b) analysis of deactivation trend by measure of hydroxyl accumulation during and after the methane combustion reaction at 325 ˚C for a time period of 50 minutes over the same catalysts as in Fig. 4(a) [67] *Reproduced with permission from* [67]. *Copyright © 2012, American Chemical Society*

These pioneering investigations of the support effect in wet methane combustion proved that the support material and its associated oxygen mobility could help decelerate the rate of catalyst deactivation, thereby improving the water tolerance significantly.

1.5. Metal oxides in catalytic combustion: oxygen binding energy

As we just established the importance of oxygen exchange in wet methane combustion, let us discuss the well-known phenomenon of how oxygen in metal oxides plays a crucial role in oxidations [68]. Thermochemical characteristics, namely, oxygen binding energy with the catalyst, has been determined to be a critical parameter defining the oxygen reactivity on the catalyst [68], [69]. In a generalized scheme for the oxygen activation process proposed in the 1980s'[70], the first step involved the primary activation resulting in the formation of highly reactive surface states of oxygen denoted by O_s. This step was then followed by the transition of these states into lattice oxygen of the catalyst denoted as O_r as depicted in Figure 1.5.a [70]. The O_s species could attack molecular sites with high electron density and thus result in the complete oxidation of organic molecules. The O_r species were identified to be more suitable for selective oxidation applications [70]. Boreskov and Muzykantov [69] carried out some isotopic oxygen experiments and demonstrated that the rate of oxygen binding was of paramount importance while considering a suitable catalyst for oxidation reactions. The authors proposed that complete oxidation could be facilitated by increased primary activation of oxygen and subsequently lower incorporation in the catalyst lattice, resulting in the formation of a large amount of active oxygen on the catalyst surface. Hence, it was identified that simple oxides of 3d elements had the highest rate of oxygen binding accompanied by the lowest heat of oxygen binding [68], [69]. The rate of transformation of the active oxygen into lattice oxygen was found to be dependent on the operating conditions such as temperature and the reaction mixture conditions. A sufficiently low concentration of oxygen vacancies would be required to be induced to decrease the rate of active oxygen to lattice oxygen transition. At lower temperatures, the rate-determining step (RDS) would be the decomposition of the oxidized surface species, while at higher temperatures the RDS would be the interaction between the oxidized hydrocarbon and the catalyst, by cleaving the weakest C-H bond of the hydrocarbon involved [68].

Taking into consideration the requirement of having highly reactive surface states of oxygen, in 2020, Murata et al. [71] reported a volcano plot as depicted in Figure 1.5.b, for methane combustion activity (in dry feed) against the support oxide formation enthalpy. Pd catalysts on Ɵ-Al_2O_3, γ- Al_2O_3, ZrO_2 and CeO_2 support which exhibited moderate values for oxide formation enthalpy demonstrated the highest activities due to the formation of Pd core-PdO shell structures. On the other hand, Pd nanoparticles deposited on supports such as TiO_2, SnO_2 and Nb_2O_5, depicted lower values of oxide formation enthalpy and hence were less active due to a lack of oxidation of the Pd particles to PdO. The catalysts were found to be inactive when Pd had been deposited on MgO and La_2O_3, as they had been completely oxidized to PdO as indicated by the high value of oxide formation enthalpy and could not be reduced by methane due to strong anchorage with the support [71]. Similarly, an earlier study by Willis et al. [72] performed on monodispersed Pd catalysts deposited on relatively inert (SiO_2), acidic (Al_2O_3), basic (MgO) and oxygen-donating support ($Ce_{0.8}Zr_{0.2}O_2$) did not show a statistically significant difference in reaction rates and activation energies for all the catalysts, except for the low activity of Pd/MgO, in dry methane combustion. The low activity on MgO was also assigned to enhancing the stability of the Pd-O bond. Chen et al. [73] compared (1 wt%)Pd@(9 wt%)ZrO_2/Si−Al_2O_3 core-shell catalyst with Pd@CeO_2. Wet methane combustion reactions for both the catalysts demonstrated that the light-off temperature shifted to higher temperatures, however, the shift was slightly less in the case of Pd@ZrO_2 and achieved 100% conversion at 500 ˚C while the Pd@CeO_2 could achieve 100% conversion only at 600 ˚C. Coulometric titration of Pd@ZrO_2 was carried out and based on the O_2 retrieved, the amount of oxygen that could be removed from the sample was determined to be 2 mol/mol of Pd. It was also observed that the reduction occurred over a wide range of P(O_2) and the reduction of both the PdO and ZrO_2 shell appeared to occur in a single gradual process. The observations led to the hypothesis that the metal-oxide interaction between Pd and ZrO_2 strongly enhanced the PdO stability which in turn significantly improved the catalytic performance [73].

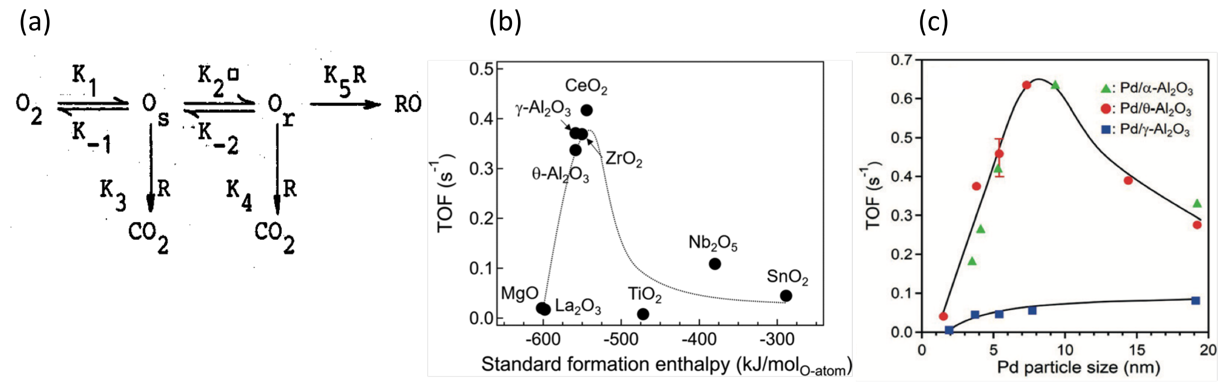

Figure 1. 5. (a) Schematic of the oxygen activation process [70]*, reproduced with permission from* [70]*; Copyright © 1969, Akadémiai Kiadó. (b) Turnover frequency (TOF) for dry-feed methane combustion at 300 °C using Pd catalysts against the standard formation enthalpy* ($\Delta_f H_{M\text{-}O}^{\circ}$) *of the metal oxide support* [71]*, reproduced with permission from* [71]*; Copyright © 2020, American Chemical Society. (c) Dependence of TOF at 300 ˚C on Pd particle size when deposited on different alumina supports* [74]*, reproduced with permission from* [74]*; Copyright © 2017 Wiley-VCH Verlag GmbH & Co. KGaA, Weinheim*

In another work by Dai et al. [75], the Pd/MnO_2 catalyst exhibited excellent performance in dry-feed methane combustion which was contributed to the redox properties of MnO_2 and its enhanced oxygen mobility. In a 2021 report by Li et al. [76], authors developed multi-element oxide (MEO) catalysts containing both easily oxidized and easily reduced elements with incorporated Pd; among those, a denary oxide $(Zr,Ce)_{0.6}(Mg,La,Y,Hf,Ti,Cr,Mn)_{0.3}Pd_{0.1}O_{2-x}$, labelled as 10-MEO-PdO exhibited high activity and stability in dry and wet methane combustion. Authors suggested that such element combination improves redox capability, creates more oxygen defects, and activates methane.

The use of CeO_2 as support for Pd in methane combustion deserves special attention as ceria is a known material with high oxygen storage capacity used in exhaust auto treatment. Various synthesis techniques have been addressed for improved performance. The most famous example is a work by Cargnello et al. on modular subunits of Pd@CeO_2 deposited on functionalized Al_2O_3. They reported exceptional activity in dry-feed methane combustion and high-temperature stability was attributed to the stabilizing effect of ceria subunits encapsulating Pd nanoparticles as well as the oxygen-donating capability of CeO_2 [77]. However, when this catalyst was exposed to the wet feed, its activity was significantly reduced [78]. As shown by Monai et al., the hydroxyl groups inhibited oxygen spillover from CeO_2 to Pd/PdO [78].

Employing a different strategy for ceria-based catalyst synthesis, Danielis et al. used a dry milling procedure to prepare Pd/CeO_2 (denoted as PdCeM) [79]. Metallic Pd nanoparticles were milled with CeO_2 powders in a mini ball mill to obtain a final loading of 1 wt%. Methane combustion runs under dry feed conditions demonstrated that the PdCeM catalyst surpassed the performance of the conventionally synthesized (by incipient wet impregnation, denoted as PdCeIW) catalyst and was also able to provide stable conversions under a six-cycle light-off test. To evaluate the hydrothermal stability of the catalyst, time on stream experiments with 10 vol% water was conducted for 24 hours, and the PdCeM catalyst reported a loss in activity of 25% as compared to a 70% activity loss for the PdCeIW catalyst. This improved performance could be attributed to the unique structure imparted by the synthesis methodology. The ceria crystallites were surrounded by an amorphous layer encompassing mixed Pd-Ce phases. As a result of the milling, more active oxygen states could be observed at the metal-oxygen interface, thereby, inducing a strong interaction between Pd and ceria resulting in a higher ceria reduction rate [79].

A study by Toso et al. [80] demonstrated that when $Pd/Ce_{0.75}Zr_{0.25}O_2$ catalyst was produced using a solution combustion synthesis (SCS) procedure, the catalyst provided an enhanced and stable activity in comparison to the same catalyst synthesized employing the traditional incipient wet impregnation technique. Methane combustion tests under both dry and wet (10 vol% water) feed conditions illustrated that the light-off curve shifted to a slightly higher temperature for the SCS catalyst under wet conditions, however not to a large extent as in the case of the impregnated catalysts. The reaction rate on the SCS catalyst was determined to be 6 times faster in comparison to the impregnated catalyst and upon the removal of water the SCS catalyst was able to recover its initial activity, confirming the presence of different and stable PdO species due to the beneficial presence of both CeO_2 and ZrO_2. The SCS catalyst could provide stable conversions due to the high oxygen storage capacity as well as the high degree of reduction of CeO_2 induced by the synthesis procedure. Furthermore, for the fresh and aged SCS catalyst the Pd particle size remained unaltered indicating the stability induced by the SCS method [80].

While speaking of an oxygen-donor capacity and ceria-based materials, we should mention that there are alternative oxides with a significantly higher capacity. For example, our recent study of various supports for Pd under dry feed with sub-stoichiometric O_2/CH_4 ratios revealed that Co_3O_4 donates its oxygen to the reaction at a higher extent and at a lower temperature as compared to the CeO_2 support [81].

Thus, supports with optimal oxygen binding energy and redox properties could provide beneficial strong metal-support interactions (SMSIs) and affect the Pd/PdO transformation process, which, in turn, is affected by the presence of water.

1.6. Pd nanoparticle structure sensitivity of methane combustion

One has to keep in mind that when comparing metal oxides as supports for Pd, the differences in catalytic behavior of Pd deposited on different supports could be due to the Pd particle size and structure effect. Typically, when Pd catalysts are prepared by impregnation of a support with a Pd molecular precursor, the support characteristics (surface area, porosity, surface chemistry) and synthesis method (metal loading, drying and calcination conditions, etc.) affect the Pd particle size and size distribution. Nanoparticles of various sizes and shapes feature different fractions of surface atoms with a certain number and orientation of neighbors, i.e., with varying electronic and geometric properties which affect the strength and mode of reactants and intermediates' chemisorption.

There is no consensus in the literature on the Pd nanoparticle structure sensitivity of methane combustion. Some studies report that the reaction is structure-insensitive [56], [63], [82], some others report the increased turnover frequencies on larger [32], [83] particles, although the majority of the studies were performed in the absence of water in the feed. Oxygen activation of Pd is known to be structure sensitive [29]. A recent study by Murata et al. in a dry feed [74] on Pd catalysts supported on different Al_2O_3 phases showed relatively mild differences in the catalytic activity of Pd/γ-Al_2O_3 with varying Pd particle sizes (Figure 1.5.c). However, Pd particles dispersed on Θ- and α-Al_2O_3 exhibited a volcano-shaped dependence on increasing particle size providing a specific high-activity for particles in the range of 5-10 nm. Turnover frequency calculated for the particles dispersed on γ-Al_2O_3 were lower than those dispersed on Θ and α-Al_2O_3. Authors suggested that the strong metal-support interactions between Pd and γ-Al_2O_3, arising from the pentacoordinate Al^{3+} sites, resulted in the formation of distorted Pd particles with a high fraction of corner sites, as compared to the other two catalysts, where the particles had a spherical shape with well-defined facets, thereby resulting in higher turnover frequencies [74].

For the monodispersed Pd nanoparticles in the range of 2 – 9 nm deposited on SiO_2, Al_2O_3, MgO, $Ce_{0.8}Zr_{0.2}O_2$, Willis et al. [72] observed only mild Pd size effect for any given support in dry conditions. However, when water was present in the feed, no structure sensitivity was observed for Pd/$Ce_{0.8}Zr_{0.2}O_2$, but apparent activation energy increased from 146 to 185 kJ/mol for Pd/Al_2O_3 catalysts with 3 and 9 nm Pd size, respectively. The Al_2O_3 support (98 m^2/g) was obtained by calcination of Pluralox TH100/150 at 900 °C for 24 h. The authors hypothesized that on Al_2O_3, the Pd particle morphology changes with the size in a different manner as compared to the ceria-zirconia support, and such sites are influenced by water to different extents suggesting structure sensitivity of water inhibition [72].

1.7. Effect of water and support on Pd reoxidation and $Pd(OH)_2$ formation

Throughout the history of methane combustion research, there was no consensus on the most active Pd or PdO phase, the preference being the oxidized PdO, although even some recent reports also provide evidence for metallic Pd as a sufficiently active phase [84]. In a 2019 study by an operando quick X-ray absorption spectroscopy of (dry) methane combustion on Pd/Al_2O_3 samples with different Pd nanoparticles sizes, Goodman et al. [85] observed the necessity of at least partial surface oxidation to PdO for the methane combustion to take place. Experimental evidence of Pd reoxidation inhibition by water was demonstrated by Monai et al. in 2015 via operando X-ray absorption near-edge structure spectroscopy (XANES) performed over 80 minutes at 600 °C on a (1 wt%)Pd@(9 wt%)CeO_2/Si-Al_2O_3 catalyst [78]. In the dry feed, palladium remained in PdO state, while in the same feed (0.5% CH_4, 2.0% O_2) but with 15% H_2O the fully initially oxidized PdO was reduced by 40% to Pd(0). The authors proposed that the hydroxyl groups formed by the dissociation of water on the oxygen vacancies inhibited the oxygen diffusion on the surface of the CeO_2 nanoparticles and hindered efficient Pd reoxidation, which resulted in the activity loss.

Nassiri et al. [23] demonstrated the temperature dependence of Pd oxidation in the wet feed. They started with a reduced Pd/Al_2O_3 catalyst and performed temperature-programmed methane combustion reactions in the dry and wet feeds while monitoring the Pd oxidation state by in situ XANES. Under dry reaction conditions, Pd(0) was fully oxidized to PdO already at 200 ˚C, while in the presence of added water in the system, oxidation to the more active PdO phase occurred gradually and only at the higher temperature range (Figure 1.6.b).

Toso et al. [86] showed that by doping Pd/CeO_2 catalyst with SiO_2, the mechanism of the PdO-Pd-PdO transformation and thus, the catalytic methane combustion activity could be altered. When tested under 10 vol% wet feed conditions, electron microscopy revealed that PdO-Pd transformation occurred via the formation of multi-domain Pd/PdO particles and the addition of silica to the catalyst decelerated the rate of decomposition of PdO causing it to occur at higher temperatures as compared to the case under the dry feed conditions. The shift in the PdO decomposition temperature could be attributed to the fact that the acid-base properties of the catalyst had been altered by the addition of SiO_2, thereby enhancing the complex redox properties of the catalyst. However, these experiments also revealed that the SiO_2 loading could influence the performance and any loading of SiO_2 above 2 wt% could result in accelerated deactivation under wet feed conditions (10 vol% water) due to possible accumulation of hydroxyls on silica which serves as an obstacle for oxygen exchange between the support and the active phase [86].

By a combination of temperature-programmed oxidation (TPO), reduction by CH_4 and reaction in the presence and absence of steam over pre-oxidized and pre-reduced Pd/Al_2O_3 catalysts, Goodman et al. [85] demonstrated that PdO is required for the reaction onset and that steam presence increases the temperature required for CH_4-TPR but does not affect the TPO peak and its position as compared to the dry conditions suggesting that the poisoning effect of H_2O is related rather to the CH_4 activation on PdO than to oxygen activation. However, the peak temperatures on the TPO and CH_4-TPR in the presence of water were the same and coincided with the reaction onset at 260 ˚C, implying that no definite conclusion can be made on the reaction RDS being Pd oxidation or methane activation.

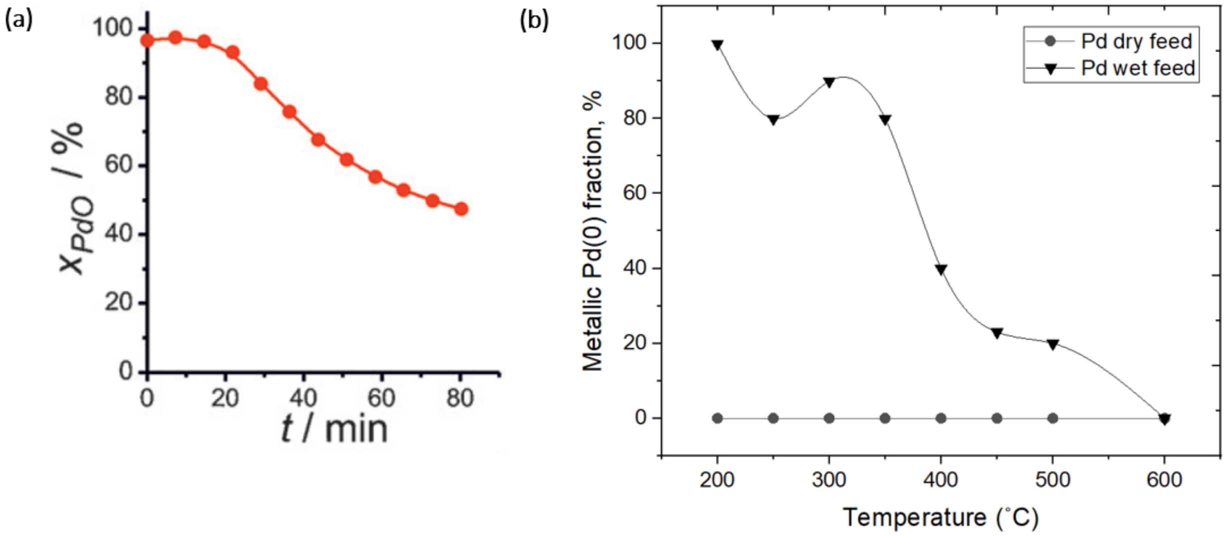

Figure 1. 6. Inhibition of Pd reoxidation as demonstrated by operando or in situ XANES in the wet feed: (a) kinetics of PdO transformation at 600 ˚C [78], *reproduced with permission from* [78]*; Copyright © 2015 WILEY-VCH Verlag GmbH & Co. KGaA, Weinheim; (b) Pd(0) oxidation in 200 - 600 ˚C temperature range in the wet and dry feed* [23], *reproduced with permission from* [23]*; Copyright © 2017 Elsevier Inc.*

Alyani et al. [87] reported that the addition of CeO_2 to the conventional Pd/Al_2O_3 catalyst resulted in an improved catalytic performance under 5 vol% wet feed conditions. Kinetic studies on the 6.5 wt% Pd/Al_2O_3 and 2.9 wt%CeO_2/6.5 wt%Pd/Al_2O_3, revealed that the addition of CeO_2 decreased the amount of adsorbed water and increased its desorption rate. XRD and XPS analysis illustrated that there was no $Pd(OH)_2$ formation in the presence of water on the CeO_2 promoted catalyst due to oxygen transfer facilitated by CeO_2 between the Pd-* (O-vacancy) and the support [87]. One should bear in mind, however, that XRD and XPS are ex situ techniques, the latter being performed under vacuum.

Quantitative analysis of $Pd(OH)_2$ formation during wet methane combustion as a function of temperature for selected Pd supported catalysts was first reported by Barrett et al. [24], [88].

They measured Pd K edge in in situ XANES spectra of pre-reduced Pd/Al_2O_3, Pd/Co_3O_4 and Pd/SnO_2 catalysts and performed fitting to the Pd spectra for PdO, metallic Pd and Pearlman's (Pd$(OH)_2$/C) catalysts (Figure 1.7). Metallic Pd in reduced Pd/Al_2O_3 catalyst (Figure 1.7.b) was progressively oxidized in situ during wet methane combustion mostly to Pd$(OH)_2$ with minor amounts of PdO; the maximum amount of formed Pd$(OH)_2$ was similar to Pd dispersion indicating metal nanoparticle surface hydroxylation. Above 450 °C, complete dehydroxylation and oxidation to PdO occurred, which is in line with the earlier observation of the temperature limit of Pd poisoning by water. Similar findings of Pd$(OH)_2$ surface formation were reported by Li et al. based on the ambient pressure X-ray photoelectron spectroscopy in situ studies of Pd/Al_2O_3 catalyst (Figure 1.8) [89].

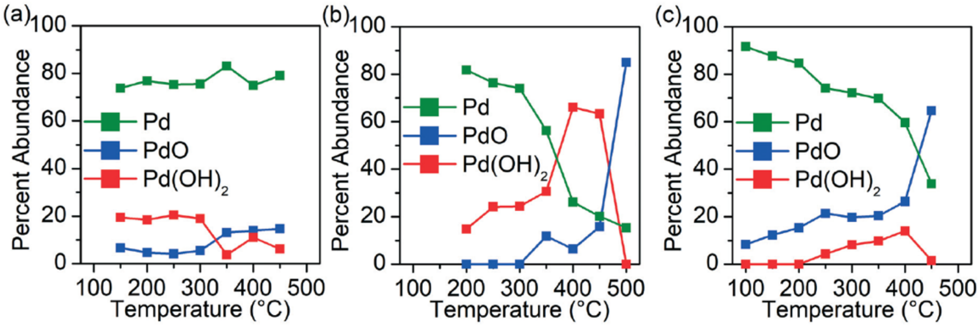

Figure 1. 7. Pd K edge XAS data for (a) Pd/CoO_x catalyst (b) Pd/Al_2O_3 catalyst and (c)Pd/SnO_2 catalyst and under in situ wet methane oxidation conditions [88]. *Reproduced with permission from* [88]. *Copyright © 2020, The Royal Society of Chemistry*

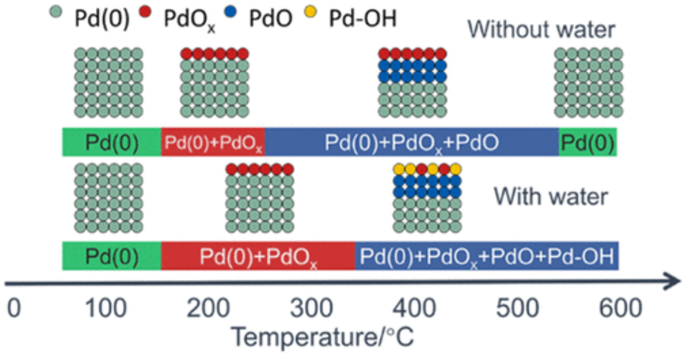

Figure 1. 8. Pd oxidation and hydroxylation during dry and wet methane combustion as determined by ambient-pressure in situ XPS [88]. *Reproduced with permission from* [88]. *Copyright © 2020, American Chemical Society*

Figure 1.7 demonstrates that with temperature increase, metallic Pd progressively oxidizes on Al_2O_3 and SnO_2 supports mostly to $Pd(OH)_2$ and PdO, respectively. Note that the maximum amount of $Pd(OH)_2$ in each graph (Figure 1.7) correlates with Pd dispersion on that particular catalyst, so $Pd(OH)_2$ formation is mostly a surface phenomenon of Pd/PdO nanoparticles on all supports. The Pd/SnO_2 tolerance to water inhibition is in line with its relatively high activity and stability during hydrothermal ageing (Figure 1.1). Co_3O_4 support did not suppress $Pd(OH)_2$ formation. Such behavior was explained by the thermodynamic affinity of Pd and supports to water when inactive $Pd(OH)_2$ can co-exist with the dehydroxylated Al_2O_3 and Co_3O_4, while only tin oxide can serve as a sink for water from $Pd(OH)_2$ based on the trend of the Gibbs free energy of dehydroxylation reactions (1.1)-(1.4) [24], [88]:

$$2/3\ Al(OH)_3 \rightarrow 1/3\ Al_2O_3 + H_2O;\ \Delta G^{\circ}_{573K} = -36\ kJ/mol_{H2O};\ \Delta H^{\circ} = 61\ kJ/mol_{H2O} \quad (1.1)$$

$$Co(OH)_2 \rightarrow CoO + H_2O;\ \Delta G^{\circ}_{573K} = -33\ kJ/mol_{H2O};\ \Delta H^{\circ} = 55\ kJ/mol_{H2O} \quad (1.2)$$

$$Pd(OH)_2 \rightarrow PdO + H_2O;\ \Delta G^{\circ}_{573K} = -25\ kJ/mol_{H2O};\ \Delta H^{\circ} = 30\ kJ/mol_{H2O} \quad (1.3)$$

$$Sn(OH)_2 \rightarrow SnO + H_2O;\ \Delta G^{\circ}_{573K} = -19\ kJ/mol_{H2O};\ \Delta H^{\circ} = 33\ kJ/mol_{H2O} \quad (1.4)$$

Among the Pd/Al_2O_3, Pd/Co_3O_4 and Pd/SnO_2 catalysts, the latter exhibited phenomenal inactivity methane steam reforming once methane was exhausted in fuel-rich feed during temperature-programmed reactions (Figure 1.9.a and 1.9.b) demonstrating Pd inability to activate water when deposited on SnO_2, which is in line with the exceptional water tolerance in methane combustion. The use of calibrated on-line mass spectrometer allowed evaluating the contribution of oxygen from a solid catalyst once molecular oxygen in the feed was exhausted. Neither Pd/Al_2O_3 nor Pd/SnO_2 catalysts donated any oxygen above what was stored in PdO [24]. Pd/Co_3O_4, on the other hand, provided a tithe of its lattice oxygen as manifested by the variation in the exhaust mass balance and formation of fully oxidized products (Figure 1.9.c) [90]. The phenomenon was not observed for a pure Co_3O_4 catalyst, which confirms SMSI between Pd and Co_3O_4 in oxygen activation for methane combustion.

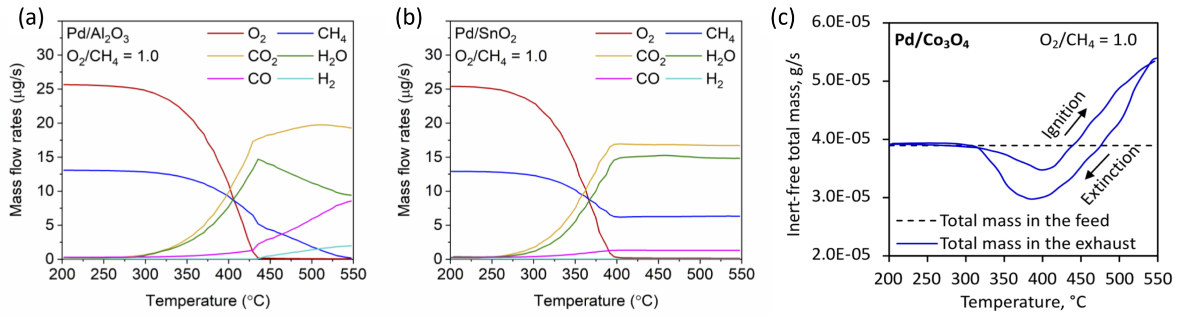

Figure 1. 9. Temperature-programmed reactions of methane-rich combustion on (a) Pd/Al$_2$O$_3$ [24], *(b)Pd/SnO$_2$* [24], *reproduced with permission from* [24]*; Copyright © 2019 Wiley-VCH Verlag GmbH & Co. KGaA, Weinheim and (c) Pd/CoOx catalysts* [81], *reproduced with permission from* [81]*; Copyright © 2019 Elsevier B.V.*

The important conclusion, considering effects discussed in Figures 1.7 and 1.9 [24], [88], [90] is that although easily reducible supports (such as Co_3O_4) do provide oxygen for methane combustion at the lack of O_2 in the feed, the governing factor in support effects for wet lean methane combustion is not support's reducibility, but its dehydroxylation feasibility as relative to PdO/Pd(OH)$_2$ equilibrium as per equations (1.1) - (1.4) above. This hypothesis brings us to recent studies where the support's affinity to water is suggested paramount in affecting the catalyst activity.

1.8. Role of support's hydrophobicity

Hydrophobic properties of the catalyst support can play a significant role in addressing the catalytic activity, particularly in reactions involving water formation [91]. In 2019, Losch et al. [92] performed a comparative study of Pd catalysts deposited on Al_2O_3 and zeolites with Si/Al ratios above 6 (Al leading to higher hydrophilicity) in wet methane combustion. Nineteen different mesoporous zeolites were prepared in total, using four zeolite frameworks (ZSM-5, MOR, Beta, USY), with different micropore sizes and different Si/Al ratios within each set. For a 0.1 wt% Pd catalyst under each set, methane combustion tests under 4.7 vol% wet feed conditions demonstrated that the Si-rich zeolites were able to surpass the performance of the Al-rich zeolites, indicating the undesirable effect of higher hydrophilicity. The results demonstrated that m-Beta(40) and m-USY(40), outperformed the γ-Al_2O_3 supported sample [92]. By quantifying the amount of water released at 350 ˚C, it was observed that m-Beta(40) and m-USY(40) did not strongly adsorb any water as it was detected within the first 30s on stream. By a combination of kinetic studies, temperature-programmed desorption of water and operando DRIFTS, the authors demonstrated that the zeolite's hydrophobicity prevented water accumulation and hydroxyl formation on the support in the vicinity of PdO (Figure 1.10) by adsorption/desorption on zeolite acid sites and molecular transport of water. Thus, Pd/zeolite catalysts displayed higher water tolerance than the hydrophilic Pd/Al_2O_3 catalyst.

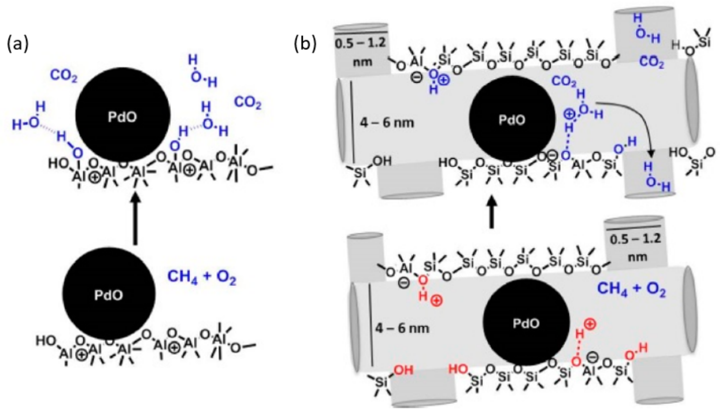

Figure 1. 10. (a) Fate of water on hydrophilic Pd/Al_2O_3 (b) Water transport mechanism via adsorption and desorption on the hydrophobic Pd/zeolite catalyst [92]. *Reproduced with permission from* [92]. *Copyright © 2019, American Chemical Society*

As an example, on how to render Al_2O_3 less hydrophilic, the alumina surface can be modified using triethoxy(octyl)silane (TEOOS). The silanol groups react with the OH groups of the alumina surface to form Si-O-Al bonds, or the silane molecules react with each other to produce multimolecular structures of bound silanes on the surface, thereby imparting a hydrophobic character to the support material [77].

In another study, Peng et al. [93] synthesized ultra-thin Pd-CeO_x nanowires (NW) and encapsulated them in a microporous SiO_2 shell resulting in a core-shell structure. The Pd-CeNW@SiO_2 catalyst provided 100% methane conversion at 350 ˚C as compared to the T_{100} of 375 ˚C and 425 ˚C for the Pd@SiO_2 and Pd/Al_2O_3 materials, respectively. In the presence of 5 vol% water, the Pd-CeNW@SiO_2 catalyst demonstrated stable conversions at 375 ˚C and 445 ˚C for 24 hours. The enhanced catalytic performance could be attributed to two factors. Firstly, the strong interactions and superior oxygen donating capability of CeO_2 significantly improved the methane combustion rate. Secondly, encapsulating the catalytic material in the microporous SiO_2 shell prevented accelerated agglomeration of the particles, thereby functioning as a shield against water and increasing the catalyst's hydrophobicity [93]. The important role of the support's hydrophobicity is also central to the following discussion on zeolites.

1.9. Zeolites as supports for Pd

In recent years, zeolites have received significant attention as Pd supports for methane combustion, not only due to their certain hydrophobic character as discussed above [92]. Zeolite's high surface area, well-defined pore structure and distribution of acid sites, as well as the ability to control the latter, are all attractive qualities for methane combustion reaction, where the small size of reactants facilitate their internal diffusion. A large disadvantage, however, which could be a potential killer variable for the use of zeolites in this application, is their low hydrothermal stability and propensity for pore collapse. As we review below, there are examples of such failures, as well as success stories to mitigate those effects by rational zeolite modifications.

Gannouni et al. [94] reported that the silica-supported Pd catalyst was more active as compared to the Pd catalyst on an aluminosilicate-support during the methane combustion reaction (under the conditions of 1% CH_4, 4% O_2 in He). On the aluminosilicate, the tetrahedral Al^{3+} functioned as anchoring sites for PdO thereby improving the metal dispersion. However, this contributed to a profound pore wall collapse, resulting in reduced metal accessibility and subsequently, lower catalytic activity [94]. Petrov et al. [95] conducted some experiments on 1 wt% Pd/H-ZSM-5 catalysts to investigate the activity of such zeolitic catalysts under both dry and wet feed conditions. It was observed that after calcination, the Pd/H-ZSM-5 catalyst contained well-dispersed particles in the size range of 1-2 nm. However, upon the introduction of the dry feed, the catalyst particles aggregated to achieve a final size in the range of 5-10 nm. Despite the initial aggregation, the catalyst was still found to be stable and provided 50% conversion at a temperature below 400 ˚C. When the catalyst was exposed to 5 vol% wet feed conditions, rapid deactivation occurred, and the methane conversion dropped from 25% to 10% in about 12 hours. Upon the removal of water, the activity did not recover to the level achieved under dry feed conditions, which was indicative of irreversible deactivation. It was illustrated that the PdO particles had sintered and also there was a collapse of the zeolite framework, causing possible deactivation and degradation of the catalyst [95]. A recent study by Friberg et al. [96] of Pd/LTA catalyst (Si/Al = 44) showed the catalyst stability when hydrothermal ageing (5% H_2O) was performed below 700 ˚C. At higher ageing temperatures (up to 900 ˚C), the catalyst deactivated not due to the structural collapse but to the excess formation of ion-exchanged Pd^{2+} and Pd sintering. To address the instability issues, Khivantsev et al. [97] also carried out some experiments on SSZ-39 supported Pd catalyst, with an optimum Si/Al ratio of 12 for methane combustion under wet feed conditions. The support material was found to be superior in terms of stability as hydrothermal ageing at 1000 ˚C did not induce any comprise in the structural stability of the material. For a 3 wt% Pd loading, it was found that these catalysts exhibited minimal deactivation under 2.7 vol% water upon being on stream up to 105 hours at 750 ˚C. These catalysts were able to surpass the performance of the conventional Pd/Al_2O_3 [97]. Dai et al. [98] synthesized $PdO/CeO_2/PdO$ catalysts supported on mesoporous SBA-15 silica through surface-assisted reduction. When the 1 wt% Pd catalyst was subjected to wet methane combustion under 5 vol% water at 370 ˚C the activity had dropped from about 98 to ~50%. After 20 hours, the flow of water from the stream was stopped and the catalyst activity recovered to 100% conversion. Even after the catalysts were subjected to hydrothermal stability tests, the mesoporous channel structure of SBA-15 was maintained, and the catalyst particles remained confined within the pores of SBA-15. This enabled to successfully avoid sintering of the PdO/CeO_2 catalyst particles, thereby improving the catalytic performance [98].

Similarly, Dai et al. [99] demonstrated that by coating HZSM-5 membrane on PdO/CeO_2 nanosheets, the thermal stability could be greatly improved due to the protection offered by the zeolitic membrane. The authors explored the effects of oxygen concentration and water (3 vol% and 10 vol% wet feed conditions) on the methane combustion reaction, The PdO/CeO_2@HZSM-5 catalyst exhibited a higher reaction rate with a stable catalytic performance as compared to the PdO/CeO_2 catalyst due to repression of PdO growth by the HZSM-5 coating, as well as due to the high hydrophobicity of the zeolite [99].

Several recent contributions by the group of van Bokhoven demonstrated how zeolites and Pd/zeolite catalyst synthesis can be altered to improve the catalyst stability in wet methane combustion. An acidic mordenite-based Pd catalyst demonstrated a rather expected loss of activity with time on stream [100]. However, when protons in Pd/H-MOR were ion-exchanged by Na^+, the catalyst demonstrated higher methane conversion which remained stable for 90 hours on stream. In the Pd/Na-MOR catalyst, the sodium ions prevented internal exchange and mobility of Pd (and thus its sintering), which occurred in the acidic catalyst [100]. A systematic study of various approaches to post-synthesis zeolite modification for the methane combustion catalyst development was reported by Petrov et al. [101] in 2019. The authors provided practical advice on how to address the causes of Pd/zeolite catalyst deactivation. For acidity-induced Ostwald ripening of Pd particles, acid sites can be exchanged with alkali metals or zeolites with high a Si/Al ratio can be used. The latter, however, decreases Pd^{2+} loading by ion-exchange. Pd nanoparticle agglomeration can be prevented by mild desilication when constricted mesopores with isolated nanoparticles are created. Another deactivation reason, specific to zeolites, such as the presence of poisoning extra framework species, can be addressed by selective dealumination. The authors demonstrated that the most stable catalysts (for ZSM-5 and MOR) could be obtained by desilication with NaOH, followed by dealumination with nitric and oxalic acid, Pd ion-exchange and Na exchange of remaining acidic sites. Thus, the modified Pd/Na-MOR-Dno catalyst showed stable methane conversion for 80 hours on stream in the presence of 5% water in the feed at 410 °C. The catalyst showed identical ignition curves before and after hydrothermal ageing with 10% water, performed at 600 °C for 24 hours. The synthetic approach was demonstrated for ZSM-5, MOR and BEA zeolite and Na, K, and Cs stabilizing ions, the nature of alkali ions not affecting the catalyst performance [101].

Similarly, Luo et al. [102] demonstrated that doping the zeolitic framework with alkali metals could prove to be beneficial to the catalytic activity. By utilizing an alkali metal hydroxide (MeOH, where Me- Li, Na, Cs and K) solution as a precipitant for synthesizing the catalyst via the deposition-precipitation method, the authors demonstrated that due to effective reduction in the Pd particle size by the precipitant, enhanced dispersions could be achieved. Moreover, the alkali metals functioned as an electron-donating component that could transfer electrons to the Pd species thereby bolstering the C-H bond cleavage with a subsequent decrease in the energy barrier for methane oxidation. It was also found that the extent of promoting effect by the alkali metals increased with an increase in the atomic number, hence illustrating that the Pd/H-ZSM-5-Cs catalyst exhibited the most enhanced methane combustion performance. This catalyst also delineated exemplary resistance against the wet and high temperature operating conditions (10 vol% at 750 ˚C for 15 hours) indicating the imparted high thermal stability to the catalytic system [102]. We have to note, based on section 1.9 below, that longer times on stream are required to fully confirm the aluminosilicate stability at hydrothermal treatments.

1.10. Consideration of promoters for Pd-based catalysts for methane combustion

For catalytic methane oxidation applications, the utilization of promoters is not uncommon. Promoters have been identified to enhance the catalytic performance either by improving the reaction rate [103]–[105], or by enhancing the thermal and chemical stability of the catalytic materials [77], [106], [107]. Various studies have been conducted to understand the mechanism by which a promoter could improve the catalytic activity [108]. Utilization of the oxides of rare earth metals such as La_2O_3 has been demonstrated to function as surface area stabilizers for support materials such as Al_2O_3 and ZrO_2 [109]. On the other hand, CeO_2 has gained popularity as a promoter due to its superior oxygen storage and release properties [110]. Transition metal (Ni, Cu, Mn, Co, Fe, and Cr) oxides have captured attention as potential candidates for promoting methane combustion reactions [111]–[113]. Pd/Al_2O_3 catalysts modified by Mn demonstrated stable methane combustion performance as it was observed that manganese helped to retard the decomposition of PdO to metallic Pd, owing to the higher oxygen mobility in the manganese oxide spinel structure [114]. Cobalt-modified Pd catalysts demonstrated excellent resistant to water poisoning in the presence and absence of water for lean burn methane combustion applications [115], [116]. Studies on CoO_x-promoted Pd/SiO_2 catalyst containing 20 wt% Co and 1 wt% Pd demonstrated exemplary catalytic performance for lean burn dry methane combustion. The authors suggested that the enhanced performance could be attributed to synergistic interactions between Pd and Co species [117].

In another study, Willis et al. [108] performed a systematic study to identify the promotional effects of various metals (V, Mn, Fe, Co, Ni, Zn, and Sn) for Pd-based methane combustion reactions. It was demonstrated that some metals (Fe, Co, and Sn) significantly helped to inhibit the sintering of the Pd particles while some metals (Ni and Zn) contributed to an increase in the intrinsic activity of the Pd catalyst [108]. Liu et al. [118] performed studies on metal oxides (Mn, Fe, La, Mg, and Ni) modified Pd/Al_2O_3 catalysts for lean-burn methane combustion. The authors demonstrated that the addition of Mg and Ni oxides to the catalyst formulation significantly improved the catalytic performance due to the formation of spinel structures on the surface of the support material [118]. A study on the highly stable Pd-Co/γ-Al_2O_3/cordierite catalyst by Li et al. [119] revealed that the presence of Co helped to decelerate the reduction of the active PdO phase to the metallic Pd phase under dry feed conditions. Todorova et al. [120] demonstrated that the incorporation of metal oxides of Ni and Co and mixed binary Co-Ce and Co-Mn oxides to the Pd/Al_2O_3 catalysts significantly improved that catalytic methane combustion activity due to the presence of highly dispersed and well stabilized PdO particles on the support surface. The presence of metal oxides could contribute to an increase in the surface oxygen species concentration thereby leading to a stabilization of the PdO species on the support surface [120]. Considering the advantages offered by promoters in enhancing the catalytic performance of Pd-based catalysts for lean-burn methane combustion reactions, it would be intriguing to investigate further the promoting effect of metals and metal oxides for similar applications under wet feed conditions. This work focuses on the utilization of a Co-promoter for lean-burn wet methane combustion applications. The choice for considering this promoter is elaborated in Section 4.1 of Chapter 4.

1.11. Decoration of Pd by support fragments

High-temperature silica volatilization in the form of hydroxyls in the presence of steam, including from aluminosilicates, is a well-known phenomenon. The type of species depends on the temperature and pressure, for example, $Si(OH)_4$ is the dominant product at 900 – 1100 °C at 1 atm pressure with 37% H_2O [121]. For lean methane combustion, with a maximum 550 °C operating temperature, this phenomenon is of lower concern, although the migration of silicon in an oxidative wet environment was reported to occur at 400 °C [122]. Gholami et al. investigated the effect of hydrothermal treatment at temperatures below 650 °C on a methane combustion Pd/SiO_2 catalyst [123]. The catalyst was subjected to thermal ageing for 16 hours in dry air and with 6.5 vol% water of air. The catalyst deactivation was found to be more severe when the catalyst was hydrothermally treated. It had been observed that the temperature of 50% CH_4 conversion had shifted from 250 ˚C for the calcined catalyst to 270 ˚C and 350 ˚C for the air-aged and hydrothermally aged catalyst, respectively [123].

Table 1. 2. Properties of 7.7 wt% Pd/SiO_2 catalyst after thermal treatments [123]. *Reproduced with permission from* [123]. *Copyright © 2014, Elsevier B.V.*

Treatment	BET area (m^2/g)	Pd/Si (at%)	Phase -	XRD (nm)	TEM (nm)
Calcined at 450 ˚C for 15 hours	291	1.29	PdO	5 (101)	2 ± 1
Air-aged at 650 ˚C for 16 hours	268	1.31	PdO	23 (101)	14 ± 6
Hydrothermally aged at 650 ˚C for 16 hours	274	0.98	PdO	11 (101)	3 ± 1

Based on the characterization data reported in Table 1.2, the average particle size increased from 2 nm for the calcined catalyst to 14 nm for the air-aged catalyst, while in the case of the hydrothermally aged catalyst the average particle size increased to only 3 nm. These results confirmed that the small PdO particles formed during calcination, grew further when subjected to thermal treatments. However, it was observed that the rate of growth of the PdO particles was retarded in the presence of water. Further clarification to the above observation was obtained by collecting the Raman spectra data for both the air-aged and hydrothermally aged catalyst. Based on the spectra, it was found that in the presence of water there was a lower conversion of Pd to PdO and subsequently lesser growth of the PdO crystallites. From the Pd/Si ratio as shown in Table 1.2, it could be concluded that migration of SiO_2 and occlusion of PdO could be a possible reason for deactivation observed in the case of the hydrothermally aged catalyst as compared to the air-aged catalyst [123]. The use of silica and aluminosilicates as supports, thus, requires prolonged times on stream to investigate their stability in wet methane combustion.

1.12. Effect of support diluents

The nature of a catalyst diluent, in terms of its water-retention ability, can also influence the observed Pd catalyst performance, assuming no other involved transport artefacts. Huang et al.

[124] measured retention of water produced from converted methane when Al_2O_3 diluent was used for either Pd/Al_2O_3 or Pd/SiO_2 catalysts (Figure 1.11). The authors proposed that water first adsorbed on the support until saturation, followed by hydroxyl accumulation on PdO. When the same catalysts were diluted with SiO_2, lower CH_4 conversion was observed, with concomitant release of steam, likely due to the inability of SiO_2 to adsorb any significant amount of water. This work illustrated that the dilution of the catalyst in the reactor should be performed with a truly inert powder, such as silica [124].

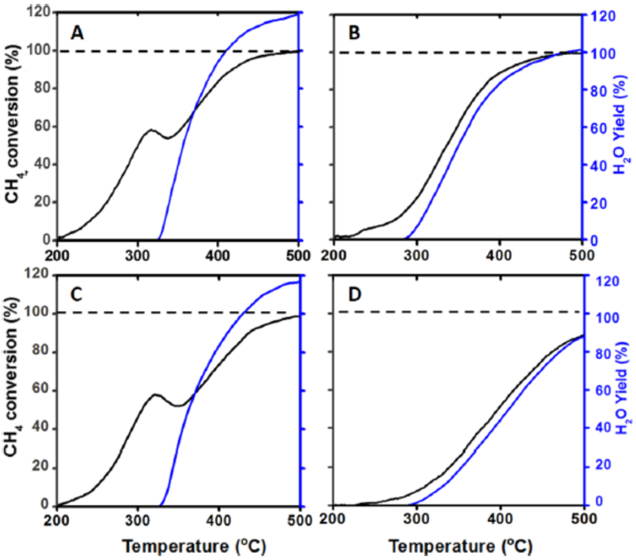

Figure 1. 11. Methane combustion activity over (A) Pd/Al_2O_3 diluted in alumina, (B) Pd/Al_2O_3 diluted in silica, (C) Pd/SiO_2 diluted in alumina and (D) Pd/SiO_2 diluted in silica [124]. *Reproduced with permission from* [124]. *Copyright © 2018, American Chemical Society*

Almohamadi et al. [125] analyzed the catalytic performance of 0.5 wt% PdO/γ-AlOOH/γ-Al_2O_3 monolith catalyst with varying concentrations of added CeO_2 (0, 1, 2 and 4 wt%) under both dry and 2 vol% and 5 vol% wet feed conditions. In the presence of water, ceria-containing catalysts provided superior conversions over the ceria-free system. When hydrothermal ageing tests were carried out under 10 vol% wet feed conditions, in the absence of CeO_2, the catalyst deactivated causing the conversion to drop to 50% in about 7 hours, while upon the removal of water the activity recovered only to 58%. In the case of the catalyst promoted with 2 wt% CeO_2, the activity had dropped to 70% in about 7 hours, however, upon the removal of water the activity rose to 80%. The addition of CeO_2 to the washcoat introduced hydrophobicity to the catalytic system, thereby causing a reduction in the adsorption of water on the catalytic surface [125].

As all great things are simple, Huang et al. [126] proposed eliminating poisoning water in the system by adopting diluents with excellent in situ water sorption properties. The catalytic performance of 40 mg 1 wt% Pd/CeO_2 catalysts were tested with 360 mg of different diluents, such as zeolites (H-beta, H-Y, and H-ZSM-5), SiC, γ-Al_2O_3 and CaO. The zeolite and alumina diluents provided higher conversions than the SiC-diluted control catalyst. Through temperature-programmed desorption (TPD), it was observed that the zeolites were capable of desorbing an appreciable amount of water, however, they could only adsorb a small amount of water at temperatures below 300 ˚C. γ-Al_2O_3 diluent could adsorb more water at the low-temperature range of interest (< 300 ˚C), enabling them to exhibit a high transient activity. The authors postulated that the presence of Lewis acid sites contributed to adsorbing more water during the reaction. Finally, a strong sorbent CaO was utilized as a diluent to carry out similar tests. Such a system exhibited a 6-fold improved methane conversion in comparison to the control catalyst. In the first stage, there was a complete reaction between water and CaO forming $Ca(OH)_2$ on the outermost surface, which was manifested by the absence of water emission. During the second stage, hydration was limited by water diffusion through the $Ca(OH)_2$ layer, and thus a small amount of water was detected from the reactor (Figure 1.12) [126]. The diluent could be regenerated to its original functioning level in diluted oxygen at 500 ˚C. Two parallel reactors were proposed to accommodate the reaction and regeneration modes of operation.

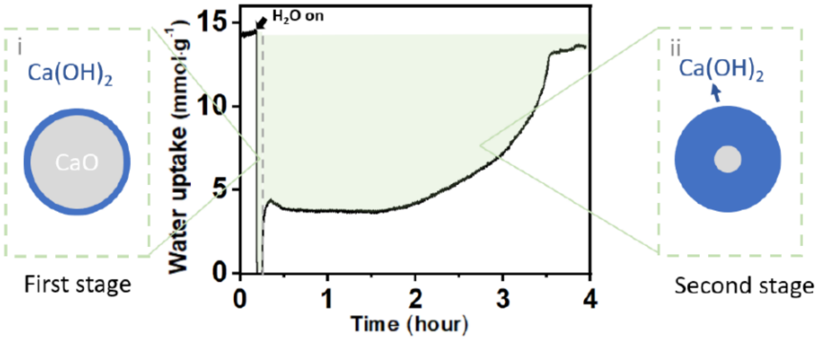

Figure 1. 12. Schematic of water uptake by CaO at 300˚C under 4.2 vol% wet feed conditions [126]. *Reproduced with permission from* [126]. *Copyright © 2018, American Chemical Society*

1.13. Specific recommendations for catalyst testing in wet methane-lean combustion

When assessing support effects in heterogeneous catalysis, it is important to perform experiments either without masking artefacts (such as difference in internal diffusion between different supports) or considering them during data analysis. In this section, we consider studies of fuel-lean wet methane combustion over PGM catalysts that have been reported by various authors, and also the experience that we have gained from our studies, not only of this topic but also other studies of automotive exhaust gas treatment. We use this as a basis for mentioning some important factors to consider and to make some recommendations for best practices when performing catalyst studies. Some of these best practices apply to any catalyst testing protocol, however, others are more specific to the methane combustion reaction. It should be borne in mind, however, that prior to starting on an evaluation of a catalyst, the objectives of the study should be determined. Depending on the goal, the experimental methods should be adapted accordingly. The sections below provide a general overview of the recommended testing practices. A detailed explanation of the experimental setup, testing procedure, and kinetic study are as elaborated in Chapter 2.

1.13.1. Experimental setup

It is always important to understand the purpose of the experiments. The main reasons for doing reactor studies are to evaluate the kinetics or to determine the catalyst's relative activity and resistance to deactivation. For kinetic studies, it is usually desirable to perform the experiments in the absence of heat and mass transfer limitation effects, or account for them. It is also advantageous to have the reactor behave in plug flow to simplify the analysis. The general criteria (based on the concept of Peclet number) to minimize the significance of by-passing and axial dispersion in the reactor is to ensure that the ratio of reactor diameter to particle diameter is greater than 10 and the ratio of catalyst bed length to particle diameter is greater than 50, respectively. For the laboratory studies, the catalyst is typically ground to attain particle sizes in the range of 40-50 μm, which are usually sufficient to mitigate the effects of internal diffusion resistance. The external diffusion limitations can be checked theoretically using the Mears criterion, to ensure that there is no existence of any mass transfer limitations. [7], [50], [127]. To incorporate the effects of the internal diffusion resistance, the effectiveness factor η should be accounted for. Based on the definition of the Thiele modulus, the effectiveness factor can be determined numerically by solving the diffusion-reaction equation. To neglect the effects of axial temperature gradients, ensure that the temperature difference across the bed is within 4 - 5 ˚C. Under isothermal and steady-state conditions, only the mole balance equation would then need to be solved [7], [50].

If the main desire is a simple activity comparison, then it is possible to relax some of these constraints. However, if it is desired to compare, for example, ignition curves, it is essential that the same basis is used for comparison. One might, for example, take a basis for the catalyst loading a fixed amount of PGM being present in the reactor. The ignition curve will also depend strongly on the gas hourly space velocity (GHSV) and, for transient experiments, the temperature ramp rate [5].

For studies with powdered catalysts, it is typical to use a micro-catalytic fixed bed reactor. Usually, small diameter reactors are employed to ensure an isothermal mode of operation [127]. The amount of catalyst loaded, and the length of the catalytic bed depends on the metal loading while preparing the catalyst. It should be noted that while packing the catalyst particles in the reactor, some amount of diluent should be added to minimize the temperature gradients in the reactor [7], [50]. The general rule of thumb is to ensure that the bed is not diluted more than 5 times by volume to avoid the effects of dilution (by-pass) on conversion [128]. If using ground monolith, this dilution may not be necessary because the catalyst is to some extent already diluted by the presence of the monolith substrate. The choice of the diluent should be such that it does not affect the kinetics of the combustion reaction and in no way can adsorb any water present in the system as elaborated in the work by Huang et al. [124], who recommended the use of SiO_2 as diluent. While assembling the reactor, layers of quartz wool are used on either side of the catalytic bed to ensure that the catalyst particles remain in place. The reactor is then placed in an electric oven equipped with a PID temperature controller. It is desirable to use two thermocouples to measure the catalyst bed temperature, one on either side of the bed. This approach allows the checking of the temperature rise across the bed. If a monolith is being used, then thin thermocouples should be inserted into the monolith channels, rather than simply measuring the upstream gas temperature. Ideally, several thermocouples would be used to measure the axial profile. Assure that appropriate mass flow controllers are present to regulate the flow rates of the feed gases.

To evaluate the inhibiting effects of water, liquid water can be pumped in at a controlled rate to provide 5 to 10 vol% water. Ensure that the reactor feed line is heated to vapourize water before it passes through the catalytic bed. The reactor effluent must be analyzed appropriately. If the reactor is being operated as a transient one, then rapid sampling and analysis are required, and for such purposes a calibrated on-line mass spectrometer or an FTIR is ideal. For steady-state experiments, a lower cost option is a gas chromatograph. In this case, it is preferable that the GC is equipped with TC and FI detectors and the water vapour must be removed through a cold trap, before analyzing the effluent [7], [50].

1.13.2. Testing procedure

Fundamental catalyst studies on, for example, metal-support interactions, can yield valuable information that allows for a basic understanding of catalyst function, which in turn leads to better material designs. In many cases, however, for an engineer, there will usually come a point where it is desirable to benchmark the catalyst performance against the competition. It may be of little value to state that Catalyst A is superior to Catalyst B if neither is of any practical interest. The use of commercial benchmark catalysts presents both opportunity and challenges. Commercial catalysts may be available in powder form, or as wash coated monoliths. In the case of monoliths, activity testing can be performed on small monolith sections cut from larger blocks. Typically, such cores are about 2.5 cm in diameter and 7.5 cm in length. Alternatively, the monoliths may be ground to powder and used as such.

Prior to the testing, catalyst de-greening must be performed. The catalysts are calcined in dry air at the highest temperature of the combustion reaction to burn off any carbon residues and to thermally age the catalyst. The choice of calcination temperature is dictated by the application, and a general rule of thumb that is applied is not to exceed the maximum process temperature. Therefore, for a lean-burn natural gas compression ignition engine, the maximum temperature to which the catalyst should be exposed is 550 ˚C, hence calcination in air at 550 ˚C for at least 16 hours would be preferred [7], [129]. Note that both catalyst suppliers and engine manufacturers use this criterion in their testing protocols.

It is important to choose correctly the catalyst loading in the reactor. The final space velocity must be chosen such that the conversion is complete within the temperature range of interest. For a lean-burn engine, the maximum temperature is 550 ˚C, however, complete conversion should be achieved at a lower temperature, of the order of 450 ˚C at the most. It is good practice to measure the conversion under dry conditions to measure the baseline activity, which then gives a measure of the susceptibility to deactivation by water. To measure activity loss from water, it is usual to age the catalyst in the presence of 5 to 10 vol. % water for around 72 hours, called hydrothermal ageing (HTA). Again, the temperature selected should be less than 550 ˚C. Because the conversion is likely to be 100 % during the whole ageing process, the reactor temperature can be lowered to some intermediate value periodically to follow the course of the deactivation [22], [49], for example, as depicted earlier in Figure 1.1.

Following ageing, the activity can be measured to determine the degree of deactivation. It should be pointed out, however, that the deactivation may not be permanent, and in the absence of exposure to water, the activity may slowly recover. Therefore, one might do one or two dry runs after HTA to check the activity, it is advisable to perform the desired runs in the presence of water immediately to avoid misleading results [7], [50].

1.13.3. Kinetic modelling

A myriad of works suggested reaction mechanisms and corresponding rate laws for methane combustion, reporting a positive (typically 1st) order to methane and negative (typically -1st) order to water for Pd catalysts supported methane combustion-inactive supports. To the best of our knowledge, support rarely has been directly included in the mechanistic model in reported studies, although different heats of water adsorption have been estimated for Pd deposited on different supports (for example [130], for Pd/Al_2O_3, Pd/SnO_2 and Pd/Al_2O_3-36NiO). A few exceptions include a review by Gholami et al. [27] who suggested the following mechanism (equations 1.5 – 1.7), based on the above-discussed studies by Pfefferle's group [17], [67]:

$Pd\text{-}O + S\text{-}^* \Leftrightarrow Pd\text{-}^* + S\text{-}O$ (1.5)

$Pd\text{-}^* + S\text{-}O^s \Leftrightarrow Pd\text{-}O^s + S\text{-}^*$ (1.6)

$Pd\text{-}^* + S\text{-}O^s \Leftrightarrow Pd\text{-}O^s + S\text{-}O$ (1.7)

where S is support, S-* is an oxygen vacancy on the support, and O^s is oxygen originally associated with the support.

Habibi et al. [131] introduced an additional step to account for water inhibiting oxygen exchange and mobility as equation (1.8) and developed a rate law satisfactorily describing wet lean methane combustion on a bimetallic catalyst:

$SO + H_2O \Leftrightarrow SO{\cdot}H_2O.$ (1.8)

As a pearl of conventional wisdom in reaction kinetics, the fact that the rate law developed from mechanistic models describes the observed kinetics does not prove that the suggested mechanism is correct, but rather that it is consistent with the catalyst behavior and support effect.

1.13.4. Catalyst characterization

As with a relatively fast deactivation occurring with Pd and supports in a high-temperature wet environment, the catalyst's prenatal, operando (or in situ) and postmortem characterization methods should ideally be applied to understand the reasons for deactivation, as well as promoting or inhibiting support effects. Table 1.3 summarizes some specifics of the catalyst characterization with regards to wet methane combustion, as discussed in detail in the above summary of the reviewed papers.

Table 1. 3. Summary of recommended catalyst characterization methods to study support effects on Pd catalysts for wet methane combustion

Method	Purpose of investigation
CO chemisorption	Pd dispersion [73], [78], Pd/PdO resistance to sintering, in combination with TEM and XPS indicates possible occlusion by support fragments [123]
TEM	Pd nanoparticle size and shape before and after catalysis, nanoparticle distribution on a support
XRD	Pd nanoparticle size (insensitive to ultrafine particles). For crystalline supports: crystallinity before and after reactions to assess support stability, e.g., for zeolites [95]
Physisorption of gases	Surface area and pore size distribution of supported catalysts before and after catalysis to assess mechanical stability
^{27}Al NMR	Zeolite framework stability and effect of extra framework species
Si, Al ICP-MS	Potential desilication of aluminosilicates after prolonged time on stream
TPD of water	Water uptake and retention by the hydrophilic/phobic support and catalyst [92]. Analysis by a calibrated mass spectrometer is recommended
CH_4-TPR without and with H_2O	TPR with CH_4 to evaluate lattice O participation in catalysis [24], [90]
TPO with and without H_2O	Potential inhibition of catalyst reoxidation by steam [132]
Operando infrared spectroscopy	Hydroxyl accumulation on the catalyst; unable to distinguish OH groups on Pd and support [66], [67]
Studies with $^{18}O_2$	A powerful tool to investigate oxygen exchange with the catalyst and participation in the reaction [17], [59], [60]
In situ XAS	Quantitative analysis of Pd speciation, including metallic, oxide and hydroxide [24], [78], [88]
Ambient pressure XPS	Quantitative analysis of surface Pd speciation [89]

1.14. Lessons from the literature review

The presence of water in the combustion system arises from water being one of the reaction products, and also the exhaust gases of a lean-burn NGV comprise around 10-15% water vapour. A conventional Pd/γ-Al_2O_3 catalyst demonstrates negative first order to water at temperatures below 450 ˚C. With the exhaust temperature not exceeding 550 ˚C and typical operating temperatures below 450 ˚C, this presence of water poses a challenge in the design of an active combustion catalyst. In the current scenario, one of the major requirements of an efficient catalyst in a lean-burn NGV would be water tolerance at low operating temperatures (i.e., at temperatures below 450 ˚C).

As a solution to improve water tolerance, incorporating Pt into the catalyst formulation and at a ratio of 1:1 Pd:Pt demonstrated stable catalytic performances. Kinetic studies on γ-Al_2O_3-supported Pd-Pt catalysts also demonstrated that the addition of Pt resulted in a reduction in the methane combustion activation barrier as opposed to that on the Pd catalyst. It was postulated that the enhanced catalytic activity and superior water tolerance on supported Pd-Pt catalysts could be attributed to the formation of metastable PdO/Pd-Pt aggregates that could participate in the reaction. While bimetallic Pd-Pt catalysts reported superior water tolerance, they were still susceptible to negative effects of water causing them to lose a part of their initial high activity. This could be possibly attributed to the increasing presence of inactive Pd^0 or $Pd(OH)_2$ on the surface.

It was demonstrated that Pd speciation (metallic, oxide of hydroxide Pd) during the reaction was found to depend strongly on the nature of the support. However, the distribution of species is not governed by the support reducibility but by its relative ability for dehydroxylation as compared to $Pd(OH)_2$. Hydroxyl accumulation can cause a decrease in the activity by possible disruption of oxygen transfer and this effect is found to be more profound on support materials that are intensely affected by water such as γ-Al_2O_3.

Those catalyst supports which can serve as a sink for the water released from $Pd(OH)_2$ had been recommended, such as SnO_2 support. The behaviour of the support could thus be related to the strength of water adsorption on the support.

1.15. Research hypothesis and thesis objective

Based on the literature review, we hypothesize that SnO_2-supported catalysts can surpass the performance of conventional PGM/γ-Al_2O_3 formulations in the exhaust aftertreatment from lean burn NGVs, by means of maintaining a high methane conversion under wet conditions. Though the water-tolerant behaviour of SnO_2 has been established earlier [24], some studies have demonstrated that long term exposure of the Pd/SnO_2 catalyst to the wet feed stream resulted in deactivation due to increase in particle size [27]. Thus, herein we hypothesize that:

- It is possible to improve the mass-based activity and hydrothermal stability of the Pd/SnO_2 catalyst by incorporating Pt to the catalyst formulation.
- It is possible to improve the mass-based activity and hydrothermal stability of the PGM/SnO_2 catalyst formulation by depositing a promoter (P) on the SnO_2 support surface.

To evaluate these hypotheses, the thesis aims to synthesize and to evaluate systematically a variety of SnO_2-support catalyst formulations in lean wet methane combustion with the overarching objective to develop a catalyst that would surpass the performance of the commercial PGM/Al_2O_3 catalyst in the exhaust aftertreatment of lean burn NGVs and meet the emission mitigation guidelines.

To test the proposed hypotheses, the following research objectives are planned:

- Assessment of Pd/SnO_2 and Pd-Pt/SnO_2 catalysts in terms of catalyst activity and hydrothermal stability.
- Development and assessment (in terms of catalyst activity and hydrothermal stability) of SnO_2-supported PGM catalysts with sequential deposition of a promoter (P) and PGM on the support surface.

There is a knowledge gap regarding methane combustion kinetics dedicated to addressing the potential benefits of utilizing SnO_2 support for wet methane combustion. Thus, all the above objectives will comprise kinetic studies in dry and wet feed, including the effects of hydrothermal aging. Furthermore, the catalysts will also be characterized following the hydrothermal ageing treatment to assess their catalytic activity.

1.16. Research plan

To accomplish the research objectives, the following tasks will be performed:

1. Synthesize high loading (1 wt.% total metal loading) Pd and Pd-Pt (1:1 Pd:Pt molar ratio) catalysts supported on γ-Al_2O_3 and SnO_2 support using incipient wetness impregnation method.
2. Evaluate the hydrothermal stability of the γ-Al_2O_3 and SnO_2-supported monometallic and bimetallic catalysts.
3. Develop a kinetic model for the γ-Al_2O_3 and SnO_2-supported catalysts to determine the kinetic parameters that could be utilized for the catalytic converter design.
4. Benchmarking the performance of the PGM/SnO_2 catalysts, perform a systematic study to choose an appropriate promoter (P) and optimize the promoter (P) loading ('y' in wt.%) in the catalyst formulation.
5. Synthesize the optimized 1 wt.% PGM/yP/S (S = γ-Al_2O_3, SnO_2) catalysts utilizing incipient wetness impregnation (similar component deposition and tests performed on the γ-Al_2O_3 support is for comparison purposes).
6. Asses the hydrothermal stability of the promoted PGM/S (S = γ-Al_2O_3, SnO_2) catalysts by subjecting the catalysts to hydrothermal ageing.
7. Perform kinetic modelling on the PGM/yP/S (M = γ-Al_2O_3, SnO_2) catalysts to obtain the kinetic parameters.
8. Compare the performances of the all-proposed catalyst formulations against the conventional PGM/γ-Al_2O_3 catalysts in terms of turnover frequency, reaction rate (per kilogram of catalyst) and water tolerance, to identify the most stable and active methane combustion catalyst.

1.17. Approach of the thesis

Chapter 1 of the thesis discusses the motivation for methane emission control from NGVs and the performance of Pd and Pd-Pt catalysts utilized in the catalytic converters of such vehicles. A detailed review of how the choice of support material can affect the catalyst's tolerance to water is elaborated. In addition to the summary of the most recent advances in the field, a brief section on recommendations for catalyst testing and characterization techniques that are specific to the application of interest is provided.

Chapter 2 of the thesis provides a brief discussion on the experimental setup utilized to carry out the hydrothermal ageing and kinetic studies. This chapter also delves into the formation of the differential equations utilized to obtain the kinetic parameters from the MATLAB code as well as the characterization techniques utilized to comprehend the catalyst structure post the ageing treatment to gain insight on the catalytic performance.

Chapter 3 of the thesis presents a kinetic study of lean-burn wet methane combustion on SnO_2-supported high loading (1 wt.%) monometallic Pd and bimetallic Pd-Pt (1:1 Pd:Pt molar ratio) catalysts. The hydrothermal stability and catalytic activity are compared against similar formulations supported on the conventional γ-Al_2O_3 support. The studies are carried out at varying methane concentrations and temperatures in the presence of 5 vol.% and 10 vol.% water. Kinetic consequences of the addition of Pt to the catalyst formulation as well as the effect of the choice of the support material are investigated. Using a rate model with a first order to methane and order 'n' to water, kinetic behaviour for all the catalyst formulations is modelled. While the bimetallic catalysts reported a -1 order to water, the Pd/SnO_2 catalyst reported a partial order to water. Attributing to the presence of different active sites in play, an additive rate model is proposed for the Pd/SnO_2 to predict the kinetic behaviour of the Pd/SnO_2 in the temperature range of consideration (200 ˚C – 550 ˚C). Utilizing the CO chemisorption data and the obtained kinetic parameter, turnover frequencies are estimated for each of the catalysts to help distinguish the performance of the catalysts under consideration.

Chapter 4 of the thesis builds on the knowledge gained on the performance of the Pd-Pt/SnO_2 catalyst and aims at improving the hydrothermal stability by incorporating cobalt as a promoter to the catalyst formulation. Employing the same catalyst loading as presented in Chapter 3, various Co promoter loadings are tested, and the optimal loading is identified to capitalize on the benefits offered by both Co_3O_4 and SnO_2. For comparison purposes, the promoter effect (based on the optimized Co loading) is investigated by performing kinetic studies on the Co-promoted

Pd-Pt/γ-Al_2O_3 catalyst. Kinetic studies and modelling are performed on the above-mentioned catalysts under the same testing conditions and rate models as illustrated in Chapter 3. Reaction rates ($mol_{methane}$ kg_{cat}^{-1} min^{-1}) were calculated and compared against the γ-Al_2O_3-supported catalyst formulations. This information could help translate the practical implication of utilizing the proposed catalyst formulations in a catalytic converter and consequently the required catalytic converter volume. As a first in the literature, this study demonstrates that optimized cobalt oxide deposition on the Pd-Pt/SnO_2 results in a catalyst with enhanced water tolerance and catalyst activity that could be exploited for the development of an efficient NGV exhaust converter catalyst.

Chapter 5 of the thesis presents the conclusions of this research along with recommendations for further investigation.

The appendices include:

- Appendix A provides the Supplementary Information for Chapter 3. It contains supporting calculations proving the inexistence of internal and external heat and mass transfer limitations for the catalysts considered in Chapter 3.
- Appendix B provides the Supplementary Information for Chapter 4. It contains supporting calculations proving the inexistence of heat and mass transfer limitations for the catalysts considered in Chapter 4. It also represents detailed calculations of the internal effective factor for the γ-Al_2O_3-supported catalysts.
- Appendix C provides the detailed MATLAB code used for the kinetic modeling studies in this thesis.

Chapter 2: Experimental Methodology

2.1. Materials

Palladium (II) nitrate dihydrate ($Pd(NO_3)_2.2H_2O$, ~ 40% Pd basis, Sigma-Aldrich), chloroplatinic acid (H_2PtCl_6, 8 wt.% solution in water, Sigma-Aldrich), aluminum oxide (γ-Al_2O_3, particle size 150 mesh, average pore size 58 Å, surface area 155 m^2/g, Sigma Aldrich), tin dioxide (SnO_2, ~ 325 mesh, 99.9% trace metals, Sigma-Aldrich), cobalt(II) nitrate hexahydrate ($Co(NO_3)_2 \cdot 6H_2O$, ACS reagent ≥98%), cobalt oxide (Cobalt(II,III) oxide, powder, <10 micron, Sigma Aldrich), cobalt aluminum oxide ($Al_2Co_2O_5$, Co 39 - 41%, Thermo Scientific Chemicals), and silica (SiO_2, 200-425 mesh, high purity grade, Sigma-Aldrich) are used as received. Milli-Q water (18.2 MΩ cm) is used throughout the work.

2.2. Catalyst synthesis procedure

All the catalysts studied in this work were synthesized using the incipient wetness impregnation method. The monometallic Pd (1 wt.%) and 1 wt.% Pd-Pt (1:1 molar ratio of Pd:Pt with 0.343 wt% Pd and 0.647 wt% Pt) catalysts are deposited with quantitative deposition of the required precursor amount on the respective support materials. In the case of the promoted catalysts, a sequential deposition of promoter precursor followed by PGM deposition is utilized. The as-synthesized catalysts are dried overnight in an oven at 60 ˚C; then, they are ground and mixed with SiO_2 diluent (size less than 270 mesh). The diluent is selected based on the recommendation provided in the work by Cargnello and coworkers as it does not affect the catalyst performance in wet feed [124]. The ground mixture is sieved (230-325 mesh, i.e., 44-63 µm) and subsequently subjected to calcination in air at 550 ˚C for 16 hours.

2.3. Experimental setup and catalyst testing procedure

2.3.1. Experimental reactor system

This thesis aims to perform kinetic studies on the catalytic oxidation of methane and obtain kinetic parameters. Methane combustion studies will be performed in a packed-bed reactor. The combustion setup consists of a reactor, furnace, thermocouples, temperature controllers, flow meters, gas (methane and dry air) flows, and water supplies. The methane combustion experimental setup (excluding the gas flow and water supplies) is illustrated in Figure 2.1. The micro-reactor is a 20″ long tubular reactor with an inner diameter of 3/8″. 0.12 g of Pd catalysts with 0.5 g of SiO_2 and 0.34g of the Pt-Pd catalysts with 0.25 g of SiO_2 will be loaded in the reactor for the methane combustion reaction, to achieve a total Pd loading of 1.2 mg. Layers of quartz wool are placed before and after the catalyst to contain the bed. The bed temperature is monitored by two K-type thermocouples inserted into the reactor. Thermocouples T1 and T2 are located before and after the catalyst bed, respectively. These thermocouples touch each end of the catalytic bed as depicted in Figure 2.1.

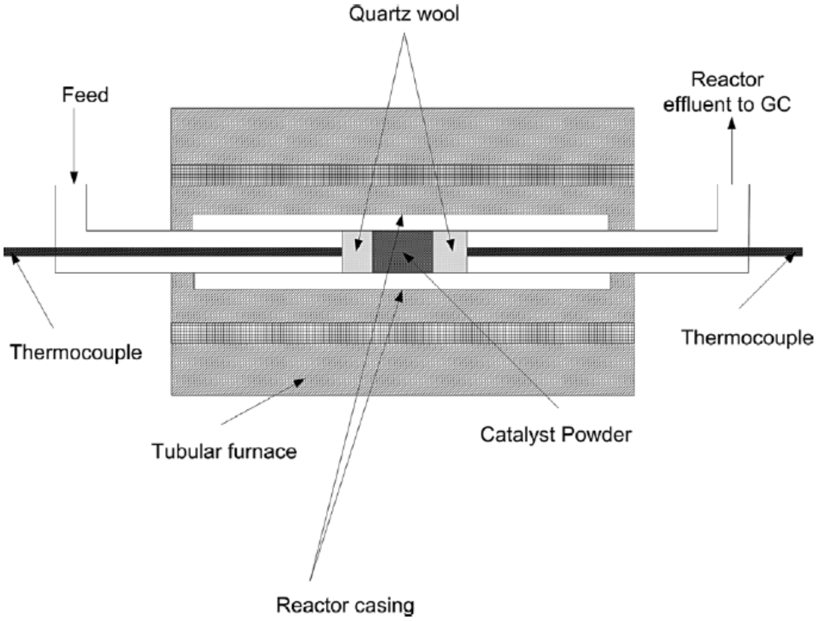

Figure 2. 1. Schematic of the reactor system [7]. *Reproduced with permission from* [7]. *Copyright © 2015, John Wiley and Sons*

The average of the temperatures recorded by these two thermocouples is reported as the reaction temperature. The maximum allowed temperature difference between the two thermocouples is about five degrees. A third thermocouple T3 is placed in the outer sleeve to ensure that the furnace reaches the desired temperature. The absolute reactor pressure is adjusted at 1.5 ± 0.3 atm. The reactor outlet is connected to a condenser to remove water accumulated during the reaction as well as that added during the reaction. The concentrations of CH_4 and CO_2 exiting from the reactor outlet (and passing through the condenser to remove water) are analyzed by an on-line gas Agilent HP-7980-A gas chromatograph equipped with a thermal conductivity detector (TCD) and a flame ionization detector (FID). The details of the gas chromatograph utilized are as follows: **Column:** HP-PLOT/Q, length 30 m, I.D. 0.530 mm, film 40 µm, He flow 3.2348 mL min^{-1}, **FID:** 275 ˚C, H_2 flow 40 mL min^{-1}, Airflow 400 mL min^{-1}, He flow 25 mL min^{-1}, **TCD:** 250 ˚C, Reference He flow 15 mL min^{-1}, He flow 0.5 mL min^{-1}, Oven: 40 ˚C. The experimental protocol is controlled by a LabVIEW program that controls the reactor temperature sequencing as well as the gas chromatograph.

2.3.2. Reactor feed gas

The feed gases for the methane combustion reaction consist of 10% CH_4 in N_2 and extra dry air and the flow rate of these gases was controlled by mass flow controllers (Matheson and MKS mass flow controllers). The flow rate of 10% CH_4 in N_2 will be varied from 2.2-11.2 mL$_{STP}$ min^{-1} depending on the desired initial CH_4 concentration (desired methane concentrations are varied and controlled through the LabVIEW program) while the flow rate of extra dry air will be maintained at 205 mL$_{STP}$ min^{-1} at STP conditions (0 ˚C and 1 atm). Thus, a total gas flow rate of 210 ± 5 mL$_{STP}$ min^{-1} (GHSV = 21,000 L$_{STP}$ kg$_{cat}^{-1}$ h^{-1}) is achieved. For the wet feed condition tests, water is added by a peristaltic pump (Lab Alliance 205SFM01 Series II Pump). The required water flow rate is varied and controlled through the LabVIEW program. Water is pre-steamed before being introduced into the methane combustion system. The feed line to the reactor is heated by utilizing a heating tape controller. The temperature inside the heating tape (and the point at which it touches the feed line) is measured to be 160 ˚C. Based on thermodynamic principles, water exists in the vapour phase at this temperature [133].

2.3.3. Ignition-Extinction (I-E) and kinetic study procedure

An initial set of dry and 10 vol.% wet ignition-extinction (I-E) curves are obtained at an inlet methane concentration of 4000 ppmv by increasing the temperature from 200 ˚C to 550 ˚C with 50 ˚C increments at a rate of 10 ˚C min^{-1} and then decreasing the temperature in the reverse order, to gain insight on the catalyst activity before hydrothermal ageing. The catalyst is then hydrothermally aged (HTA) *in situ* for 45 hours in the feed with 4000 ppmv CH_4 and 10 vol% H_2O by conducting 1-hour cycles between a lower temperature 'T' and 550 ˚C. The lower temperature (T) is chosen based on the previous 10 vol.% I-E test and is usually the temperature at which at least 50% methane conversion is achieved. After HTA, another set of dry and 10 vol% wet I-E curves is obtained in a similar manner as that before ageing to comprehend the effect of water on the catalyst activity. For the I-E tests, the temperature is held constant at each stage for 20 minutes with the post-combustion gases analyzed every 10 minutes (2 GC injections per temperature). For the hydrothermal ageing treatment, the temperature is held constant at each stage for 1 hour with the post-combustion gases analyzed every 15 minutes (4 GC injections per temperature).

For the kinetic studies, ignition curves are obtained by increasing the temperature from 200 to 550 ˚C in 25 ˚C increments at the rate of 10 ˚C min^{-1}. For a fair comparison, only ignition curves were recorded for each of the catalysts for the kinetic studies, as Pd only catalysts often show hysteresis in their ignition-extinction trends [33], [134]. During the ignition tests, the temperature at each stage will be held constant for 20 minutes, with the post combustion gases being analyzed every 10 minutes using the online gas chromatograph (2 GC injections per temperature). The ignition curves will be obtained for each methane concentration (from 1000-5000 ppmv) under dry and different water concentrations (5 vol% and 10 vol%) taken in a random order. Following each ignition test, the reactor will be purged with air to bring the temperature to 200 ˚C, to achieve the same state of catalyst for each condition. Through this procedure, an insight into the catalyst activity and as well as the kinetics of methane combustion can be acquired.

2.4. Kinetic data analysis

As a first step in analyzing the results of this work, a first-order reaction in terms of CH_4 is utilized to determine the observed activation energy, observed pre-exponential factor, and reaction order to H_2O. Assuming plug flow in the reactor, the results are analyzed at a constant temperature, using the average of the two thermocouples in the bed. In terms of catalyst mass W and fractional methane conversion (X_M), the following mole balance equations in the plug flow reactor are used:

$$-\frac{dF_M}{dW} = (-r_M) = k' C_M C_{aq}^n \tag{2.1}$$

$$\frac{dX_M}{dW} = k' * \left(\frac{1-X_M}{Q}\right) * \left(\frac{F_{aq0}+2F_{M0}X_M}{Q}\right)^n \tag{2.2}$$

where Q is the volumetric flow rate at the temperature and pressure in the reactor, subscript "M" refers to methane, "aq" to water, "0" to the flow rates in the feed at the reactor entrance. The gas flow to the reactor is measured by mass flow meters calibrated at STP. Hence, the inlet flow rate to the reactor is corrected for the appropriate inlet temperature and pressure as depicted below and implemented in Equation 2.2 for kinetic modeling.

$$Q = Q_0 * \frac{1\ \text{atm}}{P_I\ (\text{atm})} * \frac{T_I\ (\text{K})}{273.15\ \text{K}} \tag{2.3}$$

The rate constant is expressed in terms of the Arrhenius expression as follows:

$$k' = k_0\, .\exp\left(-\frac{E_a}{RT}\right) \tag{2.4}$$

where A is the observed pre-exponential factor (mol g_{PGM}^{-1} s^{-1} when overall reaction order was found 0, where PGM is Platinum Group Metal), E_a is the observed activation energy (kJ mol^{-1}), R is the universal gas constant (8.314×10^{-3} kJ mol^{-1} K^{-1}), and T is the reaction temperature (K).

For catalysts reporting a -1st order to water, rate constants were first determined analytically utilizing the equation below:

$$k = \left(-\frac{F_{W0}}{W}.\ln(1-X_M)\right) - \left(\frac{2F_{M0}\,X_M}{W}\right) - \left(\frac{2F_{M0}}{W}.\ln(1-X_M)\right) \tag{2.5}$$

Then utilizing the Arrhenius equation, kinetic parameters were obtained through linear regression of the rate constant determined utilizing Equation 2.5; the kinetic parameters obtained through such a process were utilized to fix the initial values and boundary conditions in the MATLAB code. The differential equation depicted in Equation 2.2 is utilized in the MATLAB code (refer to model1.m in Appendix C) to determine the kinetic parameters. In the differential equation, it is important to note that the water concentration takes into account the water added to the system as well as the water produced during the reaction.

For catalysts reporting a partial order to water, a rate equation with additive contributions is utilized. The first site is considered to be unaffected by H_2O, while the second active site is affected by H_2O with an order of -1 with respect to it.

$$(-r_M) = k_1 C_M + \frac{k_2 C_M}{C_{aq}} \tag{2.6}$$

$$\text{Where } k_1 = k_{01} \,.\exp\left(-\frac{E_{a1}}{RT}\right) \tag{2.7}$$

$$k_2 = k_{02} \,.\exp\left(-\frac{E_{a2}}{RT}\right) \tag{2.8}$$

For the Pd-only catalysts, the observed activation energy Ea_2 is fixed to be 158 kJ mol^{-1} resembling the apparent activation energy observed in the case of unsupported PdO catalysts [135] and Pd/γ-Al_2O_3 catalyst [136] for sites affected by water in the negative first order. For the Pd-Pt catalyst formulations, the observed activation energy Ea_2 is fixed to be 131 kJ mol^{-1} resembling the apparent activation energy observed in the case of the Pd-Pt/γ-Al_2O_3 catalyst [136].

Equation 2.6 can be written in the differential form for its implementation in the MATLAB code as follows:

$$\frac{dX_M}{dW} = \frac{k_1(1-X_M)}{Q} + \frac{k_2(1-X_M)}{F_{aq0}+2F_{M0}X_M} \tag{2.9}$$

For the γ-Al_2O_3 supported catalysts, an internal effectiveness factor is additionally incorporated to account for the internal mass transfer limitations as illustrated in Equation 2.10 (refer to model2.m in Appendix C for the MATLAB code). An internal effectiveness factor was calculated and utilized based on a first-order reaction rate to CH_4 (as the catalysts considered in this thesis depicted fractional conversions independent of methane concentration indicating a first-order behaviour to methane). Detailed calculation of the internal effectiveness factor is elaborated in Section B.3 of Appendix B.

$$\frac{dX_M}{dW} = \frac{\eta_1 k_1 (1 - X_M)}{Q} + \frac{\eta_2 k_2 (1 - X_M)}{F_{aq0} + 2F_{M0} X_M} \tag{2.10}$$

Calculations for verification of the existence of external heat and mass transfer limitations for each of the catalysts are elaborated in Appendix A and Appendix B. All the differential equations considered in this study are solved using the ode45 solver in MATLAB. The kinetic parameters are determined and optimized by utilizing the Pattern Search algorithm in MATLAB. For catalysts with a -1 order to water, only the observed activation energy and observed pre-exponential factor were determined and optimized while keeping the order to water constant (n = -1). For the catalysts reporting a partial order to water, the observed activation energy, observed pre-exponential factor, and the observed order to water was determined utilizing the optimization algorithm. Kinetic modeling is carried out under variable methane concentrations and temperatures. The objective function for the optimization problem is defined as per our previous work [131]:

$$O = \frac{1}{N} \sum_{i=1}^{N} \left(X_{\text{Predicted}} - X_{\text{Experimental}} \right)^2 \tag{2.11}$$

Optimization is carried out using the data corresponding to CH_4 conversion between approximately 15 and 85 % for all the reproducible ignition curve runs for each catalyst. The data for the 5 vol% and 10 vol% wet feed runs are optimized collectively utilizing the corresponding methane concentrations, temperatures, and conversions. The observed kinetic parameter values reported for each of the catalysts refer to the parameters estimated from the fitting algorithm. Numbers after the ± values for the kinetic parameters (activation energy and pre-exponential factor) for each catalyst represent the one standard deviation value from the estimated values. The detailed MATLAB code utilized for the kinetic modeling studies can be referred to in Appendix C of the thesis.

2.5. Catalyst characterization

To gain an insight into the catalyst structure and size, a variety of characterization techniques can be utilized. The collected information could help to analyze the surface structure of the synthesized nanoparticle formulations, which in turn would provide a more detailed understanding on the catalytic performance. In this thesis, all the characterization analyses are carried out on the hydrothermally aged catalysts. The techniques utilized in this thesis are enumerated as below:

2.5.1. Brunauer–Emmett–Teller (BET) Specific Surface Area Measurement

The BET theory is based on the principle physical adsorption of gas molecules on a solid surface, to calculate the total surface area which incorporates multilayer coverage for heterogeneous catalysts. It is a non-destructive method, wherein the isolated sites on the catalyst surface begin to absorb probe molecules such as N_2, Ar, Kr, CO_2 (choice of gas depends on an approximate knowledge of the pore size of the support) at low pressures and with increasing pressure multilayer coverage begins, with the smaller pores being covered first [137]. By means of utilizing the BET equation, the amount absorbed is measured and thereby the total specific surface area is calculated.

BET surface area measurements employing N_2 adsorption and desorption are carried out at -196.15 ˚C (77 K) using an Autosorb iQ analyzer (nanoFAB Fabrication & Characterization Center at the University of Alberta). Before analysis, the sample is degassed for 2.5 h at 150 ˚C for the SnO_2-supported catalysts and at 300 ˚C for the γ-Al_2O_3 supported catalysts under vacuum with a backfill gas of helium to remove any moisture or volatiles within the pores of the material.

2.5.2. X-ray Diffraction (XRD)

X-ray diffraction is an analytical technique utilized for identification of crystalline phases, calculation of particle size and observe how crystallinity/phase is reserved after a reaction or regeneration. The working principle involves X-ray photons being scattered by atoms in a periodic lattice, and the scattered monochromatic X-rays that are in phase provide a constructive interference. The angles of maximum intensity enable one to calculate the spacing between the lattice planes by utilizing Bragg's law and also allow for phase identification [138].

XRD profiles are obtained using the Rigaku Ultima IV D/max-RB diffractometer with D/Tex Ultra detector with Fe Filter (K-beta filter). The step scans are taken over a 2θ range of 5–90° with a step size of 0.02° and scan speed 2° min^{-1}, continuous scan mode. The radiation source used is a cobalt tube at 38 kV and 38 mA. Data is converted using JADE MDI 9.6 software and phase identification is done using DIFFRAC.EVA software with the 2022/2023 ICDD PDF 4+ and PDF 4+/Organics databases.

2.5.3. Temperature Programmed (TP) Techniques

Temperature programed methods comprise a plethora of techniques in which a chemical reaction is monitored as the temperature is increased linearly with time. These techniques are applicable to real catalysts and single crystals[138]In this thesis, the temperature programmed reduction/desorption (TPR/TPD) techniques would be utilized as they provide information on the temperature required for the complete reduction/desorption of a catalyst.

Temperature-programmed reduction (TPR) is performed using Micromeritics AutoChem 2950 HP instrument. Each of the aged catalysts are reduced in 5% H_2/He (10 mL min^{-1} with a ramping rate of 10 ˚C min^{-1}) at 550 ˚C to obtain the TPR profiles, followed by purging in He.

Temperature-programmed desorption (TPD) studies is performed in a Micromeritics AutoChem 2950 HP instrument equipped with an online Pfeiffer Vacuum Thermostar GSD 320 spectrometer. The mass spectrometer is calibrated for H_2O (m/z = 18), O_2 (m/z = 32) and an internal standard He (m/z = 4) before the characterization experiment. The aged catalyst samples are treated in He flow at 120 ˚C for 1h to remove physically adsorbed species. TPD is performed in He (50 mL min^{-1}) from 120 ˚C to 850 ˚C with a ramping rate of 5 ˚C min^{-1} and held at maximum temperature for 10 minutes. The ion currents for the m/z fragments assigned to water, and oxygen will each be scanned for 5s which (including He) will provide one complete scan every 20s.

2.5.4. CO Pulse Chemisorption

CO chemisorption is the most widely utilized technique for determination of active metal dispersion. Generally, the CO chemisorption occurs only on the surface atoms of the active metal nanoparticle and not by those on the support. In this technique, the catalyst is exposed to a known amount of CO, and then the amount of adsorbed CO is measured. The adsorbed CO is directly correlated to the number of exposed surface atoms of active metal, from which the dispersion can be calculated [139].

CO chemisorption is performed in a Micromeritics AutoChem 2950 HP instrument. The aged catalysts are reduced in 5% H_2/He at 150 ˚C, followed by purging in He. The CO pulse chemisorption analysis is performed by dosing a 3% CO/He gas mixture at room temperature. To calculate the metal dispersions, the CO:surface atom metal stoichiometric factor 1 is used.

2.5.5. Electron Microscopy techniques

Electron microscopy is a straightforward technique to determine the size and shape of the catalyst particles. Electrons have wavelengths of less than an angstrom, so they come close to providing an atomic detail. In principle, depending on the sample thickness, some electrons pass through the sample (transmitted), some electrons are diffracted, and some electrons collide with atoms and are scattered back. While in Transmission Electron Microscopy (TEM) the transmitted electrons are imaged, in Scanning Electron Microscopy (SEM) the back scattered electrons are imaged. In this thesis both the TEM and SEM imaging techniques are utilized. Additionally, these techniques are coupled with an Energy Dispersive X-ray analyzer (EDX), to yield compositional information as a function of position [140].

Transmission electron microscopy coupled with energy dispersive X-ray (TEM-EDX) analysis is performed using a JEOL JEM-ARM200cF scanning/transmission electron microscope with EDX

(Narwhal) operated at 200 kV accelerating voltage (nanoFAB Fabrication & Characterization Center at the University of Alberta).

Scanning electron microscopy coupled with energy dispersive X-ray (SEM-EDX) analysis is performed using a Quanta 250 Mineral Liberation Analyzer (FEI company). The scanning electron microscope utilizes a tungsten filament and a Bruker Xflush (133eV) detector for the elemental analysis at 15 kV accelerating voltage.

Chapter 3: Pd and Pd-Pt catalysts supported on SnO_2 and γ-Al_2O_3: Kinetic studies of wet lean methane combustion[2]

3.1. Introduction

Increasing economic growth and social development have led to an increase in the demand for energy [141]. Though the quest for the utilization of renewable energy is advancing, petroleum and natural gas still prevail as dominant choices. Due to its abundant reserves and low carbon intensity, natural gas serves as the most prevalent alternative transportation fuel [142]. Natural gas, predominantly composed of methane, burns relatively cleanly [143]; however, incomplete combustion has contributed to an unprecedented level of methane emissions to the atmosphere [144]. Hence, extensive research has been dedicated to catalytic methane reduction crucial to eliminating any fugitive sources of methane emissions arising from the exhausts of natural gas-fueled systems.

Natural gas-fueled lean-burn compression ignition engines must operate at relatively low-temperature ranges of 350-550 ˚C and in the presence of excess oxygen [12], [145] to comply with stringent emission standards [146] and enhanced energy utilization requirements [147]. However, this poses a problem due to the need for a highly active low temperature catalyst to overcome the large dissociation energy of C-H bond of methane (435 kJ mol^{-1}) [9].

---

[2] **Chapter 3** of the thesis has been published as: R. Sajiv Kumar, R.E. Hayes, N. Semagina, "Pd and Pd-Pt catalysts supported on SnO_2 and γ-Al_2O_3: Kinetic studies of wet lean methane combustion", *Chemical Engineering Science* 2023, **269**, 118488. The reaction setup for methane combustion was originally designed and built by Dr. Long Wu and Dr. Robert E. Hayes. All syntheses, reaction tests, data collection, interpretation and analyses of experimental results and other characterizations were performed by the author. The author drafted and implemented the MATLAB code for the nonlinear optimization and also performed the numerical analyses in this work. The paper was re-printed with permission from Reference [136] Copyright © 2023 Elsevier Ltd. and of the co-authors.

Considering the above requirement, catalysts based on noble metals, particularly Pd, are more widely employed in catalytic methane combustion due to their superior activity under lean-burn operating conditions [145]. However, a significant amount of water vapor (10-15 vol%) in the exhaust of automotive vehicles is known to be a major contributing factor to catalyst deactivation [148], [149]. It has been demonstrated that the inhibitory effect of water was only significant up to about 450 ˚C [14], [15], [27], [60], [78], which could be attributed to the formation of the inactive $Pd(OH)_2$ [32], [56], [150]. It has also been found that the presence and absence of water could alter the catalytic performance by affecting the oxidation state of Pd during the reaction. Under dry reaction conditions, Pd(0) readily oxidized to PdO in the temperature range of 200-550 ˚C. In the presence of added water in the system, oxidation to the more active PdO phase occurred gradually and only at higher temperature ranges [23], [88]. Hence, extensive research has been dedicated to improving the activity of Pd-based catalysts in methane combustion in the wet feed.

Several elegant solutions have been proposed in the literature to improve the Pd catalyst activity, particularly in the presence of water. [151], [152]. Experimental investigation by Nomura et al. [41] and Lapisardi et al. [43] revealed that the addition of Pt to the catalytic system improved the resistance of the Pd catalyst to water due to the presence of some synergistic effect in play between Pd and Pt. Experimental studies by Persson et al. [45] and Watanabe et al. [46] demonstrated that the bimetallic Pt-Pd catalytic systems with a higher Pt:Pd molar ratio offered enhanced catalytic activities in the presence of water. Nassiri et al. [23] proposed that in the presence of water, Pt catalyzed methane activation was observed. Further investigations by Nassiri et al. [49] also revealed that the 1:1 Pd:Pt catalyst provided the most stable conversions under lean-burn wet feed condition methane combustion studies. Pt vaporization and its subsequent trapping by PdO nanoparticles were suggested even below 550 ˚C in the presence of steam [49], similar to the phenomenon observed by Datye and coworkers at higher temperatures [44]. Studies by Goodman et al. [47] depicted that Pt incorporated catalysts remained unaffected by water due to the formation of PdO/Pd-Pt aggregates that could exhibit Pd-like activity.

Though the above-stated studies indicate that the addition of Pt can improve the catalytic performance, contrary opinions to the beneficial effects of adding Pt to the catalyst formulation have also been reported. Experimental studies by Nassiri et al. [52] on Pd-Pt/Al_2O_3 catalyst under lean-burn dry feed conditions revealed that Pt promoted the formation of reduced Pd under an oxidizing atmosphere thereby resulting in a retarded methane oxidation rate. Investigations by Nie et al. [54] demonstrated that increase in the Pt-Pd ratio led to a subsequent decrease in the catalytic activity under dry methane combustion due to the presence of a larger amount of inactive of Pt on the surface. Goodman et al. [47] reported that while the Pd-Pt/Al_2O_3 catalysts exhibited only slight changes in the reported activation energies under wet feed conditions, the same trend could not be observed under dry conditions. The bimetallic catalysts with higher Pt ratios particularly depicted this trend due to the prevention of the formation of the active PdO. The reported rates for the bimetallic catalysts under dry conditions were almost 200 times lower than that of the Pd catalysts [47]. Taking all the above-stated studies into consideration, the addition of Pt to the catalytic system seems to favor its application to provide enhanced stability and improved catalytic activity under wet feed conditions as opposed to the dry feed conditions. Hence, Pt addition to the catalyst formulation could serve as one of the potential solutions for the study explored in this work.

The issue of catalyst deactivation under wet feed conditions could also be tackled by choosing an appropriate support material. The support characteristics could influence the Pd particle size and chemical state, which is essential in promoting methane catalytic combustion [153]. It is known that the conventional Pd/Al_2O_3 catalyst progressively deactivates at temperatures below 500 ˚C under lean-burn conditions due to the possible water or hydroxyl accumulation on the active sites or support [124]. Schwartz and Pfefferle et al. [17] proved that hydroxyl accumulation caused a decrease in the catalyst activity by possible disruption of oxygen transfer and was more profound on support materials such as γ-Al_2O_3. Hence, the choice of support material or modifications to the support material becomes critical. In some studies, improving the hydrophobicity of the support material has proven to be beneficial for reactions associated with water formation [77], [91], [93], [154]. The inhibitory effects of water and the considerations for the rational choice of support material have been explained in detail in various review articles [6], [14], [36], [57]

SnO_2-supported Pd catalysts have captured some attention as they have been reported to have remarkable resistance to water-induced poisoning during methane combustion as compared to the benchmark γ-Al_2O_3 support material [22], [24]. Investigations by Sekizawa et al. [155] and Kikuchi et al. [156] revealed that the Pd/SnO_2 catalyst offered outstanding resistance to water due to its enhanced catalytic activity compared to the conventional Pd/Al_2O_3 catalyst under wet feed conditions. Sekizawa et al. [155] proposed that the improved catalytic performance in the case of Pd/SnO_2 catalyst could be attributed to the strong interaction between Pd and SnO_2 support resulting in improved oxygen adsorption. Similar conclusions were proposed from the investigations carried out by Barrett et al. [24] and Nassiri et al. [22]. These studies demonstrated that the Pd/SnO_2 catalyst offered a higher catalytic activity under high water concentrations due to the presence of the PdO phase even at 100 ˚C as compared to the Pd/Al_2O_3 catalyst. Evaluation of the dehydroxylation trend by Barrett et al. [24] indicated that in the case of SnO_2, water released from $Pd(OH)_2$ could be captured and stored by the support. These observations suggested that SnO_2 could serve as a sink to seize the water released from $Pd(OH)_2$ and would not induce any harm from the viewpoint of hydroxyls [24].

Considering the reported advantages of depositing Pd on SnO_2 and using Pt as a promoter to Pd, this work aims to investigate the kinetic behavior of Pd/SnO_2 and Pd-Pt/SnO_2 catalysts in wet methane-lean combustion and compare it with the behavior of the benchmark Pd/Al_2O_3 and Pd-Pt/Al_2O_3 catalysts. To the best of our knowledge, there are no available data on the kinetics of methane combustion over the Pd/SnO_2 and Pd-Pt/SnO_2 catalyst corresponding to the conditions usually found in environmental applications. Herein, kinetic studies at fuel lean-burn conditions were performed on the four above-mentioned catalysts under 5 vol% and 10 vol% water, and methane concentrations ranging from 1000 to 5000 ppmv, in the temperature range between 200 to 550 ˚C. The catalysts were hydrothermally aged prior to the kinetic study and verified for stable performance after their partial deactivation. The study aims to understand the kinetic consequences of using SnO_2 as catalyst support for Pd and Pd-Pt methane combustion catalysts and evaluate if it could provide an improved catalytic activity with enhanced stability under the lean-burn wet methane combustion conditions.

3.2. Experimental

3.2.1. Catalyst preparation

Palladium (II) nitrate dihydrate ($Pd(NO_3)_2.2H_2O$, ~ 40% Pd basis, Sigma-Aldrich), chloroplatinic acid (H_2PtCl_6, 8 wt% solution in water, Sigma-Aldrich), aluminum oxide (γ- Al_2O_3, particle size 150 mesh, average pore size 58 Å, surface area 155 m^2/g, Sigma Aldrich), tin dioxide (SnO_2, ~

325 mesh, 99.9% trace metals, Sigma-Aldrich) and silica (SiO_2, 200-425 mesh, high purity grade, Sigma-Aldrich) were used as received. Milli-Q water (18.2 MΩ cm) was used throughout the work.

The monometallic Pd (1 wt.%) and 1 wt.% Pd-Pt (1:1 molar ratio of Pd:Pt with 0.343 wt% Pd and 0.647 wt% Pt) bimetallic catalysts on γ-Al_2O_3 and SnO_2 were synthesized using incipient wetness impregnation with quantitative deposition of the required precursor amount. The as-synthesized catalysts were dried overnight in an oven at 60 ˚C; then, they were ground and mixed with SiO_2 diluent. The ground mixture was sieved (230-325 mesh, i.e., 44-63 μm) and subsequently subjected to calcination in air at 550 ˚C for 16 hours.

3.2.2. Catalyst characterization

All the characterization analyses were carried out on the hydrothermally aged catalysts. Temperature-programmed reduction (TPR) and CO chemisorption studies were performed using Micromeritics AutoChem 2950 HP instrument. Each of the aged catalysts were reduced in 5% H_2/He (20 mL min^{-1} with a ramping rate of 10 ˚C min^{-1}) at 550 ˚C to obtain the TPR profiles, followed by purging in He. Following the reduction treatment, CO pulse chemisorption analysis was performed by dosing a 3% CO/He gas mixture at room temperature. To calculate the metal dispersions, the CO:surface atom metal stoichiometric factor 1 was used. BET surface area measurements employing N_2 adsorption and desorption were carried out at -196.15 ˚C (77 K) using an Autosorb 1MP analyzer (nanoFAB Fabrication & Characterization Center at the University of Alberta). Before analysis, the sample was degassed for 2.5 h at 150 ˚C for the SnO_2-supported catalysts and at 300 ˚C for the γ-Al_2O_3 supported catalysts under vacuum with a backfill gas of helium to remove any moisture or volatiles within the pores of the material. Transmission electron microscopy coupled with energy dispersive X-ray (TEM-EDX) analysis were performed using a JEOL JEM-ARM200cF scanning/transmission electron microscope with EDX (Narwhal) operated at 200 kV accelerating voltage (nanoFAB Fabrication & Characterization Center at the University of Alberta). XRD profiles were obtained using Rigaku Ultima IV D/max-RB diffractometer with D/Tex Ultra detector with Fe Filter (K-beta filter). The step scans were taken over a 2θ range of 5–90˚ with a step size of 0.02˚ and scan speed 2˚ min^{-1}, continuous scan mode. Radiation source used was cobalt tube at 38 kV and 38 mA. Data was converted using JADE MDI 9.6 software and phase identification was done using DIFFRAC.EVA software with the 2022/2023 ICDD PDF 4+ and PDF 4+/Organics databases.

3.2.3. Methane combustion reactions

The kinetic studies were performed in a tubular packed-bed rector of 3/8" internal diameter. The reactor schematic and other details were described previously [129]. The catalysts with the SiO_2 diluent were charged into the reactor to achieve 1.2 mg Pd loading. The diluent was selected based on the recommendation provided in the work by Cargnello and coworkers [124]. 0.12 g of Pd catalysts with 0.5 g of SiO_2, and 0.34g of the Pt-Pd catalysts with 0.25 g of SiO_2 were used. The bed temperature was monitored by two internal thermocouples as described in [129]. The absolute reactor pressure was adjusted at 1.5 ± 0.3 atm. The concentrations of CH_4 and CO_2 at the outlet of the reactor were analyzed by online gas chromatography (Agilent HP-7890-A GC system; column: HP-PLOT/Q, length 30 m, I.D. 0.530 mm, film 40 µm, He flow 3.2348 mL min^{-1}, oven: 40 ˚C, flame ionization detector temperature 275 ˚C, thermal conductivity detector temperature 250 ˚C. The experimental protocol was controlled by a LabVIEW program. A mixture of 10 vol% methane in nitrogen and extra dry air (Praxair) were used for the combustion tests. Employing 19.5 vol% O_2, a total gas flow rate of 210 ± 5 mL_{STP} min^{-1} (21,000 L_{STP} kg_{cat}^{-1} h^{-1}) was maintained (Matheson and MKS mass flow controllers). Water was added via a heated reactor feed line to the system for the wet feed condition runs by a peristaltic pump (Lab Alliance 205SFM01 Series II Pump).

The catalysts were subjected to the hydrothermal ageing (HTA) for 45 hours by performing one-hour long cycles between 400 ˚C and 550 ˚C under 10 vol% wet feed conditions and 4000 ppmv CH_4 concentration. Each catalyst after the HTA treatment would be referred to as the aged catalyst. Before and after the HTA, a set of dry and 10 vol% wet ignition-extinction (I-E) curves were obtained at an inlet methane concentration of 4000 ppmv by increasing the temperature from 200 ˚C to 550 ˚C with 50 ˚C increments at a rate of 10 ˚C min^{-1} and then decreasing the temperature in the reverse order. The temperature was held constant at each stage for 20 minutes.

The kinetic studies were performed on the aged catalysts. Ignition curves were obtained for five methane concentrations (1000, 2000, 3000, 4000 and 5000 ppmv) under dry and different water concentrations (5 vol% and 10 vol%) taken in random order (Table A.1). The studies were carried out by increasing the temperature from 200 ˚C to 550 ˚C with 25 ˚C increments at a rate of 10 ˚C min^{-1}. The temperature was held constant at each stage for 20 minutes, and the post-combustion gases were measured every 10 minutes using an online gas chromatograph. Following each ignition test, the reactor was purged with air to bring the temperature to 200 ˚C to achieve the same state of catalyst for each condition. The runs were repeated until repeatable conversions were obtained.

3.2.4. Reactor model and optimization

For the analysis, steady-state mole balance in an ideal packed bed plug flow reactor with no pressure drop was solved to predict the conversion data, which were then compared to the experimental results. Wall effects and axial dispersion effects were verified [157], and it was observed that ideal plug flow conditions were satisfied. Similarly, the Mears criterion and the external and internal mass and heat transfer limitations were calculated as per our previous work [23] to ensure the absence of such limitations. The calculations used to verify these criteria are available in Appendix A (Section A.1) of the thesis.

Several models have been defined in literature to define the rate equation in the presence of water. Considering that water demonstrates a strong inhibition effect on Pd-based catalysts, it is common to see the rate expression expressed in a power-law form as follows [56]:

$$(-r_M) = k[CH_4]^m[O_2]^n[H_2O]^l \tag{3.1}$$

Typically, 'm' is near unity, 'n' is near zero in the case of most catalysts [158], [159], and 'l' is often close to negative one depending on the type of catalyst [56].

As a first step in analyzing the results of this work, we utilized a first-order reaction in terms of CH_4. We then determined the observed activation energy, pre-exponential factor, and reaction order to H_2O. Assuming plug flow in the reactor, the results were analyzed at a constant temperature, using the average of the two thermocouples in the bed. In terms of catalyst mass W and fractional methane conversion (X_M), the following mole balance equations in the plug flow reactor were used:

$$-\frac{dF_M}{dW} = (-r_M) = \frac{kC_M}{KC_{aq}^n} = \frac{k'C_M}{C_{aq}^n} \tag{3.2}$$

$$\frac{dX_M}{dW} = \frac{\frac{k'(1-X_M)}{Q}}{\left(\frac{F_{aq0}+2F_{M0}X_M}{Q}\right)^n} \tag{3.3}$$

where Q is the volumetric flow rate at the temperature and pressure in the reactor, subscript "M" refers to methane, "aq" to water, "0" to the flow rates in the feed.

The kinetic parameters in Equation 3.3 were determined and optimized by utilizing the Pattern Search algorithm in MATLAB. The objective function for the optimization problem was defined as per our previous work [131]:

$$O = \frac{1}{N}\sum_{i=1}^{N}\left(X_{Predicted} - X_{Experimental}\right)^2 \tag{3.4}$$

For catalysts reporting a -1 order to water, rate constants first were obtained analytically; the linearly regressed kinetic parameters were determined utilizing the Arrhenius equation. Adopting the kinetic parameters obtained through such a process, the initial values and the bounds for the optimization process was fixed in the MATLAB code. Optimization was carried out using the data corresponding to CH_4 conversion between approximately 15 and 85 % for all the reproducible ignition curve runs for each catalyst. The data for the 5 vol% and 10 vol% wet feed runs were optimized collectively. The rate constant was expressed in terms of the Arrhenius expression as follows:

$$k' = k_0 \,.\, \exp\left(-\frac{E_a}{RT}\right) \tag{3.5}$$

where A is the observed pre-exponential factor (mol g_{PGM}^{-1} s^{-1} when overall reaction order was found 0, where PGM is Platinum Group Metal), E_a is the observed activation energy (kJ mol^{-1}), R is the universal gas constant (8.314 × 10^{-3} kJ mol^{-1} K^{-1}), and T is the reaction temperature (K).

3.3. Results and Discussion

3.3.1. Hydrothermal ageing

The ignition-extinction (I-E) results under the 10 vol% wet conditions for an initial methane concentration of 4000 ppmv are shown in Figure 3.1.a. The I-E curves for the dry runs under the same testing conditions are depicted in Figure A.1. Hydrothermal ageing (HTA, Figure 3.1.b) was performed under 10 vol% added water and 4000 ppmv methane concentration by cycling the temperature between 400 and 550 ˚C for a total duration of 45 hours. Following HTA, it was evident that the addition of Pt to monometallic Pd catalysts slowed down their deactivation. Pd/SnO_2 catalyst provided higher conversions than the conventional Pd/γ-Al_2O_3 catalyst. The I-E trends following HTA also depicted that the Pd-Pt catalysts exhibited similar activities irrespective of the support material.

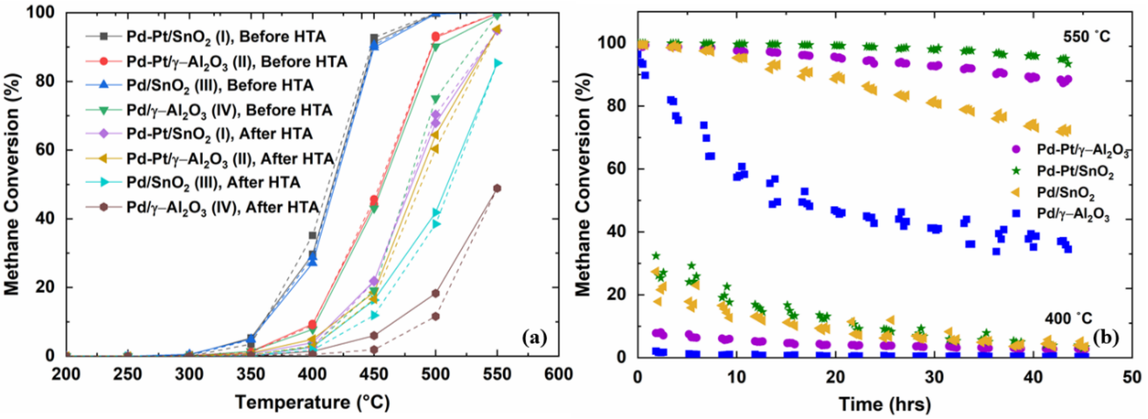

Figure 3. 1. (a) I-E curves for runs before and after hydrothermal ageing (HTA) under 10 vol% wet feed conditions for 4000 ppmv methane concentration (solid lines – ignition curves and dashed lines – extinction curves); (b) HTA curves under 10 vol% wet feed conditions for 4000 ppmv methane concentration

The catalysts after HTA were used for the following kinetics studies. The metal dispersion in the hydrothermally aged catalysts was evaluated by CO chemisorption as 12% and 11% for the aged Pd and Pd-Pt catalysts deposited on γ-Al_2O_3, and 4% and 5% for the aged Pd and Pd-Pt catalysts deposited on SnO_2. Pt addition did not improve metal dispersion. Larger particle sizes for the SnO_2-supported catalysts are expected because of the lower support surface area (The calculated external surface area for the hydrothermally aged SnO_2-supported catalysts was ~ 6 m^2/g which could be correlated to the reported BET surface area of 6 m^2/g, indicating that the catalyst is non-porous. The catalyst also depicted a Type II isotherm, consistent with those reported for a non-porous system. The hydrothermally aged γ-Al_2O_3-supported catalysts on the other hand reported a BET surface area of 140-144 m^2/g, pore diameter of 5.5-5.6 nm, and a Type IV isotherm, indicating that the catalytic system was mesoporous. The isotherms and the pore size distribution are as depicted in Figures A.2 and A.3 respectively). Thus, the positive effect of Pt addition and use of SnO_2 is unlikely attributed to the metal dispersion.

Figure A.4 represents the TPR profiles for the hydrothermally aged catalysts. In the case of all four catalysts, the negative peak refers to the low-temperature PdO reduction, Pd hydride formation, and decomposition. In the case of the SnO_2-supported catalysts, the first three low-intensity reduction peaks (α, β, γ for pure SnO_2 and α', β', γ' for SnO_2-supported catalysts) can be assigned as follows : the α peaks can be assigned to anionic oxygen [160], the β peaks can be assigned to the reduction of surface adsorbed oxygen species, lattice oxygen in the SnO_2 surface, and amorphous SnO_2 [161], and the γ peaks can be assigned to dissociatively adsorbed oxygen on the SnO_2 surface that participate in CH_4 oxidation [162], [163]. The sharp increase in hydrogen consumption for the SnO_2-supported catalysts beyond 450 ˚C corresponds to the reduction of bulk SnO_2 to metallic Sn [164], [165]. It is known that bulk SnO_2 reduction occurs at temperatures above 500 ˚C [166]; however, adding Pd expectedly shifts the SnO_2 reduction at lower temperatures due to hydrogen spillover from reduced Pd. These findings align with those observed by Barrett et al. [24] and Nassiri et al. [22], and it could also be concluded that the addition of Pt does not affect the reducibility of the support materials considered in this study.

High-resolution TEM of the hydrothermally aged catalysts (Figure A.5) demonstrated that all observed lattice spacings for Pd species in Pd/γ-Al_2O_3 catalyst belong to the metallic Pd, no PdO formation was noticed. When Pd was deposited on SnO_2, both metallic Pd and PdO were distinguished. These observations are in line with the earlier in situ X-ray absorption spectroscopy findings that water presence inhibits Pd reoxidation on the alumina-supported catalyst to a larger extent than on the tin oxide-supported Pd [23], [24], which is responsible for the higher activity and water tolerance of Pd/SnO_2 catalyst.

Investigation into the TEM-EDX images of hydrothermally aged Pd-Pt/γ-Al_2O_3 catalyst (Figure A.6) revealed the formation of clusters of bulk Pd-Pt alloy. The lattice fringe was measured to be 0.2258 nm which confirmed the formation of the Pd-Pt alloy. The formation of such structures has also been reported in the studies by Yang et al. [51] and Goodman et al. [47] on the Pd-Pt/γ-Al_2O_3 catalyst under similar testing conditions. Pd segregation to the surface was observed owing to the smaller surface free energies for Pd than Pt, resulting in the preferential migration of Pd onto the small alloy clusters to minimize the overall Gibbs free energy of the system. In some portions of the TEM, a Pd-rich phase was observed to segregate out. The lattice fringe was measured to be 0.265 nm, which is typically expected for the PdO {101} phase. Hence, hydrothermal ageing has resulted in the existence of PdO/Pd-Pt structures, with PdO segregating out as a separate phase co-existing with alloyed Pd-Pt aggregates, which is in line with similar observations reported by Goodman et al. [47]. For the aged Pd-Pt/SnO_2 catalyst (Figure 3.2), similarly to the Pd-Pt/γ-Al_2O_3 catalyst, PdO segregation was observed, as well 0.23 nm lattice fringe, which could correspond to the Pd-Pt alloy structures. The formation of these PdO/Pd-Pt structures could attribute to the observed improvement in the methane combustion activity and the ability to provide enhanced stability to the bimetallic catalyst performance.

The XRD analysis of the hydrothermally aged catalysts (Figure A.7) could corroborate the findings from the TEM-EDX analysis. The bimetallic catalysts exhibited peaks for Pd, Pt, and PdO phases, validating the possibility of PdO segregating out as a separate phase and co-existing with alloyed Pd-Pt aggregates [47]. While only a majority of Pd peaks were observed for the aged Pd/γ-Al_2O_3 catalyst, the Pd/SnO_2 catalyst exhibited a distribution of peaks for both the Pd and PdO phases, further verifying the observations of the TEM-EDX images. These PdO-Pd structures could contribute to an enhanced methane combustion activity compared to the benchmark Pd/γ-Al_2O_3 catalyst.

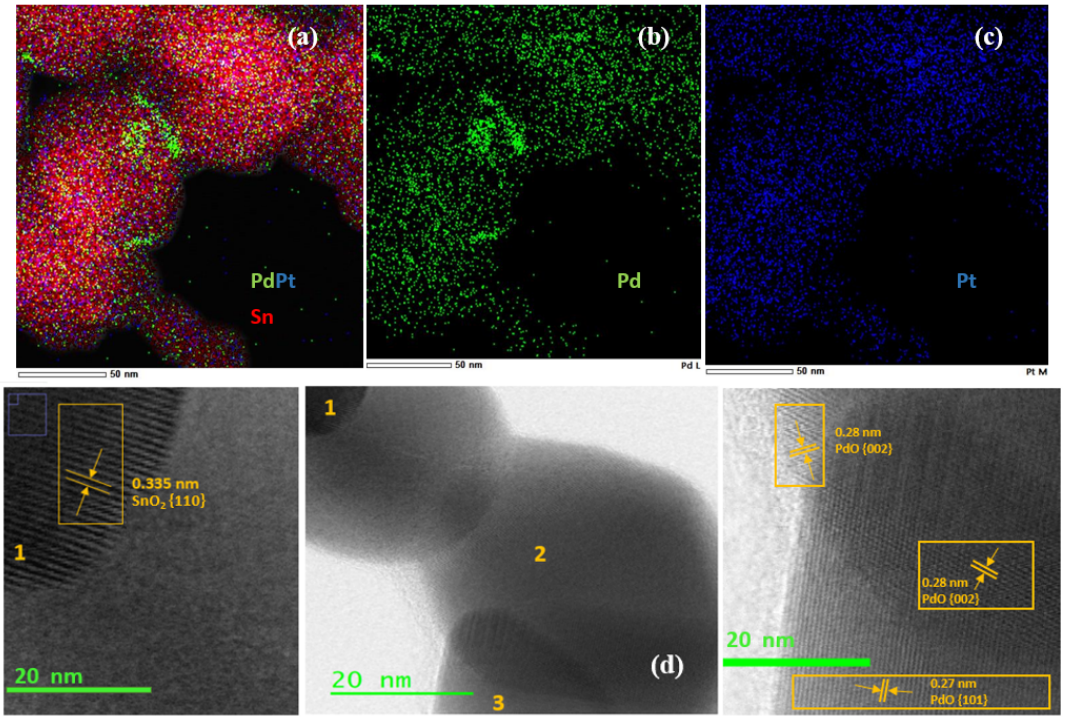

Figure 3. 2. Hydrothermally aged Pd-Pt/SnO_2 catalyst: (a)-(c) TEM-EDX analysis showing Pd (green) and Pt (blue) distribution; (d) a representation of the SnO_2 and PdO phases [167] *(numbered as regions 1, 2 and 3) : (Region 2 lattice fringe = 0.23 nm – possible Pd {111} or Pt {111} or Pd-Pt alloy)*

3.3.2. Kinetic study of the benchmark Pd/γ-Al_2O_3 catalyst

The kinetic studies were performed after catalyst deactivation during their hydrothermal ageing. Several repeated experiments were done to ensure that the effect of continuing deactivation is negligible. The ignition curves of the reproducible runs for an initial CH_4 concentration of 1000 ppmv and 5000 ppmv in the presence of 5 vol% and 10 vol% water is as illustrated in Figure 3.3.a. The reproducibility of the experimental points at the other initial CH_4 concentrations (2000 ppmv, 3000 ppmv, and 4000 ppmv) have been depicted in Figure A.8 (for the 5 vol% runs) and Figure A.9 (for the 10 vol% runs). For each trial, the fractional conversion was independent of the CH_4 concentration, indicating first-order behavior to CH_4. The ignition curves illustrated that the fractional conversion decreased with an increase in the water concentration, indicating that the effect of water was significant. The results obtained from the optimization problem are as tabulated in Table 3.1.

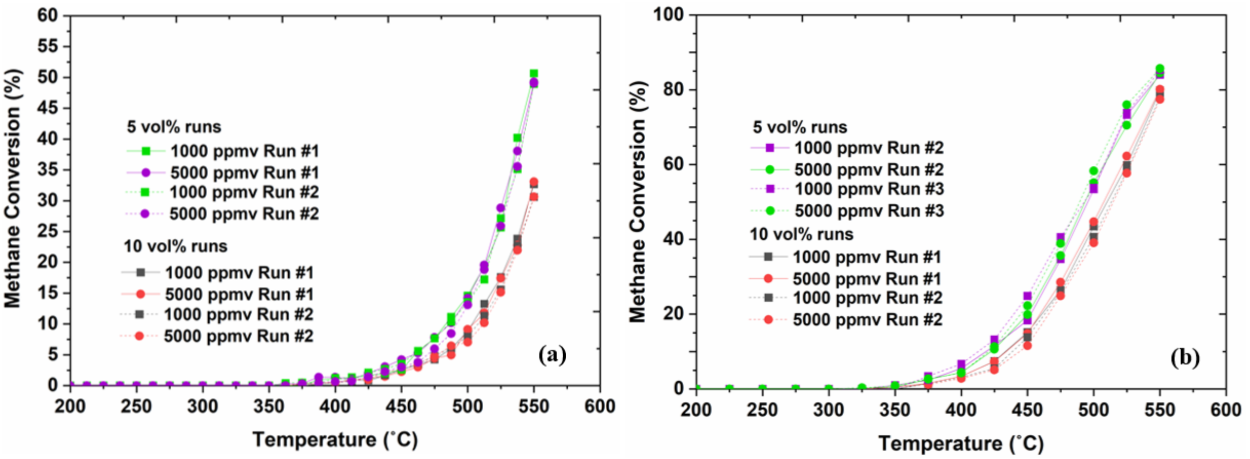

Figure 3. 3. Summary of the effect of water and initial concentration on the ignition curves for the (a) Pd/γ-Al_2O_3 catalyst and (b) Pd-Pt/γ-Al_2O_3 catalyst. For other concentrations and runs, refer to Figures A.8 and A.9 for the Pd/γ-Al_2O_3 catalyst and Figures A.10 and A.11 for the Pd-Pt/γ-Al_2O_3 catalyst

Table 3. 1. Estimated kinetic parameters for the Pd/γ-Al_2O_3 and Pd-Pt/γ-Al_2O_3 catalyst based on combined modeling using Eq. (3.2) under 5 vol% and 10 vol% wet feed conditions for all CH_4 concentrations from the reproducible runs. Rate law: $(-r_M) = \frac{k' C_M}{C_{aq}^n}$

Catalyst	**Pd/γ-Al_2O_3**	**Pd-Pt/γ-Al_2O_3**
Observed activation energy (kJ mol^{-1})	158 ± 3	131 ± 4
Observed pre-exponential factor (mol g_{PGM}^{-1} s^{-1})	$(55 \pm 8) \times 10^6$	$(15 \pm 3) \times 10^5$
Observed order with respect to H_2O (-n) in Eq. (3.2)	-1	-1
Objective function value	2×10^{-3}	3×10^{-3}

Figure 3.4 depicts the parity plot comparing the experimental and predicted conversion and the ±10% error lines. The parity plot confirmed that the optimized parameters correlated the experimental and predicted conversions with the maximum deviation between the error lines.

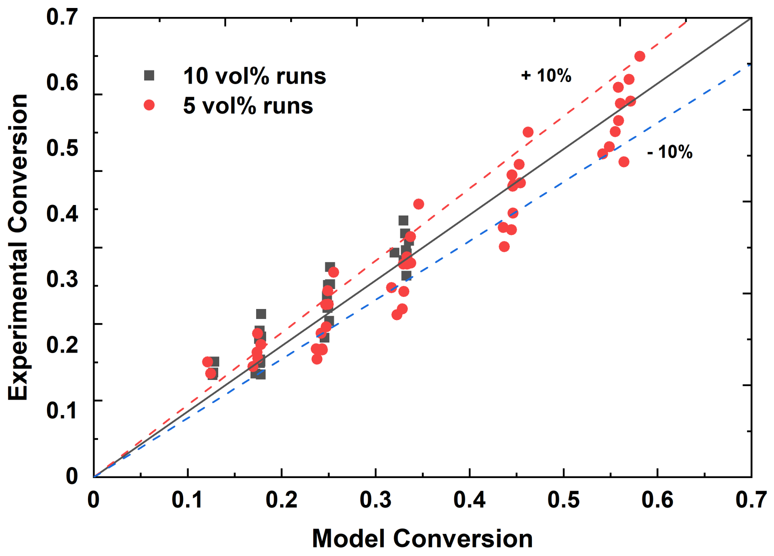

Figure 3. 4. Comparison of the predicted and experimental conversion for the combined wet feed condition studies on the Pd/γ-Al_2O_3 catalyst

Extensive literature is available on catalytic methane combustion studies for the Pd/γ-Al_2O_3 catalyst. Several studies conducted under wet feed conditions have revealed that the reaction was first order to CH_4 and negative first order to H_2O [56], [168], [169], and the obtained order to water in this study was consistent with those reported in the literature. Alyani et al. conducted wet methane combustion studies on the 6.5Pd/Al_2O_3 catalyst. They obtained an apparent activation energy value of 142.1 kJ mol^{-1} [169], which agrees with the observed activation energy reported in this work. Similar studies by Yang et al. on 1Pd/Al_2O_3 predicted activation energy in the range of 123-142 kJ mol^{-1} [51], further confirming the validity of the results depicted in Table 3.1. Both these studies revealed that the observed activation energy could be depicted as follows [51], [169]:

$$E_{\mathrm{eff,Pd,H_2O}} = E_{\mathrm{C-H,Pd}} + Q_{\mathrm{H_2O,Pd}}$$

DFT studies by Kan et al. [170] revealed that the heat of adsorption of water ($Q_{H2O,Pd}$) on Pd(101) surfaces saturated with substrates had a value of 81 kJ mol^{-1}. A similar value was reported by Alyani et al. [169] in their modeling studies. The activation energy associated with splitting the first C-H bond ($E_{C-H,Pd}$) was determined to be around 60-72 kJ mol^{-1}, as reported by the groups mentioned above [51], [169]. Based on the apparent activation energy reported in this work (E_a = 158 ± 3 kJ mol^{-1}) and utilizing the value of 81 kJ mol^{-1} for the heat of water adsorption on the PdO(101) faces, the activation energy required to split the C-H bond would be 77 kJ mol^{-1}.

3.3.3. Effect of Pt addition to Pd/γ-Al_2O_3 catalyst

Though Pd-based catalysts exhibit the highest methane combustion activity, it is evident that the initial high activity declines, as illustrated in Figure 3.1.a, which induces complications in igniting the fuel [171] and offers poor stability under steady-state conditions [18], [45]. As proposed in various studies, the addition of Pt has been suggested as one of the possible solutions to improve the catalyst stability in the presence of water. The section below provides the detailed kinetic investigation on the effect of adding Pt to the benchmark catalyst.

The ignition curves of the reproducible runs for an initial CH_4 concentration of 1000 ppmv and 5000 ppmv in the presence of 5 vol% and 10 vol% water is as illustrated in Figure 3.3.b. The reproducibility of the experimental points at the other initial CH_4 concentrations (2000 ppmv, 3000 ppmv, and 4000 ppmv) have been depicted in Figure A.10 (for the 5 vol% runs) and Figure A.11 (for the 10 vol% runs). In this case, the fractional conversion also appeared to be independent of the CH_4 concentration, indicating a first-order behavior with respect to CH_4.

The ignition curves in Figure 3.3.b demonstrated that despite the HTA treatment, the effect of deactivation was less pronounced on the bimetallic catalyst, thereby providing a more stable combustion performance than the Pd/γ-Al_2O_3. The results obtained from the optimization problem is as tabulated in Table 3.1.

Figure 3.5 depicts the parity plot comparing the experimental and predicted conversion and the ±10% error lines. As in the case of the monometallic catalyst, the parity plot confirmed that the obtained optimized parameters provided a good correlation between the experimental and predicted conversions with the maximum deviation between the error lines.

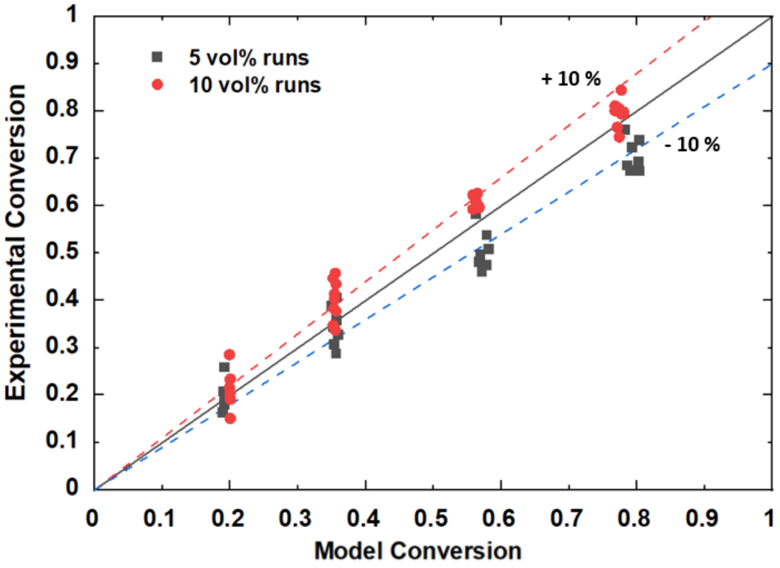

Figure 3. 5. Comparison of the predicted and experimental conversion for the combined wet feed condition studies on the Pd-Pt/γ-Al_2O_3 catalyst

The observed activation energies indicated that adding Pt to the monometallic Pd catalyst helped bring down the effective barrier, thereby enabling higher activities on the bimetallic catalyst. Methane combustion studies under 4.2 vol% wet feed conditions on γ-Al_2O_3 supported Pd-Pt catalysts with varying Pd:Pt ratios [47] revealed that the addition of Pt to Pd affected the observed activation energies. While the Pd catalyst had an apparent activation energy of 180 kJ mol^{-1}, the Pd-Pt catalysts revealed activation energies in the range of 60 - 120 kJ mol^{-1}, with the 4:1 Pt:Pd catalyst revealing the lowest observed activation energy at 60 kJ mol^{-1}. Goodman et al. observed that the Pd-Pt catalysts depicted a negative first order to water [47]. Studies on reduced Pd-Pt/Al_2O_3 catalysts (with varying Pd:Pt ratios) by Cargnello and coworkers [172] illustrated that though Pt rendered Pd to exist in a reduced-activity state, with an increase in time on stream in methane combustion at 400 ˚C, a gradual increase in the activity was observed. Due to the formation of PdO/Pd-Pt aggregates, enhanced catalytic activities could be achieved with a PdO-rich phase segregating out. The formation of such structures could be observed in the hydrothermally aged Pd-Pt/γ-Al_2O_3 catalyst considered in this study (Figure A.6), that could possibly contribute to the improved catalytic performance. Similarly, for the Pd-Pt/γ-Al_2O_3 catalyst, Karinshak et al. [48] illustrated the presence of an increased amount of metallic Pd along with an increased amount of alloyed Pd-Pt structures. The authors proposed that the presence of metallic Pd could possibly destabilize the Pd-O bond, and the presence of metastable Pd-PdO species resulted in enhanced catalytic activities. In comparison to the Pd-Pt/CeO_2-ZrO_2-Y_2O_3-La_2O_3 catalyst, a higher proportion of alloyed Pd-Pt structures were observed in the case of the Pd-Pt/γ-Al_2O_3 catalyst further validating that a combination of the PdO-Pd and Pd-Pt structures could contribute to enhanced activities [48]. Yang et al. [51] observed a reduction in the apparent activation barrier between the 1Pd and 1Pd-Pt catalysts supported on Al_2O_3 support. While the 1Pd/Al_2O_3 reported an apparent activation energy of 127 kJ mol^{-1}, the inclusion of Pt to the above catalyst significantly reduced the activation barrier to 58 kJ mol^{-1} under lean-burn, 5 vol% wet methane combustion conditions. The 1Pd/Al_2O_3 catalyst was found to depict a minus first order to water, while the bimetallic 1Pd-Pt/Al_2O_3 catalyst depicted an order of -0.23 to water [51]. These findings are a testimonial to the fact that Pt addition does indeed help in the reduction of the activation barrier, which is in line with the findings reported in this work.

3.3.4. Effect of SnO_2 support on the catalytic behavior of Pd and Pd-Pt catalysts

The involved support material and its oxygen mobility could help decelerate the rate of catalyst deactivation and significantly improve the water tolerance. As elucidated in the introduction section, SnO_2-supported catalysts have depicted some promising potential from the viewpoint of enhanced catalytic performances in the presence of water. Hence, this section aims at determining the kinetic performance limits for the Pd and Pd-Pt catalysts supported on SnO_2.

The ignition curves of the reproducible runs for the SnO_2-supported catalysts, for an initial CH_4 concentration of 1000 ppmv and 5000 ppmv in the presence of 5 vol% and 10 vol% water, is as illustrated in Figure 3.6. The reproducibility of the experimental points for the Pd/SnO_2 catalyst at the other initial CH_4 concentrations (2000 ppmv, 3000 ppmv, and 4000 ppmv) have been depicted in Figure A.12 (for the 5 vol% runs) and Figure A.13 (for the 10 vol% runs). Similarly, the reproducibility of the experimental points for the Pd-Pt/SnO_2 catalyst at the other initial CH_4 concentrations (2000 ppmv, 3000 ppmv, and 4000 ppmv) have been depicted in Figure A.14 (for the 5 vol% runs) and Figure A.15 (for the 10 vol% runs).

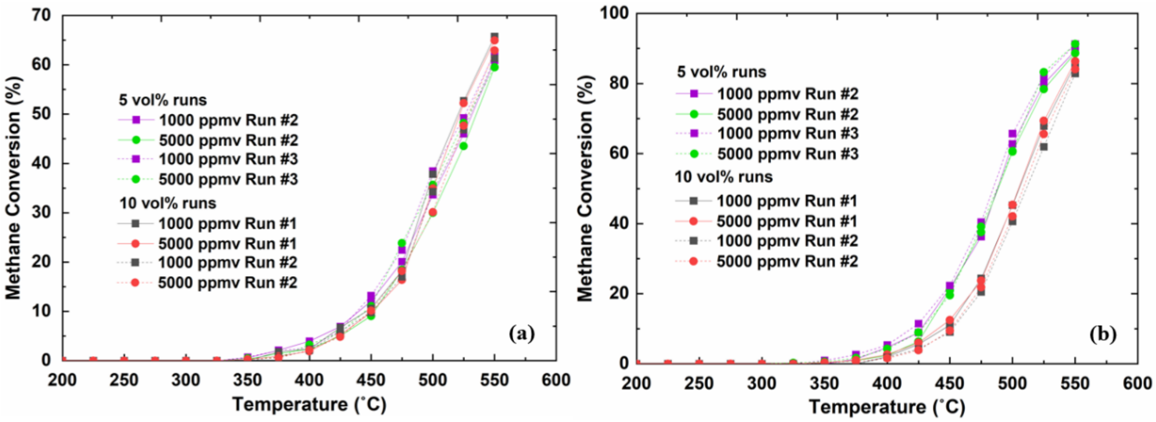

Figure 3. 6. Summary of the effect of water and initial concentration on the ignition curves for the (a) Pd/SnO_2 catalyst and (b) Pd-Pt/SnO_2 catalyst. For other concentrations and runs, refer to Figures A.12 and A.13 for the Pd/SnO_2 catalyst and Figures A.14 and A.15 for the Pd-Pt/SnO_2 catalyst

Based on the ignition curves for the Pd/SnO_2 catalyst (Figure 3.6.a), the fractional conversion appeared to be first order to CH_4; however, the trend does not seem to exhibit a negative first order with respect to H_2O, as opposed to the case of the Pd-Pt/SnO_2 catalyst. A hypothesis considering a decreased water inhibition (negative first order to water) on a single site type was tested for the Pd/SnO_2 catalyst, however the fit of the data was not satisfactory (Figure A.16) hence the model was abandoned. The results thus obtained from the optimization problem for the SnO_2-supported catalysts are as tabulated in Table 3.2.

Table 3. 2. Estimated kinetic parameters for the Pd/SnO_2 and Pd-Pt/SnO_2 catalysts based on combined modeling using Eq. (3.2) under 5 vol% and 10 vol% wet feed conditions for all CH_4 concentrations from the reproducible runs. Rate law: $(-r_M) = \frac{k' C_M}{C_{aq}^n}$

Catalyst	**Pd/SnO_2**	**Pd-Pt/SnO_2**
Observed activation energy (kJ mol^{-1})	110 ± 6	137 ± 3
Observed pre-exponential factor (mol g_{PGM}^{-1} s^{-1})	$(19 \pm 5) \times 10^3$	$(41 \pm 9) \times 10^5$
Observed order with respect to H_2O (-n) in Eq. (3.2)	-0.11	-1
Objective function value	9×10^{-4}	3×10^{-3}

Figures 3.7.a and 3.7.b depict the parity plot that compares the experimental and predicted conversion and the ±10% error lines for the monometallic and bimetallic catalysts, respectively. Like the previous cases, the parity plot confirmed that the obtained optimized parameters provided a good correlation between the experimental and predicted conversions with the maximum deviation between the error lines. An interesting observation was that the reaction order was 1 with respect to CH_4 and -1 with respect to H_2O for the Pd-Pt catalysts supported on both the SnO_2 and γ-Al_2O_3 supports. The observed kinetic parameters for the bimetallic catalysts were strikingly in the same range, proposing that the choice of support material could be insignificant when Pt was added to the catalyst formulation.

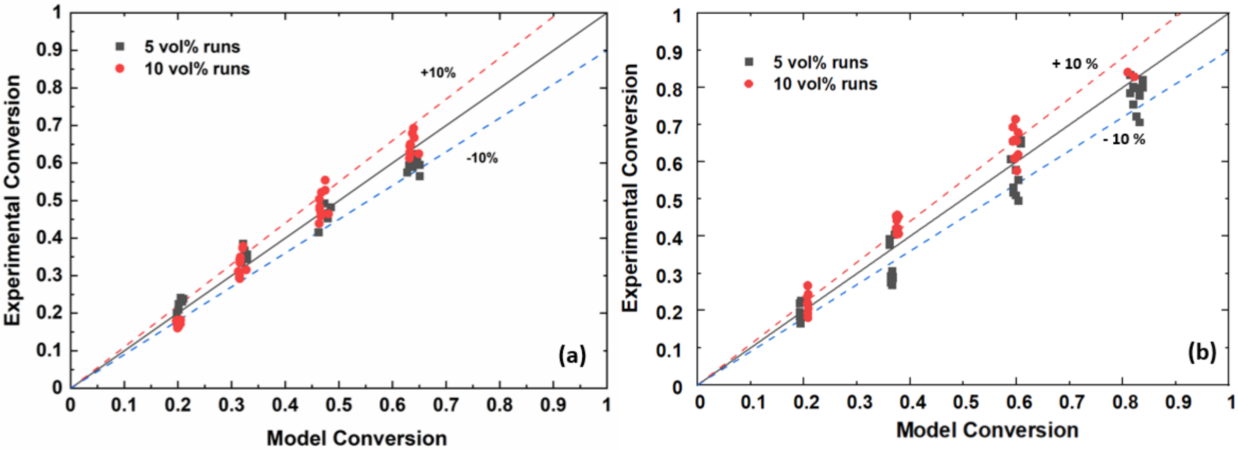

Figure 3. 7. Comparison of the predicted and experimental conversion for the combined wet feed condition studies on the (a) Pd/SnO_2 catalyst and (b) Pd-Pt/SnO_2 catalyst

The modeling results in Table 3.2 illustrated a significant difference in the water dependency between the Pd and Pd-Pt catalysts supported on SnO_2. The partial order to H_2O for the Pd/SnO_2 catalyst could be a characteristic of the presence of different active sites in play.

Compared to the modeling results reported by Kikuchi et al. [156], the results reported in this work are quite distinct. Kikuchi et al. utilized a model (proposed model by Mezaki and Watson [173]) of the following form:

$$(-r_M) = \frac{k_r C_M}{1+K_{aq}C_{aq}} \tag{3.6}$$

The modeling results for studies carried out at varying water concentrations (0-20 vol%) revealed that the Pd/SnO_2 catalyst had an apparent activation energy of 111 ± 21.9 kJ mol^{-1} and a heat of water adsorption of -31.3 ± 12.2 kJ mol^{-1} [156]. The validation of this model indicates that the catalyst has some vacant sites and some sites affected by water. The rate model in Equation (3.6) was tested on the experimental data obtained in this work, and the parity plot obtained from the optimization problem is depicted in Figure A.17. The apparent activation energy and heat of water adsorption were estimated to be 81 kJ mol^{-1} and 67 kJ mol^{-1}, respectively, but the parity plots depict a lack of overlap between the 5 vol%, and 10 vol% wet feed concentration runs. Most of the predicted values do not lie within 10% of the experimental values, as opposed to that observed in Figure 3.6.a. Additionally, the product of the $K_{aq}C_{aq}$ values in the denominator was quite large (as depicted in Table A.5) in the temperature range of interest, indicating that the catalyst should follow a perfect minus first order to water. However, considering that it does not agree with the parity plots obtained between the experimental and predicted conversions, the suggested model (Equation 3.6) is not acceptable.

The observed order of -0.11 with respect to H_2O in this work would suggest that methane combustion on the Pd/SnO_2 catalyst could follow the Mars-van Krevelen mechanism. However, our earlier temperature-programmed study at the temperature range of interest (below 550 °C) indicated that no oxygen was supplied to the reaction from the support [24]. Thus, herein, a hypothesis was tested where the reaction rate had additive contributions from the presence of two different active sites. The first site was considered to be unaffected by H_2O, while the second active site was affected by H_2O with an order of -1 with respect to it.

$$(-r_M) = k_1 C_M + \frac{k_2 C_M}{C_{aq}} \tag{3.7}$$

$$\text{Where } k_1 = k_{01} \, . \exp\left(-\frac{E_{a1}}{RT}\right) \tag{3.8}$$

$$k_2 = k_{02} \, . \exp\left(-\frac{E_{a2}}{RT}\right) \tag{3.9}$$

The observed activation energy Ea_2 was fixed to be 158 kJ mol^{-1} resembling the apparent activation energy observed in the case of the Pd/γ-Al_2O_3 catalyst for sites affected by water in the negative first order. The optimized parameters obtained in this case are as tabulated below:

Table 3. 3. Estimated kinetic parameters for the Pd/SnO$_2$ catalyst based on equations (3.7)-(3.9) for the combined modeling under 5 vol% and 10 vol% wet feed conditions for all CH$_4$ concentrations from the reproducible runs. Rate law: $(-r_M) = k_1 C_M + \frac{k_2 C_M}{C_{aq}}$

Observed activation energy 1 (kJ mol^{-1})	108 ± 7
Observed activation energy 2 (kJ mol^{-1})	158
Observed pre-exponential factor 1 (m$^3_{fluid}$ g$_{PGM}^{-1}$ s^{-1})	$(16 \pm 9) \times 10^3$
Observed pre-exponential factor 2 (mol g$_{PGM}^{-1}$ s^{-1})	$(14 \pm 6) \times 10^6$
Objective function value	1×10^{-3}

Figure 3.8 depicts the parity plot comparing the experimental and predicted conversion and the ±10% error lines. The parity plot confirmed that the obtained optimized parameters provided a good correlation between the experimental and predicted conversions with the maximum deviation between the error lines, thereby suggesting that the proposed hypothesis could be a possible mechanism for the methane combustion reaction on the Pd/SnO$_2$ catalyst.

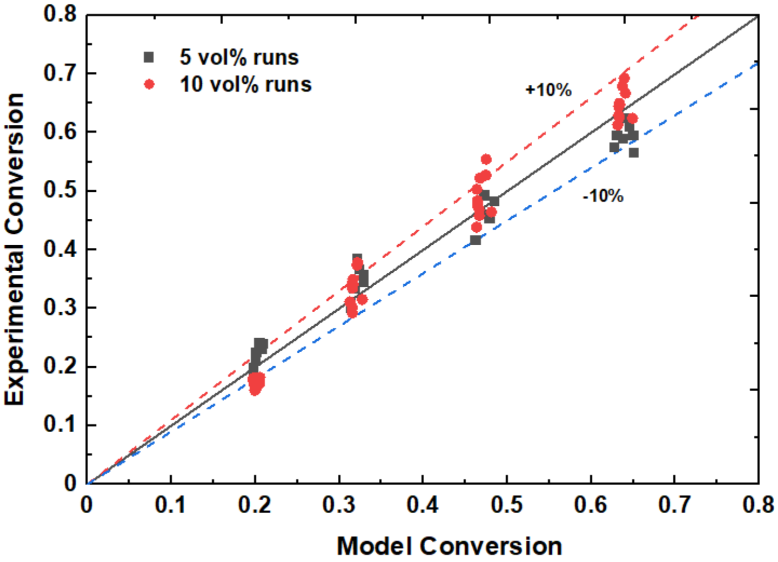

Figure 3. 8. Comparison of the predicted and experimental conversion for the combined wet feed condition studies on the Pd/SnO$_2$ catalyst based on the new proposed model Eq. (3.7)

While the second active site in the proposed model (Equation 3.7) could likely be a PdO phase, the first active site unaffected by water could be a possible PdO-Pd structure that is less susceptible to water poisoning leading to the enhanced catalytic performance. TEM and XRD analysis for the Pd/SnO_2 catalyst (Figure A.5.c and Figure A.7 in Appendix A, respectively) could verify the presence of PdO-Pd phases, possibly suggesting that the proposed active sites could have the above-stated structures. To fully understand the structures of the active sites, in-situ characterization techniques would need to be implemented, which were beyond the scope of this work. The presence of such metastable PdO-Pd structures contributing to increased methane combustion activity has been illustrated in the studies by Karinshak et al. [48]. The presence of PdO-Pd phases and the consequent activity enhancement on the SnO_2-supported Pd-catalyst could also be attributed to the electronic and chemical effects that occur over SnO_2 support. Due to electron transfer from SnO_2 to PdO, a depletion layer was found to form between PdO and SnO_2 surface [60], [174], [175]. In the presence of water, this depletion layer hampers the dissociative adsorption of water on SnO_2 and the O^{2-} on the SnO_2 surface seems to facilitate the oxidation of metallic Pd during the reaction [176]. It has also been proposed that Pd particles function as portholes to exchange oxygen between the gas phase and the support and then reoxidize through the reverse spillover of O atoms from the SnO_2 support [60], [67], [175], [177]. Studies by Nassiri et al. [22] demonstrated that the activity of Pd/SnO_2 surpassed that of the Pd-Pt/Al_2O_3 catalyst, even in the presence of a 20 vol% wet feed. The authors proposed that in the case of tin, the presence of dual Sn^{4+}/Sn^{2+} valency could contribute to the improved surface oxygen exchange and migration between PdO and the support surface. Another contributing factor to the high-water stability of Pd/SnO_2 could be attributed to the less negative enthalpy of water adsorption on Pd/SnO_2 as compared to Pd/Al_2O_3, leading to less inhibition by water in the case of Pd/SnO_2 [22].

When Pt is added to the Pd/SnO_2 system, it has been demonstrated in previous studies that Pt remains in its metallic form [23]; thus, only PdO exists as the active metal oxide. TEM analysis for the Pd-Pt/SnO_2 catalyst demonstrated that PdO segregates out as a separate phase (Figure 3.2), co-existing with Pd-Pt alloyed structures, thus possibly contributing to the enhanced catalytic performance. By means of H_2 reductive pulses during methane combustion, Karinshak et al. [48] illustrated the presence of partially reduced Pd-PdO structures contributing to higher combustion activity for Pd-Pt catalysts supported on γ-Al_2O_3 and CeO_2-ZrO_2-Y_2O_3-La_2O_3

supports. However, a larger proportion of PdO-Pd and Pd-Pt structures were observed in the case of the Al_2O_3 supported catalyst. The authors proposed that the support characteristics could affect the formation of such structures. The increased mobility of the lattice oxygen in the case of the CeO_2-ZrO_2-Y_2O_3-La_2O_3 support could have hindered the reduction of PdO to Pd or could have facilitated fast reoxidation of Pd to PdO, leading to lower combustion activity. Thus, optimal choice of the Pd-Pt ratio along with the support material could be crucial to obtaining optimized performances [48]. It could be possibly suggested that the SnO_2 catalyst enables the existence of PdO-Pd structures in the case of both Pd and Pd-Pt catalysts. For the Pd-Pt/SnO_2 catalyst, existence of both PdO-Pd and alloyed Pd-Pt structures, could contribute to the superior stability and enhanced performance even after the hydrothermal ageing treatment. Based on the TPR profiles (Figure A.4), it could be stated that SnO_2-containing samples were able to release associated oxygen species in comparison to γ-Al_2O_3, thereby enabling the SnO_2-supported catalysts to exhibit remarkable resistance to water-induced poisoning.

It is crucial to note that the rate model proposed in this study should only be considered a mathematical model. The type and number of active sites, surface intermediates, or rate-determining steps were beyond the scope of this work. The reasonable fitting of the simulated data to the experimental data does not signify that this reaction mechanism occurs; the study mainly focuses on obtaining a value of the kinetic parameters for reactor design purposes.

The dispersion data obtained from the CO chemisorption studies (as depicted in Table 3.4) were utilized to calculate and plot the turnover frequency (TOF) at 425 ˚C for various initial CH_4 concentrations (1000-5000 ppmv) at the reactor conditions (Figure 3.9).

Table 3. 4. The metal loadings, dispersion, and CH_4 turnover frequency data for the catalysts under study at 425 ˚C and 3000 ppmv CH_4 concentration

Catalyst	**Rate Model**	**Rate constant @ 425 ˚C**	**Dispersion (%)**	**CH_4 turnover frequency @ 425 ˚C ($mol_{methane}/mol_{surface\ PGM}.s$)**	
				5 vol%	**10 vol%**
Aged Pd/γ-Al_2O_3	$(-r) = \frac{kC_M}{C_{aq}}$	k = 8.29× 10^{-5} (mol/g_{PGM}.s)	12	0.0044	0.0022
Aged Pd/SnO_2	$(-r) = k_1C_M + \frac{k_2C_M}{C_{aq}}$	k_1 = 1.33 × 10^{-4} (m^3/g_{PGM}.s) k_2 = 2.11 × 10^{-5} (mol/g_{PGM}.s)	4	0.019	0.017
Aged Pd-Pt/ γ-Al_2O_3	$(-r) = \frac{kC_M}{C_{aq}}$	k = 2.37× 10^{-4} (mol/g_{PGM}.s)	11	0.019	0.0096
Aged Pd-Pt/SnO_2	$(-r) = \frac{kC_M}{C_{aq}}$	k = 2.30 × 10^{-4} (mol/g_{PGM}.s)	5	0.038	0.019

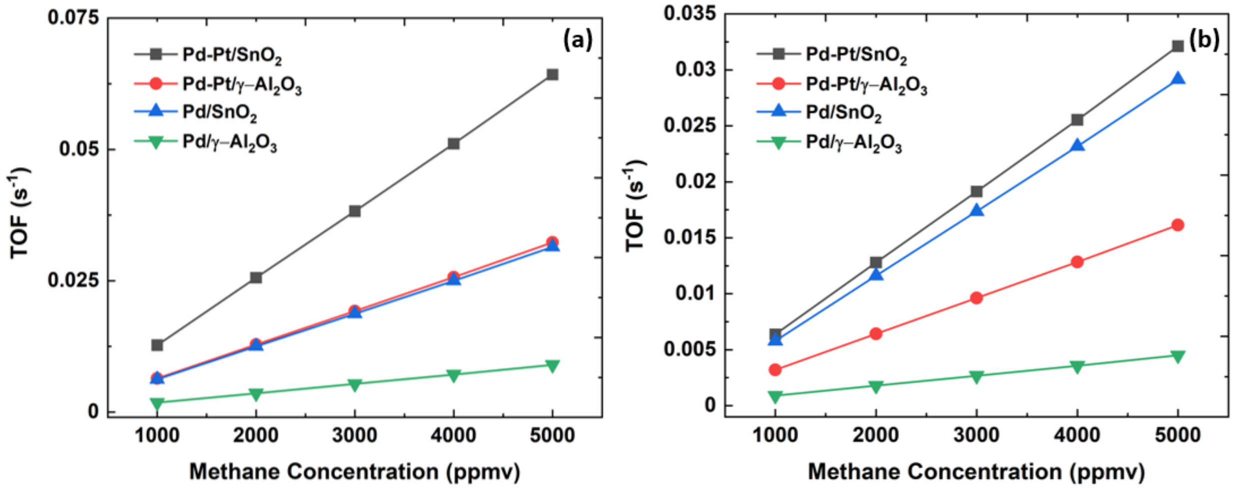

Figure 3. 9. Comparison of the TOFs (Turnover Frequency in units $mol_{methane}/mol_{surfacePGM}.s$*) at 425 ˚C and various* CH_4 *concentrations (1000-5000 ppmv) over the four catalysts under consideration for the (a) 5 vol% wet feed conditions and (b) 10 vol% wet feed conditions*

Table 3.4 and Figure 3.9 illustrate that the bimetallic Pd-Pt catalysts provide higher TOFs than their respective monometallic Pd catalyst counterparts. Nassiri et al. [49] demonstrated similar observations wherein the addition of Pt to the Pd/γ-Al_2O_3 catalyst significantly improved the TOF under lean-burn wet feed conditions. Based on the total surface atoms, the TOFs were found to be nearly constant for Pd-Pt catalysts supported on γ-Al_2O_3 with Pd:Pt ratios varying from 4:1 to 1:1. However, further enrichment of the catalyst with Pt (Pd:Pt above 1:3 ratio) resulted in a decline in the TOF, due to a possible deficit of oxygen essential for the combustion reaction [49]. Goodman et al. [47] reported that in the presence of steam, the TOF on the Pd/Al_2O_3 was reduced by three orders of magnitude compared to the dry feed conditions. On the contrary, Pt inclusion in the catalyst formulation demonstrated minimal deactivation, with the TOF values decreasing only 3-9 times [47]. Studies under lean-burn dry feed conditions by Nie et al. [54] demonstrated that 0.5Pt-1Pd/Al_2O_3 catalyst demonstrated the highest TOF compared to the 1Pd/Al_2O_3 catalyst. However, a further increase in the Pt:Pd ratio from the ideal 0.5:1 Pt:Pd ratio resulted in a lower TOF than the monometallic Pd catalyst due to the presence of a more significant proportion of inactive Pt sites [54]. In this study, though the observed kinetic parameters for the bimetallic catalysts were in the same range, the amount of Pd-Pt exposed on the surface was quite distinct, resulting in different turnover rates, consequently suggesting the existence of different active sites in each of the catalysts. The SnO_2-supported bimetallic catalyst provided a turnover rate almost 2 times the amount observed in the case of the γ-Al_2O_3-supported catalyst.

3.4. Conclusion

Complications arising from the presence of water could severely affect the performance of Pd catalysts in methane combustion. The ability to overcome the inhibitory effects of water highly depends on the catalyst formulation and the choice of the support material. In this work, kinetic investigations of methane combustion in the presence of water (5 vol% and 10 vol%) were performed on 1 wt% Pd and Pd-Pt (1:1 molar ratio) catalysts supported on SnO_2 and γ-Al_2O_3 support materials. The observed activation energy (158 ± 3 kJ mol^{-1}) determined for the benchmark Pd/γ-Al_2O_3 catalyst and negative first order with respect to water is consistent with those reported in the literature. Incorporating Pt into the benchmark catalyst helped significantly reduce the effective barrier (131 ± 4 kJ mol^{-1}), thereby enabling higher activities on the bimetallic catalyst.

When supported on SnO_2 the same bimetallic catalyst revealed that the observed activation energies were in the same range of 137 ± 3 kJ mol^{-1} and the same negative first order to water. Hence, from the viewpoint of the activation energy, the choice of support material between SnO_2 and γ-Al_2O_3 could be insignificant upon adding Pt to the formulation.

The modeling results for the Pd/SnO_2 catalyst illustrated a partial -0.11 order to water, which could indicate the presence of different active sites. A hypothesis was tested where the reaction rate had additive contributions due to the presence of two different active sites. Keeping the observed activation energy Ea_2 fixed at 158 kJ mol^{-1} (resembling the apparent activation energy as of the Pd/γ-Al_2O_3 catalyst) for the site affected by water, the value of Ea_1 was significantly smaller (88 ± 10 kJ mol^{-1}) and had the lowest value in comparison to the observed activation energy for all the catalysts under study.

From the viewpoint of turnover frequency, calculated using PGM dispersion, the Pd-Pt/SnO_2 catalyst exhibited the highest turnover frequency (even at 10 vol% wet feed conditions) compared to the other catalysts considered in this study. The Pd-Pt/SnO_2 catalyst provided a methane turnover rate almost 2 times higher than that demonstrated in the case of the Pd-Pt/γ-Al_2O_3 catalyst.

Chapter 4: Kinetic investigation of the promoting effect of cobalt on Pd-Pt/SnO_2 catalyzed wet methane combustion[3]

4.1. Introduction

Abatement of methane emissions from mobile sources remains a challenge [178]. There has been an exponential growth in natural gas fueled vehicles (NGVs) because methane is cleaner burning compared to gasoline or diesel fuel [5]. However incomplete combustion allows some amount of methane to slip, unburned, through the exhaust [9]. Because CH_4 is a much more potent greenhouse gas compared to CO_2 [179], there has been a surge in interest to optimize the catalytic system for NGV vehicles to reduce methane emissions. Pd-based catalyst formulations [14], [36] have been widely utilized for the reduction of methane emissions from the exhaust of NGVs [180], [181]. Due to the presence of a significant amount of water vapour in the vehicle exhaust [14], [18]–[21], [67], the addition of Pt [48], [182] to the catalytic system has been identified to be beneficial due to its superior stability against sulfur poisoning [183]–[185] as well as its ability to inhibit the negative effects induced by the presence of steam in the exhaust stream [47], [49], [131], [186], [187]. Specifically, while under dry feed conditions, Pt could render Pd to exist in its reduced state [52], under wet feed conditions, Pt-incorporated catalysts exhibited stable catalytic performances due to the formation of PdO/Pd-Pt aggregates [47], [48].

---

[3] **Chapter 4** of the thesis has been published as: R. Sajiv Kumar, R. E. Hayes, N. Semagina, "Kinetic investigation of the promoting effect of cobalt on Pd-Pt/SnO_2 catalyzed wet methane combustion", *Applied Catalysis A: General* 2023, **666**, 119416. The reaction setup for methane combustion was originally designed and built by Dr. Long Wu and Dr. Robert E. Hayes. All syntheses, reaction tests, data collection, interpretation and analyses of experimental results and other characterizations were performed by the author. The author drafted and implemented the MATLAB code for the nonlinear optimization and also performed the numerical analyses in this work. The paper was re-printed with permission from Reference [188] Copyright © 2023 Elsevier B.V. and of the co-authors.

Studies by Nassiri et al. [23] suggested that under wet feed conditions, the substrate could be considered oxygen deficient which protects Pt from oxygen poisoning, thereby enabling Pt to activate methane.

While the consideration of the active metals for methane combustion is critical, enhancing the catalytic activity and stability is equally important and requires the selection of an appropriate support material [57], [136], [189], [190]. Pd-based catalysts deposited on conventional γ-Al_2O_3 support demonstrate progressive deactivation at temperatures below 500 ˚C due to probable hydroxyl accumulation on the active sites [124]. To mitigate the effect of hydroxyl accumulation, SnO_2 has captured some attention due to its ability to serve as a sink for the water released from $Pd(OH)_2$ [22], [24]. SnO_2, due to its remarkable water-tolerant behaviour is believed to support Pd in its active PdO form, thereby resulting in enhanced catalytic performances [88]. Based on the kinetic studies in our previous work [136] the Pd/SnO_2 catalyst reported the lowest activation energy compared to similar formulations on the γ-Al_2O_3-support [51], [169]. Similar conclusions were reported by Kikuchi et al. [130] and Keller et al. [190] based on their kinetic studies on the Pd/SnO_2 catalyst under lean burn wet methane combustion. The Pd/SnO_2 catalyst also reported a higher tolerance compared to the conventional Pd/γ-Al_2O_3 catalyst [136]. In our recent work, it was also demonstrated that the addition of Pt to the Pd/SnO_2 catalyst and Pd/γ-Al_2O_3 catalyst significantly helped to reduce the measured methane combustion activation barrier (129 ± 9 kJ mol^{-1}) compared to that of a conventional Pd/γ-Al_2O_3 catalyst (143 ± 11 kJ mol^{-1}) [136]. Studies by Yang et al. [51] and Goodman et al. [47] reported similar conclusions, wherein the addition of Pt to the catalyst formulation helped to lower the activation barrier for methane combustion [51]. In our earlier studies, while the Pd-Pt/SnO_2 catalyst demonstrated a higher turnover frequency (TOF) in comparison to the γ-Al_2O_3-supported bimetallic catalyst, the former catalyst still did exhibit some slow deactivation. The decrease in reaction rate might be attributed to the sintering of the active metals on the low surface area SnO_2 support. A temperature-programmed study at the temperature range of interest (200 ˚C – 550 ˚C) demonstrated that no oxygen was supplied from the SnO_2 support to the reaction [24]. However, studies by Ciuparu et al. [60] has demonstrated how the associated oxygen mobility on the support could potentially play a crucial role in the catalyst activity.

Thus, an ideal support material would be one that could have the ability to supply oxygen to the precious metal centers while simultaneously being able to tackle the inhibitory effects of water vapor present in the system. Cobalt oxide has captured attention as an active catalyst [68], [191]–[198], as a catalyst promoter [115], [199] and as a support (or) support modifier for precious metal catalysts in oxidation catalysis [191], [200]–[204]. The inclusion of cobalt oxide into a combustion catalyst formulation might be beneficial as it is known to oxidize CO [205] and decompose N_2O [206] in the vehicle exhaust streams. Co_3O_4 is known to be highly active in terms of oxygen activation rate as well as possessing the lowest oxygen binding heat [68], [69]. While SnO_2 and Al_2O_3 have similar oxygen bond dissociation energies (~ 502 kJ mol^{-1} for Al_2O_3 and ~ 548 kJ mol^{-1} for SnO_2), the bond dissociation energy for Co-O at 298 ˚C is ~ 398 kJ mol^{-1} [207]. Due to their lower metal-oxygen bond strength, higher oxygen mobility could be enabled [208].

When used as a catalyst for CH_4 combustion under dry feed conditions, the rate-determining step was determined to be the breaking of the Co-O bond or oxygen migration from the bulk of CoO_x to its surface in the absence of oxygen [209]. Similar studies by Sojka and colleagues [192], [193] demonstrated that highly active suprafacial tetrahedral cobalt oxo-centers catalyzed methane combustion via a Langmuir-Hinshelwood mechanism at temperatures below 450 ˚C. At higher temperatures, the less active intrafacial lattice oxygen participated in methane combustion via a Mars-van Krevelen mechanism [192], [193]. Cobalt oxide as a support material has been suggested to serve as an oxygen reservoir that could enable Pd to remain in its oxidized state where it is more active for combustion reactions [115], [204]. Shen et al. [90] demonstrated that under a dry oxygen-deficient feed condition, cobalt oxide provided a tithe of its oxygen to Pd in the 400 ˚C – 550 ˚C temperature range, enabling Pd to catalyze methane. Composite cobalt oxide supports have also been reported to demonstrate enhanced catalytic performances under dry methane combustion conditions. Wang et al. [210] reported that the Pd/CoO_x-SiO_2 catalyst performed well in lean methane combustion due to synergistic interactions between the cobalt and Pd species. Co_3O_4-SnO_2 hybrid oxides prepared by the coprecipitation method demonstrated high methane combustion activities and considerable stability [211]. The authors proposed that while SnO_2 behaved as a support or promoting component, Co_3O_4 functioned as the active species for methane combustion [211]. When cobalt was added as a promoter to the Pd/γ-Al_2O_3

catalyst, Willis et al. [199] demonstrated that the catalyst activity significantly improved due to improved sintering resistance as well as lower activation energy in the range of 78 to 87 kJ mol^{-1}. Utilizing in-situ infrared spectroscopic studies, Jodłowski et al. [200] proposed that Pd-Co catalyzed dry methane combustion relied on the adsorbed O* species on the surface of the catalyst. The authors proposed that the mechanism of methane activation occurred via adsorption of methane on the catalyst surface with pre-adsorbed oxygen [200].

Another compelling feature of cobalt oxide is its reported high tolerance to water. DFT calculations by Zasada et al. [212] reported that at 0.1 atm H_2O and a temperature as low as 250 ˚C, the Co_3O_4 (110) surface was only 14% hydroxylated. Computationally it has been demonstrated that the (111) surface could not be considered a primary catalytic surface due to its higher affinity to water coverage in comparison to the (110) and (100) surfaces [212]. While under dry feed conditions utilization of Co_3O_4, as an active catalyst was favorable, in the presence of water, the Co_3O_4 catalyst activity was impaired, though the catalyst provided stable methane conversions for 150 hours on stream [197]. Studies by Nasr et al. [116] demonstrated that though the Co_3O_4 catalyst deactivated progressively, doping with Pd helped stabilize the catalytic activity under wet methane combustion conditions. Kinetic studies on Co_3O_4 and Pd/Co_3O_4 catalysts by Nasr et al. [116] under 5 vol% and 10 vol% wet feed conditions demonstrated that cobalt oxide contributed to about 70% of the catalyst activity. While Co_3O_4 reported a zero-order dependence on water, the Pd/Co_3O_4 catalyst reported a partial order to water (-0.37). Though the observed activation energy on the Co_3O_4 catalyst was lower than that on the Pd/Co_3O_4 catalyst catalysts, the former catalyst reported a much lower number of active sites. The studies also revealed that the kinetic parameters on the Pd/Co_3O_4 resulted from synergistic contributions rather than additive ones [116]. Based on the reported kinetic results for the Co_3O_4-supported catalyst, in-situ XAS analysis was performed by Barrett et al. [88] to comprehend the distribution of Pd and Co species as a function of temperature. The *in-situ* XAS studies, by Barrett et al. [88] illustrated that cobalt oxide behaved more as a preferential oxygen acceptor than a hydroxyl acceptor under wet feed conditions. The studies also demonstrated that the dehydroxylated Co_3O_4 could co-exist with the inactive $Pd(OH)_2$ [88]. Studies by Basavalingu et al. [213] on the dehydroxylation trend of the $Co(OH)_2$-CoO system illustrated that dehydroxylation occurred at temperatures below 300 ˚C at a water pressure up to 2000 bar, further verifying the observations reported by Barret et al. In-situ XAS analysis of the Pd/Co_3O_4 catalyst by Barrett et al. [88] also revealed that while Pd oxidation was inhibited, cobalt oxide reoxidation occurred via migration of activated oxygen from the PdO surface as well as from the oxygen gas phase. Interestingly, when cobalt was incorporated as a promoter to the Pd/γ-Al_2O_3 catalyst, the catalytic system exhibited enhanced catalytic activity and stability for wet methane combustion [115]. Kinetic studies by Stefanov et al. [115] under 1 vol% wet feed conditions on the Pd-Co/Al_2O_3 catalyst revealed that the methane combustion reaction occurred via a Mars-van Krevelen mechanism, with oxidation of the catalyst surface being the rate-determining step.

Thus, though the cobalt oxide supports' reducibility and oxygen mobility can improve catalytic activity, it does not necessarily mean that the metal oxide can provide its O* to the combustion reaction under all conditions. While reducible oxide supports could be beneficial under dry feed conditions, the support's water tolerance seems more important when significant amounts of water vapor are present in the feed stream. For streams with significant water vapor SnO_2 appears to be the superior choice [22], [24], [88]. This work explores the opportunity to combine the SnO_2 and Co_3O_4 substrates in a bimetallic precious metal catalyst composition for methane combustion in the wet feed. It was considered that the SnO_2 could resist the hydroxyl formation that would otherwise hamper the reaction rate [24], [88] while CoO_x could participate in catalyzing methane under wet feed conditions due to synergistic interactions between Pd and CoO_x [88], [90], [115], [116]. The use of a bimetallic Pd-Pt mixture was expected to provide metastable PdO/Pd-Pt aggregates that could actively participate in the wet methane combustion reaction. If synergy could be found between the individual contributors, then a catalyst could be developed that has a high reaction rate for lean methane combustion and long-term catalytic stability in the presence of water vapor.

Thus, this work aims to investigate the kinetic behaviour of cobalt modified Pd-Pt/SnO_2 catalyst in wet methane combustion and compare it against the benchmark Pd/γ-Al_2O_3 catalyst and earlier reported Pd-Pt/SnO_2 catalyst [136]. To determine the optimized promoter loading, a systematic investigation with different cobalt loadings (2, 10, 20 wt.%) was performed. Based on the optimized 10 wt.% cobalt loading, kinetic studies were carried out on the Pd-Pt(1wt.%)/Co(10wt.%)/SnO_2 catalyst. For comparison purposes, the promoter effect of cobalt was investigated by performing kinetic studies on the Pd-Pt(1wt.%)/Co(10wt.%)/γ-Al_2O_3

catalyst. To the best of our knowledge, there are no available data on the kinetics of methane combustion on the proposed catalyst formulations corresponding to the conditions usually found in environmental applications. Herein, kinetic studies at fuel lean-burn conditions were performed on the above-mentioned catalysts under 5 vol% and 10 vol% water, and methane concentrations ranging from 1000 to 5000 ppmv, in the temperature range of 200 ˚C to 550 ˚C. The catalysts were hydrothermally aged before the kinetic study and verified for stable performance. The study aims to understand the kinetic consequences and advantages of using cobalt as a promoter for the SnO_2-supported Pd-Pt catalyst and evaluate whether it could provide enhanced catalytic activity with improved stability under the lean-burn wet methane combustion conditions.

4.2. Experimental

4.2.1. Catalyst preparation and characterization

Palladium (II) nitrate dihydrate ($Pd(NO_3)_2.2H_2O$, ~ 40% Pd basis, Sigma-Aldrich), chloroplatinic acid (H_2PtCl_6, 8 wt.% solution in water, Sigma-Aldrich), aluminum oxide (γ- Al_2O_3, particle size 150 mesh, average pore size 58 Å, surface area 155 m^2/g, Sigma Aldrich), tin dioxide (SnO_2, ~ 325 mesh, 99.9% trace metals, Sigma-Aldrich), cobalt(II) nitrate hexahydrate ($Co(NO_3)_2{\cdot}6H_2O$, ACS reagent ≥98%), cobalt oxide (Cobalt(II,III) oxide, powder, <10 micron, Sigma Aldrich), cobalt aluminum oxide ($Al_2Co_2O_5$, Co 39 - 41%, Thermo Scientific Chemicals), and silica (SiO_2, 200-425 mesh, high purity grade, Sigma-Aldrich) were used as received. Milli-Q water (18.2 MΩ cm) was used throughout the work.

Cobalt was deposited on the desired support materials 'S' (S = γ-Al_2O_3 and SnO_2) utilizing the incipient wetness impregnation method. To determine the optimized cobalt deposition, different cobalt compositions 'y' (wt.%) (y = 2, 10 and 20) were deposited with quantitative deposition of $Co(NO_3)_2{\cdot}6H_2O$ on 'S'. The cobalt loadings of 2, 10 and 20 wt.% would correspond to a 3, 13 and 26 wt% Co_3O_4 loadings on the impregnated samples, respectively. Following impregnation, the samples were dried at 60 ˚C and calcined in air at 550 ˚C for 16 hours. The cobalt impregnated samples will be referred to as yCo/S. 1 wt.% Pd-Pt (1:1 molar ratio of Pd:Pt with 0.343 wt% Pd and 0.647 wt% Pt) was then deposited on the calcined yCo/S samples using the synthesis procedure reported in our previous work [136]. The as-synthesized catalysts (referred to as Pd-Pt/yCo/S) were dried overnight in an oven at 60 ˚C; then, they were ground and mixed with SiO_2 diluent. The catalyst was diluted with SiO_2 to improve the isothermality of the catalyst bed and to suppress axial dispersion and bypassing [214]. The diluent was selected based on the recommendation provided in the work by Cargnello and coworkers as it does not affect the catalyst performance in wet feed [124]. The ground mixture was sieved (230-325 mesh, i.e., 44-63 μm) and subsequently subjected to calcination in air at 550 ˚C for 16 hours. The $10Co/SnO_2$ sample was prepared by incipient wetness impregnation method. 10 wt.% cobalt loading was deposited on the SnO_2 support with quantitative deposition of $Co(NO_3)_2{\cdot}6H_2O$. Following impregnation, the samples were dried at 60 ˚C; then, they were ground and mixed with SiO_2 diluent. The ground mixture was sieved (230-325 mesh, i.e., 44-63 μm) and subsequently subjected to calcination in air at 550 ˚C for 16 hours.

4.2.2. Catalyst characterization

BET surface area measurements employing N_2 adsorption and desorption, transmission electron microscopy coupled with energy dispersive X-ray (TEM-EDX) analysis, and CO pulse chemisorption studies were performed on the hydrothermally aged Pd-Pt/yCo/S catalysts utilizing the same characterization procedures as described in our previous work [136]. Temperature-programmed desorption (TPD) studies were performed in a Micromeritics AutoChem 2950 HP instrument equipped with an online Pfeiffer Vacuum Thermostar GSD 320 spectrometer. The mass spectrometer was calibrated for H_2O ($m/z = 18$), O_2 ($m/z = 32$) and an internal standard He ($m/z = 4$) before the characterization experiment. The aged catalyst samples (0.1 g of each catalyst was utilized) were treated in He flow at 120 ˚C for 1h to remove physically adsorbed species. TPD was performed in He (50 mL min^{-1}) from 120 ˚C to 850 ˚C with a ramping rate of 5 ˚C min^{-1} and held at maximum temperature for 10 minutes. The ion currents for the m/z fragments assigned to water, and oxygen were each scanned for 5s which (including He) provided one complete scan every 20s. Temperature-programmed reduction (TPR) profiles of the calcined yCo/S samples (0.3 g of each sample was utilized) were obtained by reduction treatment in 5% H_2/He (10 mL min^{-1} with a ramping rate of 10 ˚C min^{-1}) from 200 ˚C to 800 ˚C utilizing Micromeritics AutoChem 2950 HP instrument. Scanning electron microscopy coupled with energy dispersive X-ray (SEM-EDX) analysis was performed on the calcined Pd-Pt/yCo/SnO_2 catalysts using Quanta 250 Mineral Liberation Analyzer (FEI company). The scanning electron microscope utilizes a tungsten filament and a Bruker Xflush (133eV) detector for the elemental analysis at 15 kV accelerating voltage. X-ray diffraction (XRD) profiles of the calcined yCo/S samples were obtained using Rigaku Ultima IV D/max-RB diffractometer with D/Tex Ultra detector with Fe Filter (K-beta filter). The step scans were taken over a 2θ range of 5–90˚ with a step size of 0.02˚ and scan speed 2˚ min^{-1}, continuous scan mode. Radiation source used was cobalt tube at 38 kV and 38 mA. Data was converted using JADE MDI 9.6 software and phase identification was done using DIFFRAC.EVA software with the 2022/2023 ICDD PDF 4+ and PDF 4+/Organics databases [27].

4.2.3. Methane combustion reactions

The kinetic studies were performed in a tubular packed-bed reactor of 3/8" internal diameter equipped with an online gas chromatograph (GC) as detailed in our previous work [136]. 0.12 g of Pd catalysts with 0.5 g of SiO_2, and 0.34 g of the Pt-Pd catalysts with 0.25 g of SiO_2 were used (verification of the negligible effect of dilution on conversion is depicted in Table B.1 in Appendix B) which provided 1.2 mg of Pd loading in the packed bed reactor. A mixture of 10 vol% methane in nitrogen and extra dry air (Praxair) was used for the testing. Employing 19.5 vol% O_2, a total gas flow rate of 210 ± 5 mL_{STP} min^{-1} (21,000 L_{STP} kg_{cat}^{-1} h^{-1}) was maintained (Matheson and MKS mass flow controllers). A peristaltic pump (Lab Alliance 205SFM01 Series II Pump) was used to inject water into the gas feed mixture via a heated reactor feed line to the system for the wet feed condition runs.

A set of dry and 10 vol% wet ignition-extinction (I-E) curves was obtained at an inlet methane concentration of 4000 ppmv by increasing the catalyst bed temperature from 200 ˚C to 550 ˚C with 50 ˚C increments at a rate of 10 ˚C min^{-1}. To simulate the effect of long-term exposure to water vapor under typical exhaust gas conditions, the catalysts were subjected to hydrothermal ageing (HTA) for 45 hours. The catalysts were continuously cycled between 400 ˚C and 550 ˚C using a gas feed containing 4000 ppmv CH_4 concentration and 10 vol% water vapor. Each thermal cycle lasted one hour. The catalyst after the HTA treatment is referred to as the aged catalyst. After ageing, a final set of dry and 10 vol% wet I-E curves were obtained under the same test conditions implemented before ageing.

The kinetic studies were performed on the aged catalysts. Ignition curves were obtained for five methane concentrations (1000, 2000, 3000, 4000 and 5000 ppmv) under dry and different water concentrations (5 vol% and 10 vol%) taken in the same random order as our previous work [136]. The studies were carried out by increasing the temperature from 200 ˚C to 550 ˚C with 25 ˚C increments at a rate of 10 ˚C min^{-1}. A 20-minute isothermal dwell was utilized at each temperature and the post-combustion gases were measured every 10 minutes using the inline gas chromatograph. Following each ignition test, the reactor was purged with air to bring the temperature to 200 ˚C. Replicates of the ignition curves were run for each experimental condition and were found to be reproducible.

4.2.4. Reactor model and optimization

The particle size (~ 50 μm) and diluent ratio in the catalyst bed were selected to ensure that the kinetic study analysis was carried out under plug flow conditions. Calculations verifying the absence of axial dispersion and wall effects are depicted in Section B.1 [157], and it was observed that plug flow conditions were satisfied. As a first step in analyzing the results of this work, we utilized a first-order reaction in terms of CH_4. The observed activation energy, pre-exponential factor, and reaction order to H_2O for the Pd-Pt/yCo/S (S = γ-Al_2O_3 and SnO_2) catalysts were determined utilizing the rate model in Equation 4.1 [27].

$$-\frac{dF_M}{dW} = (-r_M) = k' C_M C_{aq}^n \tag{4.1}$$

$$\frac{dX_M}{dW} = k' * \left(\frac{1-X_M}{Q}\right) * \left(\frac{F_{aq0}+2F_{M0}X_M}{Q}\right)^n \tag{4.2}$$

where Q is the volumetric flow rate at the temperature and pressure in the reactor, subscript “M” refers to methane, “aq” to water, and “0” to the flow rates in the feed at the reactor entrance.
The rate constant was expressed in terms of the Arrhenius expression as follows:

$$k' = k_0 \,.\, \exp\left(-\frac{E_a}{RT}\right) \tag{4.3}$$

where A is the observed pre-exponential factor (mol g_{PGM}^{-1} s^{-1} when overall reaction order was found 0, where PGM is Platinum Group Metal), E_a is the observed activation energy (kJ mol^{-1}), R is the universal gas constant (8.314×10^{-3} kJ mol^{-1} K^{-1}), and T is the reaction temperature (K). For the γ-Al_2O_3 supported catalyst, an internal effectiveness factor was incorporated into the rate model to account for the internal mass transfer effects. The optimized kinetic parameters in the proposed models were obtained by utilizing the Pattern Search algorithm in MATLAB as delineated in our previous work [131], [136]. For catalysts reporting a -1 order to water, rate constants first were obtained analytically; the linearly regressed kinetic parameters were determined utilizing the Arrhenius equation. Adopting the kinetic parameters obtained through such a process, the initial values and the bounds for the optimization process was fixed in the MATLAB code. Optimization was carried out using the data corresponding to CH_4 conversion between approximately 15 and 85 % for all the reproducible replicate runs for each catalyst. The data for the 5 vol% and 10 vol% wet feed runs were optimized collectively. The applicability of the ideal PBR mole balance as well as the absence of mass and heat transfer limitations based on the rate parameters obtained from Equation 4.1 is depicted in Section B.2 and Section B.3 in Appendix B.

4.3. Results and Discussion

4.3.1. Effect of cobalt loading on the performance of SnO_2-supported bimetallic catalyst

Considering the advantages offered by the inclusion of cobalt as a promoter to the Pd-based catalyst [115] as well as the utilization of SnO_2 as a support material for wet methane combustion [24], [88], cobalt was incorporated as a promoter to our highest performing Pd-Pt/SnO_2 catalyst [136] to optimize resistance to deactivation. 2 wt.%, 10 wt.% and 20 wt.% cobalt was deposited on SnO_2, and compared with Co_3O_4 and SnO_2-only supports, to identify the optimized promoter loading on the substrate. The precious metal (Pd-Pt) loading was maintained the same for all catalysts [27].

Optimized promoter loading was identified by subjecting the proposed catalyst formulations to ignition-extinction (I-E) tests and hydrothermal ageing (HTA). The results from the hydrothermal ageing are depicted in Figure 4.1.a. The tests were performed under 10 vol% added water and 4000 ppmv methane concentration by cycling the temperature between 400 ˚C and 550 ˚C for a total duration of 45 hours. For comparison, the same tests were carried out on 1 wt.% Pd-Pt/SnO_2 and 1 wt.% Pd-Pt/Co_3O_4 catalysts synthesized similarly to our previous work [136]. The I-E studies, before and after HTA are illustrated in Figures 4.1.b and 4.1.c, respectively. The I-E curves for the dry runs (before and after HTA) under the same testing conditions are depicted in Figure B.1.

The HTA treatment (Figure 4.1.a) demonstrated that Pd-Pt/10Co/SnO_2 catalyst exhibited superior water tolerance and provided stable conversions despite the cyclic hydrothermal treatment. While the catalysts under consideration performed quite similarly before HTA (Figure 4.1.b), significant differences in the catalytic activity could be observed after HTA (Figure 4.1.c). Following HTA, it was evident that Pd-Pt/10Co/SnO_2 catalyst outperformed the other catalysts in terms of catalytic activity; particularly at 400 ˚C where the negative effect of water is known to be significant for Pd catalysts [15], [215].

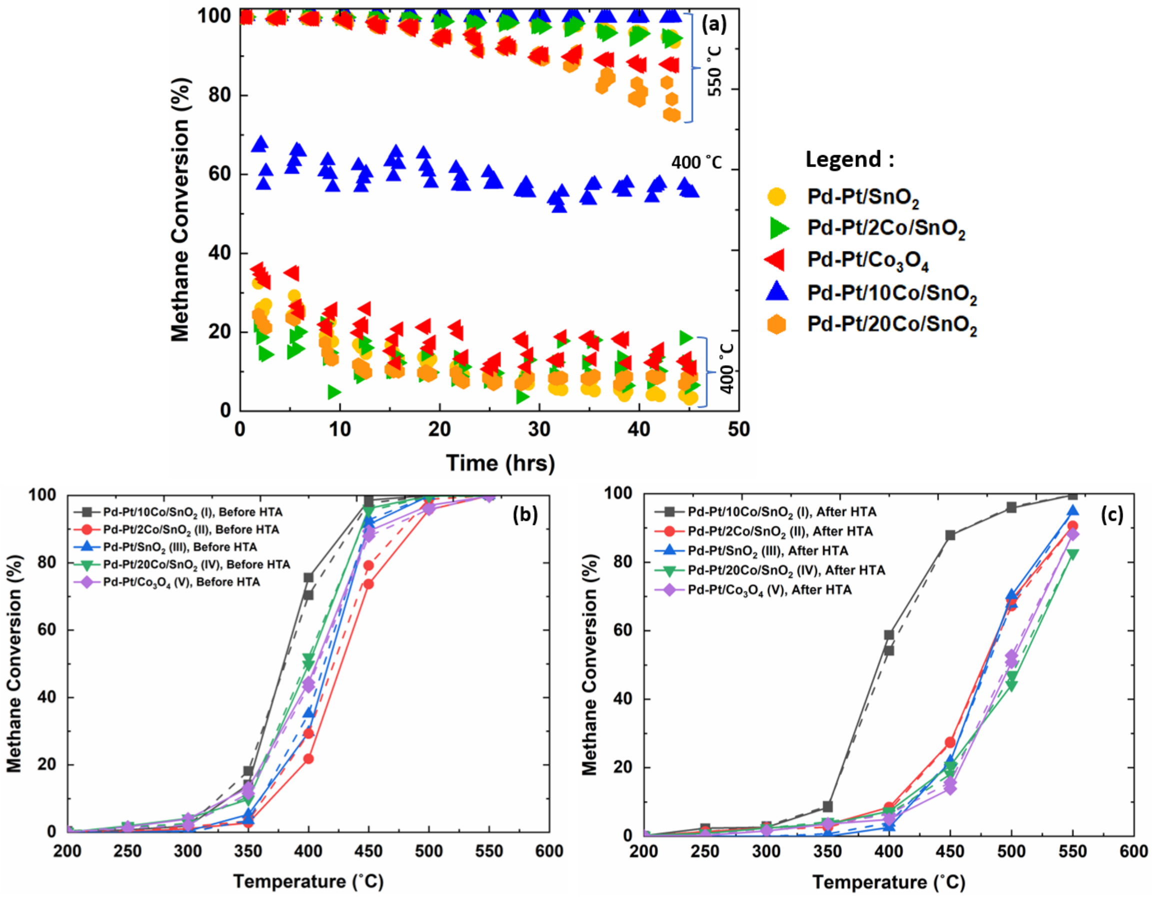

Figure 4. 1. Effect of cobalt loading on the performance of SnO_2-supported bimetallic catalysts: (a) HTA curves under 10 vol% wet feed conditions for 4000 ppmv methane concentration; (b-c) I-E curves for runs before and after hydrothermal ageing (HTA) respectively under 10 vol% wet feed conditions for 4000 ppmv methane concentration (solid lines – ignition curves and dashed lines – extinction curves)

SEM-EDX analysis was performed on the calcined Pd-Pt/yCo/SnO_2 catalysts. The SEM images may be found in the Supporting Information (Figure B.2). EDX data were obtained at 5 different spots for each catalyst and the Sn/Co atomic ratio was calculated at each of the spots as depicted in Figure 4.2. Theoretically, the Sn/Co atomic ratio was calculated to be 19, 4 and 2 for the 2, 10 and 20 wt.% cobalt loadings, respectively (depicted as the dashed lines in Figure 4.2). In general, the samples with 2 and 10 wt.% Co demonstrated the expected ratios (within 0.8 – 1.2-fold deviations), while the ratio was systematically twice lower for the sample with 20 wt.% Co. It is likely that Co_3O_4 is segregated at such high loadings, resulting in a lack of contact with SnO_2 and inefficient interactions between all the components in the catalyst formulation. Indeed, the I-E and HTA trends (Figure 4.1a-c) demonstrated that the Pd-Pt/20Co/SnO_2 catalyst performed quite similarly to the Pd-Pt/Co_3O_4 catalyst, suggesting the above hypothesis could be a possibility. In the case of the 2 wt.% Co loading, the catalyst behaved similarly to the Pd-Pt/SnO_2 (Figure 4.11a-c) catalyst suggesting that the amount of Co was not sufficient to be in close proximity to the active Pd-Pt components. Thus, the enhanced performance of the 10 wt.% Co-impregnated sample suggests that the amount of precursor deposition in the optimized amount is paramount to reap the benefits offered by its uniform deposition and influence the interaction among the various components present in the catalyst formulation.

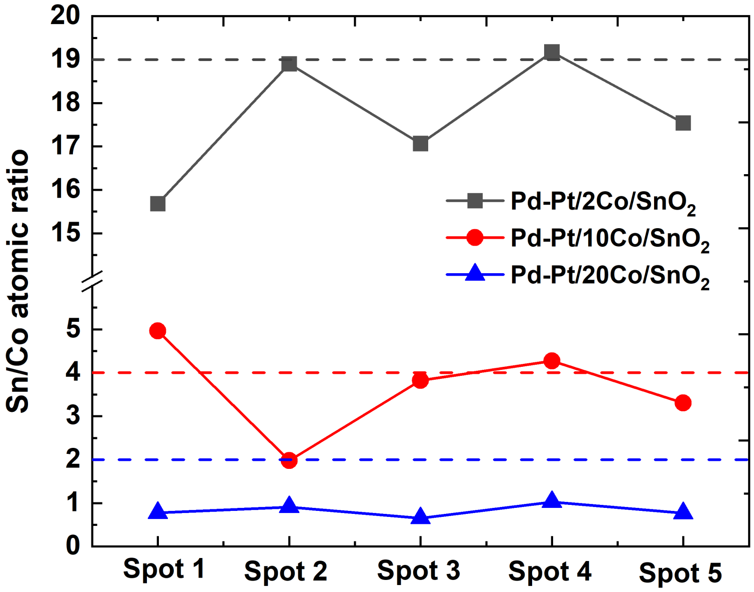

Figure 4. 2. Graphical representation of the Sn/Co atomic ratio at the 5 different analyzed spots for the calcined Pd-Pt/yCo/SnO_2 (y = 2, 10, 20) catalysts

Experimental studies by Tang et al. [211] demonstrated that Co_3O_4-SnO_2 hybrid oxides with a molar ratio of Co/(Co+Sn) = 0.75 had the highest catalytic activity and stability. The authors proposed that electronic interaction between SnO_2 and Co_3O_4 coupled with the high reactivity of Co_3O_4 contributed to the highest catalytic activity. Based on the quantitative amount of cobalt deposition, the Pd-Pt/10Co/SnO_2 reported a Co/(Co+Sn) molar ratio of 0.7. These results are consistent with that reported by Tang et al. [211], thus proposing a possible explanation to observed enhanced catalytic performance of the Pd-Pt/10Co/SnO_2 catalyst.

4.3.2. Ignition-extinction tests and hydrothermal ageing as compared to benchmark catalysts

The performance of the Pd-Pt/10Co/SnO_2 catalyst was compared against the benchmark Pd/γ-Al_2O_3 and Pd-Pt/γ-Al_2O_3 catalysts. In order to contrast the performance of the four-component catalyst system, the same ratio of precious metal and cobalt oxide (1 wt.% Pd-Pt and 10 wt.% Co) was deposited and tested on the conventional γ-Al_2O_3 support. Similar to the previous section, I-E and HTA (45 hours ageing by cycling the temperature between 400 ˚C and 550 ˚C) studies were performed on Pd-Pt/10Co/γ-Al_2O_3 catalyst under the 10 vol% wet conditions for an initial methane concentration of 4000 ppmv. The observed I-E and HTA trends are depicted in Figure 4.3. The I-E curves for the dry runs under the same testing conditions are depicted in Figure B.3. Following HTA (Figure 4.3.a), it could be observed that the Pd-Pt/10Co/SnO_2 catalyst does surpass the conventional Pd/γ-Al_2O_3 catalyst in terms of hydrothermal stability and activity. Though the Pd-Pt/10Co/γ-Al_2O_3 catalyst surpassed the performance of the benchmark catalyst, it could not perform to the level of the SnO_2-supported catalyst.

While the Pd-Pt/10Co/SnO_2 catalyst was able to provide enhanced and stable catalytic conversions, it is crucial to understand the role of the various active components and the interactions existing between them. Thus, the 10Co/SnO_2 sample was subjected to I-E and HTA (45 hours ageing by cycling the temperature between 400 ˚C and 550 ˚C) studies under the 10 vol% wet conditions for an initial methane concentration of 4000 ppmv (Figure 4.3. a-b). The I-E curves for the dry runs under the same testing conditions are depicted in Figure B.3 in Appendix B. Based on the HTA trends (Figure 4.3.a) it could be observed that while the sample did not achieve 100% methane conversion at 550 ˚C, the sample however was able to provide stable conversion at ~55%. Following HTA, it could also be observed that while the catalyst had deactivated, the deactivation was not as drastic and significant as that observed on the benchmark Pd/γ-Al_2O_3 catalyst. Based on previous studies, cobalt is known to be active for methane activation and could remain unaffected by the presence of water [116]. However, it had been demonstrated that the cobalt-based catalyst was liable to progressively losing its active sites by sintering in the wet feed [116]. Similarly, Pd-Pt components have been known to be active for methane combustion reaction [47], [48], however, under wet feed conditions they are susceptible to deactivation due to possible sintering of active components [136]. Thus, deposition of 10 wt.%

cobalt to the Pd-Pt/SnO_2 catalytic system could have possibly resulted in some synergistic interactions between the Co and Pd-Pt active components, enabling different component to participate in the reaction, thereby resulting in the enhanced catalytic activity. Hence, this work delves into comprehending the kinetic consequences of incorporating 10 wt.% Co to the 1wt.% Pd-Pt (1:1 Pd:Pt molar ratio)/SnO_2 catalyst leading to its improved catalytic activity and stability.

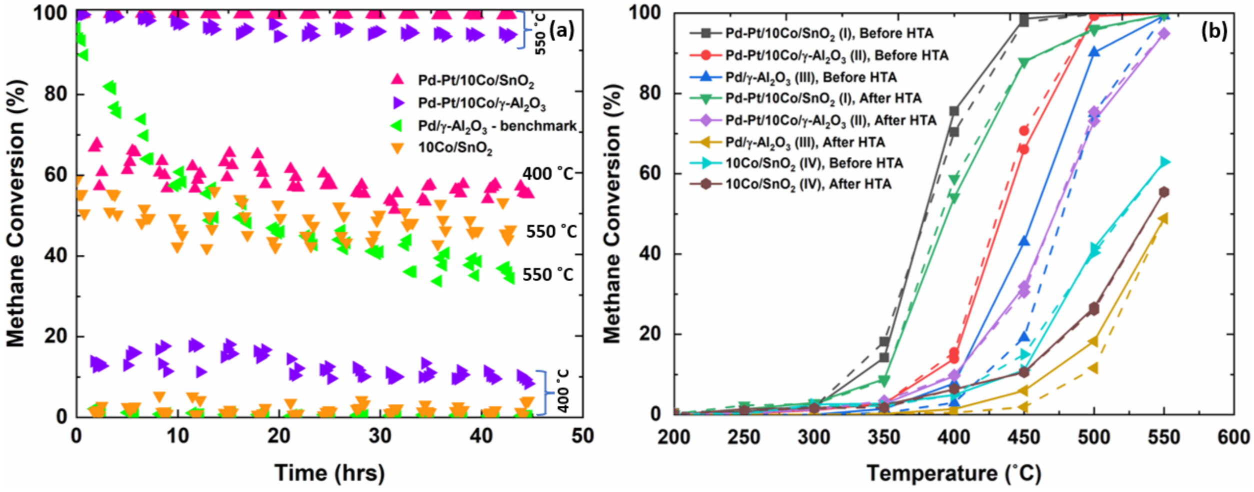

Figure 4. 3. Comparison with benchmark catalysts: (a) HTA curves under 10 vol% wet feed conditions for 4000 ppmv methane concentration; (b) I-E curves for runs before and after hydrothermal ageing (HTA) under 10 vol% wet feed conditions for 4000 ppmv methane concentration (solid lines – ignition curves and dashed lines – extinction curves)

4.3.3. Characterization of the cobalt-promoted catalysts

Based on the observed differences in the catalytic performance (Figure 4.3.b), the above-mentioned catalysts were subjected to various characterization techniques to help comprehend the contrasting catalytic activities and stabilities. The characteristics of the aged catalysts are summarized in Table 4.1. Prior to CO chemisorption tests on the Pd-Pt/10Co/S (S = γ-Al_2O_3, SnO_2) catalysts, the same analysis was performed on the reduced 10Co/S (S = γ-Al_2O_3, SnO_2) samples and it was found that Co_3O_4 did not adsorb any CO on its surface. To calculate the metal dispersions, the CO:surface atom metal stoichiometric factor 1 was used. It can be observed that the addition of cobalt to the bimetallic catalysts has significantly improved the dispersion in comparison to that reported in our earlier work [136]. Studies by Willis et al. [108] demonstrated that the inclusion of cobalt as a promoter to the Pd/γ-Al_2O_3 catalyst had resulted in reduced sintering of active PdO on the surface. Thus, the improved dispersion on the Pd-Pt/10Co/S (S = γ-Al_2O_3, SnO_2) catalysts could be attributed to improved sintering resistance imparted by the deposition of cobalt. The hydrothermally aged γ-Al_2O_3-supported catalyst reported a pore diameter of 4.3 nm and a Type IV isotherm, indicating that the catalytic system was mesoporous. Thus, the momentous collapse of the pore structure was not observed despite the inclusion of cobalt to the γ-Al_2O_3-support. However, the pore size reduced from 5.6 nm to 4.3 nm indicating that some of the big pores on the γ-Al_2O_3 support could be blocked by Co_3O_4. The isotherms and the pore size distribution for the γ-Al_2O_3-supported catalyst is depicted in Figure B.4. The calculated external surface area for the hydrothermally aged SnO_2-supported catalyst was ~ 6 m^2/g which could be correlated to the reported BET surface area in Table 4.1, indicating that the catalyst was non-porous. The catalyst also depicted a Type II isotherm (Figure B.5 in Appendix B) consistent with those reported for a non-porous system. Larger particle sizes for the SnO_2-supported catalysts are expected because of the lower support surface area as reported in Table 4.1. Though the dispersion was greatly improved on the Pd-Pt/10Co/S (S = γ-Al_2O_3, SnO_2) catalysts, the γ-Al_2O_3-supported catalyst could not achieve the same performance as that of the SnO_2-supported catalyst. In our previous work, it had been demonstrated that the Pd-Pt catalysts provided similar conversions despite being deposited on different support materials [136]. Based on the XRD analysis of the aged Pd-Pt/SnO_2 and Pd-Pt/γ-Al_2O_3 catalysts, no structural changes could be observed for the support materials of interest [136]. Thus, differences in the catalytic activities could be attributed to variations arising from the effects of cobalt deposition on these support materials. In an effort to interpret the cause for the lower activity on the γ-Al_2O_3-supported catalyst, XRD analysis was carried out on the calcined 10Co/S (S = γ-Al_2O_3, SnO_2) samples.

Table 4. 1. Physical properties of the aged Pd-Pt catalysts

Sample	**Metal dispersion (%)^a**	**Nanoparticle sizes (nm)^a**	**Surface area (m^2/g)^b**
Pd-Pt/10Co/γ-Al_2O_3	30	3	120
Pd-Pt/γ-Al_2O_3	11	8	144
Pd-Pt/10Co/SnO_2	19	6	6
Pd-Pt/SnO_2	5	18	6

^{a}Determined by CO chemisorption

^{b}Determined by BET surface area measurement

XRD analysis was performed on the calcined 10Co/S (S = γ-Al_2O_3, SnO_2) samples to discern the structural changes observed for Co_3O_4 when deposited on the support materials under investigation. The XRD analysis of the desired samples is depicted in Figure 4.4. XRD profiles of the calcined Co_3O_4 and γ-Al_2O_3 were also obtained to enable clear identification of the components observed in the catalysts under study (the reference peaks for all the components under study can be referred to Figure B.6). Sharp peaks corresponding to Co_3O_4 signals could be observed on the SnO_2 (Figure 4.4) suggesting no observable Co_3O_4 structural changes. Though similar peaks could be seen on the γ-Al_2O_3 support, broadening of the peaks could be observed possibly indicating a loss of crystallinity of Co_3O_4. The signals at $2\Theta = 42.956^o$, 45.089^o, and 52.539^o could be a possible indication of $Co_2Al_2O_4$ spinel formation due to overlapping signals between Co_3O_4 and $Co_2Al_2O_4$ (reference peaks for both components can be referred to Figure B.6). Choya et al. [216] reported similar observations based on their studies for supported Co_3O_4/Al_2O_3 catalysts for lean-burn wet (10 vol%) methane combustion. Though conclusive evidence of $Co_2Al_2O_4$ spinel formation cannot be extracted from the XRD analysis, it still does indicate structural changes occurring for Co_3O_4 when deposited on γ-Al_2O_3 support.

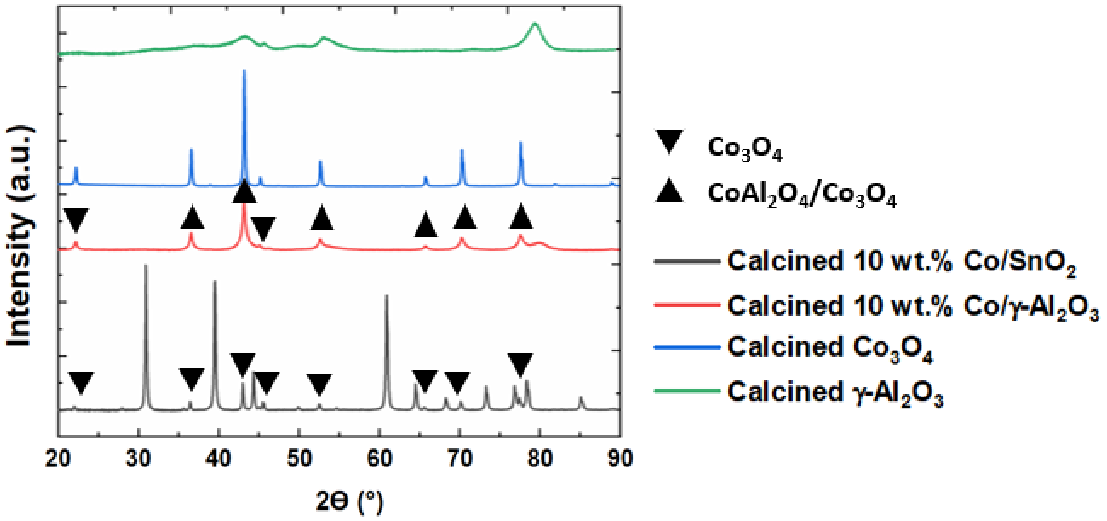

Figure 4. 4. XRD profiles of the calcined 10Co/S (S = γ-Al_2O_3, SnO_2) samples

To obtain conclusive evidence for spinel formation on γ-Al_2O_3, redox properties were investigated utilizing TPR analysis on the calcined 10Co/S (S = γ-Al_2O_3, SnO_2) samples (the TPR curves normalized per surface area of the respective samples is as depicted in Figure B.7). Based on the H_2 reduction treatment up to 800 ˚C, reduction of free Co_3O_4 in the 380 ˚C – 440 ˚C region was observed for the SnO_2-supported sample. This reduction peak could be corroborated with the reduction peak observed for calcined Co_3O_4 in Figure 4.5.b as well as those reported in previous studies [90], [216], [217]. However, as seen in Figure 4.5.a, SnO_2 reduction could also be observed in the same temperature range. The peaks for SnO_2 ranging between 280 ˚C – 480 ˚C correspond to dissociatively adsorbed oxygen that participates in CH_4 oxidation [22], [162], [163]. The sharp increase in hydrogen consumption for SnO_2 and 10Co/SnO_2 beyond 550 ˚C corresponds to the reduction of bulk SnO_2 to metallic Sn [164], [165]; and it can be observed that the addition of cobalt does not affect the reducibility of the support material considered in this study. Thus, the presence of free cobalt oxide species that could either provide oxygen or participate in the combustion reaction could result in the improved catalytic performance observed on the Pd-Pt/10Co/SnO_2 catalyst. On the other hand, reduction peaks on the 10Co/γ-Al_2O_3 could only be observed at 552 ˚C (first peak) and 715 ˚C (second peak). Similar reduction peaks for Co_3O_4/Al_2O_3 catalysts were reported by Choya et al. [216] and Sirijaruphan et al. [217]. The first observed peak located at about 550 ˚C – 600 ˚C could be related to Co species with lower reducibility owing to the strong interaction between the Co species and alumina support [218], [219]. The second high-temperature peak located at about 680 ˚C – 800 ˚C could be attributed to the formation of cobalt aluminate $Co_2Al_2O_4$ species [220], [221]. To confirm the formation of the spinel structure, TPR studies were performed on commercial cobalt-aluminate spinel. The studies were carried out by H_2 reduction treatment from 100 ˚C – 1000 ˚C followed by holding the temperature at 1000 ˚C for 3 hours to ensure complete reduction of the spinel compounds. As illustrated in Figure 4.5.b, similar reduction peaks could be observed for the $10Co_3O_4/\gamma\text{-}Al_2O_3$ sample and the commercial cobalt-aluminate sample. The high-temperature reduction peak at ~ 950 ˚C could be attributed to the reduction of the cobalt-aluminate spinel structure, while the peaks at 550 ˚C could be related to the reduction of Co species with strong Co-Al interaction. Differences in the peak strengths could be attributed to different sizes and compositions of Co_3O_4 on the substrate. To ensure no reduction peak contributions from pure Co_3O_4 and $\gamma\text{-}Al_2O_3$ at temperatures above 400 ˚C, the same procedure was carried out; no peaks were observed, thereby providing promising evidence of the formation of spinel structures on the $10Co/\gamma\text{-}Al_2O_3$ sample. Thus, the unavailability of free Co_3O_4 on the surface of the $\gamma\text{-}Al_2O_3$ support could explain the reduced catalytic activity on the Pd-Pt/$10Co/\gamma Al_2O_3$ catalyst.

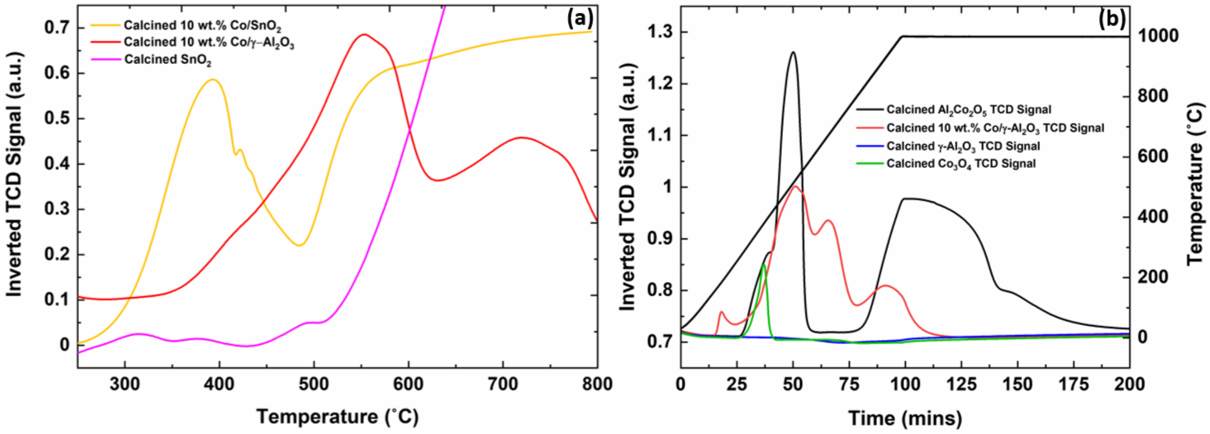

Figure 4. 5. (a) TPR analysis of calcined 10Co/S (S = γ-Al_2O_3, SnO_2) samples and SnO_2 support up to 800 ˚C; (b) TPR analysis comparison of the calcined 10Co/γ-Al_2O_3 against the commercial $Co_2Al_2O_4$ sample for H_2 reduction treatment up to 1000 ˚C (0.3 g of each sample). The surface-area normalized TPR are shown in Figure B.7.

Investigation into the TEM-EDX images of hydrothermally aged Pd-Pt/10Co/SnO_2 catalyst (Figure 4.6) revealed the formation of clusters of bulk Pd-Pt alloy with a measured lattice spacing of 0.2258 nm. Pd segregation to the surface was also observed owing to the smaller surface free energies for Pd than Pt, resulting in the preferential migration of Pd onto the small alloy clusters to minimize the overall Gibbs free energy of the system. A Pd-rich phase was observed to segregate out with a lattice spacing of 0.265 nm, which was typically expected for the PdO {101} phase. For the aged Pd-Pt/10Co/γ-Al_2O_3 catalyst (Figure B.8), PdO segregation was observed. A 0.23 nm lattice fringe, which could correspond to the Pd-Pt alloy structure was also observed after ageing. Similar observations were reported in the studies by Yang et al. [51] and Goodman et al. [47] for bimetallic catalysts supported on alumina support. Hence, hydrothermal ageing resulted in the existence of PdO/Pd-Pt structures, with PdO segregating out as a separate phase co-existing with alloyed Pd-Pt aggregates for both catalysts under study [47].

Co_3O_4 {220} phase with a lattice spacing of 0.285 nm could be observed on both catalysts. The aged Pd-Pt/10Co_3O_4/γ-Al_2O_3 catalyst also demonstrated the presence of the Co_3O_4 {311} phase with a lattice fringe of 0.245 nm. It is interesting to note that the Co_3O_4 {110} and Co_3O_4 {112} phases (lattice spacing of 0.57 nm and 0.33 nm respectively) were evident on the SnO_2-supported catalyst which has been recognized to be highly active for CH_4 combustion [195], [212]. Studies by Han et al. [222] demonstrated that for the Co_3O_4 {112} phase, the surface atomic arrangement of Co^{2+}/Co^{3+} active sites, especially the presence of octahedrally coordinated Co^{3+} species, resulted in optimized adsorption, activation, and desorption of oxygen species. DFT studies by Tyo et al. [223] demonstrated that the Co_3O_4 {110} phase had weakly held O* species on the surface formed in the presence of oxygen. These species are crucial as they could replenish the active surface O*-O* sites that could activate the C-H bond [223]. Thus, the formed Co_3O_4 phases could either contribute to activating the C-H bond or supplying oxygen to reactivate Pd. The presence of the observed Co_3O_4 phases combined with the presence of PdO/Pd-Pt structures could thereby attribute to the observed improvement in the methane combustion activity and stability for the Pd-Pt/10Co/SnO_2 catalyst.

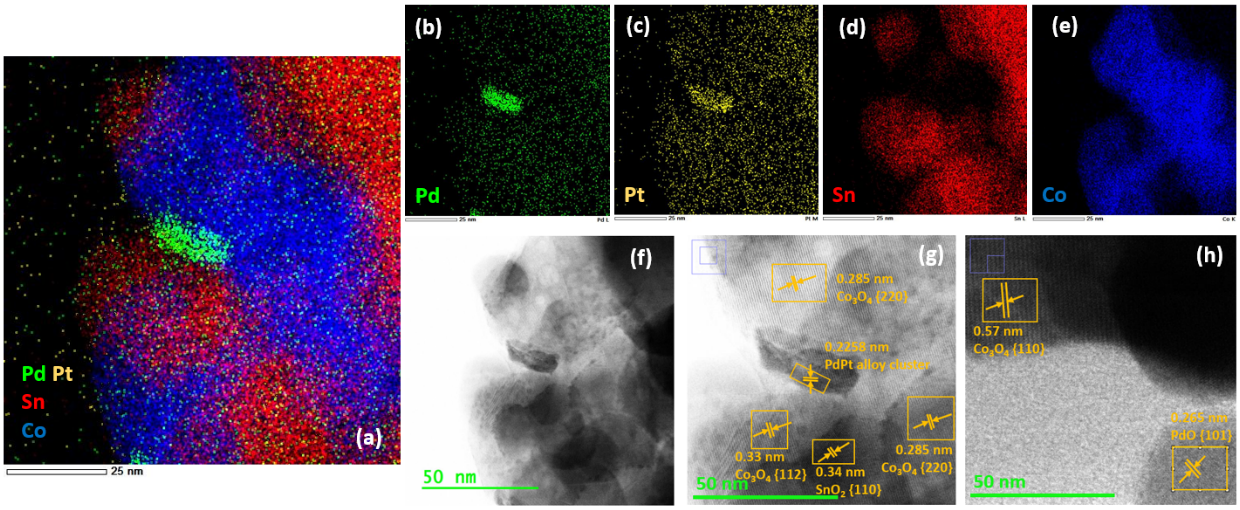

Figure 4. 6. Hydrothermally aged Pd-Pt/10Co/SnO_2 catalyst: (a)-(e) TEM-EDX analysis showing Pd (green), Pt (yellow) Sn (red), and Co (blue) distribution; (f-h) a representation of the SnO_2, Co_3O_4, PdO and PdPt phases

To evaluate the catalyst's affinity to water, TPD analysis was performed on the aged Pd-Pt/10Co/S (S = γ-Al_2O_3, SnO_2) catalysts (Figure 4.7 and Figure B.9 in Appendix B). The amounts of the released water, based on the areas of the TPD profiles for H_2O evolution, were found as 0.18 mmol/g and 0.67 mmol/g for the SnO_2- and Al_2O_3-supported samples, respectively. The surface area of the Al_2O_3-supported catalyst is 20-fold higher than that of the SnO_2-based catalyst, implying that the latter catalyst adsorbs a 5-fold higher amount of water on its surface. It is accepted that support's hydrophobicity is beneficial to water tolerance of methane combustion catalysts [92], [97], [101], [154]. In this case, the more hydrophilic SnO_2-based catalyst demonstrates a significantly improved catalytic performance as compared to a relatively hydrophobic Al_2O_3-catalyst, indicating that other phenomena overpower the hydrophobicity requirement. No concurrent O_2 evolution in the temperature range of combustion (up to 550 °C) was observed for either catalyst.

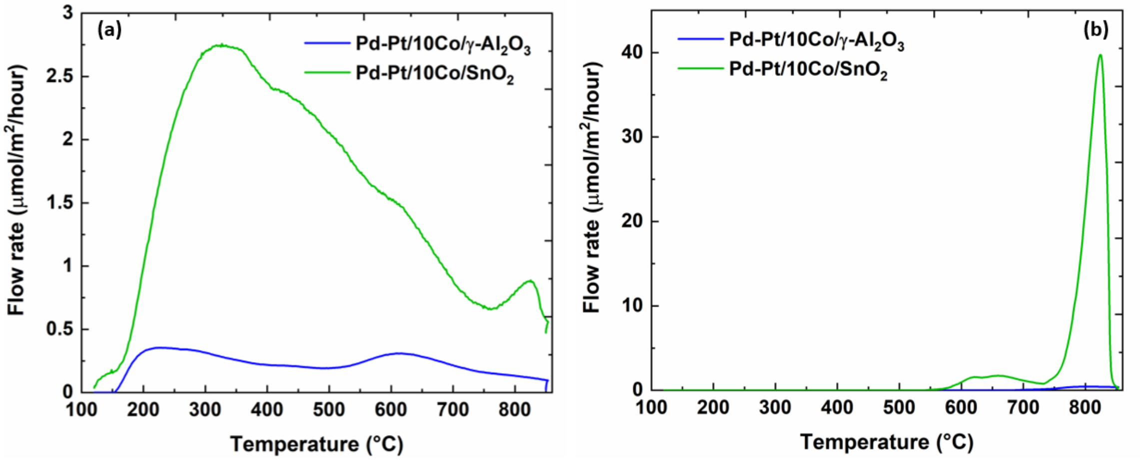

Figure 4. 7. TPD profiles: (a) Water and; (b) oxygen evolution trends normalized per sample surface area obtained from the TPD studies on the aged Pd-Pt/10Co/S (S = γ-Al_2O_3, SnO_2) catalysts (0.1 g of each catalyst has been utilized for the TPD studies)

4.3.4. Kinetic study of the Pd-Pt/10Co/S (S = γ-Al_2O_3, SnO_2) catalysts

The kinetic studies were performed after catalyst deactivation during their hydrothermal ageing. Several repeated experiments were done to ensure that the effect of continuing deactivation was negligible. The ignition curves of the reproducible runs for the Pd-Pt/10Co/S (S = γ-Al_2O_3, SnO_2) catalysts for an initial CH_4 concentration of 1000 ppmv and 5000 ppmv in the presence of 5 vol% and 10 vol% water is as illustrated in Figure 4.8. The reproducibility of the experimental points for the Pd-Pt/10Co/γ-Al_2O_3 catalyst at the other initial CH_4 concentrations (2000 ppmv, 3000 ppmv, and 4000 ppmv) have been depicted in Figure B.10 (for the 5 vol% runs) and Figure B.11 (for the 10 vol% runs). Similarly, the reproducibility of the experimental points for Pd-Pt/10Co/SnO_2 catalyst at the other initial CH_4 concentrations (2000 ppmv, 3000 ppmv, and 4000 ppmv) have been depicted in Figure B.12 (for the 5 vol% runs) and Figure B.13 (for the 10 vol% runs).

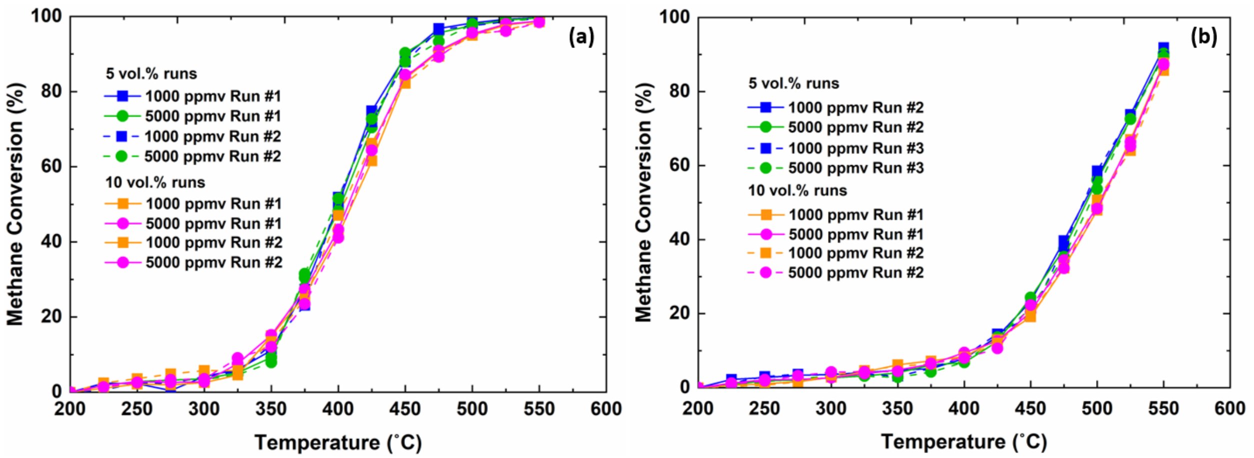

Figure 4. 8. Summary of the effect of water and initial concentration on the ignition curves for the (a) Pd-Pd/10Co/SnO_2 catalyst and (b) Pd-Pt/10Co/γ-Al_2O_3 catalyst. For other concentrations and runs, refer to Figures B.10 and B.11 for the Pd-Pt/10Co/γ-Al_2O_3 catalyst and Figures B.12 and B.13 for the Pd-Pd/10Co/SnO_2 catalyst

Based on the ignition curves for both catalysts, the fractional conversion appeared to be first order to CH_4; however, the trend did not seem to exhibit a negative first order to H_2O as seen in the case of the conventional Pd/γ-Al_2O_3 catalyst. The results obtained from the optimization problem are tabulated in Table 4.2. Figures B.14.a and B.14.b depict the parity plot comparing the experimental and predicted conversion based on the kinetic parameters in Table 4.2 for the Pd-Pd/10Co/SnO_2 and Pd-Pt/10Co/γ-Al_2O_3 catalysts, respectively. The parity plot confirmed that the optimized parameters correlated the experimental and predicted conversions with the maximum deviation existing between the ±10% error lines.

Table 4. 2. Estimated kinetic parameters for the Pd-Pt/10Co/S (S = γ-Al_2O_3, SnO_2) catalysts based on equation (4.1) for the combined modeling under 5 vol% and 10 vol% wet feed conditions for all CH_4 concentrations from the reproducible runs. Rate law (Eq. 4.1): $(-r_M) = k'C_M C_{aq}^n$

Catalyst	Pd-Pt/10Co/γ-Al_2O_3	Pd-Pt/10Co/SnO_2
Observed activation energy (kJ mol^{-1})	151 ± 8	90 ± 7
Observed pre-exponential factor (mol g_{PGM}^{-1} s^{-1})	$(44 \pm 5) \times 10^6$	$(20 \pm 7) \times 10^3$
Observed order to H_2O (n)	- 0.55	- 0.37
Objective function value	8×10^{-4}	2×10^{-3}

The observed orders to H_2O for the SnO_2 and Al_2O_3 supported catalysts in this study are quite distinct from those reported for the Pd-Pt catalysts on the same support material in our recent work [116], [136]. While the bimetallic catalysts (Pd-Pt/γ-Al_2O_3 and Pd-Pt/SnO_2) reported a negative first order to water based on our previous work [136], the addition of cobalt to the bimetallic system has altered the order of water dependency on either catalyst. In the case of the Pd-Pt/10Co/SnO_2 and Pd/SnO_2 catalysts, the observed activation energies were the same, while the observed pre-exponential factor was significantly higher on the former catalyst. Interestingly, the dependency of water on the SnO_2-supported catalyst and the γ-Al_2O_3-supported catalyst were relatively similar to the -0.37 order to water on the Pd/Co_3O_4 catalyst [116].

The partial order to H_2O for both these catalysts could be a characteristic of the presence of different active sites in play. Fujimoto et al. [32] proposed a methane combustion mechanism over PdO_x/ZrO_2 catalyst, which follows the 1st order to methane and -1st order to water. Methane interacts with coordinately unsaturated metal site, following which a sequential hydrogen atom abstraction from the adsorbed methane backbone occurs, ultimately resulting in the formation of a surface hydroxyl. With the first H-atom abstraction from the methane molecule being the rate determining step, the following rate equation was proposed [32]:

$$r = \frac{k_2K_1[O_2]}{3\left[1+K_3[CH_4]+\left(\frac{k_2K_1[O_2]}{3k_4K_3[CH_4]}\right)+K_1[O_2]+\left(\frac{k_2K_1[O_2][H_2O]}{3k_4K_3K_5[CH_4]}\right)^{0.5}+\left(\frac{1}{K_6}+\frac{k_2K_1[O_2]}{3k_4K_3K_7[CH_4]}\right)[CO_2]\right]^2} \tag{4.4}$$

For the Pd-based catalysts, water is accepted as the most abundant surface intermediate (MASI), which gives rise to negative first order to water (as also observed in the case of the Pd-Pt/SnO_2 catalyst [136]). Thus, Equation 4.4 could be modified to have the following rate equation [32], [135]:

$$r = \frac{k^*[CH_4]^{1.0}}{[H_2O]^{1.0}} \tag{4.5}$$

However, the partial order to water on the catalysts considered in this study could suggest that some empty sites are largely available and not poisoned by water, methane, oxygen, and/or carbon dioxide. Such a scenario could be possible on the Co active sites as it has been demonstrated previously for cobalt catalysts to exhibit a zero order to water and first order to methane [116]. Thus, Equation 4.4 could alternatively have the form:

$$r = k^*[CH_4]^{1.0} \tag{4.6}$$

The order of water being between 0 and -1 observed in the case of the Pd-Pt/10Co/SnO_2 and Pd-Pt/10Co/γ-Al_2O_3 catalysts could be assumed to be due to additive contributions between the Co and Pd-Pt active components. Thus, a rate model with additive contributions (Equation 4.7) from two different active sites was proposed to obtain the kinetic parameters. The first site was considered to be unaffected by H_2O (possible Co active site; Equation 4.6), while the second active site was affected by H_2O with an order of -1 to it (possible PGM site; Equation 4.5). For the γ-Al_2O_3-supported catalyst, an internal effectiveness factor was additionally incorporated for each of the additive contributions in the rate model to account for the mass transfer effects. The calculation of the internal effectiveness factor and incorporation into the additive rate model is elaborated in Section B.3 of Appendix B.

$$(-r_M) = k_1C_M + \frac{k_2C_M}{C_{aq}} \tag{4.7}$$

$$\text{Where } k_1 = k_{01}\,.\exp\left(-\frac{E_{a1}}{RT}\right); \tag{4.8}$$

$$k_2 = k_{02}\,.\exp\left(-\frac{E_{a2}}{RT}\right); \tag{4.9}$$

The calculation of the criteria satisfying the inexistence of internal and external heat transfer limitations as well as the inexistence of external mass transfer limitations have been elaborated in Sections B.2 and B.3 in Appendix B. Considering that the site affected by water was considered to be a PGM site, the observed activation energy Ea_2 was fixed to be 131 kJ mol^{-1} resembling the apparent activation energy observed in the case of the conventional Pd-Pt/γ-Al_2O_3 catalyst based on our previous work [136]. The optimized parameters obtained in this case are as provided in Table 4.3.

Table 4. 3. Estimated kinetic parameters for the Pd-Pt/10Co/S (S = γ-Al_2O_3, SnO_2) catalysts based on equations (4.7)-(4.9) for the combined modeling under 5 vol% and 10 vol% wet feed conditions for all CH_4 concentrations from the reproducible runs.

Rate law (Eq. 4.7): $(-r_M) = k_1 C_M + k_2 C_M C_{aq}^{-1}$

Catalyst	**Pd-Pt/10Co/γ-Al_2O_3**	**Pd-Pt/10Co/SnO_2**
Observed activation energy 1 (kJ mol^{-1})	150 ± 8	89 ± 9
Observed activation energy 2 (kJ mol^{-1})	131	131
Observed pre-exponential factor 1 (m^3_{fluid} g_{PGM}^{-1} s^{-1})	$(21 \pm 4) \times 10^6$	$(83 \pm 5) \times 10^2$
Observed pre-exponential factor 2 (mol_M g_{PGM}^{-1} s^{-1})	$(16 \pm 2) \times 10^5$	$(50 \pm 9) \times 10^5$
Rate constant k_1 @ 500 °C (m^3 g_{PGM}^{-1} s^{-1})	1.54×10^{-3}	8.05×10^{-3}
Rate constant k_2 @ 500 °C (mol_M g_{PGM}^{-1} s^{-1})	2.26×10^{-3}	7.05×10^{-3}
Objective function value	6×10^{-4}	1×10^{-3}

Figure 4.9 depicts the parity plot comparing the experimental and predicted conversion and the ±10% error lines. The parity plot confirmed that the obtained optimized parameters provided a good correlation between the experimental and predicted conversions with the maximum deviation between the error lines, thereby suggesting that the proposed rate model (Equation 4.7)

could be a possible mechanism for the methane combustion reaction on the Pd-Pt/10Co/S (S = γ-Al_2O_3, SnO_2) catalysts. The reasonable fitting of the simulated data to the experimental data depicted below does not signify that this reaction mechanism occurs; the study mainly focuses on obtaining a value of the kinetic parameters for reactor design purposes.

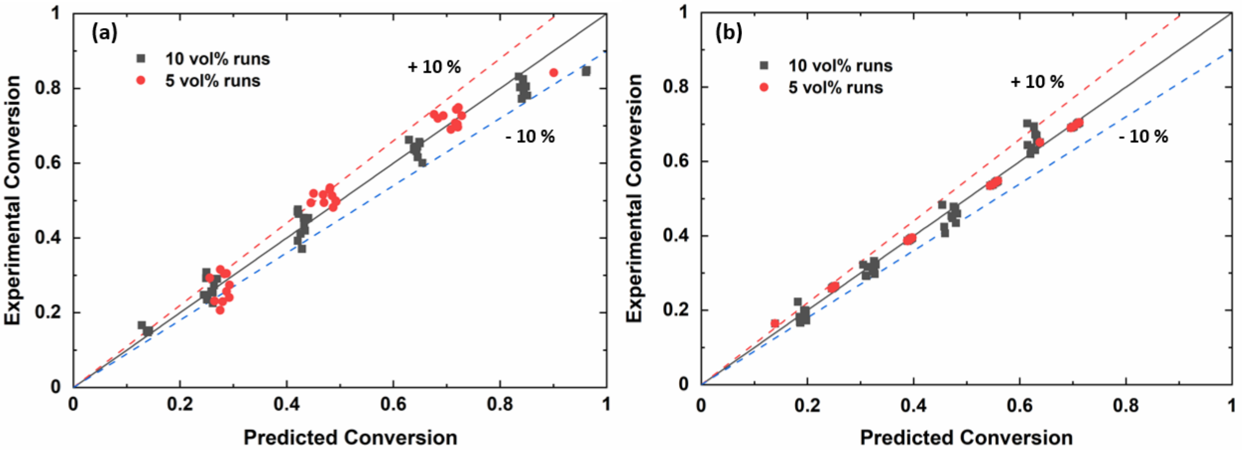

Figure 4. 9. Comparison of the predicted and experimental conversion for the combined wet feed condition studies on the (a) Pd-Pt/10Co/SnO_2 catalyst and (b) Pd-Pt/10Co/γ-Al_2O_3 catalyst based on the additive rate model Eq. (4.7)

The observed activation energy Ea_1 was lower on the Pd-Pt/10Co/SnO_2 catalyst than on the Pd-Pt/10Co/γ-Al_2O_3 catalyst (Table 4.3). It is interesting to note here that the observed activation energy Ea_1 is quite like that observed on the Pd/SnO_2 catalyst [136], indicating that the kinetics could be dictated by the SnO_2 support. Pd-Pt/10Co/γ-Al_2O_3 catalyst on the other hand reported an observed activation energy of $Ea_1 = 150 \pm 8$ kJ mol^{-1}. Kinetic studies by Stefanov et al. [115] on the Pd-Co/Al_2O_3 catalyst reported an activation energy of $E_a = 113$ kJ mol^{-1} for lean-burn wet methane combustion on oxidized active sites on the catalyst surface. The authors proposed that the reaction pathway proceeded via a Mars-van-Krevelen mechanism, and the rate-determining step was attributed to the oxidation of the catalyst surface. However, based on our temperature-programmed desorption studies (Figure 4.7.b) at the temperature range of interest (below 550 °C), no oxygen is supplied to the reaction from the support [24], thus a rate model following the Mars-van-Krevelen mechanism was not adopted.

To discern if the kinetic contributions were dictated by Co_3O_4 or the support materials (SnO_2 and γ-Al_2O_3) under investigation, kinetic studies were performed on 1 wt.% Pd-Pt (1:1 molar ratio of Pd:Pt with 0.343 wt% Pd and 0.647 wt% Pt) supported on Co_3O_4. The catalyst was synthesized, and kinetic studies were performed in the same manner as the bimetallic catalysts investigated in our previous studies [136]. The aged Pd-Pt/Co_3O_4 catalyst reported a dispersion of 7% and a surface area of 9 m^2/g (non-porous system exhibiting Type II isotherm; Figure B.15). The Pd-Pt/Co_3O_4 reported a partial order of - 0.42 to water with an observed activation energy of 140 ± 9 kJ mol^{-1} based on the rate model in Equation 4.1 (Table B.7). Due, to the observed partial order to water, an additive rate model (Equation 4.7) was implemented similarly as above, and the obtained optimized kinetic parameters are illustrated in Table B.8. The kinetic study ignitions curves as well as the parity plots confirming the validity of the obtained optimized parameters are depicted in Figure B.16 and Figure B.17.

The modeling results based on Equation 4.1 indicate that the Co_3O_4-supported bimetallic catalyst had a similar apparent activation energy as that of the Pd-Pt/10Co/γ-Al_2O_3 catalyst, though the pre-exponential factor was much larger on the Co_3O_4-supported bimetallic catalyst. Based on the additive rate model, the observed activation energy Ea_1 for the Pd-Pt/Co_3O_4 catalyst was similar to that of the Pd-Pt/10Co/γ-Al_2O_3 catalyst, indicating that the kinetics could be dictated by Co_3O_4. However, based on the studies by Nasr et al. [116], depositing Pd on Co_3O_4 did not result in a reduction in the activation barrier. The Pd/Co_3O_4 catalyst reported an apparent activation energy like that observed on the γ-Al_2O_3-supported catalyst [116]. Thus, the kinetic dependencies on the Pd-Pt/10Co/γ-Al_2O_3 catalyst could be attributed to either Co_3O_4 or γ-Al_2O_3 support. In the case of the Pd-Pt/10Co/SnO_2 catalyst, it is evident that SnO_2 dictates the kinetics as the activation energy Ea_1 was more similar to the Pd/SnO_2 catalyst than to the catalyst deposited on the Co_3O_4 support. In terms of the order of water dependency, it can be stated that the addition of cobalt has altered the reaction order to water, as the bimetallic catalysts supported on SnO_2 and γ-Al_2O_3 reported a -1 order to water. While the Pd/SnO_2 catalyst depicted a partial order to water, the inclusion of Pt could have resulted in different mechanisms of SnO_2 and Pt actions thereby causing the bimetallic catalyst to exhibit an order or -1 to water. Studies by Nasr et al. [116] demonstrated that when Pd was added to the Co_3O_4 catalyst, strong-metal support interactions resulted in a higher water tolerance in comparison to the conventional Pd/γ-Al_2O_3 catalyst. Therefore, reduced water inhibition on the Pd-Pt/10Co/SnO_2 catalyst could be associated with the synergistic effects imparted by Co_3O_4 as well as due to the ability of SnO_2 to serve as a sink to hydroxyls [88], [116].

It was observed that the pre-exponential factor was significantly increased on the SnO_2-supported catalyst. The increase in the number of active sites possibly due to reduced sintering on the SnO_2 support surface could be discerned as a positive effect imparted by the deposition of cobalt on the substrate surface [108]. Based on the TEM images for the hydrothermally aged catalysts (Figure 4.6), Pd and Pt were more uniformly dispersed on the catalyst, validating the hypothesis. It could also be suggested that not only Pd and Pt were active on the surface, but due to some synergistic effects in play, CoO_x also participated in the reaction. Thus, the lower activation barrier, higher water tolerance and increase in the number of active sites could contribute to improved catalytic performance on the Pd-Pt/10Co/SnO_2 catalyst. In comparison to the Pd-Pt/Co_3O_4 catalyst, the Pd-Pt/10Co/γ-Al_2O_3 catalyst had a lower number of active sites (based on the pre-exponential factors) though the dispersion was improved on the latter catalyst. It can be postulated that while the active Pd and Pt were more dispersed, the absence of active CoO_x (due to the majority of its incorporation into the spinel structure) resulted in a lower pre-exponential factor in comparison to the Pd-Pt/Co_3O_4 catalyst. These results signify that the presence of free Co_3O_4 is therefore crucial as they could possibly aid in catalyzing the reaction on some sites as well as enable Pd/PdO transformations.

4.3.5. Turnover frequency and reaction rate trends

The dispersion data (based on surface PGM) obtained from the CO chemisorption studies (as depicted in Table 4.1) were utilized to calculate and plot the apparent turnover frequency (TOF) at 500 ˚C for various CH_4 concentrations (1000-5000 ppmv) (Table 4.4 and Figure 4.10.a and Figure 4.10.b). It is to be noted that while CoO_x is an active component for the cobalt impregnated catalysts in the wet methane combustion reaction, the apparent TOF was calculated based only on the PGM dispersion on the surface for consistent comparison against all the catalyst formulations. The TOF for the SnO_2 and γ-Al_2O_3 supported Pd and Pd-Pt catalysts are based on the results from our previous work [136]. Based on the apparent TOF trends observed in Figure 4.10.a and Figure 4.10.b, it is evident that the Pd-Pt/10Co/SnO_2 catalyst outperforms all the catalysts under consideration. The Pd-Pt/10Co/SnO_2 catalyst provided a turnover rate that was 12 times that reported on the conventional Pd/γ-Al_2O_3 catalyst at 10 vol% wet feed conditions.

The higher TOF on the bimetallic catalysts under the wet conditions could be attributed to the presence of PdO/Pd-Pt aggregates which have been demonstrated to be favourable for enhancing catalytic performances [47], [48], [54]. Despite the deactivation observed at 550 ˚C (Figure 4.1.a), the TOF on the Pd-Pt/Co_3O_4 catalyst surpassed that of the Pd-Pt/γ-Al_2O_3 catalyst. The higher TOF on the Pd-Pt/Co_3O_4 catalyst could be attributed to the higher water tolerance, synergistic effects existing between Pd and Co_3O_4 as well as the presence of certain active Pd-PdO-Pt aggregates. It could be observed that the Pd-Pt/Co_3O_4 catalyst also outperformed the Pd-Pt/10Co_3O_4/γ-Al_2O_3 catalyst. Though PdO/Pd-Pt structures were present (Figure B.8), Co_3O_4 existing in a spinel structure in the Pd-Pt/10Co_3O_4/γ-Al_2O_3 catalyst could possibly not contribute to catalyzing methane, despite the improved water tolerance in comparison to the Pd-Pt/γ-Al_2O_3 catalyst.

Table 4. 4. Calculated apparent CH_4 turnover frequency data for the catalysts considered in this study at 773 K and 5000 ppmv CH_4 concentration. The apparent TOF is based only on the PGM dispersion.

Catalyst	**Rate Model**	**Rate constant**	**Apparent CH_4 turnover frequency ($mol_{methane}/mol_{surface\ PGM}.s$)**	
			5 vol%	**10 vol%**
Aged Pd-Pt/γ-Al_2O_3	$(-r) = \frac{k_1 C_M}{C_{aq}}$	$k = 2.18 \times 10^{-3}$ ($mol/g_{PGM}.s$)	0.29	0.14
Aged Pd-Pt/SnO_2	$(-r) = \frac{k_1 C_M}{C_{aq}}$	$k = 2.26 \times 10^{-3}$ ($mol/g_{PGM}.s$)	0.63	0.32
Aged Pd-Pt/Co_3O_4	$(-r) = k_1 C_M + \frac{k_2 C_M}{C_{aq}}$	$k_1 = 6.69 \times 10^{-4}$ ($m^3/g_{PGM}.s$) $k_2 = 5.92 \times 10^{-4}$ ($mol/g_{PGM}.s$)	0.24	0.18
Aged Pd-Pt/10Co/γ-Al_2O_3	$(-r) = k_1 C_M + \frac{k_2 C_M}{C_{aq}}$	$k_1 = 1.54 \times 10^{-3}$ ($m^3/g_{PGM}.s$) $k_2 = 2.26 \times 10^{-3}$ ($mol/g_{PGM}.s$)	0.18	0.12
Aged Pd-Pt/10Co/SnO_2	$(-r) = k_1 C_M + \frac{k_2 C_M}{C_{aq}}$	$k_1 = 8.05 \times 10^{-3}$ ($m^3/g_{PGM}.s$) $k_2 = 7.05 \times 10^{-3}$ ($mol/g_{PGM}.s$)	1.0	0.76

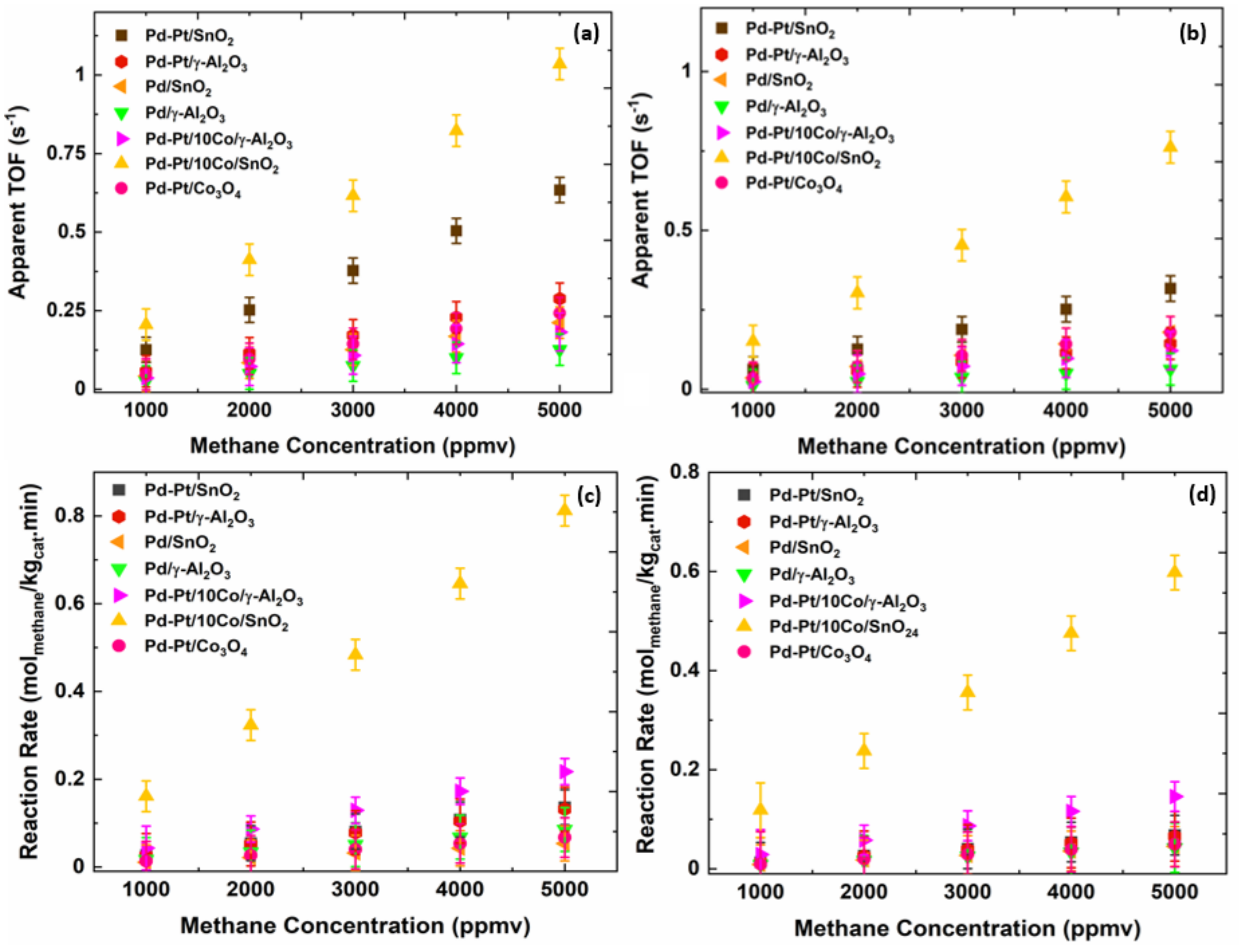

Figure 4. 10. Comparison of the calculated apparent TOFs (Turnover Frequency in units $mol_{methane}/mol_{surfacePGM}.s$) under (a) 5 vol% wet feed conditions and (b) 10 vol% wet feed conditions; and reaction rate (in units of $mol_{methane}/kg_{cat}.min$) under (c) 5 vol% wet feed conditions and (d) 10 vol% wet feed conditions at 773 K and various CH_4 concentrations over various catalysts under consideration

While an additive rate model was proposed to obtain the kinetic parameters for the Pd-Pt/10Co/SnO_2 catalyst, the question arises whether there is a potential synergism between the components contributing to the enhanced performance. To assess this hypothesis, reaction rates were calculated at 673 K (where the effect of water is still significant), 10 vol% water in the feed and 4000 ppmv CH_4 concentrations. The reaction rates for 10Co/SnO_2 and Pd-Pt/SnO_2 catalysts were found as 6.96×10^{-3} and 4.41×10^{-3} $mol_{methane}\ kg_{cat}^{-1}\ min^{-1}$. At the same conditions, the Pd-Pt/10Co/SnO_2 catalyst provided the reaction rate of 5.30×10^{-2} $mol_{methane}\ kg_{cat}^{-1}\ min^{-1}$, which is 8-12 times higher than either of the individual rates and 5-fold higher than the sum of the two rates. If one subtracts the contribution of the $10Co/SnO_2$ catalyst rate (6.96×10^{-3}) from the 5.30×10^{-2} $mol_{methane}$ kg_{cat}^{-1} min^{-1} value for the Pd-Pt/$10Co/SnO_2$ catalyst, the difference of 4.60×10^{-2} $mol_{methane}$ kg_{cat}^{-1} min^{-1} corresponds to potential Pd-Pt only contribution, which is one order of magnitude higher than the value for the Pd-Pt/SnO_2 catalyst. PGM dispersion for Pd-Pt/$10Co/SnO_2$ and Pd-Pt/SnO_2 catalysts are 19% and 5%, which differ only 4-fold and cannot explain the improved performance of the former catalyst if the reaction is structure-insensitive. Considering a potential structure-sensitivity of the reaction, the catalysts feature 6 nm and 18 nm particles, respectively (Table 4.1). Above 5 nm, Pd particle size effect is negligible as reported by Willis et al. [224] for Pd-based catalysts supported on Al_2O_3 and SiO_2. Even if there is a potential contribution from the particle size, TOFs increase with the particle size in methane combustion, so the discrepancy in additive contributions of different components in Pd-Pt/$10Co/SnO_2$ with 18 nm particles become even larger. Although we cannot exclude the contribution of different segregation and Pd/PdO/Pt collocation in the two catalysts, this analysis suggests that the enhanced performance on the Pd-Pt/$10Co/SnO_2$ catalyst is as a result of synergistic interactions (rather than additive effects) existing between the Co and Pd-Pt counterparts.

Given the above kinetic evidence, it can be stated that SnO_2 helped lower the activation barrier, while inclusion of Co to the catalyst formulation had altered the reaction order to water, thereby enhancing the water tolerance in comparison to the Pd-Pt/SnO_2 catalyst. Existence of synergistic interactions between the various active components significantly contributed to the improved activity observed on the Pd-Pt/$10Co/SnO_2$ catalyst. It can be stated the addition of Co to the catalyst formulation could have induced the following outcomes: (1) CoO_x could serve as an active component in the methane combustion reaction by extracting O* from PdO [88]; (2) presence of hydrated and non-hydrated Co active sites (Figure 4.6) could contribute to the enhanced catalytic activity and presence of different active sites on the catalyst [212]; (3) inclusion of Co could have reduced the sintering of the active Pd-Pt components [199], thereby resulting in these active components present uniformly on the catalyst surface for the methane combustion reaction.

In the case of both the SnO_2 and γ-Al_2O_3-supported catalysts, the site affected by water could have a Pd-Pt structure. As illustrated by Nassiri et al. [23] presence of water increases the fraction of Pd, while Pt provides oxygen-free sites for methane activation. Alloyed Pd-Pt structures could be observed on both the Pd-Pt/10Co/γ-Al_2O_3 catalyst (Figure B.8) and Pd-Pt/10Co/SnO_2 catalyst (Figure 4.6). Thus, the presence of Pd-Pt structures could be a realistic possibility for the sites affected by water. It could also be postulated that CH_4 activation on the water-affected site could be CoO_x catalyzed. Barrett et al. [88] demonstrated that under lean burn wet feed conditions Co_3O_4 helped neither oxidize Pd, nor dehydroxylate $Pd(OH)_2$. Instead of providing O* to Pd, CoO_x extracted O from PdO which helped catalyze the methane combustion reaction [88]. Kinetic evidence of strong metal-support interactions existing between Pd and Co_3O_4 has been demonstrated in the work by Nasr et al. [116], thus validating the possibility of such structures to exist. Based on previous studies Co_3O_4 is known to have multiple sites with different affinities to water that could participate in the methane combustion reaction [212]. The presence of different Co_3O_4 sites could be observed from the TEM images (Figure 4.6 and Figure B.8) as well, thereby suggesting the possibility of such structures existing on the site affected by water. The site unaffected by water could be a possible PdO-Pd structure. The presence of PdO phases segregating out was observable from the TEM images of the Pd-Pt/10Co/S (S = γ-Al_2O_3, SnO_2) catalysts (Figure B.8 and Figure 4.6, respectively). As illustrated by Karinshak et al. [48], the presence of metastable PdO-Pd structure in the Pd-Pt/γ-Al_2O_3 catalyst resulted in an increased methane combustion activity. Similarly, Goodman et al. [85] demonstrated that the formation of PdO/Pd aggregates contributed to an improved catalytic performance for the Pd-Pt/γ-Al_2O_3 catalyst. However, Co_3O_4 is known to exhibit a zero order to water [116] possibly suggesting that site unaffected by water could also have a Co_3O_4 structure.

Thus, it could be hypothesized that symbiotic structures rather than a particular Pd-Pt or Co_3O_4 structure exists between the two active sites. Owing to the synergistic effects existing between PdO/Pd and CoO_x and the presence of Pt that could catalyze CH_4 under wet feed conditions, various active structures are available to participate in the reaction.

4.3.6. Practical implications

Calculation of reaction rate per kilogram of catalyst (Figures 4.10.c and 4.10.d) is critical as the practicality of a new catalyst formulation is to provide small catalytic converter volumes. Habibi et al. [131] demonstrated that the Pd-Pt catalyst encapsulated in a porous silica shell with a 11.2

wt.% PGM loading (4.2 wt.% Pd and 7 wt.% Pt) resulted in an approximate PGM loading of 284 g/ft^3 of catalytic converter monolith. Such a PGM loading could result in a significantly feasible size of a catalytic converter. Though the PdPt@SiO$_2$ catalyst had a high PGM loading, the catalyst was resistant to nanoparticle sintering. However, increasing the metal loading could usually increase the severity of sintering in the case of most impregnated catalysts. Typical PGM loadings for commercial catalytic converter monoliths are in the order of 90 – 200 g/ft^3 [5], [131]. A catalyst loading of 1 wt% PGM on alumina usually corresponds to an approximate PGM loading of 90 g/ft^3 of monolith, which is in the typically expected range. Thus, the focus in this work is on relatively high loadings (1 wt.% PGM) that can give reasonable converter sizes without the overbearing concern of particle sintering. Based on the calculated reaction rates ($mol_{methane}/kg_{cat}.s$) at 10 vol.% wet feed conditions and 500 ˚C (Figure 4.11), the reaction rates were found to be in the order of Pd/γ-Al$_2$O$_3$("x") < Pd-Pt/γ-Al$_2$O$_3$(1.5x) < Pd-Pt/10Co/SnO$_2$(14x). Thus, only a lower amount of Pd-Pt/10Co/SnO$_2$ catalyst would be required to convert 1 mole of CH$_4$ as compared to the γ-Al$_2$O$_3$-supported catalysts, thereby resulting in a smaller catalytic converter volume. It is crucial to note that the use of Co and SnO$_2$ in the catalyst formulation adds to its cost if the amount of PGM remains the same as in the benchmark Al$_2$O$_3$-supported catalysts. In this work, no attempt was made to optimize (reduce) the amount of PGM on the Co/Sn-containing catalysts with the aim to maintain high activity per the converter volume and the reduced cost. The absence of PGM in the catalyst formulation (such as Co-only catalysts) would result in larger catalytic converter sizes [225]. Therefore, there is a need to strike a compromise between the cost of the catalyst and its activity.

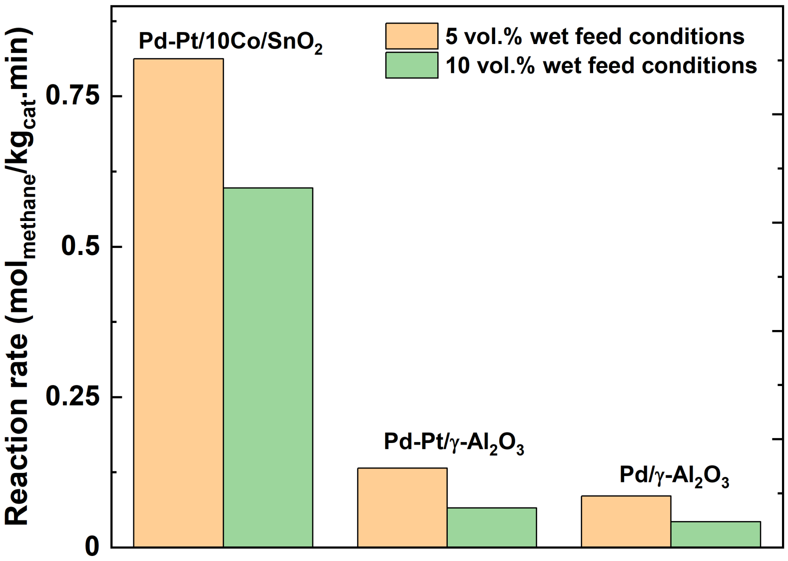

Figure 4. 11. Comparison of the calculated reaction rate ($mol_{methane}/kg_{cat}.min$) at 773 K and 5000 ppmv CH_4 concentration under 5 vol.% and 10 vol.% wet feed conditions

4.4. Conclusions

The effort to optimize Pd-based catalysts for the complete combustion of methane in the exhaust of NGVs is advancing. An ideal catalytic system would be one that is impervious to the effects of water as well as could have symbiotic structures that could continuously engage in the combustion reaction. Thus, in an attempt to develop a highly stable and active catalyst, cobalt was incorporated as a promoter to our best-identified Pd-Pt/SnO_2 catalyst [136]. To reap the benefits offered by both Co_3O_4 and SnO_2, an optimization of the amount of cobalt deposited on the support surface was performed. It was determined that 10 wt.% deposition of Co on the SnO_2 support was ideal to procure the advantages offered by its incorporation. Hence, in this work, kinetic investigations of methane combustion in the presence of water (5 vol% and 10 vol%) were performed on 1 wt% Pd-Pt (1:1 molar ratio) catalysts supported on 10 wt.% Co impregnated SnO_2 and γ-Al_2O_3 support materials. The modeling results illustrated a partial order of -0.37 and -0.55 to water for the Pd-Pt/10Co/SnO_2 and Pd-Pt/10Co/γ-Al_2O_3 catalysts, respectively. Thereby, modeling studies were carried out utilizing a reaction rate with additive contributions due to the presence of two different active sites as indicated by the partial order to water. The rate model is as depicted below:

$$(-r_M) = k_1 C_M + \frac{k_2 C_M}{C_{aq}}$$

Keeping the observed activation energy Ea_2 fixed at 131 kJ mol^{-1} (resembling the apparent activation energy as that of the Pd-Pt/γ-Al_2O_3 catalyst with negative first order to water) for the site affected by water, the value of Ea_1 was significantly small (89 ± 9 kJ mol^{-1}) on the SnO_2-supported catalyst in comparison to the γ-Al_2O_3-supported catalyst (150 ± 8 kJ mol^{-1}). Based on kinetic comparisons with the Pd-Pt/Co_3O_4 catalyst, it could be verified that SnO_2 dictated the kinetics of the Pd-Pt/10Co/SnO_2 catalyst. However, the higher water tolerance on the Pd-Pt/10Co/SnO_2 catalyst could be attributed to synergistic effects imparted by the interactions between Pd/PdO/Pt and CoO_x as well as due to the inability of SnO_2 to activate water on the surface. Though the Pd-Pt/10Co/γ-Al_2O_3 catalyst reported a higher water tolerance in comparison to the Pd-Pt/γ-Al_2O_3 catalyst, it could not perform to the level of the Pd-Pt/10Co/SnO_2 catalyst. Due to Co_3O_4 existing in a spinel structure on the former catalyst, it could not possibly participate in the combustion reaction as opposed to when it was deposited on the SnO_2 support.

From the viewpoint of turnover frequency, calculated using PGM dispersion, the Pd-Pt/10Co/SnO_2 catalyst surpassed all the catalysts considered in this work. The Pd-Pt/10Co/SnO_2 catalyst provided a methane turnover rate almost 2 times higher than that demonstrated in the case of our Pd-Pt/SnO_2 catalyst. Even in terms of the turnover rate per kilogram of catalyst, the Pd-Pt/10Co/SnO_2 catalyst outplayed the Pd-Pt/SnO_2 catalyst by 9 times. While the bimetallic catalysts performed similarly in terms of methane turnover rate per gram of catalyst, differences arising from contrasting dispersions on each of the catalysts resulted in different turnover frequencies. Synergistic interactions resulting from the inclusion of Co on the Pd-Pt/SnO_2 catalyst could have resulted in the presence of different active sites on the surface subsequently resulting in enhanced stability and improved catalytic activity on the Pd-Pt/10Co/SnO_2 catalyst. Reaction rates normalized per catalyst mass provided kinetic evidence that the enhanced catalytic performance observed on the Pd-Pt/10Co/SnO_2 catalyst was indeed as a result of synergistic interactions (rather than additive contributions) existing between the various active components in the catalyst formulation. Calculation of the reaction rate per kilogram of catalyst is also crucial as it could help translate the required catalytic converter volume. Utilization of the Pd-Pt/10Co/SnO_2 catalyst could in a significant reduction of the catalytic converter volume as the reaction rate per kilogram of the cobalt promoted catalyst exceeded that of γ-Al_2O_3-supported Pd and Pd-Pt catalysts by 14 and 9 times, respectively.

Chapter 5: Conclusions and recommendations for future work

5.1. Conclusions

The presence of water in the exhaust of NGVs is known to severely affect the performance of Pd-based catalysts in methane combustion. Support hydrophobicity, its ability to serve as a sink for the hydroxyls and oxygen mobility are some of the crucial factors that have contributed to improved catalyst stability and activity. This thesis reports the development and assessment of a water tolerant catalyst for lean-burn wet methane combustion. SnO_2 due to its ability to serve as sink for the hydroxyls released from $Pd(OH)_2$ was chosen as a support material for the PGM catalyzed wet methane combustion. The first step was to investigate the hydrothermal stability of the Pd/SnO_2 and Pd-Pt/SnO_2 catalysts. In comparison to the conventional PGM/γ-Al_2O_3 catalysts, the SnO_2-supported catalysts exhibited an improvement in the hydrothermal stability. Following this, kinetics of wet methane combustion over the Pd/SnO_2 catalyst and Pd-Pt/SnO_2 catalyst was investigated. Both catalysts depicted a first order reaction to methane. However, the Pd/SnO_2 reported a negative 0.11 order to water while the Pd-Pt/SnO_2 catalyst reported a -1 order to water. It was concluded that for the Pd/SnO_2 catalyst, the partial order to water and improved water tolerance could be due to the presence of two different active sites in play. Interestingly, for the bimetallic Pd-Pt catalysts, the choice of support material seemed to be insignificant as the γ-Al_2O_3 and SnO_2-supported Pd-Pt catalysts reported similar activation energies. Though the observed kinetic parameters for the bimetallic catalysts were in the same range, the amount of Pd-Pt exposed on the surface was quite distinct, resulting in a higher turnover frequency (TOF) on the Pd-Pt/SnO_2 catalyst.

While the Pd-Pt/SnO_2 catalyst demonstrated a higher TOF in comparison to the γ-Al_2O_3-supported bimetallic catalyst, the former catalyst still did exhibit some slow deactivation. An ideal catalytic system would be one that is impervious to the effects of water as well as could have symbiotic structures that could continuously engage in the combustion reaction. It is known that when Co_3O_4 is utilized as a support material, synergistic interaction between Pd and Co_3O_4 could result in CoO_x participating in the wet methane combustion reaction. Thus, cobalt was incorporated as a promoter to our best-identified Pd-Pt/SnO_2 catalyst in an attempt to develop a highly stable and active wet methane combustion catalyst. From a systematic study it was revealed that 10 wt.% Co deposition on the SnO_2 support was ideal to procure the advantages offered by both CoO_x and SnO_2. Hydrothermal ageing treatment demonstrated that Pd-Pt/10Co/SnO_2 catalyst exhibited superior water tolerance and provided stable conversions possibly due to some synergistic interactions in play. Investigation into the kinetics of wet methane combustion revealed a lower methane activation barrier (89 ± 9 kJ mol^{-1}), higher water tolerance ($n = -0.37$) and increase in the number of active sites on the Co-promoted catalyst, thereby contributing to the improved hydrothermal stability and catalytic performance. From the viewpoint of activation energy, it was revealed that SnO_2 dictated the kinetics, while cobalt addition altered the reaction order to water, thereby enhancing the water tolerance compared to the Pd-Pt/SnO_2 catalyst. To test the practicality of the proposed Pd-Pt/10Co/SnO_2 catalyst, for its application in a commercial catalytic converter, reaction rates were calculated per unit catalyst mass. Based on the normalized reaction rate, it was determined that only a small amount of the Pd-Pt/10Co/SnO_2 catalyst would be required to achieve complete methane combustion at the required conditions. Thus, utilization of the Pd-Pt/10Co/SnO_2 catalyst could result in a small-footprint catalytic converter for methane mitigation from lean combustion engine exhausts.

5.2. Recommendations for future work

5.2.1. Further study on various catalyst formulations

A variety of catalyst formulations could be tested for stable methane combustion activity and improved water resistance. Catalyst formulations with different Pd to Pt molar ratios and different PGM loading could be investigated on the Co-promoted catalysts. The amount of Pd and Pt (both in terms of molar amounts and loading) could alter the synergistic interactions between CoO_x and the precious metals, resulting in different catalytic behaviours. It is also suggested to carry out kinetic modeling for catalysts with varying PGM loadings and Pd:Pt molar ratio as it could help distinguish the various active sites and the fraction of the active metal present at each site. Investigation of the Pd-Co/SnO_2 catalyst in terms of catalytic activity and hydrothermal stability could be explored as the exclusion of Pt could help reduce the total catalyst cost. Alternatively, the Co-promoted PGM catalysts could be tested on other water tolerant zeolite support materials such as Beta, USY, and Na-modified Mordenite.

5.2.2. *In-situ* catalyst characterization

In-situ characterization techniques are powerful tools that could provide fundamental information about the catalyst during the reaction. Only *ex-situ* characterization techniques have been utilized in this work to gain information on the state of the precious metals on the surface of the catalyst post-reaction. It is recommended to implement *in-situ* characterization techniques such as *in-situ* transmission electron microscopy (TEM), *in-situ* X-ray diffraction (XRD) and *in-situ* X-ray photon spectroscopy to gain insights into the structure of the active sites as the reaction progresses. Detailed investigation of the changes in the catalyst composition during the reaction could provide constructive feedback on the catalyst activity. Utilizing this information experimentation could be modified to identify the accurate mechanism and thus optimize the kinetic modeling in MATLAB not just to determine the kinetic parameters, but also to effectively maximize model discrimination.

5.2.3. Prepare wash coat material and test the proposed catalyst formulation in a real feed

The catalyst formulations proposed in this work have only been tested in the presence of a simple gas feed in a micro-catalytic fixed bed reactor under ideal plug flow conditions. Thus, it is proposed to assess the catalyst activity and stability in an actual prototype catalytic converter. The proposed catalyst formulations need to be wash-coated on a honeycomb monolith and tested in a real feed. The real exhaust gas feed is far more complex than the gas feed utilized in this work. The real exhaust feed would not only contain methane and water but also high levels of CO, SO_2 and NOx. Thus, long-term ageing as well as catalytic test protocols are recommended to be modified to mimic the actual operation conditions that would exist in a real engine.

Bibliography

[1] "Comparing the Sustainability Parameters of Renewable, Nuclear and Fossil Fuel Electricity Generation Technologies (Conference) - ETDEWEB https://www.osti.gov/etdeweb/biblio/21396864," 2019.

[2] "Natural gas explained - U.S. Energy Information Administration." https://www.eia.gov/energyexplained/natural-gas/ (accessed Jan. 27, 2021).

[3] M. L. Poulton, "Fuel Efficient Car Technology," *Computational Mechanics Publications, Southampton, UK.*, 1997.

[4] G. and P. E. Genchi, "Octane Rating of Natural Gas-Gasoline Mixtures on CFR Engine," *SAE Int. J. Fuels Lubr.*, vol. 7, pp. 1041–1049, 2014.

[5] R. E. Hayes and S. T. Kolaczkowski, *Introduction to Catalytic Combustion*. 1998.

[6] R. Sajiv Kumar, R. E. Hayes, and N. Semagina, "Effect of support on Pd-catalyzed methane-lean combustion in the presence of water: Review," *Catal Today*, vol. 382, no. June, pp. 82–95, 2021, doi: 10.1016/j.cattod.2021.07.024.

[7] R. Abbasi, G. Huang, G. M. Istratescu, L. Wu, and R. E. Hayes, "Methane oxidation over Pt, Pt: Pd, and Pd based catalysts: Effects of pre-treatment," *Canadian Journal of Chemical Engineering*, vol. 93, no. 8, pp. 1474–1482, 2015, doi: 10.1002/cjce.22229.

[8] "Understanding Global Warming Potentials | US EPA." https://www.epa.gov/ghgemissions/understanding-global-warming-potentials (accessed Sep. 13, 2023).

[9] R. B. Jackson, E. I. Solomon, J. G. Canadell, M. Cargnello, and C. B. Field, "Methane removal and atmospheric restoration," *Nat Sustain*, vol. 2, no. 6, pp. 436–438, 2019, doi: 10.1038/s41893-019-0299-x.

[10] L. R., J. S.G., and C. P., "Partial oxidation of methane over supported ruthenium catalysts," *Appl. Catal. A.*, vol. 325, no. 1, pp. 57–67, 2007.

[11] L. Urfels, P. Gélin, M. Primet, and E. Tena, “Complete oxidation of methane at low temperature over Pt catalysts supported on high surface area SnO 2,” *Top Catal*, vol. 30–31, no. July, pp. 427–432, 2004, doi: 10.1023/B:TOCA.0000029785.34330.57.

[12] A. Taichi, I. Yusuke, S. Daisuke, D. Yasuhiro, and K. Jin, “Homogeneous charge compression ignition and combustion characteristics of natural gas mixtures: the visualization and analysis of combustion,” *JSAE Rev.*, vol. 24, no. 1, pp. 33–40, 2003.

[13] A. Habibi, “Silica-Encapsulated Catalysts for Lean Methane Combustion,” 2018.

[14] T. V. Choudhary, S. Banerjee, and V. R. Choudhary, “Catalysts for combustion of methane and lower alkanes,” *Appl Catal A Gen*, vol. 234, no. 1–2, pp. 1–23, 2002, doi: 10.1016/S0926-860X(02)00231-4.

[15] R. Burch, P. K. Loader, and F. J. Urbano, “Methane combustion over palladium catalysts: The effect of carbon dioxide and water on activity,” *Appl. Catal. A.*, vol. 1, no. 173–184, 1995.

[16] R. Burch, P. K. Loader, and F. J. Urbano, “Some aspects of hydrocarbon activation on platinum group metal combustion catalysts,” *Catal. Today*, vol. 27, no. 1–2, pp. 243–248, 1996.

[17] W. R. Schwartz and L. D. Pfefferle, “Combustion of methane over palladium-based catalysts: Support interactions,” *Journal of Physical Chemistry C*, vol. 116, no. 15, pp. 8571–8578, 2012, doi: 10.1021/jp2119668.

[18] A. Ersson, H. Kušar, R. Carroni, T. Griffin, and S. Järås, “Catalytic combustion of methane over bimetallic catalysts a comparison between a novel annular reactor and a high-pressure reacto,” *Catal. Today*, vol. 83, pp. 265–277, 2003.

[19] K. Persson *et al.*, “Supported palladium-platinum catalyst for methane combustion at high pressure,” *Catal. Today*, vol. 100, no. 3–4, pp. 479–483, 2005.

[20] K. Narui, H. Yata, K. Furuta, A. Nishida, Y. Kohtoku, and T. Matsuzaki, “Effects of addition of Pt to PdO/Al2O3 catalyst on catalytic activity for methane combustion and TEM observations of supported particles,” *Appl. Catal. A*, vol. 179, no. 1–2, pp. 165–173, 1999.

[21] L. S. Escandón, D. Niño, E. Díaz, S. Ordóñez, and F. V. Díez, “Effect of hydrothermal ageing on the performance of Ce-promoted PdO/ZrO2 for methane combustion,” *Catal. Commun.*, vol. 9, pp. 2291–2296, 2008.

[22] H. Nassiri, R. E. Hayes, and N. Semagina, “Tin Dioxide as an Alternative to Platinum Promoter in Palladium-Catalyzed Wet Lean Methane Combustion,” *Top Catal*, vol. 62, no. 1–4, pp. 386–390, 2019, doi: 10.1007/s11244-018-1084-1.

[23] H. Nassiri, K. E. Lee, Y. Hu, R. E. Hayes, R. W. J. Scott, and N. Semagina, “Water shifts PdO-catalyzed lean methane combustion to Pt-catalyzed rich combustion in Pd–Pt catalysts: In situ X-ray absorption spectroscopy,” *J Catal*, vol. 352, pp. 649–656, 2017, doi: 10.1016/j.jcat.2017.06.008.

[24] W. Barrett, J. Shen, Y. Hu, R. E. Hayes, R. W. J. Scott, and N. Semagina, “ Understanding the Role of SnO 2 Support in Water-Wolerant Methane Combustion: In situ Observation of Pd(OH) 2 and Comparison with Pd/Al 2 O 3 ,” *ChemCatChem*, pp. 1–10, 2019, doi: 10.1002/cctc.201901744.

[25] D. Jiang, K. Khivantsev, and Y. Wang, “Low-Temperature Methane Oxidation for Efficient Emission Control in Natural Gas Vehicles: Pd and beyond,” *ACS Catal*, vol. 10, no. 23, pp. 14304–14314, 2020, doi: 10.1021/acscatal.0c03338.

[26] A. K. Datye and M. Votsmeier, “Opportunities and challenges in the development of advanced materials for emission control catalysts,” *Nat Mater*, 2020.

[27] R. Gholami, M. Alyani, and K. J. Smith, *Deactivation of Pd catalysts by water during low temperature methane oxidation relevant to natural gas vehicle converters*, vol. 5, no. 2. 2015. doi: 10.3390/catal5020561.

[28] H. Stotz, L. Maier, A. Boubnov, A. T. Gremminger, J. D. Grunwaldt, and O. Deutschmann, “Surface reaction kinetics of methane oxidation over PdO,” *J Catal*, vol. 370, pp. 152–175, 2019, doi: 10.1016/j.jcat.2018.12.007.

[29] Y. H. Chin, C. Buda, M. Neurock, and E. Iglesia, “Consequences of metal-oxide interconversion for C-H bond activation during CH4 reactions on Pd catalysts,” *J Am Chem Soc*, vol. 135, no. 41, pp. 15425–15442, 2013, doi: 10.1021/ja405004m.

[30] Y. H. C. Chin, M. García-Diéguez, and E. Iglesia, "Dynamics and thermodynamics of Pd-PdO phase transitions: Effects of pd cluster size and kinetic implications for catalytic methane combustion," *Journal of Physical Chemistry C*, vol. 120, no. 3, pp. 1446–1460, 2016, doi: 10.1021/acs.jpcc.5b06677.

[31] C. A. Müller, M. Maciejewski, R. A. Koeppel, R. Tschan, and A. Baiker, "Role of lattice oxygen in the combustion of methane over PdO/ZrO2: Combined pulse TG/DTA and MS study with 18O-labeled catalyst," *Journal of Physical Chemistry*, vol. 100, no. 51, pp. 20006–20014, 1996, doi: 10.1021/jp961903a.

[32] K. I. Fujimoto, F. H. Ribeiro, M. Avalos-Borja, and E. Iglesia, "Structure and reactivity of PdOx/ZrO2 catalysts for methane oxidation at low temperatures," *J Catal*, vol. 179, no. 2, pp. 431–442, 1998, doi: 10.1006/jcat.1998.2178.

[33] G. Centi, "Supported palladium catalysts in environmental catalytic technologies for gaseous emissions," *J Mol Catal A Chem*, vol. 173, no. 1–2, pp. 287–312, 2001, doi: 10.1016/S1381-1169(01)00155-8.

[34] J. N. Carstens, S. C. Su, and A. T. Bell, "Factors affecting the catalytic activity of Pd/ZrO2 for the combustion of methane," *J Catal*, vol. 176, no. 1, pp. 136–142, 1998, doi: 10.1006/jcat.1998.2029.

[35] A. Yamaguchi and E. Iglesia, "Catalytic activation and reforming of methane on supported palladium clusters," *J Catal*, vol. 274, no. 1, pp. 52–63, 2010, doi: 10.1016/j.jcat.2010.06.001.

[36] D. Ciuparu, M. R. Lyubovsky, E. Altman, L. D. Pfefferle, and A. Datye, "Catalytic combustion of methane over palladium-based catalysts," *Catalysis Reviews - Science and Engineering*. 2002. doi: 10.1081/CR-120015482.

[37] Y. Cui *et al.*, "Onset of High Methane Combustion Rates over Supported Palladium Catalysts: From Isolated Pd Cations to PdO Nanoparticles," *JACS Au*, vol. 1, no. 4, pp. 396–408, Apr. 2021, doi: 10.1021/JACSAU.0C00109/ASSET/IMAGES/LARGE/AU0C00109_0007.JPEG.

[38] D. Ferri, M. Elsener, and O. Kröcher, “Methane oxidation over a honeycomb Pd-only three-way catalyst under static and periodic operation,” *Appl Catal B*, vol. 220, pp. 67–77, Jan. 2018, doi: 10.1016/J.APCATB.2017.07.070.

[39] H. Xiong *et al.*, “Design considerations for low-temperature hydrocarbon oxidation reactions on Pd based catalysts,” *Appl Catal B*, vol. 236, pp. 436–444, Nov. 2018, doi: 10.1016/J.APCATB.2018.05.049.

[40] M. Lyubovsky and L. Pfefferle, “Methane combustion over the α-alumina supported Pd catalyst: Activity of the mixed Pd/PdO state,” *Appl Catal A Gen*, vol. 173, no. 1, pp. 107–119, Oct. 1998, doi: 10.1016/S0926-860X(98)00149-5.

[41] K. Nomura *et al.*, “Pd-Pt bimetallic catalyst supported on SAPO-5 for catalytic combustion of diluted methane in the presence of water vapor,” *Catal Letters*, vol. 53, no. 3–4, pp. 167–169, 1998, doi: 10.1023/a:1019082611978.

[42] H. Yamamoto and H. Uchida, “Oxidation of methane over Pt and Pd supported on alumina in lean-burn natural-gas engine exhaust,” *Catal Today*, vol. 45, no. 1–4, pp. 147–151, Oct. 1998, doi: 10.1016/S0920-5861(98)00265-X.

[43] G. Lapisardi *et al.*, “Superior catalytic behaviour of Pt-doped Pd catalysts in the complete oxidation of methane at low temperature,” *Catal Today*, vol. 117, no. 4, pp. 564–568, 2006, doi: 10.1016/j.cattod.2006.06.004.

[44] C. Carrillo *et al.*, “Trapping of mobile Pt species by PdO nanoparticles under oxidizing conditions,” *Journal of Physical Chemistry Letters*, vol. 5, no. 12, pp. 2089–2093, 2014, doi: 10.1021/jz5009483.

[45] K. Persson, A. Ersson, K. Jansson, J. L. G. Fierro, and S. G. Järås, “Influence of molar ratio on Pd-Pt catalysts for methane combustion,” *J Catal*, vol. 243, no. 1, pp. 14–24, 2006, doi: 10.1016/j.jcat.2006.06.019.

[46] G. Watanabe, T., Kawashima, K., Tagawa, Y., Tashiro, K., Anoda, H., Ichioka, K., Sumiya, S., Zhang, “New DOC for Light Duty Diesel DPF System,” *SAE Technical Paper Series*, 2007.

[47] E. D. Goodman *et al.*, “Uniform Pt/Pd Bimetallic Nanocrystals Demonstrate Platinum Effect on Palladium Methane Combustion Activity and Stability,” *ACS Catal*, vol. 7, no. 7, pp. 4372–4380, 2017, doi: 10.1021/acscatal.7b00393.

[48] K. A. Karinshak, P. Lott, M. P. Harold, and O. Deutschmann, “In situ Activation of Bimetallic Pd−Pt Methane Oxidation Catalysts,” *ChemCatChem*, vol. 12, no. 14, pp. 3712–3720, 2020, doi: 10.1002/cctc.202000603.

[49] H. Nassiri, R. E. Hayes, and N. Semagina, “Stability of Pd-Pt catalysts in low-temperature wet methane combustion: Metal ratio and particle reconstruction,” *Chem Eng Sci*, vol. 186, pp. 44–51, 2018, doi: 10.1016/j.ces.2018.04.028.

[50] R. Abbasi, L. Wu, S. E. Wanke, and R. E. Hayes, “Kinetics of methane combustion over Pt and Pt-Pd catalysts,” *Chemical Engineering Research and Design*, vol. 90, no. 11, pp. 1930–1942, 2012, doi: 10.1016/j.cherd.2012.03.003.

[51] Y. Yang *et al.*, “Active site structure and methane oxidation reactivity of bimetallic Pd and Pt nanoparticles,” *Applied Catalysis A: General*, vol. 629. 2022. doi: 10.1016/j.apcata.2021.118290.

[52] H. Nassiri, K. E. Lee, Y. Hu, R. E. Hayes, R. W. J. Scott, and N. Semagina, “Platinum Inhibits Low-Temperature Dry Lean Methane Combustion through Palladium Reduction in Pd−Pt/Al2O3: An In Situ X-ray Absorption Study,” *ChemPhysChem*, vol. 18, no. 2, pp. 238–244, 2017, doi: 10.1002/cphc.201600993.

[53] N. M. Kinnunen, J. T. Hirvi, M. Suvanto, and T. A. Pakkanen, “Methane combustion activity of Pd-PdO x-Pt/Al 2O 3 catalyst: The role of platinum promoter,” *J Mol Catal A Chem*, vol. 356, pp. 20–28, Apr. 2012, doi: 10.1016/J.MOLCATA.2011.12.023.

[54] H. Nie, J. Y. Howe, P. T. Lachkov, and Y. H. C. Chin, “Chemical and Structural Dynamics of Nanostructures in Bimetallic Pt-Pd Catalysts, Their Inhomogeneity, and Their Roles in Methane Oxidation,” *ACS Catal*, vol. 9, no. 6, pp. 5445–5461, 2019, doi: 10.1021/acscatal.9b00485.

[55] C. F. Cullis, T. G. Nevell, and D. L. Trimm, “Role of the catalyst support in the oxidation of methane over palladium,” *J. Chem. Soc., Faraday Trans.*, vol. 68, pp. 1406–1412, 1972.

[56] F. H. Ribeiro, M. Chow, and R. A. Dalla Betta, "Kinetics of the complete oxidation of methane over supported palladium catalysts," *Journal of Catalysis*, vol. 146, no. 2. pp. 537–544, 1994. doi: 10.1006/jcat.1994.1092.

[57] D. Ciuparu and L. D. Pfefferle, "Support and water effects on palladium based methane combustion catalysts," *Appl. Catal. A*, vol. 209, no. 1–2, pp. 415–428, 2001.

[58] D. Ciuparu, N. Katsikis, and L. Pfefferle, "Temperature and Time Dependence of the Water Inhibition Effect on Supported Palladium Catalyst for Methane Combustion," *Appl. Catal. A*, vol. 216, pp. 209–215, 2001.

[59] D. Ciuparu and L. Pfefferle, "Contributions of lattice oxygen to the overall oxygen balance during methane combustion over PdO-based catalysts," *Catal Today*, vol. 77, no. 3, pp. 167–179, 2002, doi: 10.1016/S0920-5861(02)00243-2.

[60] D. Ciuparu, L. D. Pfefferle, and F. Bozon-Verduraz, "Oxygen Exchange between Palladium and Oxide Supports in Combustion Catalysts," *J. Phys, Chem. B*, vol. 106, no. 13, pp. 3434–3442, 2002.

[61] B. D. Darwent, "Bond Dissociation Energies in Simple Molecules," *U. S. National Bureau of Standards: Washington, D.C.*, 1970.

[62] R. J. Card, J. L. Schmitt, and J. M. Simpson, "Palladium-carbon hydrogenolysis catalysts: The effect of preparation variables on catalytic activity," *J Catal*, vol. 79, no. 1, pp. 13–20, 1983, doi: 10.1016/0021-9517(83)90285-3.

[63] C. F. Cullis and B. M. Willatt, "Oxidation of methane over supported precious metal catalysts," *J Catal*, vol. 83, no. 2, pp. 267–285, 1983, doi: 10.1016/0021-9517(83)90054-4.

[64] D. Ciuparu, E. Perkins, and L. Pfefferle, "In situ DR-FTIR investigation of surface hydroxyls on γ-Al 2O3 supported PdO catalysts during methane combustion," *Appl Catal A Gen*, vol. 263, no. 2, pp. 145–153, 2004, doi: 10.1016/j.apcata.2003.12.006.

[65] D. Gao, S. Wang, C. Zhang, Z. Yuan, and S. Wang, "Methane combustion over Pd/Al2O3 catalyst: Effects of chlorine ions and water on catalytic activity," *Cuihua Xuebao / Chinese Journal of Catalysis*, vol. 29, no. 12, pp. 1221–1225, 2008, doi: 10.1016/s1872-2067(09)60027-9.

[66] P. Velin *et al.*, “Water Inhibition in Methane Oxidation over Alumina Supported Palladium Catalysts,” *Journal of Physical Chemistry C*, vol. 123, no. 42, pp. 25724–25737, 2019, doi: 10.1021/acs.jpcc.9b07606.

[67] W. R. Schwartz, D. Ciuparu, and L. D. Pfefferle, “Combustion of methane over palladium-based catalysts: Catalytic deactivation and role of the support,” *Journal of Physical Chemistry C*, vol. 116, no. 15, pp. 8587–8593, 2012, doi: 10.1021/jp212236e.

[68] V. D. Sokolovskii, *Principles of Oxidative Catalysis on Solid Oxides*, vol. 32, no. 1–2. 1990. doi: 10.1080/01614949009349939.

[69] G. K. Boreskov and V. S. Muzykantov, “Investigation of Oxide-Type Oxidation Catalysts By Reactions of Oxygen Isotopic Exchange,” *Ann N Y Acad Sci*, vol. 213, no. 1, pp. 137–170, 1973, doi: 10.1111/j.1749-6632.1973.tb51065.x.

[70] V. D. Sokolovskii, “Some principles of choosing catalysts for selective conversions of organic compounds at C−H bonds,” *Reaction Kinetics and Catalysis Letters*, vol. 35, pp. 337–347, 1987.

[71] K. Murata *et al.*, “Exploiting Metal-Support Interactions to Tune the Redox Properties of Supported Pd Catalysts for Methane Combustion,” *ACS Catal*, vol. 10, no. 2, pp. 1381–1387, 2020, doi: 10.1021/acscatal.9b04524.

[72] J. J. Willis *et al.*, “Systematic Structure-Property Relationship Studies in Palladium-Catalyzed Methane Complete Combustion,” *ACS Catal*, vol. 7, no. 11, pp. 7810–7821, 2017, doi: 10.1021/acscatal.7b02414.

[73] C. Chen, Y. H. Yeh, M. Cargnello, C. B. Murray, P. Fornasiero, and R. J. Gorte, “Methane oxidation on Pd@ZrO2/Si-Al2O3 is enhanced by surface reduction of ZrO2,” *ACS Catal*, vol. 4, no. 11, pp. 3902–3909, 2014, doi: 10.1021/cs501146u.

[74] K. Murata, Y. Mahara, J. Ohyama, Y. Yamamoto, S. Arai, and A. Satsuma, “The Metal–Support Interaction Concerning the Particle Size Effect of Pd/Al2O3 on Methane Combustion,” *Angewandte Chemie - International Edition*, vol. 56, no. 50, pp. 15993–15997, 2017, doi: 10.1002/anie.201709124.

[75] Y. Dai, H. Wang, S. Liu, M. J. Maclachlan, M. O. Wolf, and K. J. Smith, “PdO Nanoparticles Supported on MnO2Nanowire Aerogels as Catalysts for Low-Temperature

Methane Combustion," *ACS Appl Nano Mater*, vol. 3, no. 7, pp. 6972–6978, 2020, doi: 10.1021/acsanm.0c01286.

[76] T. Li *et al.*, "Denary oxide nanoparticles as highly stable catalysts for methane combustion," *Nat Catal*, vol. 4, no. January, 2021, doi: 10.1038/s41929-020-00554-1.

[77] M. Cargnello *et al.*, "Exceptional activity for methane combustion over modular Pd@CeO2 subunits on functionalized Al2O3," *Science (1979)*, vol. 337, no. 6095, pp. 713–717, 2012, doi: 10.1126/science.1222887.

[78] M. Monai, T. Montini, C. Chen, E. Fonda, R. J. Gorte, and P. Fornasiero, "Methane Catalytic Combustion over Hierarchical Pd@CeO2/Si-Al2O3: Effect of the Presence of Water," *ChemCatChem*, vol. 7, no. 14, pp. 2038–2046, 2015, doi: 10.1002/cctc.201402717.

[79] M. Danielis, S. Colussi, C. De Leitenburg, J. Llorca, and A. Trovarelli, "Outstanding Methane Oxidation Performance of Palladium-Embedded Ceria Catalysts Prepared by a One-Step Dry Ball-Milling Method Zuschriften," pp. 10369–10373, 2018, doi: 10.1002/ange.201805929.

[80] A. Toso, S. Colussi, S. Padigapaty, C. de Leitenburg, and A. Trovarelli, "High stability and activity of solution combustion synthesized Pd-based catalysts for methane combustion in presence of water," *Appl Catal B*, vol. 230, no. December 2017, pp. 237–245, 2018, doi: 10.1016/j.apcatb.2018.02.049.

[81] J. Shen, R. E. Hayes, and N. Semagina, "On the contribution of oxygen from Co3O4 to the Pd-catalyzed methane combustion," *Catal Today*, vol. 360, no. September 2019, pp. 435–443, 2021, doi: 10.1016/j.cattod.2019.12.041.

[82] G. Zhu, K. I. Fujimoto, D. Y. Zemlyanov, A. K. Datye, and F. H. Ribeiro, "Coverage of palladium by silicon oxide during reduction in H2 and complete oxidation of methane," *J Catal*, vol. 225, no. 1, pp. 170–178, 2004, doi: 10.1016/j.jcat.2004.03.033.

[83] D. Roth, P. Gélin, A. Kaddouri, E. Garbowski, M. Primet, and E. Tena, "Oxidation behaviour and catalytic properties of Pd/Al2O 3 catalysts in the total oxidation of methane," *Catal Today*, vol. 112, no. 1–4, pp. 134–138, 2006, doi: 10.1016/j.cattod.2005.11.048.

[84] A. Hellman *et al.*, “The active phase of palladium during methane oxidation,” *Journal of Physical Chemistry Letters*, vol. 3, no. 6, pp. 678–682, 2012, doi: 10.1021/jz300069s.

[85] E. D. Goodman *et al.*, “Palladium oxidation leads to methane combustion activity: Effects of particle size and alloying with platinum,” *Journal of Chemical Physics*, vol. 151, no. 15, 2019, doi: 10.1063/1.5126219.

[86] A. Toso, S. Colussi, J. Llorca, and A. Trovarelli, “The dynamics of PdO-Pd phase transformation in the presence of water over Si-doped Pd/CeO2 methane oxidation catalysts,” *Appl Catal A Gen*, vol. 574, no. November 2018, pp. 79–86, 2019, doi: 10.1016/j.apcata.2019.01.023.

[87] M. Alyani and K. J. Smith, “Kinetic Analysis of the Inhibition of CH4 Oxidation by H2O on PdO/Al2O3 and CeO2/PdO/Al2O3 Catalysts,” *Ind Eng Chem Res*, vol. 55, no. 30, pp. 8309–8318, 2016, doi: 10.1021/acs.iecr.6b01881.

[88] W. Barrett *et al.*, “Strong metal-support interactions in Pd/Co3O4catalyst in wet methane combustion: In situ X-ray absorption study,” *Catal Sci Technol*, vol. 10, no. 13, pp. 4229–4236, 2020, doi: 10.1039/d0cy00465k.

[89] X. Li, X. Wang, K. Roy, J. A. Van Bokhoven, and L. Artiglia, “Role of Water on the Structure of Palladium for Complete Oxidation of Methane,” *ACS Catal*, vol. 10, no. 10, pp. 5783–5792, 2020, doi: 10.1021/acscatal.0c01069.

[90] J. Shen, R. E. Hayes, and N. Semagina, “On the contribution of oxygen from Co3O4 to the Pd-catalyzed methane combustion,” *Catal Today*, no. December, pp. 0–1, 2019, doi: 10.1016/j.cattod.2019.12.041.

[91] D. Cavuoto, F. Zaccheria, and N. Ravasio, “Some critical insights into the synthesis and applications of hydrophobic solid catalysts,” *Catalysts*, vol. 10, no. 11, pp. 1–26, 2020, doi: 10.3390/catal10111337.

[92] P. Losch, W. Huang, O. Vozniuk, E. D. Goodman, W. Schmidt, and M. Cargnello, “Modular Pd/Zeolite Composites Demonstrating the Key Role of Support Hydrophobic/Hydrophilic Character in Methane Catalytic Combustion,” *ACS Catal*, vol. 9, no. 6, pp. 4742–4753, 2019, doi: 10.1021/acscatal.9b00596.

[93] H. Peng *et al.*, “Confined Ultrathin Pd-Ce Nanowires with Outstanding Moisture and SO2 Tolerance in Methane Combustion,” *Angewandte Chemie - International Edition*, vol. 57, no. 29, pp. 8953–8957, 2018, doi: 10.1002/anie.201803393.

[94] A. Gannouni, B. Albela, M. S. Zina, and L. Bonneviot, “Metal dispersion, accessibility and catalytic activity in methane oxidation of mesoporous templated aluminosilica supported palladium,” *Appl Catal A Gen*, vol. 464–465, pp. 116–127, 2013, doi: 10.1016/j.apcata.2013.05.017.

[95] A. W. Petrov, D. Ferri, M. Tarik, O. Kröcher, and J. A. van Bokhoven, “Deactivation Aspects of Methane Oxidation Catalysts Based on Palladium and ZSM-5,” *Top Catal*, vol. 60, no. 1–2, pp. 123–130, 2017, doi: 10.1007/s11244-016-0724-6.

[96] I. Friberg, A. Wang, and L. Olsson, “Hydrothermal Aging of Pd/LTA Monolithic Catalyst for Complete CH4 Oxidation,” *Catalysts*, vol. 10, no. 5, p. 517, 2020, doi: https://doi.org/10.3390/catal10050517.

[97] K. Khivantsev *et al.*, “The superior hydrothermal stability of Pd/SSZ-39 in low temperature passive NOx adsorption (PNA) and methane combustion,” *Appl Catal B*, vol. 280, no. August 2020, p. 119449, 2021, doi: 10.1016/j.apcatb.2020.119449.

[98] Y. Dai, V. P. Kumar, C. Zhu, M. J. Maclachlan, K. J. Smith, and M. O. Wolf, “Mesoporous Silica-Supported Nanostructured PdO / CeO 2 Catalysts for Low-Temperature Methane Oxidation,” 2018, doi: 10.1021/acsami.7b13408.

[99] Q. Dai, S. Bai, Y. Lou, X. Wang, Y. Guo, and G. Lu, “Sandwich-like PdO/CeO2 nanosheet@HZSM-5 membrane hybrid composite for methane combustion: Self-redispersion, sintering-resistance and oxygen, water-tolerance,” *Nanoscale*, vol. 8, no. 18, pp. 9621–9628, 2016, doi: 10.1039/c6nr01800a.

[100] A. W. Petrov, D. Ferri, F. Krumeich, M. Nachtegaal, J. A. Van Bokhoven, and O. Kröcher, “Stable complete methane oxidation over palladium based zeolite catalysts,” *Nat Commun*, vol. 9, no. 1, 2018, doi: 10.1038/s41467-018-04748-x.

[101] A. W. Petrov, D. Ferri, O. Kröcher, and J. A. Van Bokhoven, “Design of Stable Palladium-Based Zeolite Catalysts for Complete Methane Oxidation by Postsynthesis

Zeolite Modification," *ACS Catal*, vol. 9, no. 3, pp. 2303–2312, 2019, doi: 10.1021/acscatal.8b04486.

[102] L. Luo *et al.*, "Promoting effect of alkali metal cations on the catalytic performance of Pd/H-ZSM-5 in the combustion of lean methane," *Appl Catal A Gen*, vol. 602, no. April, 2020, doi: 10.1016/j.apcata.2020.117678.

[103] S. Cao, J. R. Monnier, and J. R. Regalbuto, "Alkali promotion of alumina-supported ruthenium catalysts for hydrogenation of levulinic acid to γ-valerolactone," *J Catal*, vol. 347, pp. 72–78, Mar. 2017, doi: 10.1016/J.JCAT.2017.01.009.

[104] A. Vojvodic *et al.*, "Exploring the limits: A low-pressure, low-temperature Haber–Bosch process," *Chem Phys Lett*, vol. 598, pp. 108–112, Apr. 2014, doi: 10.1016/J.CPLETT.2014.03.003.

[105] K. ichi Aika, H. Hori, and A. Ozaki, "Activation of nitrogen by alkali metal promoted transition metal I. Ammonia synthesis over ruthenium promoted by alkali metal," *J Catal*, vol. 27, no. 3, pp. 424–431, Dec. 1972, doi: 10.1016/0021-9517(72)90179-0.

[106] E. J. Peterson *et al.*, "Low-temperature carbon monoxide oxidation catalysed by regenerable atomically dispersed palladium on alumina," *Nat Commun*, vol. 5, 2014, doi: 10.1038/NCOMMS5885.

[107] S. T. Hunt, T. Nimmanwudipong, and Y. Román-Leshkov, "Engineering Non-sintered, Metal-Terminated Tungsten Carbide Nanoparticles for Catalysis," *Angewandte Chemie International Edition*, vol. 53, no. 20, pp. 5131–5136, May 2014, doi: 10.1002/ANIE.201400294.

[108] J. J. Willis *et al.*, "Systematic Identification of Promoters for Methane Oxidation Catalysts Using Size- and Composition-Controlled Pd-Based Bimetallic Nanocrystals," *J Am Chem Soc*, vol. 139, no. 34, pp. 11989–11997, Aug. 2017, doi: 10.1021/JACS.7B06260.

[109] B. Béguin, E. Garbowski, and M. Primet, "Stabilization of alumina by addition of lanthanum," *Appl Catal*, vol. 75, no. 1, pp. 119–132, Aug. 1991, doi: 10.1016/S0166-9834(00)83128-0.

[110] "Design better cerium-based oxidation catalysts (Journal Article) | OSTI.GOV." https://www.osti.gov/biblio/514757 (accessed Sep. 14, 2023).

[111] J. Li, X. Liang, S. Xu, and J. Hao, "Catalytic performance of manganese cobalt oxides on methane combustion at low temperature," *Appl Catal B*, vol. 90, no. 1–2, pp. 307–312, Jul. 2009, doi: 10.1016/J.APCATB.2009.03.027.

[112] D. Qiao *et al.*, "Effect of Ca doping on the catalytic performance of CuO–CeO2 catalysts for methane combustion," *Catal Commun*, vol. 11, no. 9, pp. 858–861, Apr. 2010, doi: 10.1016/J.CATCOM.2010.03.010.

[113] L. F. Liotta *et al.*, "Combined CO/CH4 oxidation tests over Pd/Co3O4 monolithic catalyst: Effects of high reaction temperature and SO2 exposure on the deactivation process," *Appl Catal B*, vol. 75, no. 3–4, pp. 182–188, Sep. 2007, doi: 10.1016/J.APCATB.2007.04.012.

[114] J. Requies *et al.*, "Palladium-manganese catalysts supported on monolith systems for methane combustion," *Appl Catal B*, vol. 79, no. 2, pp. 122–131, Feb. 2008, doi: 10.1016/J.APCATB.2007.10.014.

[115] P. Stefanov *et al.*, "On the development of active and stable Pd–Co/γ-Al2O3 catalyst for complete oxidation of methane," *Chemical Engineering Journal*, vol. 266, pp. 329–338, Apr. 2015, doi: 10.1016/J.CEJ.2014.12.099.

[116] S. Nasr, N. Semagina, and R. E. Hayes, "Kinetic Modelling of Co 3 O 4 - and Pd / Co 3 O 4 -Catalyzed Wet Lean Methane Combustion," *Emission Control Science and Technology*, vol. 6, pp. 269–278, 2020.

[117] B. Wang *et al.*, "Catalytic combustion of lean methane at low temperature over palladium on a CoOx-SiO2 composite support," *Catal Letters*, vol. 143, no. 5, pp. 411–417, May 2013, doi: 10.1007/S10562-013-0988-4/FIGURES/6.

[118] S. Wang, Y. Liu, S. Wang, D. Gao, T. Sun, and C. Zhang, "Influence of metal oxides on the performance of Pd/Al2O3 catalysts for methane combustion under lean-fuel conditions," *Fuel Processing Technology*, vol. 111, pp. 55–61, Jul. 2013, doi: 10.1016/J.FUPROC.2013.01.013.

[119] J. Li, J. Zhang, Z. Lei, and B. Chen, "Pd-Co coating onto cordierite monoliths as structured catalysts for methane catalytic combustion," *Energy and Fuels*, vol. 26, no. 1, pp. 443–450, Jan. 2012, doi: 10.1021/EF201540H.

[120] S. Todorova, P. Stefanov, A. Naydenov, and H. Kolev, “Catalytic oxidation of methane over Pd-MeOx (Me = Mn, Co, Ni, Ce) catalysts - Influence of metal oxides,” *Rev. Roum. Chim*, vol. 59, no. 4, pp. 251–257, 2014, Accessed: Sep. 15, 2023. [Online]. Available: http://web.icf.ro/rrch/

[121] P. S. Gentile, S. W. Sofie, C. F. Key, and R. J. Smith, “Silicon volatility from alumina and aluminosilicates under solid oxide fuel cell operating conditions,” *Int J Appl Ceram Technol*, vol. 9, no. 6, pp. 1035–1048, 2012, doi: 10.1111/j.1744-7402.2011.02688.x.

[122] C. R. F. Lund and J. A. Dumesic, “Strong oxide-oxide interactions in silica-supported Fe3O4. III. Water-induced migration of silica on geometrically designed catalysts,” *J Catal*, vol. 72, no. 1, pp. 21–30, 1981, doi: 10.1016/0021-9517(81)90074-9.

[123] R. Gholami and K. J. Smith, “Activity of PdO/SiO2 catalysts for CH4 oxidation following thermal treatments,” *Appl Catal B*, vol. 168–169, pp. 156–163, 2015, doi: 10.1016/j.apcatb.2014.12.037.

[124] W. Huang, E. D. Goodman, P. Losch, and M. Cargnello, “Deconvoluting Transient Water Effects on the Activity of Pd Methane Combustion Catalysts,” *Ind Eng Chem Res*, vol. 57, no. 31, pp. 10261–10268, 2018, doi: 10.1021/acs.iecr.8b01915.

[125] H. Almohamadi and K. J. Smith, “The Impact of CeO2 Loading on the Activity and Stability of PdO/ γ-AlOOH/ γ-Al2O3 Monolith Catalysts for CH4 Oxidation,” vol. 4, 2019.

[126] W. Huang, X. Zhang, A. C. Yang, E. D. Goodman, K. C. Kao, and M. Cargnello, “Enhanced Catalytic Activity for Methane Combustion through in Situ Water Sorption,” *ACS Catal*, vol. 10, no. 15, pp. 8157–8167, 2020, doi: 10.1021/acscatal.0c02087.

[127] R. E. Hayes and J. P. Mmbaga, *Introduction to chemical reactor analysis, second edition*, 2nd ed. Taylor and Francis Group, CRC Press, 2012.

[128] C. M. Van Den Bleek, K. Van Der Wiele, and P. J. Van Den Berg, “The effect of dilution on the degree of conversion in fixed bed catalytic reactors,” *Chem Eng Sci*, vol. 24, no. 4, pp. 681–694, 1969, doi: 10.1016/0009-2509(69)80061-8.

[129] R. Abbasi, L. Wu, S. E. Wanke, and R. E. Hayes, "Kinetics of methane combustion over Pt and Pt-Pd catalysts," *Chemical Engineering Research and Design*, vol. 90, no. 11, pp. 1930–1942, 2012, doi: 10.1016/j.cherd.2012.03.003.

[130] R. Kikuchi, S. Maeda, K. Sasaki, S. Wennerström, and K. Eguchi, "Low-temperature methane oxidation over oxide-supported Pd catalysts : inhibitory effect of water vapor," vol. 232, no. x, pp. 23–28, 2002.

[131] A. H. Habibi, N. Semagina, and R. E. Hayes, "Kinetics of Low-Temperature Methane Oxidation over SiO 2 -Encapsulated Bimetallic Pd-Pt Nanoparticles," *Ind Eng Chem Res*, vol. 57, no. 24, pp. 8160–8171, 2018, doi: 10.1021/acs.iecr.8b01338.

[132] E. D. Goodman *et al.*, "Palladium oxidation leads to methane combustion activity: Effects of particle size and alloying with platinum," *Journal of Chemical Physics*, vol. 151, no. 15, 2019, doi: 10.1063/1.5126219.

[133] O. C. Bridgeman and E. W. Aldrich, "Vapor Pressure Tables for Water," *J. Heat Transfer*, vol. 86, no. 2, pp. 279–286, 1964, doi: 10.1115/1.3687121.

[134] J. G. McCarty, "Kinetics of PdO combustion catalysis," *Catal Today*, vol. 26, no. 3–4, pp. 283–293, 1995, doi: 10.1016/0920-5861(95)00150-7.

[135] G. Zhu, J. Han, D. Y. Zemlyanov, and F. H. Ribeiro, "The turnover rate for the catalytic combustion of methane over palladium is not sensitive to the structure of the catalyst," *J Am Chem Soc*, vol. 126, no. 32, pp. 9896–9897, Aug. 2004, doi: 10.1021/JA049406S/SUPPL_FILE/JA049406SSI20040605_125358.PDF.

[136] R. S. Kumar, R. E. Hayes, and N. Semagina, "Pd and Pd-Pt catalysts supported on SnO2 and γ-Al2O3: Kinetic studies of wet lean methane combustion," *Chem Eng Sci*, vol. 269, p. 118488, 2023, doi: 10.1016/j.ces.2023.118488.

[137] P. J. Sinko, "Micromeritics," *Martin's Physical Pharmacy and Pharmaceutical Sciences: Physical Chemical and Biopharmaceutical Principles in the Pharmaceutical Sciences: Sixth Edition*, pp. 442–468, 2011, doi: 10.2105/ajph.34.6.660-b.

[138] J. W. Niemantsverdriet, *Spectroscopy in Catalysis: An Introduction*, 3rd ed. 2007.

[139] J. Hargen, *Industrial Catalysis: a practical approach*, 2nd ed. 2006.

[140] J. W. Niemantsverdriet, "Spectroscopy in catalysis : an introduction," p. 325, 2007, Accessed: Jun. 26, 2023. [Online]. Available: https://books.google.com/books/about/Spectroscopy_in_Catalysis.html?id=Kzeuul_zdKQC

[141] G. Karavalakis, T. D. Durbin, M. Villela, and J. W. Miller, "Air pollutant emissions of light-duty vehicles operating on various natural gas compositions," *J Nat Gas Sci Eng*, vol. 4, pp. 8–16, 2012, doi: 10.1016/j.jngse.2011.08.005.

[142] U.S. EIA, "Annual Energy Outlook 2022," vol. 2022, no. March, 2022.

[143] E. Liu, B., Hayes, R.E., Checkel, M.D., Zheng, M., Mirosh, "Reversing flow catalytic converter for a natural gas-diesel dual fuel engine," *Chem Eng Sci*, vol. 56, pp. 2641–2658, 2001.

[144] "Understanding Global Warming Potentials | Greenhouse Gas (GHG) Emissions | US EPA." https://www.epa.gov/ghgemissions/understanding-global-warming-potentials (accessed May 19, 2021).

[145] P. Gélin and M. Primet, "Complete oxidation of methane at low temperature over noble metal based catalysts: A review," *Appl Catal B*, vol. 39, no. 1, pp. 1–37, 2002, doi: 10.1016/S0926-3373(02)00076-0.

[146] T. W. Hesterberg, C. A. Lapin, and W. B. Bunn, "A comparison of emissions from vehicles fueled with diesel or compressed natural gas," *Environ Sci Technol*, vol. 42, no. 17, pp. 6437–6445, 2008, doi: 10.1021/es071718i.

[147] D. T. T. US, "Advanced Combustion and Emission Control Technical Team Roadmap," no. June, 2013.

[148] R. Burch, "Low NOx options in catalytic combustion and emission control," *Catal. Today*, vol. 35, no. 1–2, pp. 27–36, 1997.

[149] C. F. Cullis, T. G. Nevell, and D. L. Trimm, "Role of the catalyst support in the oxidation of methane over palladium," *Journal of the Chemical Society, Faraday Transactions 1: Physical Chemistry in Condensed Phases*, vol. 68, pp. 1406–1412, 1972, doi: 10.1039/F19726801406.

[150] R. Burch, D. J. Crittle, and M. J. Hayes, “C-H bond activation in hydrocarbon oxidation on heterogeneous catalysts,” *Catal Today*, vol. 47, no. 1–4, pp. 229–234, 1999, doi: 10.1016/S0920-5861(98)00303-4.

[151] P. Gélin, L. Urfels, M. Primet, and E. Tena, “Complete oxidation of methane at low temperature over Pt and Pd catalysts for the abatement of lean-burn natural gas fuelled vehicles emissions: Influence of water and sulphur containing compounds,” *Catal Today*, vol. 83, no. 1–4, pp. 45–57, 2003, doi: 10.1016/S0920-5861(03)00215-3.

[152] J. K. Lampert, M. S. Kazi, and R. J. Farrauto, “Palladium catalyst performance for methane emissions abatement from lean burn natural gas vehicles,” *Appl Catal B*, vol. 14, no. 3–4, pp. 211–223, 1997, doi: 10.1016/S0926-3373(97)00024-6.

[153] Z. Zhao *et al.*, “Catalytic combustion of methane over Pd/SnO2 catalysts,” *Cuihua Xuebao/Chinese Journal of Catalysis*, vol. 38, no. 8, pp. 1322–1329, 2017, doi: 10.1016/S1872-2067(17)62864-X.

[154] A. W. Petrov, D. Ferri, F. Krumeich, M. Nachtegaal, J. A. Van Bokhoven, and O. Kröcher, “Stable complete methane oxidation over palladium based zeolite catalysts,” *Nat Commun*, vol. 9, no. 1, 2018, doi: 10.1038/s41467-018-04748-x.

[155] K. Sekizawa, H. Widjaja, S. Maeda, Y. Ozawa, and K. Eguchi, “Low temperature oxidation of methane over Pd/SnO2 catalyst,” *Appl Catal A Gen*, vol. 200, no. 1, pp. 211–217, 2000, doi: 10.1016/S0926-860X(00)00634-7.

[156] R. Kikuchi, S. Maeda, K. Sasaki, S. Wennerström, and K. Eguchi, “Low-temperature methane oxidation over oxide-supported Pd catalysts: Inhibitory effect of water vapor,” *Appl Catal A Gen*, vol. 232, no. 1–2, pp. 23–28, 2002, doi: 10.1016/S0926-860X(02)00096-0.

[157] F. M. Dautzenberg, “Ten Guidelines for Catalyst Testing,” pp. 99–119, 1989, doi: 10.1021/bk-1989-0411.ch011.

[158] T. R. Baldwin and R. Burch, “Catalytic combustion of methane over supported palladium catalysts: I. Alumina supported catalysts,” *Appl Catal*, vol. 66, no. 1, pp. 337–358, 1990, doi: 10.1016/S0166-9834(00)81648-6.

[159] K. Otto, “Methane Oxidation over Pt on 7-Alumina : Kinetics and Structure Sensitivity,” vol. 21, no. 6, pp. 1364–1369, 1989.

[160] N. Yamazoe, J. Fuchigami, M. Kishikawa, and T. Seiyama, “Interactions of tin oxide surface with O2, H2O AND H2,” *Surf Sci*, vol. 86, no. C, pp. 335–344, 1979, doi: 10.1016/0039-6028(79)90411-4.

[161] H. Yamaura, S. Hirao, S. Yamaguchi, and H. Yahiro, “Investigation on Reduction Behaviors of SnO2 and SnO2-Supported CuO Sensor Materials by Temperature-Programmed Reduction Method Combined with Resistance Measurement,” *Sensors and Materials*, vol. 28, no. 11, p. 1203, 2016, doi: 10.18494/sam.2016.1410.

[162] X. Wang and Y.-C. Xie, “Preparation and characterization of SnO 2-based composite metal oxides: active and thermally stable catalysts for CH 4 oxidation,” *Catal Letters*, vol. 75, no. 2, 2001.

[163] X. Wang and Y. C. Xiang, “CH4 deep oxidation over active and thermally stable catalysts based on Sn-Cr composite oxide,” *New Journal of Chemistry*, vol. 25, no. 12, pp. 1621–1626, 2001, doi: 10.1039/b104458n.

[164] S. Chai *et al.*, “Effect of phase interaction on catalytic CO oxidation over the SnO 2 /Al 2 O 3 model catalyst,” *Appl Surf Sci*, vol. 402, pp. 12–20, 2017, doi: 10.1016/j.apsusc.2017.01.058.

[165] P. W. Park, H. H. Kung, D.-W. Kim, and M. C. Kung, “Characterization of SnO2/Al2O3 Lean NOx Catalysts,” *J Catal*, pp. 184:440-454, 1999, [Online]. Available: http://dx.doi.org/10.1016/j.apcatb.2011.06.029

[166] A. Auroux, D. Sprinceana, and A. Gervasini, “Support effects on de-NOx catalytic properties of supported tin oxides,” *J Catal*, vol. 195, no. 1, pp. 140–150, 2000, doi: 10.1006/jcat.2000.2970.

[167] W. Chamorro-Coral, A. Caillard, P. Brault, P. Andreazza, C. Coutanceau, and S. Baranton, “The role of oxygen on the growth of palladium clusters synthesized by gas aggregation source,” *Plasma Processes and Polymers*, vol. 16, no. 7, 2019, doi: 10.1002/ppap.201900006.

[168] R. F. Hicks, H. Qi, M. L. Young, and R. G. Lee, “Structure sensitivity of methane oxidation over platinum and palladium,” *J Catal*, vol. 122, no. 2, pp. 280–294, 1990, doi: 10.1016/0021-9517(90)90282-O.

[169] M. Alyani and K. J. Smith, “Kinetic Analysis of the Inhibition of CH4 Oxidation by H2O on PdO/Al2O3 and CeO2/PdO/Al2O3 Catalysts,” *Ind Eng Chem Res*, vol. 55, no. 30, pp. 8309–8318, 2016, doi: 10.1021/acs.iecr.6b01881.

[170] H. H. Kan, R. J. Colmyer, A. R. Asthagiri, and J. F. Weaver, “Adsorption of water on a Pdo(101) thin film: Evidence of an adsorbed HO-H2O complex,” *AIChE Annual Meeting, Conference Proceedings*, no. 101, pp. 1495–1506, 2008.

[171] K. Persson, K. Jansson, and S. G. Järås, “Characterisation and microstructure of Pd and bimetallic Pd-Pt catalysts during methane oxidation,” *J Catal*, vol. 245, no. 2, pp. 401–414, 2007, doi: 10.1016/j.jcat.2006.10.029.

[172] E. D. Goodman *et al.*, “Palladium oxidation leads to methane combustion activity: Effects of particle size and alloying with platinum,” *Journal of Chemical Physics*, vol. 151, no. 15, 2019, doi: 10.1063/1.5126219.

[173] C. C. Watson and R. Mezaki, “Catalytic Oxidation Of Methane,” *Ind. Eng. Chem. Process Design Develop*, vol. 5, no. 1, pp. 62–65, 1966.

[174] N. Murata, T. Suzuki, M. Kobayashi, F. Togoh, and K. Asakura, “Characterization of Pt-doped SnO2 catalyst for a high-performance micro gas sensor,” *Physical Chemistry Chemical Physics*, vol. 15, no. 41, pp. 17938–17946, 2013, doi: 10.1039/c3cp52490f.

[175] O. V. Safonova, T. Neisius, A. Ryzhikov, B. Chenevier, A. M. Gaskov, and M. Labeau, “Characterization of the H2 sensing mechanism of Pd-promoted SnO2 by XAS in operando conditions,” *Chemical Communications*, no. 41, pp. 5202–5204, 2005, doi: 10.1039/b509826b.

[176] N. Ma, K. Suematsu, M. Yuasa, T. Kida, and K. Shimanoe, “Effect of Water Vapor on Pd-Loaded SnO2 Nanoparticles Gas Sensor,” *ACS Appl Mater Interfaces*, vol. 7, no. 10, pp. 5863–5869, 2015, doi: 10.1021/am509082w.

[177] C. Descorme and D. Duprez, “Oxygen surface mobility and isotopic exchange on oxides: Role of the nature and the structure of metal particles,” *Appl Catal A Gen*, vol. 202, no. 2, pp. 231–241, 2000, doi: 10.1016/S0926-860X(00)00537-8.

[178] A. Raj, “Methane emission control,” *Johnson Matthey Technology Review*, vol. 60, no. 4, pp. 228–235, 2016, doi: 10.1595/205651316X692554.

[179] J. C. Peters, “Natural gas and spillover from the US Clean Power Plan into the Paris Agreement,” *Energy Policy*, vol. 106, pp. 41–47, 2017, doi: 10.1016/j.enpol.2017.03.039.

[180] J. Englund *et al.*, “Deactivation of a Pd/Pt Bimetallic Oxidation Catalyst Used in a Biogas-Powered Euro VI Heavy-Duty Engine Installation,” *Catalysts 2019, Vol. 9, Page 1014*, vol. 9, no. 12, p. 1014, Dec. 2019, doi: 10.3390/CATAL9121014.

[181] K. Karinshak, P. W. Chen, R. F. Liu, S. J. Golden, and M. P. Harold, “Optimizing feed modulation for coupled methane and NOx conversion over Pd-Pt/Mn0.5Fe2.5O4/Al2O3 monolith catalyst,” *Appl Catal B*, vol. 304, p. 120607, May 2022, doi: 10.1016/J.APCATB.2021.120607.

[182] N. J. Divins *et al.*, “Investigation of the evolution of Pd-Pt supported on ceria for dry and wet methane oxidation,” *Nat Commun*, vol. 13, no. 1, p. 5080, 2022, doi: 10.1038/s41467-022-32765-4.

[183] G. Corro, C. Cano, and J. L. G. Fierro, “A study of Pt-Pd/gamma-Al2O3 catalysts for methane oxidation resistant to deactivation by sulfur poisoning,” *J Mol Catal A Chem*, vol. 315, no. 1, pp. 35–42, Mar. 2009, doi: 10.1016/J.MOLCATA.2009.08.023.

[184] M. S. Wilburn and W. S. Epling, “Sulfur deactivation and regeneration of mono- and bimetallic Pd-Pt methane oxidation catalysts,” *Appl Catal B*, vol. 206, pp. 589–598, Mar. 2009, doi: 10.1016/J.APCATB.2017.01.050.

[185] P. Lott *et al.*, “Understanding sulfur poisoning of bimetallic Pd-Pt methane oxidation catalysts and their regeneration,” *Appl Catal B*, vol. 278, p. 119244, Dec. 2020, doi: 10.1016/J.APCATB.2020.119244.

[186] N. Sadokhina, G. Smedler, U. Nylén, M. Olofsson, and L. Olsson, “The influence of gas composition on Pd-based catalyst activity in methane oxidation − inhibition and

promotion by NO," *Appl Catal B*, vol. C, no. 200, pp. 351–360, Jan. 2017, doi: 10.1016/J.APCATB.2016.07.012.

[187] J. Chen *et al.*, "Insights into the role of Pt on Pd catalyst stabilized by magnesia-alumina spinel on gama-alumina for lean methane combustion: Enhancement of hydrothermal stability," *Molecular Catalysis*, vol. 496, p. 111185, Nov. 2020, doi: 10.1016/J.MCAT.2020.111185.

[188] R. Sajiv Kumar, R. E. Hayes, and N. Semagina, "Kinetic investigation of the promoting effect of cobalt on Pd-Pt/SnO2 catalyzed wet methane combustion," *Appl Catal A Gen*, vol. 666, p. 119416, Sep. 2023, doi: 10.1016/J.APCATA.2023.119416.

[189] T. R. Baldwin and R. Burch, "Remarkable activity enhancement in the catalytic combustion of methane on supported palladium catalysts," *Catal Letters*, vol. 6, no. 1, pp. 131–138, 1990, doi: 10.1007/BF00764062.

[190] K. Keller *et al.*, "Methane oxidation over PdO: Towards a better understanding of the influence of the support material," *ChemCatChem*, p. e202300366, Apr. 2023, doi: 10.1002/CCTC.202300366.

[191] Z. Li and G. B. Hoflund, "Catalytic oxidation of methane over Pd/Co3O4," *Reaction Kinetics and Catalysis Letters*, vol. 66, no. 2, pp. 367–374, 1999, doi: 10.1007/BF02475814/METRICS.

[192] F. Zasada, J. Janas, W. Piskorz, M. Gorczyńska, and Z. Sojka, "Total Oxidation of Lean Methane over Cobalt Spinel Nanocubes Controlled by the Self-Adjusted Redox State of the Catalyst: Experimental and Theoretical Account for Interplay between the Langmuir-Hinshelwood and Mars-Van Krevelen Mechanisms," *ACS Catal*, vol. 7, no. 4, pp. 2853–2867, Apr. 2017, doi: 10.1021/ACSCATAL.6B03139/ASSET/IMAGES/LARGE/CS-2016-03139V_0011.JPEG.

[193] F. Zasada, W. Piskorz, J. Janas, J. Gryboš, P. Indyka, and Z. Sojka, "Reactive Oxygen Species on the (100) Facet of Cobalt Spinel Nanocatalyst and their Relevance in 16O2/18O2 Isotopic Exchange, deN2O, and deCH4 Processes-A Theoretical and Experimental Account," *ACS Catal*, vol. 5, no. 11, pp. 6879–6892, Nov. 2015, doi: 10.1021/ACSCATAL.5B01900/ASSET/IMAGES/LARGE/CS-2015-01900C_0012.JPEG.

[194] A. Setiawan, E. M. Kennedy, B. Z. Dlugogorski, A. A. Adesina, and M. Stockenhuber, "The stability of Co3O4, Fe2O3, Au/Co3O4 and Au/Fe2O3 catalysts in the catalytic combustion of lean methane mixtures in the presence of water," *Catal Today*, vol. 258, no. Part 2, pp. 276–283, May 2015, doi: 10.1016/J.CATTOD.2014.11.031.

[195] L. Hu, Q. Peng, and Y. Li, "Selective synthesis of Co3O4 nanocrystal with different shape and crystal plane effect on catalytic property for methane combustion," *J Am Chem Soc*, vol. 130, no. 48, pp. 16136–16137, Dec. 2008, doi: 10.1021/JA806400E/SUPPL_FILE/JA806400E_SI_001.PDF.

[196] W. Hu, J. Lan, Y. Guo, X. M. Cao, and P. Hu, "Origin of Efficient Catalytic Combustion of Methane over Co3O4(110): Active Low-Coordination Lattice Oxygen and Cooperation of Multiple Active Sites," *ACS Catal*, vol. 6, no. 8, pp. 5508–5519, Aug. 2016, doi: 10.1021/ACSCATAL.6B01080.

[197] A. Choya, B. de Rivas, J. R. González-Velasco, J. I. Gutiérrez-Ortiz, and R. López-Fonseca, "Oxidation of residual methane from VNG vehicles over Co3O4-based catalysts: Comparison among bulk, Al2O3-supported and Ce-doped catalysts," *Appl Catal B*, vol. 237, pp. 844–854, Dec. 2018, doi: 10.1016/J.APCATB.2018.06.050.

[198] F. Teng *et al.*, "High combustion activity of CH4 and catalluminescence properties of CO oxidation over porous Co3O4 nanorods," *Appl Catal B*, vol. 110, pp. 133–140, 2011, Accessed: May 04, 2023. [Online]. Available: https://www.academia.edu/7745210/High_combustion_activity_of_CH_4_and_catalluminescence_properties_of_CO_oxidation_over_porous_Co_3O_4_nanorods

[199] J. J. Willis *et al.*, "Systematic Identification of Promoters for Methane Oxidation Catalysts Using Size- and Composition-Controlled Pd-Based Bimetallic Nanocrystals," *J Am Chem Soc*, vol. 139, no. 34, pp. 11989–11997, 2017, doi: 10.1021/jacs.7b06260.

[200] P. J. Jodłowski, R. J. Jędrzejczyk, D. Chlebda, M. Gierada, and J. Łojewska, "In situ spectroscopic studies of methane catalytic combustion over Co, Ce, and Pd mixed oxides deposited on a steel surface," *J Catal*, vol. 350, pp. 1–12, Jun. 2017, doi: 10.1016/J.JCAT.2017.03.022.

[201] G. Ercolino, G. Grzybek, P. Stelmachowski, S. Specchia, A. Kotarba, and V. Specchia, "Pd/Co3O4-based catalysts prepared by solution combustion synthesis for residual methane oxidation in lean conditions," *Catal Today*, vol. Part 1, no. 257, pp. 66–71, Sep. 2015, doi: 10.1016/J.CATTOD.2015.03.006.

[202] C. Zhao, Y. Zhao, S. Li, and Y. Sun, "Effect of Pd doping on CH4 reactivity over Co3O4 catalysts from density-functional theory calculations," *Cuihua Xuebao/Chinese Journal of Catalysis*, vol. 38, no. 5, pp. 813–820, May 2017, doi: 10.1016/S1872-2067(17)62817-1.

[203] L. Hu, Q. Peng, and Y. Li, "Low-temperature CH4 Catalytic Combustion over Pd Catalyst Supported on Co3O4 Nanocrystals with Well-Defined Crystal Planes," *ChemCatChem*, vol. 3, no. 5, pp. 868–874, May 2011, doi: 10.1002/CCTC.201000407.

[204] G. Ercolino, P. Stelmachowski, G. Grzybek, A. Kotarba, and S. Specchia, "Optimization of Pd catalysts supported on Co3O4 for low-temperature lean combustion of residual methane," *Appl Catal B*, vol. C, no. 206, pp. 712–725, 2017, doi: 10.1016/J.APCATB.2017.01.055.

[205] M. P. Woods, P. Gawade, B. Tan, and U. S. Ozkan, "Preferential oxidation of carbon monoxide on Co/CeO2 nanoparticles," *Appl Catal B*, vol. 97, no. 1–2, pp. 28–35, Jun. 2010, doi: 10.1016/J.APCATB.2010.03.015.

[206] D. Pietrogiacomi, M. C. Campa, L. Ardemani, and M. Occhiuzzi, "Operando FTIR study of Fe-MOR, Co-MOR, and Ni-MOR as catalysts for simultaneous abatement of NOx and N2O with CH4 in the presence of O2. An insight on reaction pathway.," *Catal Today*, vol. 336, pp. 131–138, Oct. 2019, doi: 10.1016/J.CATTOD.2018.12.053.

[207] Y. R. Luo, "Bond dissociation energies, in: W. M. Haynes (ed.)," *CRC Press Taylor & Francis Groupandbook Chemistry Physics 93rd edition, CRC Press Taylor & Francis Group*, pp. 9–65, 2012.

[208] D. Martin and D. Duprez, "Mobility of Surface Species on Oxides. 1. Isotopic Exchange of 18 O 2 with 16 O of SiO Activation by Noble Metals. Correlation with Oxide Basicity †," 1996, Accessed: May 04, 2023. [Online]. Available: https://pubs.acs.org/sharingguidelines

[209] H. A. Alalwan, D. M. Cwiertny, and V. H. Grassian, “Co3O4 nanoparticles as oxygen carriers for chemical looping combustion: A materials characterization approach to understanding oxygen carrier performance,” *Chemical Engineering Journal*, vol. 319, pp. 279–287, Jul. 2017, doi: 10.1016/J.CEJ.2017.02.134.

[210] B. Wang *et al.*, “Catalytic combustion of lean methane at low temperature over palladium on a CoOx-SiO2 composite support,” *Catal Letters*, vol. 143, no. 5, pp. 411–417, May 2013, doi: 10.1007/S10562-013-0988-4/METRICS.

[211] X. Tang, J. Hao, and J. Li, “Complete oxidation of methane on Co3O4-SnO2 catalysts,” *Frontiers of Environmental Science and Engineering in China*, vol. 3, no. 3, pp. 265–270, 2009, doi: 10.1007/s11783-009-0019-2.

[212] F. Zasada, W. Piskorz, S. Cristol, J. F. Paul, A. Kotarba, and Z. Sojka, “Periodic density functional theory and atomistic thermodynamic studies of cobalt spinel nanocrystals in wet environment: Molecular interpretation of water adsorption equilibria,” *Journal of Physical Chemistry C*, vol. 114, no. 50, pp. 22245–22253, Dec. 2010, doi: 10.1021/JP109264B/SUPPL_FILE/JP109264B_SI_001.PDF.

[213] B. Basavalingu, J. A. K. Tareen, and G. T. Bhandage, “Thermodynamic properties of Co(OH)2 from hydrothermal equilibria in cobalt oxide systems,” *J Mater Sci Lett*, vol. 5, no. 12, pp. 1227–1229, Dec. 1986, doi: 10.1007/BF01729373/METRICS.

[214] R. J. Berger, J. Pérez-Ramírez, F. Kapteijn, and J. A. Moulijn, “Catalyst performance testing: bed dilution revisited,” *Chem Eng Sci*, vol. 57, no. 22–23, pp. 4921–4932, Nov. 2002, doi: 10.1016/S0009-2509(02)00273-7.

[215] P. Gélin and M. Primet, “Complete oxidation of methane at low temperature over noble metal based catalysts: A review,” *Appl Catal B*, vol. 39, no. 1, pp. 1–37, Nov. 2002, doi: 10.1016/S0926-3373(02)00076-0.

[216] A. Choya, B. de Rivas, J. R. González-Velasco, J. I. Gutiérrez-Ortiz, and R. López-Fonseca, “Oxidation of residual methane from VNG vehicles over Co3O4-based catalysts: Comparison among bulk, Al2O3-supported and Ce-doped catalysts,” *Appl Catal B*, vol. 237, no. February, pp. 844–854, 2018, doi: 10.1016/j.apcatb.2018.06.050.

[217] A. Sirijaruphan, A. Horváth, J. G. Goodwin, and R. Oukaci, “Cobalt aluminate formation in alumina-supported cobalt catalysts: Effects of cobalt reduction state and water vapor,” *Catal Letters*, vol. 91, no. 1–2, pp. 89–94, 2003, doi: 10.1023/B:CATL.0000006322.80235.8f.

[218] Q. Wang, Y. Peng, J. Fu, G. Z. Kyzas, S. M. R. Billah, and S. An, “Synthesis, characterization, and catalytic evaluation of Co3O4/γ-Al2O3 as methane combustion catalysts: Significance of Co species and the redox cycle,” *Appl Catal B*, vol. 168–169, pp. 42–50, 2015, doi: 10.1016/j.apcatb.2014.12.016.

[219] B. Solsona, T. E. Davies, T. Garcia, I. Vázquez, A. Dejoz, and S. H. Taylor, “Total oxidation of propane using nanocrystalline cobalt oxide and supported cobalt oxide catalysts,” *Appl Catal B*, vol. 84, no. 1–2, pp. 176–184, 2008, doi: 10.1016/j.apcatb.2008.03.021.

[220] L. G. A. van de Water, G. L. Bezemer, J. A. Bergwerff, M. Versluijs-Helder, B. M. Weckhuysen, and K. P. de Jong, “Spatially resolved UV-vis microspectroscopy on the preparation of alumina-supported Co Fischer-Tropsch catalysts: Linking activity to Co distribution and speciation,” *J Catal*, vol. 242, no. 2, pp. 287–298, 2006, doi: 10.1016/j.jcat.2006.06.004.

[221] I. Zacharaki, C. G. Kontoyannis, S. Boghosian, A. Lycourghiotis, and C. Kordulis, “Cobalt oxide supported on alumina catalysts prepared by various methods for use in catalytic afterburner of PEM fuel cell,” *Catal Today*, vol. 143, no. 1–2, pp. 38–44, 2009, doi: 10.1016/j.cattod.2008.09.026.

[222] X. Han *et al.*, “Engineering Catalytic Active Sites on Cobalt Oxide Surface for Enhanced Oxygen Electrocatalysis,” *Adv Energy Mater*, vol. 8, no. 10, pp. 1–13, 2018, doi: 10.1002/aenm.201702222.

[223] E. C. Tyo *et al.*, “Oxidative dehydrogenation of cyclohexane on cobalt oxide (Co 3O 4) nanoparticles: The effect of particle size on activity and selectivity,” *ACS Catal*, vol. 2, no. 11, pp. 2409–2423, 2012, doi: 10.1021/cs300479a.

[224] J. J. Willis *et al.*, “Systematic Structure-Property Relationship Studies in Palladium-Catalyzed Methane Complete Combustion,” *ACS Catal*, 2017, doi: 10.1021/acscatal.7b02414.

[225] S. Nasr, R. E. Hayes, and N. Semagina, “Stability of kinetic parameters of Co3O4/CeO2 catalyzed methane combustion,” *Can J Chem Eng*, vol. 99, no. 12, pp. 2670–2676, Dec. 2021, doi: 10.1002/CJCE.24054.

[226] W. Lyons, G. Plisga, and M. Lorenz, *Standard handbook of petroleum and natural gas engineering*, 3rd ed. Elsevier, 2016.

[227] E. N. Fuller, P. D. Schettler, and J. C. Giddings, “A new method for prediction of binary gas-phase diffusion coefficients,” *Ind Eng Chem*, vol. 58, no. 5, pp. 18–27, 1966, doi: 10.1021/ie50677a007.

[228] S. Fogler, *Elements of Chemical Reaction Engineering*, 5th ed., vol. 44, no. 8. 2011.

[229] “Dry Air Properties.” https://www.engineeringtoolbox.com/dry-air-properties-d_973.html

[230] R. J. Madon and M. Boudart, “Experimental criterion for the absence of artifacts in the measurement of rates of heterogeneous catalytic reactions,” *Industrial and Engineering Chemistry Fundamentals*, vol. 21, no. 4, pp. 438–447, 1982, doi: 10.1021/i100008a022.

[231] K. Mürtezaoğlu, E. Oray, T. Doğu, G. Doğu, N. Saraçoğlu, and C. Cabbar, “Effective Thermal Conductivity of Monolithic and Porous Catalyst Supports by the Moment Technique,” *J Chem Eng Data*, vol. 40, no. 4, pp. 720–725, 1995, doi: 10.1021/je00020a001.

[232] R. G. Shahrestani, “Kinetic and Deactivation Studies of Methane Oxidation over Palladium Catalysts in the Presence of Water,” University of British Columbia, 2015. [Online]. Available: https://open.library.ubc.ca/soa/cIRcle/collections/ubctheses/24/items/1.0166751

[233] J. Pérez-Ramírez, R. J. Berger, G. Mul, F. Kapteijn, and J. A. Moulijn, “Six-flow reactor technology a review on fast catalyst screening and kinetic studies,” *Catal Today*, vol. 60, no. 1, pp. 93–109, 2000, doi: 10.1016/S0920-5861(00)00321-7.

Appendix A: The Supporting Information of Chapter 3

Table A. 1. Order of runs for the kinetic study for each of the four aged catalysts considered in this study

Trial 1					
5 vol%	3000 ppmv	1000 ppmv	5000 ppmv	2000 ppmv	4000 ppmv
Dry	4000 ppmv	2000 ppmv	1000 ppmv	5000 ppmv	3000 ppmv
10 vol%	2000 ppmv	5000 ppmv	3000 ppmv	1000 ppmv	4000 ppmv
Trial 2					
10 vol%	5000 ppmv	1000 ppmv	3000 ppmv	2000 ppmv	4000 ppmv
5 vol%	1000 ppmv	4000 ppmv	3000 ppmv	5000 ppmv	2000 ppmv
Dry	3000 ppmv	5000 ppmv	1000 ppmv	4000 ppmv	2000 ppmv
Trial 3					
5 vol%	4000 ppmv	1000 ppmv	2000 ppmv	5000 ppmv	3000 ppmv
10 vol%	5000 ppmv	3000 ppmv	4000 ppmv	1000 ppmv	2000 ppmv
Dry	2000 ppmv	4000 ppmv	3000 ppmv	1000 ppmv	5000 ppmv

SECTION A.1: Verification of ideal plug flow conditions and mass transfer limitations

Verification of Plug Flow conditions for Pd-Pt/SnO_2 catalyst –

The plug flow conditions were verified for the Pd-Pt/SnO_2 catalyst as delineated below:

Amount of catalyst + diluent = 0.34 + 0.25 = 0.59 g
Based on measured density of catalyst + diluent = 0.5017 g/mL
Bed volume = 0.59/0.5017 = 1.176 mL
Reactor ID = 0.9525 cm (3/8 ″)
Bed length = (1.176 * 4)/(π * 0.9525^2) = 1.65 cm

Step 1: Dynamic Viscosity of Air at Atmospheric Pressure and 673.15 K

$\mu = 3.4\times10^{-5}$ Ns/m^2 [226]

Step 2: Calculation of Superficial Velocity

$u = Q/A_c$

Reactor I.D. = 3/8" = 0.009525 m

$A_c = (\pi/4)*d_p^2 = 7.1256\times10^{-5}$ m^2

Q_0 = 210 mL/min = 3.5×10^{-6} m^3/s

$Q = Q_0 * (T/273.15) * (1/2.837) = 3.5\times10^{-6} * (673.15/273.15) * (1/2.837) =$
3.04×10^{-6} m^3/s
$u = 3.04\times10^{-6} / 7.1256\times10^{-5} = 0.04266$ m/s [157]

Step 3: Calculate Particle Reynolds Number
ρ of air at 673.15K = 0.5247 kg/m^3
$d_p = 5\times10^{-5}$ m
$^{N}Re_{P} = (0.04266 * 0.5247 * 5\times10^{-5})/(3.4\times10^{-5}) = 0.03292$ [157]

Step 4: Calculate the Peclet Number (for gas-phase operations)
L = 0.0165 m
$N_{Pe} = 0.087 * (0.03292)^{0.23} * (0.0165/5\times10^{-5}) = 13.09$ [157]

Step 5: Calculate the Minimum Peclet Number (for gas-phase operations)
n (order of reaction) = 1
X (conversion) = 0.5 (50%)
$^{N}Pe_{min} = 8 * 1 * \ln(1/(1-0.5)) = 5.5452$ [157]

Step 6: Calculate minimum L/d$_p$
$L/d_p > 92 * 13.09^{-0.23} * 1 * \ln(1/(1-0.5)) = 35.30$
In our case, L/dp = 330 [157]
Hence, the condition is satisfied for plug flow

Verification of inexistence of Mass Transfer Limitations

The kinetic regime was verified at 400 ˚C in the wet (10 vol%) feed for the Pd-Pt/SnO_2 catalyst and 4000 ppmv methane concentration. Since the catalyst is non-porous internal mass and heat transfer limitations do not exist.

Parameter	Equation	Value (calculated or experimental)
Reaction rate -r_M,	$-r_M = \frac{F_{Mo}X}{W}$	**9.19×10^{-5}** For initial methane molar flow rate

[mol/(s·kg$_{cat}$)]		$F_{Mo} = 6.25\times 10^{-7}$ mol/s, catalyst amount W = 0.34 g, conversion at differential conditions X = 0.05
Methane bulk diffusivity in air at 673.15 K D_{AB} [m^2/s]	$D_{AB} = \frac{1.013\cdot 10^{-2} T^{1.75}\left[\frac{1}{M_A}+\frac{1}{M_B}\right]^{0.5}}{P\left[\left(\sum \nu_i\right)_A^{\frac{1}{3}}+\left(\sum \nu_i\right)_B^{\frac{1}{3}}\right]^2}$ (Fuller formula [127], [227])	**8.95 × 10^{-5}** For P =101325 Pa, molecular masses and diffusion volumes for methane and air as 16 g/mol, 29 g/mol, 24.42, and 20.1 [127], [227]
Particle Reynolds number Re$_p$	$Re = \frac{U\rho_g d_p}{\mu}$ [228]	**0.033** For dynamic viscosity $\mu = 3.4\times10^{-5}$ Pa·s [226] and density $\rho_g = 0.5247$ kg/m^3 (ideal gas) of air at 673.15 K [229] , $d_p = 5\times10^{-5}$ m, free-stream velocity 0.04266 m/s (for 3/8” reactor i.d. and assuming bed porosity of 0.4)
Schmidt number	$Sc = \frac{\mu}{D_{AB}\rho_g}$ [228]	**0.72**
Sherwood number Sh	$Sh = 2 + 0.6Re^{\frac{1}{2}}Sc^{\frac{1}{3}}$ (Frössling correlation [228])	**2.10**
Mass transfer coefficient k$_c$ [m/s]	$k_c = \frac{D_{AB}Sh}{d_p}$ [228]	**3.76**
Mears criterion for external diffusion	$\frac{-r_M\rho_b Rn}{k_c C_M} < 0.15$ If the condition is satisfied, then no external MTL is present [228]	**1.43 × 10^{-5}** For ρ_b bed density 3954 kg/m^3 (catalyst density ρ_c 6590 kg/m^3, bed porosity 0.4), particle radius R = 2.5 × 10^{-5} m, order n = 1, $C_M = C_{Mo}(1\text{-}X)$ with initial methane

		concentration of 0.178 mol/m^3
Thus, the Mears criterion shows the absence of external mass transfer limitations		
Nusselt number Nu	$\mathrm{Nu} = 2 + 0.6\mathrm{Re}^{\frac{1}{2}}\mathrm{Pr}^{\frac{1}{3}}$ [228]	**2.10** For Prandtl number Pr = 0.683 for air at 673.15 K [229]
Heat transfer coefficient h [kJ/(m^2·s·K)]	$\mathrm{h} = \frac{\mathrm{k_t Nu}}{\mathrm{d_p}}$ [228]	**2.13** For thermal conductivity of air at 673.15 K as 5.08 × 10^{-5} kW/(m·K) [229]
External temperature gradient criterion	$\left\lvert \frac{-\mathrm{r_M}(-\Delta \mathrm{H_{rx}})\rho_\mathrm{b}\mathrm{RE}}{\mathrm{hT^2R_{gas}}} \right\rvert < 0.15$ If the condition is satisfied, then no external HTL are present [228]	**1.29 × 10^{-4}** For the heat of reaction -890 kJ/mol [129] and activation energy E = 127.9 kJ/mol (as reported in Table 3.3)
Thus, the external temperature gradient criterion shows the absence of external HTL		
All the criteria above confirm that the reaction at 400 ˚C occurs in the kinetic regime and that the ideal PBR mole balance is applicable		

Verification of Plug Flow conditions for Pd-Pt/γ-Al_2O_3 catalyst -

The plug flow conditions were verified for the Pd-Pt/γ-Al_2O_3 catalyst as delineated below:

Amount of catalyst + diluent = 0.34 + 0.25 = 0.59 g
Based on measured density of catalyst + diluent = 0.6115 g/mL
Bed volume = 0.59/0.6115 = 0.9648 mL
Reactor ID = 0.9525 cm (3/8 ″)
Bed length = (0.9648 * 4)/(π * 0.9525^2) = 1.35 cm

Step 1: Dynamic Viscosity of Air at Atmospheric Pressure and 673.15 K

$\mu = 3.4\times10^{-5}$ Ns/m^2 [226]

Step 2: Calculation of Superficial Velocity

$u = Q/A_c$

Reactor I.D. = 3/8" = 0.009525 m

$A_c = (\pi/4)*d_p^2 = 7.1256 \times 10^{-5}\ m^2$

$Q_0 = 210$ mL/min $= 3.5\times10^{-6}\ m^3/s$

$Q = Q_0 * (T/273.15) * (1/2.837) = 3.5\times10^{-6} * (673.15/273.15) * (1/2.837) =$

$3.04\times10^{-6}\ m^3/s$

$u = 3.04\times10^{-6} / 7.1256\times10^{-5} = 0.04266$ m/s [157]

Step 3: Calculate Particle Reynolds Number

ρ of air at 673.15K = 0.5247 kg/m^3

$d_p = 5\times10^{-5}$ m

$^{N}Re_{P} = (0.04266 * 0.5247 * 5\times10^{-5})/(3.4\times10^{-5}) = 0.03292$ [157]

Step 4: Calculate the Peclet Number (for gas-phase operations)

L = 0.0135 m

$N_{Pe} = 0.087 * (0.03292)^{0.23} * (0.0135/5\times10^{-5}) = 10.71$ [157]

Step 5: Calculate the Minimum Peclet Number (for gas-phase operations)

n (order of reaction) = 1

X (conversion) = 0.5 (50%)

$^{N}Pe_{min} = 8 * 1 * \ln(1/(1-0.5)) = 5.5452$ [157]

Step 6: Calculate minimum L/d_p

$L/d_p > 92 * 10.71^{-0.23} * 1 * \ln(1/(1-0.5)) = 36.96$

In our case, L/dp = 270 [157]

Hence, the condition is satisfied for plug flow

Verification of inexistence of Mass Transfer Limitations

The kinetic regime was verified at 400 ˚C in the wet (10 vol%) feed for the Pd-Pt/γ-Al_2O_3 catalyst and 4000 ppmv methane concentration.

Parameter	Equation	Value (calculated or experimental)
Reaction rate -r_M, [mol/(s·kg_{cat})]	$$-r_M = \frac{F_{Mo}X}{W}$$	**7.35×10^{-5}** For initial methane molar flow rate $F_{Mo} = 6.25 \times 10^{-7}$ mol/s, catalyst amount W = 0.34 g, conversion at differential conditions X = 0.04
Methane bulk diffusivity in air at 613 K D_{AB} [m^2/s]	$$D_{AB} = \frac{1.013 \cdot 10^{-2} T^{1.75} \left[\frac{1}{M_A} + \frac{1}{M_B}\right]^{0.5}}{P\left[\left(\sum \nu_i\right)_A^{\frac{1}{3}} + \left(\sum \nu_i\right)_B^{\frac{1}{3}}\right]^2}$$ (Fuller formula [127], [227])	**8.95×10^{-5}** For P =101325 Pa, molecular masses and diffusion volumes for methane and air as 16 g/mol, 29 g/mol, 24.42, and 20.1 [127], [227]
Particle Reynolds number Re_p	$$Re = \frac{U\rho_g d_p}{\mu}$$ [228]	**0.033** For dynamic viscosity $\mu = 3.4\times10^{-5}$ Pa·s [226] and density $\rho_g = 0.5247$ kg/m^3 (ideal gas) of air at 673.15 K [229] , $d_p = 5\times10^{-5}$ m, free-stream velocity 0.04266 m/s (for 3/8" reactor i.d. and assuming bed porosity of 0.4)
Schmidt number	$$Sc = \frac{\mu}{D_{AB}\rho_g}$$ [228]	**0.72**
Sherwood number Sh	$$Sh = 2 + 0.6Re^{\frac{1}{2}}Sc^{\frac{1}{3}}$$ Frössling correlation [228]	**2.10**
Mass transfer coefficient k_c [m/s]	$$k_c = \frac{D_{AB}Sh}{d_p}$$ [228]	**3.76**
Mears criterion for external	$$\frac{-r_M\rho_b Rn}{k_c C_M} < 0.15$$	**6.68×10^{-6}** For ρ_b bed density 2334 kg/m^3

diffusion	If the condition is satisfied, then no external MTL is present [228]	(catalyst density ρ_c 3890 kg/m^3, bed porosity 0.4), particle radius R = 2.5×10^{-5} m, order n = 1, $C_M = C_{Mo}(1-X)$ with initial methane concentration of 0.178 mol/m^3
Thus, the Mears criterion shows the absence of external mass transfer limitations		
Knudsen diffusivity [m^2/s]	$D_K = \frac{d_{pore}}{3}\sqrt{\frac{8RT}{\pi M}}$ [127]	**1.76×10^{-6}** For methane (molecular mass M 0.016 kg/mol) and catalyst pore diameter d_{pore} = 5.6 nm (specified by Sigma-Aldrich)
Diffusivity in a pore [m^2/s]	$D_{pore} = \left(\frac{1}{D_{AB}} + \frac{1}{D_K}\right)^{-1}$ [127]	**1.73×10^{-6}**
Particle porosity	$\phi_p = \frac{S\rho_c\, d_{Pore}}{4}$ [127]	**0.84** For catalyst surface area 155 m^2/g and catalyst density 3890 kg/m^3 (specified by Sigma-Aldrich)
Effective diffusivity [m^2/s]	$D_{eff} = \frac{\phi_P D_{pore}}{\tau}$ [127]	**3.74×10^{-7}** For tortuosity 3.9
Weisz-Prater criterion for internal MTL	$C_{WP} = \frac{-r_M \rho_c R^2}{D_{eff} C_M}$ If $C_{WP} < 0.6$ for a first-order reaction, then no internal MTL is present [230]	**2.79×10^{-3}** For C_M as the bulk concentration of 0.171 mol/m^3 since the absence of external MTL was proved
Thus, the Weisz-Prater criterion shows the absence of internal mass transfer limitations		
Nusselt number Nu	$Nu = 2 + 0.6Re^{\frac{1}{2}}Pr^{\frac{1}{3}}$ [228]	**2.10** For Prandtl number Pr = 0.683 for

		air at 673.15 K [229]
Heat transfer coefficient h [kJ/($m^2 \cdot s \cdot K$)]	$h = \frac{k_t Nu}{d_p}$ [228]	**2.13** For thermal conductivity of air at 673.15 K as 0.03365 W/(m·K) [229]
External temperature gradient criterion	$\left\lvert \frac{-r_M(-\Delta H_{rx})\rho_b RE}{hT^2 R_{gas}} \right\rvert < 0.15$ If the condition is satisfied, then no external HTL are present [228]	**6.14×10^{-5}** For the heat of reaction -890 kJ/mol and activation energy E 129.1 kJ/mol (as reported in Table 3.2)
Thus, the external temperature gradient criterion shows the absence of external HTL		
Prater number β	$\beta = \frac{-H_{rxn} D_{eff} C_M}{k_{eff} T}$ [127]	**2.42×10^{-6}** For effective thermal conductivity of Al_2O_3 as 0.035 kW/(m·K) [231]
Maximum internal temperature rise [K]	$\Delta T_{max} = \beta T$ [127]	**1.63×10^{-3}** The maximum internal T can be 673.15 K which is the same as 673.15 K surface. The catalyst particle is thus isothermal
Thus, the Prater number shows the absence of internal HTL		
All the criteria above confirm that the reaction at 400 ˚C occurs in the kinetic regime and that the ideal PBR mole balance is applicable		

Verification of Plug Flow conditions for Pd/SnO_2 catalyst –

The plug flow conditions were verified for the Pd/SnO_2 catalyst as delineated below:

Amount of catalyst + diluent = 0.12 + 0.50 = 0.62 g
Based on measured density of catalyst + diluent = 0.4494 g/mL
Bed volume = 0.62/0.4494 = 1.380 mL
Reactor ID = 0.9525 cm (3/8 ″)
Bed length = (1.380 * 4)/(π * 0.9525^2) = 1.94 cm

Step 1: Dynamic Viscosity of Air at Atmospheric Pressure and 673.15 K

$\mu = 3.4\times10^{-5}$ Ns/m^2 [226]

Step 2: Calculation of Superficial Velocity

$u = Q/A_c$

Reactor I.D. = 3/8" = 0.009525 m

$A_c = (\pi/4)*d_p^2 = 7.1256\times10^{-5}$ m^2

Q_0 = 210 mL/min = 3.5×10^{-6} m^3/s

$Q = Q_0 * (T/273.15) * (1/2.837) = 3.5\times10^{-6} * (673.15/273.15) * (1/2.837) =$

3.04×10^{-6} m^3/s

$u = 3.04\times10^{-6} / 7.1256\times10^{-5} = 0.04266$ m/s [157]

Step 3: Calculate Particle Reynolds Number

ρ of air at 673.15K = 0.5247 kg/m^3

$d_p = 5\times10^{-5}$ m

$^{N}Re_{P} = (0.04266 * 0.5247 * 5\times10^{-5})/(3.4\times10^{-5}) = 0.03292$ [157]

Step 4: Calculate the Peclet Number (for gas-phase operations)

L = 0.0194 m

$N_{Pe} = 0.087 * (0.03292)^{0.23} * (0.0194/5\times10^{-5}) = 15.39$ [157]

Step 5: Calculate the Minimum Peclet Number (for gas-phase operations)

n (order of reaction) = 1

X (conversion) = 0.5 (50%)

$^{N}Pe_{min} = 8 * 1 * \ln(1/(1-0.5)) = 5.5452$ [157]

Step 6: Calculate minimum L/d_p

$L/d_p > 92 * 13.09^{-0.23} * 1 * \ln(1/(1-0.5)) = 35.30$

In our case, L/dp = 388 [157]

Hence, the condition is satisfied for plug flow

Verification of inexistence of Mass Transfer Limitations

The kinetic regime was verified at 400 ˚C in the wet (10 vol%) feed for the Pd/SnO_2 catalyst and 4000 ppmv methane concentration. Since the catalyst is non-porous internal mass and heat transfer limitations do not exist.

Parameter	Equation	Value (calculated or experimental)
Reaction rate -r_M, [mol/(s·kg_{cat})]	$-r_M = \frac{F_{Mo}X}{W}$	**1.04 × 10^{-4}** For initial methane molar flow rate F_{Mo} = 6.25 × 10^{-7} mol/s, catalyst amount W = 0.12 g, conversion at differential conditions X = 0.02
Methane bulk diffusivity in air at 673.15 K D_{AB} [m^2/s]	$D_{AB} = \frac{1.013 \cdot 10^{-2} T^{1.75} \left[\frac{1}{M_A} + \frac{1}{M_B}\right]^{0.5}}{P\left[\left(\sum \nu_i\right)_A^{\frac{1}{3}} + \left(\sum \nu_i\right)_B^{\frac{1}{3}}\right]^2}$ (Fuller formula [127], [227])	**8.95 × 10^{-5}** For P =101325 Pa, molecular masses and diffusion volumes for methane and air as 16 g/mol, 29 g/mol, 24.42, and 20.1 [127], [227]
Particle Reynolds number Re_p	$Re = \frac{U\rho_g d_p}{\mu}$ [228]	**0.033** For dynamic viscosity μ = 3.4×10^{-5} Pa·s [226] and density ρ_g = 0.5247 kg/m^3 (ideal gas) of air at 673.15 K [229] , d_p = 5×10^{-5} m, free-stream velocity 0.04266 m/s (for 3/8" reactor i.d. and assuming bed porosity of 0.4)
Schmidt number	$Sc = \frac{\mu}{D_{AB}\rho_g}$ [228]	**0.72**
Sherwood number Sh	$Sh = 2 + 0.6Re^{\frac{1}{2}}Sc^{\frac{1}{3}}$ (Frössling correlation [228])	**2.10**

Mass transfer coefficient k_c [m/s]	$k_c = \frac{D_{AB}Sh}{d_p}$ [228]	**3.76**
Mears criterion for external diffusion	$\frac{-r_M \rho_b R n}{k_c C_M} < 0.15$ If the condition is satisfied, then no external MTL is present [228]	**1.57×10^{-5}** For ρ_b bed density 3954 kg/m^3 (catalyst density ρ_c 6590 kg/m^3, bed porosity 0.4), particle radius R = 2.5×10^{-5} m, order n = 1, $C_M = C_{Mo}(1-X)$ with initial methane concentration of 0.178 mol/m^3
Thus, the Mears criterion shows the absence of external mass transfer limitations		
Nusselt number Nu	$Nu = 2 + 0.6Re^{\frac{1}{2}}Pr^{\frac{1}{3}}$ [228]	**2.10** For Prandtl number Pr = 0.708 for air at 673.15 K [229]
Heat transfer coefficient h [kJ/(m^2·s·K)]	$h = \frac{k_t Nu}{d_p}$ [228]	**2.13** For thermal conductivity of air at 673.15 K as 5.08×10^{-5} kW/(m·K) [229]
External temperature gradient criterion	$\left\lvert \frac{-r_M(-\Delta H_{rx})\rho_b R E}{h T^2 R_{gas}} \right\rvert < 0.15$ If the condition is satisfied, then no external HTL are present [228]	**1.17×10^{-4}** For the heat of reaction -890 kJ/mol [129] and activation energy E = 102.8 kJ/mol (as reported in Table 3.3)
Thus, the external temperature gradient criterion shows the absence of external HTL		
All the criteria above confirm that the reaction at 400 °C occurs in the kinetic regime and that the ideal PBR mole balance is applicable		

Verification of Plug Flow conditions for Pd/γ-Al_2O_3 catalyst -

The plug flow conditions were verified for the Pd/γ-Al_2O_3 catalyst as delineated below:

Amount of catalyst + diluent = 0.12 + 0.5 = 0.62 g
Based on measured density of catalyst + diluent = 0.5222 g/mL
Bed volume = 0.62/0.5222 = 1.1873 mL
Reactor ID = 0.9525 cm (3/8 ″)
Bed length = $(1.1873 * 4)/(\pi * 0.9525^2) = 1.67$ cm

Step 1: Dynamic Viscosity of Air at Atmospheric Pressure and 673.15 K

$\mu = 3.4\times10^{-5}$ Ns/m^2 [226]

Step 2: Calculation of Superficial Velocity

$u = Q/A_c$

Reactor I.D. = 3/8" = 0.009525 m

$A_c = (\pi/4)*d_p^2 = 7.1256\times10^{-5}$ m^2

$Q_0 = 210$ mL/min $= 3.5\times10^{-6}$ m^3/s

$Q = Q_0 * (T/273.15) * (1/2.837) = 3.5\times10^{-6} * (673.15/273.15) * (1/2.837) =$

3.04×10^{-6} m^3/s

$u = 3.04\times10^{-6} / 7.1256\times10^{-5} = 0.04266$ m/s [157]

Step 3: Calculate Particle Reynolds Number

ρ of air at 673.15K = 0.5247 kg/m^3

$d_p = 5\times10^{-5}$ m

$^{N}Re_{P} = (0.04266 * 0.5247 * 5\times10^{-5})/(3.4\times10^{-5}) = 0.03292$ [157]

Step 4: Calculate the Peclet Number (for gas-phase operations)

L = 0.0167 m

$N_{Pe} = 0.087 * (0.03292)^{0.23} * (0.0167/5\times10^{-5}) = 13.25$ [157]

Step 5: Calculate the Minimum Peclet Number (for gas-phase operations)

n (order of reaction) = 1

X (conversion) = 0.5 (50%)

$^{N}Pe_{min} = 8 * 1 * \ln(1/(1-0.5)) = 5.5452$ [157]

Step 6: Calculate minimum L/d_p

$L/d_p > 92 * 10.71^{-0.23} * 1 * \ln(1/(1-0.5)) = 36.96$

In our case, L/dp = 334 [157]

Hence, the condition is satisfied for plug flow

Verification of inexistence of Mass Transfer Limitations

The kinetic regime was verified at 400 ˚C in the wet (10 vol%) feed for the Pd/γ-Al_2O_3 catalyst and 4000 ppmv methane concentration.

Parameter	Equation	Value (calculated or experimental)
Reaction rate -r_M, [mol/(s·kg_{cat})]	$-r_M = \frac{F_{Mo}X}{W}$	**5.21×10^{-5}** For initial methane molar flow rate $F_{Mo} = 6.25 \times 10^{-7}$ mol/s, catalyst amount W = 0.12 g, conversion at differential conditions X = 0.01
Methane bulk diffusivity in air at 613 K D_{AB} [m^2/s]	$D_{AB} = \frac{1.013 \cdot 10^{-2} T^{1.75} \left[\frac{1}{M_A} + \frac{1}{M_B}\right]^{0.5}}{P\left[\left(\sum \nu_i\right)_A^{\frac{1}{3}} + \left(\sum \nu_i\right)_B^{\frac{1}{3}}\right]^2}$ (Fuller formula [127], [227])	**8.95×10^{-5}** For P =101325 Pa, molecular masses and diffusion volumes for methane and air as 16 g/mol, 29 g/mol, 24.42, and 20.1 [127], [227]
Particle Reynolds number Re_p	$Re = \frac{U\rho_g d_p}{\mu}$ [228]	**0.033** For dynamic viscosity $\mu = 3.4\times10^{-5}$ Pa·s [226] and density ρ_g = 0.5247 kg/m^3 (ideal gas) of air at 673.15 K [229] , $d_p = 5\times10^{-5}$ m, free-stream velocity 0.04266 m/s (for 3/8" reactor i.d. and assuming bed porosity of 0.4)

Schmidt number	$$\mathrm{Sc} = \frac{\mu}{\mathrm{D_{AB}}\rho_g}$$ [228]	**0.72**
Sherwood number Sh	$$\mathrm{Sh} = 2 + 0.6\mathrm{Re}^{\frac{1}{2}}\mathrm{Sc}^{\frac{1}{3}}$$ Frössling correlation [228]	**2.10**
Mass transfer coefficient k_c [m/s]	$$\mathrm{k_c} = \frac{\mathrm{D_{AB}Sh}}{\mathrm{d_p}}$$ [228]	**3.76**
Mears criterion for external diffusion	$$\frac{-\mathrm{r_M}\rho_b\mathrm{Rn}}{\mathrm{k_c C_M}} < 0.15$$ If the condition is satisfied, then no external MTL is present [228]	**4.60×10^{-6}** For ρ_b bed density 2334 kg/m^3 (catalyst density ρ_c 3890 kg/m^3, bed porosity 0.4), particle radius R = 2.5×10^{-5} m, order n = 1, $C_M = C_{Mo}(1-X)$ with initial methane concentration of 0.178 mol/m^3
Thus, the Mears criterion shows the absence of external mass transfer limitations		
Knudsen diffusivity [m^2/s]	$$\mathrm{D_K} = \frac{\mathrm{d_{pore}}}{3}\sqrt{\frac{8\mathrm{RT}}{\pi \mathrm{M}}}$$ [127]	**1.76×10^{-6}** For methane (molecular mass M 0.016 kg/mol) and catalyst pore diameter d_{pore} = 5.6 nm (specified by Sigma-Aldrich)
Diffusivity in a pore [m^2/s]	$$\mathrm{D_{pore}} = \left(\frac{1}{\mathrm{D_{AB}}} + \frac{1}{\mathrm{D_K}}\right)^{-1}$$ [127]	**1.73×10^{-6}**
Particle porosity	$$\phi_p = \frac{\mathrm{S}\rho_c\,\mathrm{d_{Pore}}}{4}$$ [127]	**0.84** For catalyst surface area 155 m^2/g and catalyst density 3890 kg/m^3 (specified by Sigma-Aldrich)
Effective diffusivity	$$\mathrm{D_{eff}} = \frac{\phi_P \mathrm{D_{pore}}}{\tau}$$	**3.74×10^{-7}** For tortuosity 3.9

[m^2/s]	[127]	
Weisz-Prater criterion for internal MTL	$$C_{WP} = \frac{-r_M \rho_c R^2}{D_{eff} C_M}$$ If $C_{WP} < 0.6$ for a first-order reaction, then no internal MTL is present [230]	**1.92×10^{-3}** For C_M as the bulk concentration of 0.176 mol/m^3 since the absence of external MTL was proved
Thus, the Weisz-Prater criterion shows the absence of internal mass transfer limitations		
Nusselt number Nu	$$Nu = 2 + 0.6 Re^{\frac{1}{2}} Pr^{\frac{1}{3}}$$ [228]	**2.10** For Prandtl number Pr = 0.683 for air at 673.15 K [229]
Heat transfer coefficient h [kJ/(m^2·s·K)]	$$h = \frac{k_t Nu}{d_p}$$ [228]	**2.13** For thermal conductivity of air at 673.15 K as 5.08×10^{-5} kW/(m·K) [229]
External temperature gradient criterion	$$\left\lvert \frac{-r_M(-\Delta H_{rx}) \rho_b R E}{h T^2 R_{gas}} \right\rvert < 0.15$$ If the condition is satisfied, then no external HTL is present [228]	**4.83×10^{-5}** For the heat of reaction -890 kJ/mol and activation energy E 143.3 kJ/mol (as reported in Table 3.1)
Thus, the external temperature gradient criterion shows the absence of external HTL		
Prater number □	$$\beta = \frac{-H_{rxn} D_{eff} C_M}{k_{eff} T}$$ [127]	**2.49×10^{-6}** For effective thermal conductivity of Al_2O_3 as 0.035 kW/(m·K) [231]
Maximum internal temperature rise [K]	$$\Delta T_{max} = \beta T$$ [127]	**1.67×10^{-3}** The maximum internal T can be 673.26 K instead of 673.15 K surface. The catalyst particle is thus isothermal
Thus, the Prater number shows the absence of internal HTL		
All the criteria above confirm that the reaction at 400 ˚C occurs in the kinetic regime		

and that the ideal PBR mole balance is applicable

Mass transfer limitations are more prominent at conditions when the intrinsic rate is the highest. Hence, the absence of mass and heat transfer limitations was verified for the most susceptible case of the most active bimetallic catalysts and highest methane concentration (5000 ppmv), with rate parameters calculated at the corresponding temperatures as illustrated below. Since the kinetic modeling was carried out for conversions ranging from 20% to 80%, the mass and heat transfer limitations have been calculated at these boundary limits, for the above stated feed conditions.

Table A. 2. Details of calculations to verify inexistence of internal and external mass transfer limitations and ΔT_{max} for the bimetallic catalysts when 5 vol% water is added to the system

Catalyst	**Parameter**	**Unit**	**Value**	
Pd-Pt/γ-Al_2O_3	X		0.80	0.20
	T	˚C	525	450
	F_{W0}	mol/s	7.81×10^{-6}	
	F_{M0}	mol/s	7.86×10^{-7}	
	k'	mol/ kg_{cat}.s	4.13×10^{-2}	5.32×10^{-3}
	$(-r_M)$	mol/ kg_{cat}.s	7.15×10^{-4}	4.12×10^{-4}
	C_{WP} (Weisz-Prater Criterion) < 0.6		**0.09**	**0.01**
	C_M (Mears Criterion) < 0.15		1.85×10^{-4}	3.14×10^{-5}
	External Temperature Gradient Criteria < 0.15		3.76×10^{-4}	2.89×10^{-4}
	β (Prater Number)		5.83×10^{-7}	2.46×10^{-6}
	$\Delta T_{max} = \beta * T < 0.3$	˚C	4.66×10^{-4}	1.78×10^{-3}
Pd-Pt/SnO_2	X		0.80	0.20
	T	˚C	525	450
	F_{W0}	mol/s	7.81×10^{-6}	
	F_{M0}	mol/s	7.86×10^{-7}	
	k'	mol/ kg_{cat}.s	4.40×10^{-2}	5.17×10^{-3}
	$(-r_M)$	mol/ kg_{cat}.s	7.63×10^{-4}	4.00×10^{-4}
	C_M (Mears Criterion) < 0.15		3.43×10^{-4}	5.32×10^{-5}
	External Temperature Gradient Criteria < 0.15		5.91×10^{-8}	3.81×10^{-8}

Table A. 3. Details of calculations to verify inexistence of internal and external mass transfer limitations and ΔT_{max} for the bimetallic catalysts when 10 vol% water is added to the system

Catalyst	Parameter	Unit	Value	
Pd-Pt/γ-Al$_2$O$_3$	X		0.80	0.20
	T	˚C	550	475
	F_{W0}	mol/s	1.56×10^{-5}	
	F_{M0}	mol/s	7.86×10^{-7}	
	k'	mol/ $kg_{cat}.s$	7.51×10^{-2}	1.10×10^{-2}
	$(-r_M)$	mol/ $kg_{cat}.s$	7.01×10^{-4}	4.36×10^{-4}
	C_{WP} (Weisz-Prater Criterion) < 0.6		**0.09**	**0.01**
	C_M (Mears Criterion) < 0.15		1.72×10^{-4}	3.07×10^{-5}
	External Temperature Gradient Criteria < 0.15		3.39×10^{-4}	2.49×10^{-4}
	β (Prater Number)		5.75×10^{-7}	2.42×10^{-6}
	$\Delta T_{max} = \beta * T < 0.3$	˚C	4.73×10^{-4}	1.81×10^{-3}
Pd-Pt/SnO$_2$	X		0.80	0.20
	T	˚C	550	475
	F_{W0}	mol/s	1.56×10^{-5}	
	F_{M0}	mol/s	7.86×10^{-7}	
	k'	mol/ $kg_{cat}.s$	8.24×10^{-2}	1.11×10^{-2}
	$(-r_M)$	mol/ $kg_{cat}.s$	7.68×10^{-4}	4.38×10^{-4}
	C_M (Mears Criterion) < 0.15		3.28×10^{-4}	5.48×10^{-5}
	External Temperature Gradient Criteria < 0.15		5.58×10^{-8}	3.87×10^{-8}

Since the $C_{WP} < 0.6$ and the $C_M < 0.15$, internal mass transfer limitations can be neglected for the Pd-Pt/γ-Al_2O_3 catalyst. Similarly, the Prater Number and ΔT_{max} values exhibit the absence of internal heat transfer limitations and thus the catalyst particle can be considered isothermal for conversion ranges of interest. Since SnO_2 is non-porous, only external mass and heat transfer limitations needs to be checked for; and the satisfactory criteria is met. As illustrated in the kinetic studies of Pd-based catalysts for methane combustion by Shahrestani et al. [232], the existence of internal mass transfer limitations are possible. However, the inexistence of such limitations in this work could be justified as the particles are 5 times smaller than those considered in the work by Shahrestani et al. [232].

Verification of inexistence of dilution effect on conversion

In order to evaluate the effect of dilution on conversion, the criteria below should be satisfied:

$$\frac{2.5bD_p}{(1-b)L_b} < 0.05 \quad [233]$$

Table A. 4. Criteria check to evaluate effect of dilution on conversion for the four catalysts under study

Catalyst	b (Dilution factor by volume)	L_b (Bed Length - m)	Criteria
Pd-Pt/SnO_2	0.088057554	0.0165	3.6×10^{-4}
Pd-Pt/γ-Al_2O_3	0.157326478	0.0135	8.6×10^{-4}
Pd/SnO_2	0.015539568	0.0194	5.1×10^{-5}
Pd/γ-Al_2O_3	0.027763496	0.0167	1.1×10^{-4}

Since the criteria of dilution is met by all of the catalysts, the effect of dilution on conversion can be neglected.

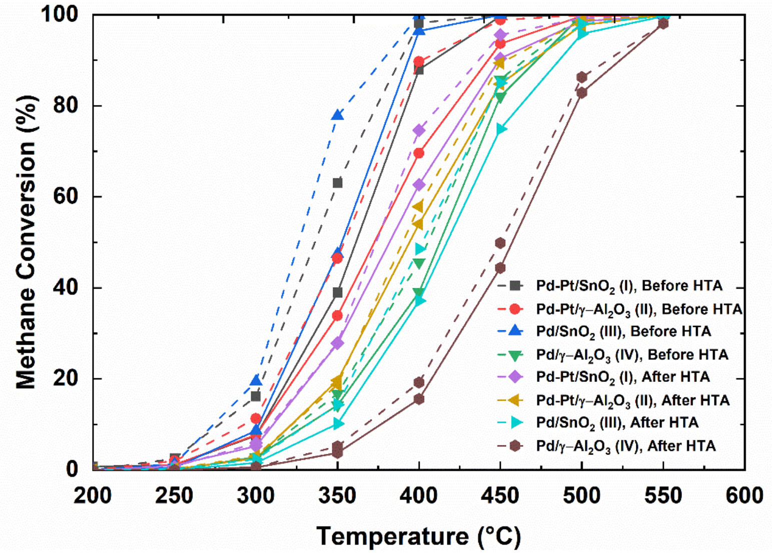

Figure A. 1. IE curves for runs before and after HTA under dry feed conditions for 4000 ppmv methane concentration (solid lines – ignition curves and dashed lines – extinction curves)

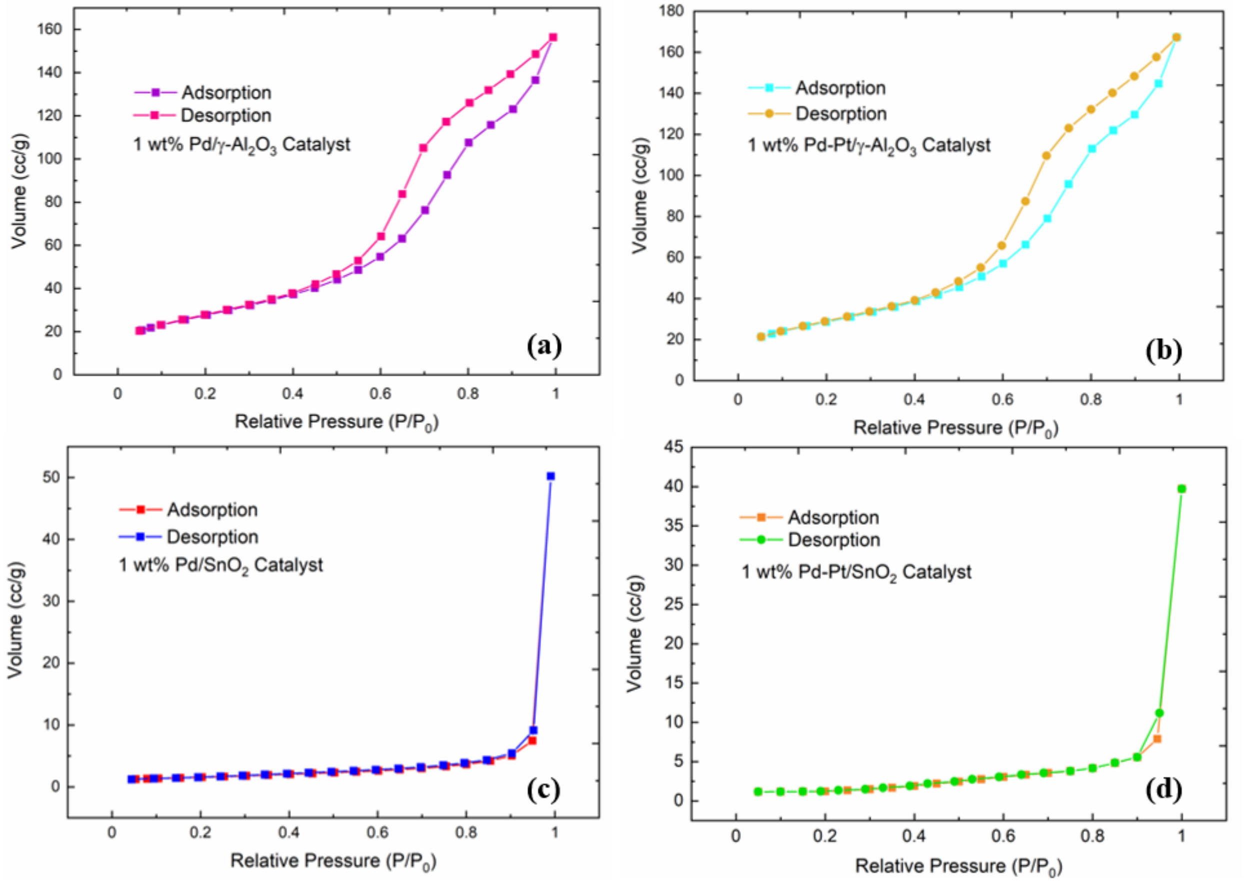

Figure A. 2. BET Isotherms for the hydrothermally aged (a) Pd/γ-Al$_2$O$_3$ catalyst (BET constant C = 87; Type IV isotherm; BET surface area = 140 m^2/g); (b) Pd-Pt/γ-Al$_2$O$_3$ catalyst (BET constant C = 93; Type IV isotherm; BET surface area = 144 m^2/g); (c) Pd/SnO$_2$ catalyst (BET constant C = 58; Type II isotherm; BET surface area = 6 m^2/g); and (d) Pd-Pt/SnO$_2$ catalyst (BET constant C = 150; Type II isotherm; BET surface area = 6 m^2/g)

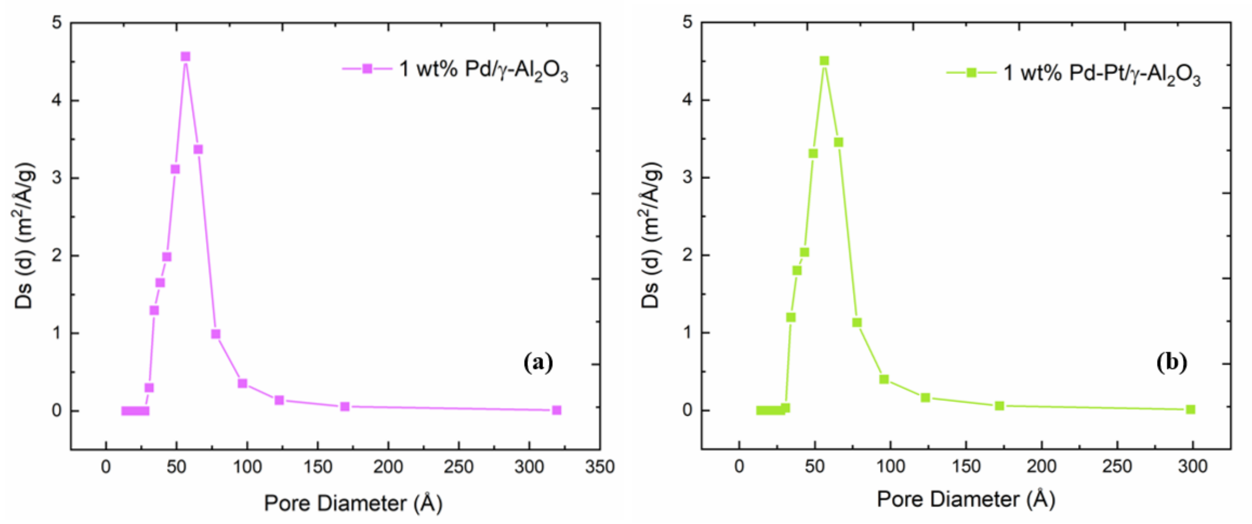

Figure A. 3. Pore size distribution for the hydrothermally aged (a) Pd/γ-Al_2O_3 catalyst (pore diameter = 5.6 nm); (b) Pd-Pt/γ-Al_2O_3 catalyst (pore diameter = 5.5 nm)

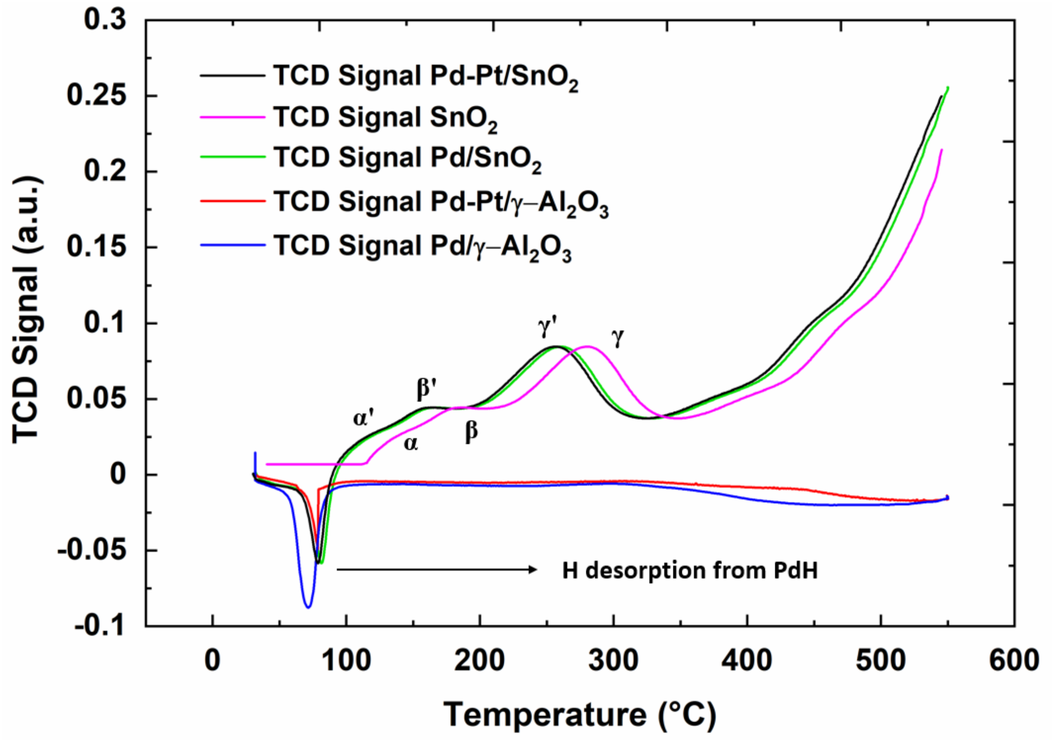

Figure A. 4. TPR Profiles for the hydrothermally aged catalysts

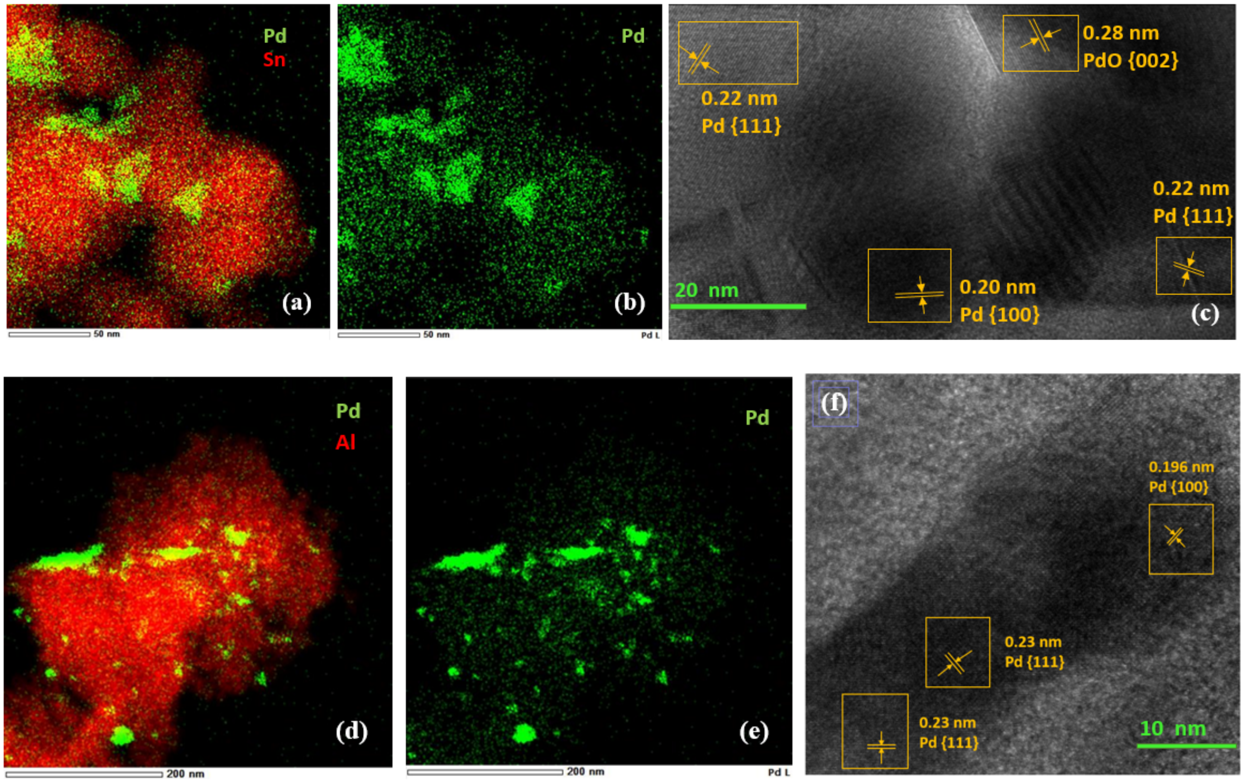

Figure A. 5. (a)-(c) Hydrothermally aged Pd/SnO$_2$ catalyst: (a)-(b) TEM-EDX analysis showing Pd (green) distribution; (c) a representation of the Pd and PdO phases [167]; *(d)-(f) Hydrothermally aged Pd/γ-Al$_2$O$_3$ catalyst: (d)-(e) TEM-EDX analysis showing Pd (green) distribution; (f) a representation of the Pd phases*

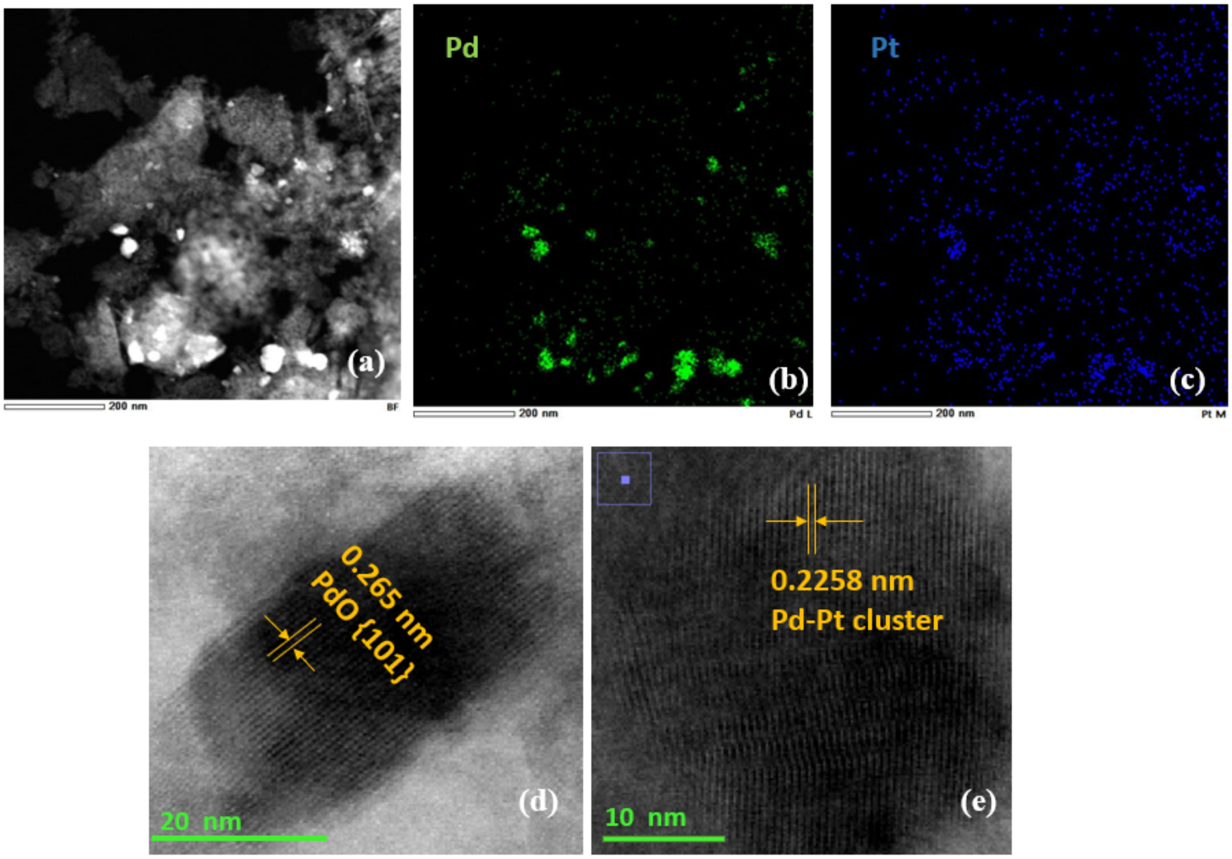

Figure A. 6. TEM-EDX analysis of hydrothermally aged Pd-Pt/γ-Al$_2$O$_3$ catalyst: (a)-(c) Pd (green) and Pt (blue) distribution; (d) a representation of the PdO phase; (e) a representative metal cluster.

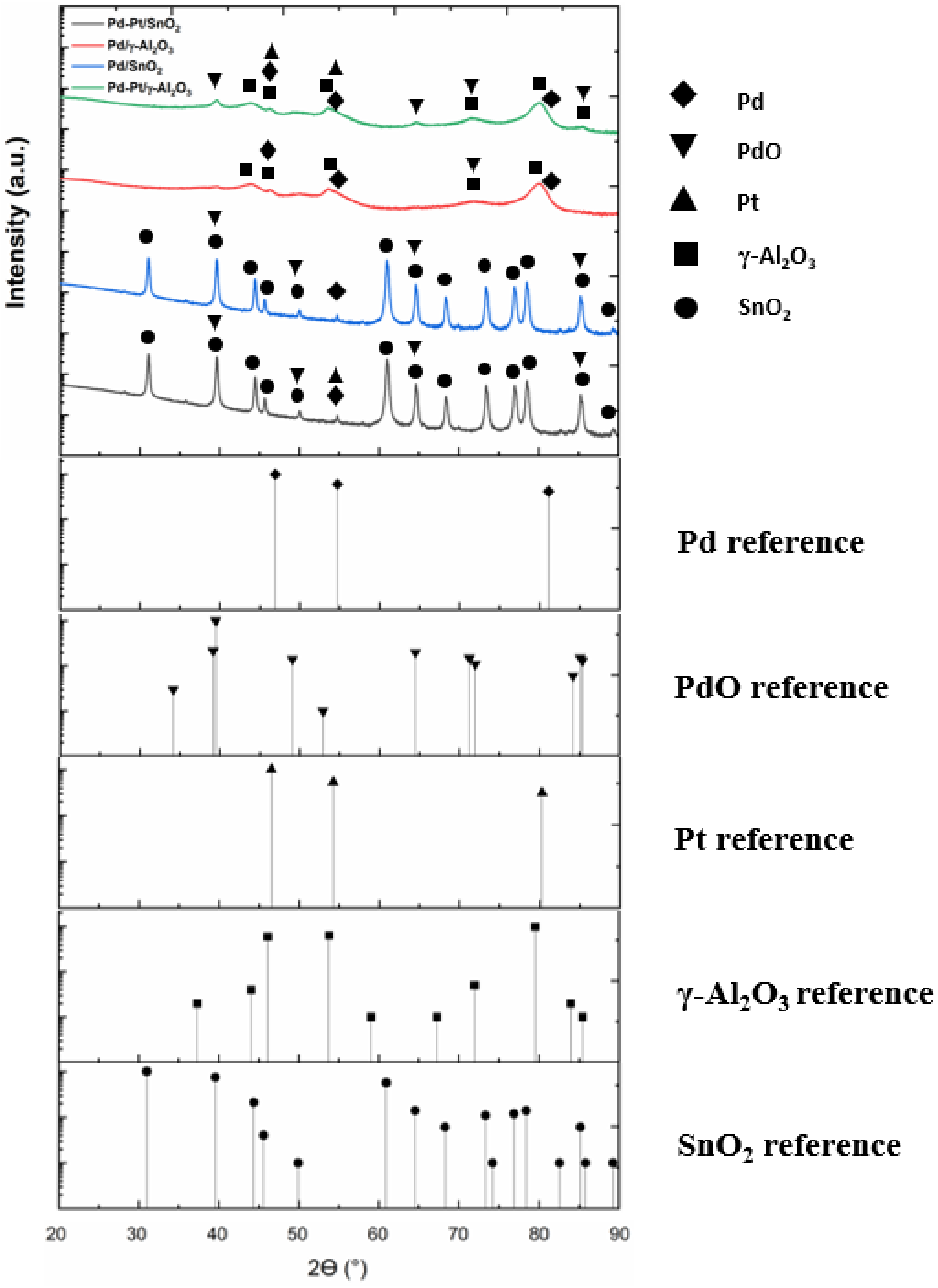

Figure A. 7. XRD profiles of the four hydrothermally aged catalysts under study

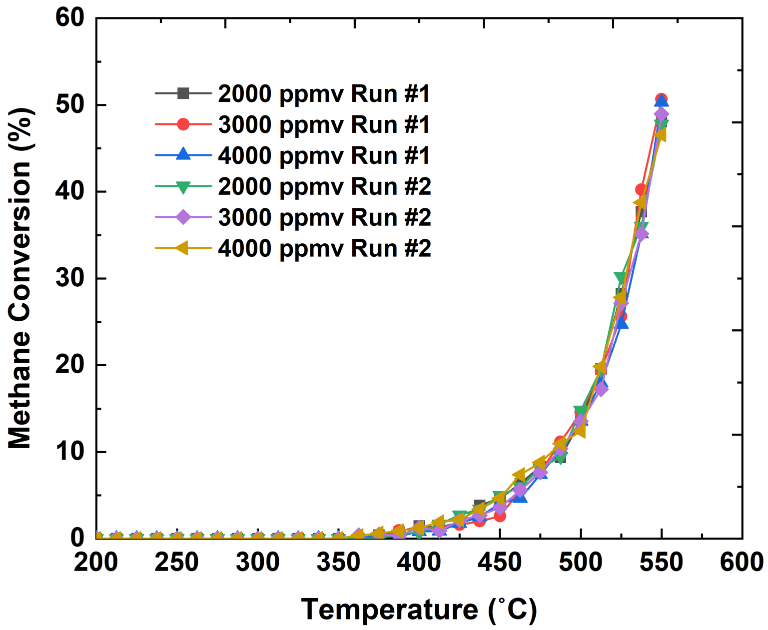

Figure A. 8. Ignition curves for the reproducible runs for the initial methane concentrations of 2000 ppmv, 3000 ppmv, and 4000 ppmv for the Pd/γ-Al_2O_3 catalyst under 5 vol% wet feed conditions

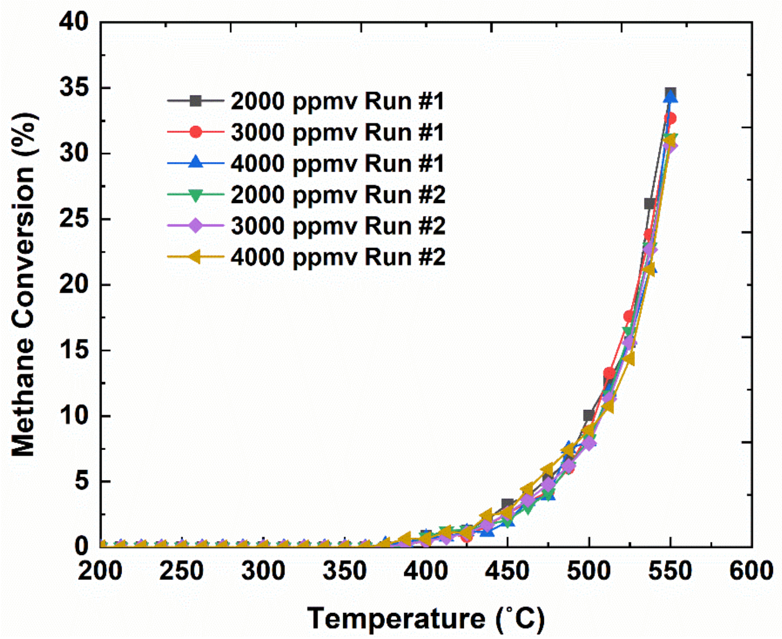

Figure A. 9. Ignition curves for the reproducible runs for the initial methane concentrations of 2000 ppmv, 3000 ppmv, and 4000 ppmv for the Pd/γ-Al_2O_3 catalyst under 10 vol% wet feed conditions

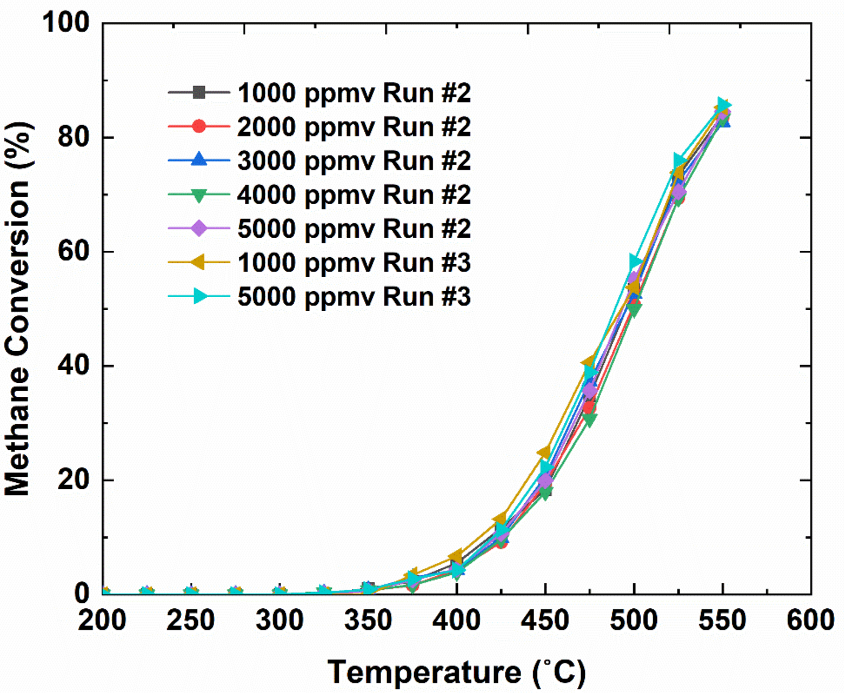

Figure A. 10. Ignition curves for all the reproducible runs for the Pd-Pt/γ-Al_2O_3 catalyst under 5 vol% wet feed conditions

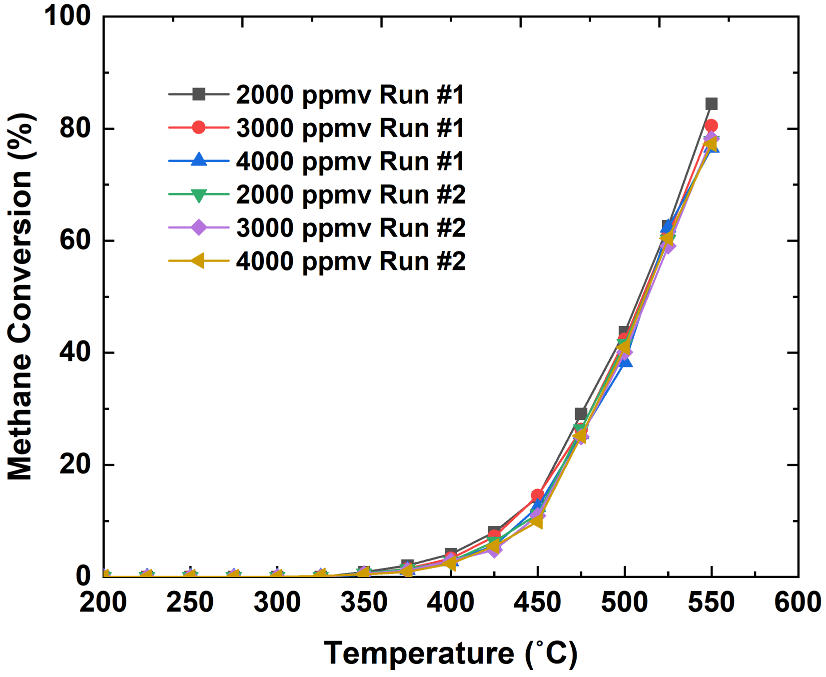

Figure A. 11. Ignition curves for the reproducible runs for the initial methane concentrations of 2000 ppmv, 3000 ppmv, and 4000 ppmv for the Pd-Pt/γ-Al_2O_3 catalyst under 10 vol% wet feed conditions

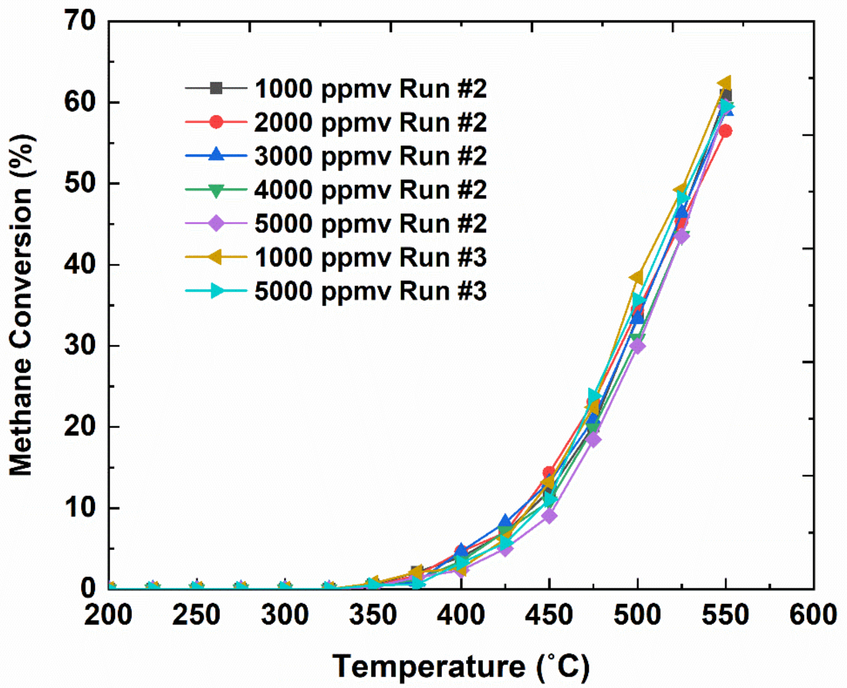

Figure A. 12. Ignition curves for all the reproducible runs for the Pd/SnO₂ catalyst under 5 vol% wet feed conditions

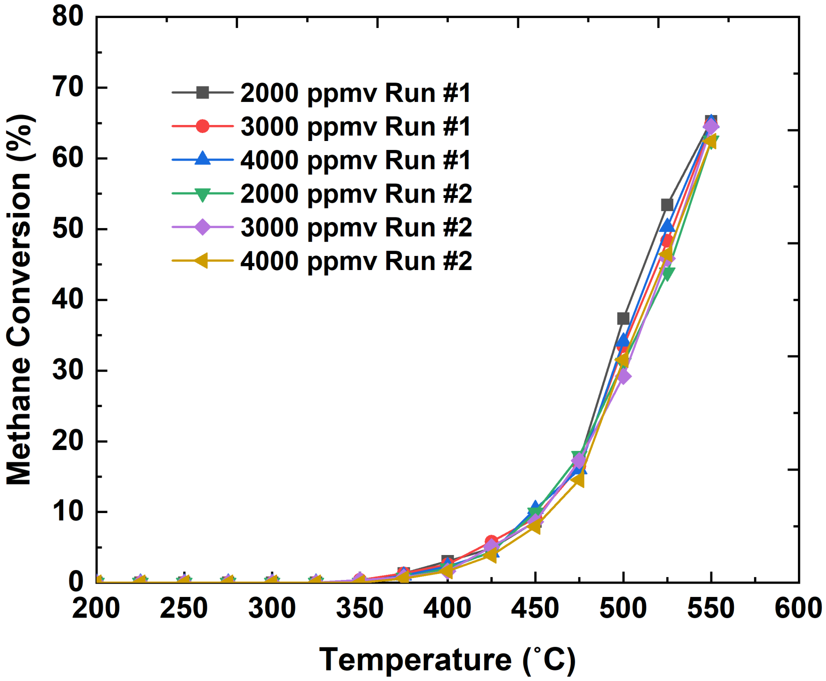

Figure A. 13. Ignition curves for the reproducible runs for the initial methane concentrations of 2000 ppmv, 3000 ppmv, and 4000 ppmv for the Pd/SnO₂ catalyst under 10 vol% wet feed conditions

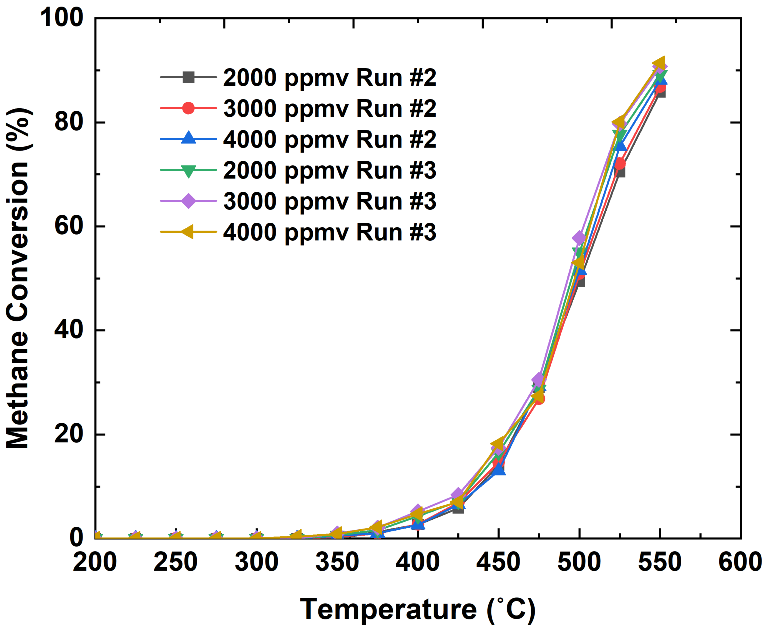

Figure A. 14. Ignition curves for the reproducible runs for the initial methane concentrations of 2000 ppmv, 3000 ppmv, and 4000 ppmv for the Pd-Pt/SnO$_2$ catalyst under 5 vol% wet feed conditions

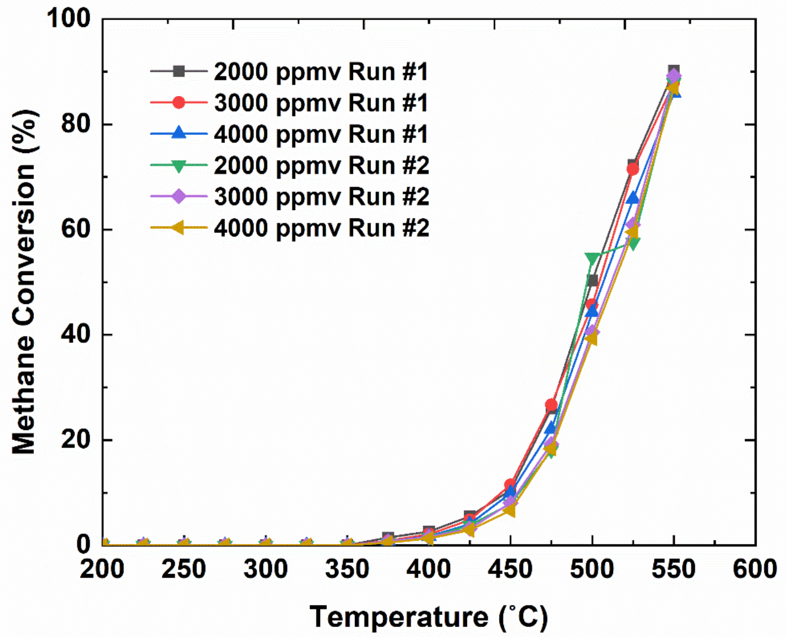

Figure A. 15. Ignition curves for the reproducible runs for the initial methane concentrations of 2000 ppmv, 3000 ppmv, and 4000 ppmv for the Pd-Pt/SnO$_2$ catalyst under 10 vol% wet feed conditions (the outlier at 500 ˚C for 2000 ppmv CH$_4$ concentration has been omitted in the analysis)

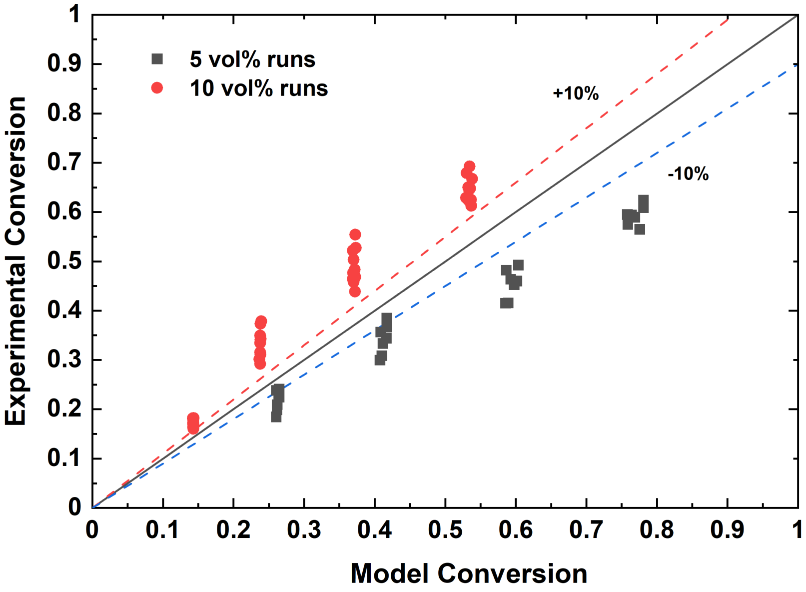

Figure A. 16. Comparison of the predicted and experimental conversion for the combined wet feed condition studies on the Pd/SnO₂ catalyst based on decreased water inhibition on a single site. The model was abandoned based on these results.

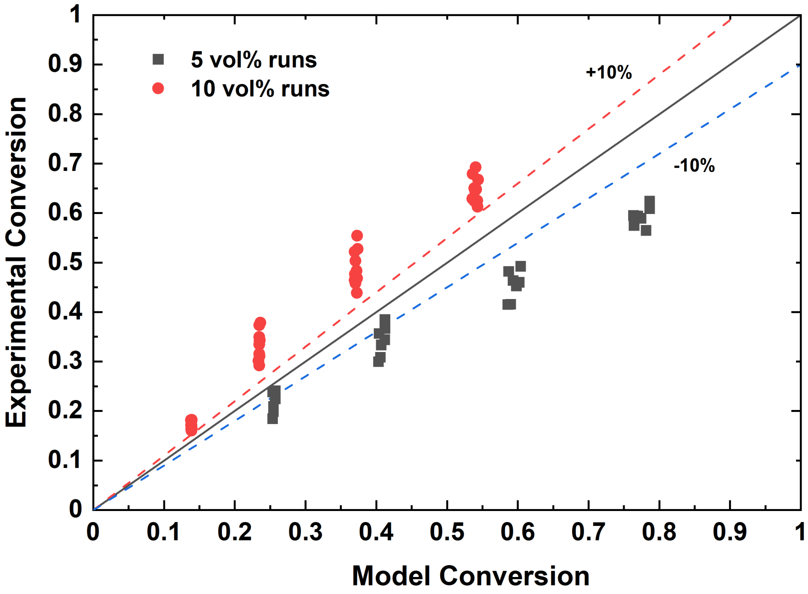

Figure A. 17. Comparison of the predicted and experimental conversion for the combined wet feed condition studies on the Pd/SnO₂ catalyst based on Equation 3.6. The model was abandoned based on these results

Table A. 5. $K_{aq}C_{aq}$ calculations for the Pd/SnO_2 catalyst based on the model in Equation 3.6 under 5 vol% and 10 vol% wet feed conditions

T (˚C)	K_{aq} (m^3 mol^{-1})	C_{aq} (5 vol%, mol m^{-3})	K_{aq} C_{aq} (5 vol%)	C_{aq} (10 vol%, mol m^{-3})	K_{aq} C_{aq} (10 vol%)
225	9992969	2.41	24038897	4.81	48077794
250	5376202	2.31	12435469	4.63	24870938
275	3028298	2.23	6745201	4.45	13490402
300	1777163	2.15	3817062	4.30	7634124
325	1081981	2.07	2243786	4.15	4487572
350	680893	2.00	1364952	4.01	2729905
375	441484	1.94	856472	3.88	1712944
400	294111	1.88	552741	3.76	1105481
425	200816	1.82	365970	3.64	731939
450	140228	1.77	248036	3.54	496073
475	99950	1.72	171741	3.44	343482
500	72594	1.67	121271	3.34	242542
525	53644	1.63	87193	3.25	174386
550	40277	1.58	63744	3.17	127488

Appendix B: The Supporting Information of Chapter 4

SECTION B.1: Verification of ideal plug flow conditions

Verification of Plug Flow conditions for Pd-Pt/10Co/SnO_2 catalyst –

The plug flow conditions were verified for the Pd-Pt/10Co/SnO_2 catalyst as delineated below:

Amount of catalyst + diluent = 0.34 + 0.25 = 0.59 g
Based on measured density of catalyst + diluent = 0.583 g/mL
Bed volume = 0.59/0.583 = 1.012 mL
Reactor ID = 0.9525 cm (3/8 ″)
Bed length = (1.012 * 4)/(π * 0.9525^2) = 1.42 cm

Step 1: Dynamic Viscosity of Air at Atmospheric Pressure and 673.15 K

$\mu = 3.4\times10^{-5}\ \mathrm{Ns/m^2}$ [226]

Step 2: Calculation of Superficial Velocity

$u = Q/A_c$

Reactor I.D. = 3/8" = 0.009525 m

$A_c = (\pi/4)*d_p^2 = 7.1256\times10^{-5}\ \mathrm{m^2}$

$Q_0 = 210\ \mathrm{mL/min} = 3.5\times10^{-6}\ \mathrm{m^3/s}$

$Q = Q_0 * (T/273.15) * (1/1.323) = 3.5\times10^{-6} * (673.15/273.15) * (1/1.323) = 6.52\times10^{-6}\ \mathrm{m^3/s}$

$u = 3.04\times10^{-6} / 7.1256\times10^{-5} = 0.0915\ \mathrm{m/s}$ [157]

Step 3: Calculate Particle Reynolds Number

ρ of air at 673.15K = $0.5247\ \mathrm{kg/m^3}$

$d_p = 5\times10^{-5}$ m

$^{N}Re_{P} = (0.0915 * 0.5247 * 5\times10^{-5})/(3.4\times10^{-5}) = 0.0706$ [157]

Step 4: Calculate the Peclet Number (for gas-phase operations)

L = 0.0142 m

$N_{Pe} = 0.087 * (0.0706)^{0.23} * (0.0142/5\times10^{-5}) = 13.43$ [157]

Step 5: Calculate the Minimum Peclet Number (for gas-phase operations)

n (order of reaction) = 1

X (conversion) = 0.5 (50%)

$^{N}Pe_{min} = 8 * 1 * \ln(1/(1-0.5)) = 5.5452$ [157]

Step 6: Calculate minimum L/d_p

$L/d_p > 92 * 13.43^{-0.23} * 1 * \ln(1/(1-0.5)) = 35.09$

In our case, L/dp = 284 [157]

Hence, the condition is satisfied for plug flow

Verification of Plug Flow conditions for Pd-Pt/10Co/γ-Al_2O_3 catalyst -

The plug flow conditions were verified for the Pd-Pt/10Co/γ-Al_2O_3 catalyst as delineated below:

Amount of catalyst + diluent = 0.34 + 0.25 = 0.59 g
Based on measured density of catalyst + diluent = 0.4223 g/mL
Bed volume = 0.59/0.4223 = 1.397 mL
Reactor ID = 0.9525 cm (3/8 ″)
Bed length = (1.397 * 4)/(π * 0.9525^2) = 1.96 cm

Step 1: Dynamic Viscosity of Air at Atmospheric Pressure and 673.15 K

$\mu = 3.4\times10^{-5}$ Ns/m^2 [226]

Step 2: Calculation of Superficial Velocity

$u = Q/A_c$

Reactor I.D. = 3/8" = 0.009525 m

$A_c = (\pi/4)*d_p^2 = 7.1256\times10^{-5}$ m^2

Q_0 = 210 mL/min = 3.5×10^{-6} m^3/s

$Q = Q_0 * (T/273.15) * (1/1.17) = 3.5\times10^{-6} * (673.15/273.15) * (1/1.17) = 7.39\times10^{-6}$ m^3/s

$u = 7.39\times10^{-6} / 7.1256\times10^{-5} = 0.1038$ m/s [157]

Step 3: Calculate Particle Reynolds Number

ρ of air at 673.15K = 0.5247 kg/m^3

$d_p = 5\times10^{-5}$ m

$^{N}Re_P = (0.1038 * 0.5247 * 5\times10^{-5})/(3.4\times10^{-5}) = 0.08001$ [157]

Step 4: Calculate the Peclet Number (for gas-phase operations)

L = 0.0196 m

$N_{Pe} = 0.087 * (0.08001)^{0.23} * (0.0196/5\times10^{-5}) = 19.08$ [157]

Step 5: Calculate the Minimum Peclet Number (for gas-phase operations)

n (order of reaction) = 1

X (conversion) = 0.5 (50%)

$^{N}Pe_{min} = 8 * 1 * \ln(1/(1-0.5)) = 5.5452$ [157]

Step 6: Calculate minimum L/d_p

$L/d_p > 92 * 19.08^{-0.23} * 1 * \ln(1/(1-0.5)) = 32.37$

In our case, L/dp = 392 [157]

Hence, the condition is satisfied for plug flow

Verification of inexistence of dilution effect on conversion

To evaluate the effect of dilution on conversion, the criteria below should be satisfied:

$$\frac{2.5bD_p}{(1-b)L_b} < 0.05 \quad [233]$$

Table B. 1. Criteria check to evaluate effect of dilution on conversion for the catalysts under study

Catalyst	**b (Dilution factor by volume)**	**L_b (Bed Length - m)**	**Criteria**
Pd-Pt/10Co/SnO_2	0.088057554	0.0142	3.66×10^{-4}
Pd-Pt/10Co/γ-Al_2O_3	0.157326478	0.0196	8.64×10^{-4}

SECTION B.2: Verification of inexistence of mass transfer limitations

Table B. 2. Example of detailed calculations of criteria to confirm the absence of mass and heat transfer limitations at 350 ˚ C in the wet (10 vol%) feed for the Pd-Pt/10Co/SnO₂ catalyst and 5000 ppmv methane concentration. Since the catalyst is non-porous internal mass and heat transfer limitations do not exist.

Parameter	Equation	Value (calculated or experimental)
Reaction rate -r_M, [mol/(s·kg_{cat})]	$-r_M = \frac{F_{Mo}X}{W}$	**2.31×10^{-4}** For initial methane molar flow rate $F_{Mo} = 7.86 \times 10^{-7}$ mol/s, catalyst amount W = 0.34 g, conversion at differential conditions X = 0.1
Methane bulk diffusivity in air at 623.15 K D_{AB} [m^2/s]	$D_{AB} = \frac{1.013 \cdot 10^{-2} T^{1.75} \left[\frac{1}{M_A} + \frac{1}{M_B}\right]^{0.5}}{P\left[\left(\sum \nu_i\right)_A^{\frac{1}{3}} + \left(\sum \nu_i\right)_B^{\frac{1}{3}}\right]^2}$ (Fuller formula [127], [227])	**7.82×10^{-5}** For P =101325 Pa, molecular masses and diffusion volumes for methane and air as 16 g/mol, 29 g/mol, 24.42, and 20.1 [127], [227]
Particle Reynolds number Re_p	$Re = \frac{U\rho_g d_p}{\mu}$ [228]	**0.0772** For dynamic viscosity $\mu = 3.4\times10^{-5}$ Pa·s [226] and density $\rho_g = 0.5247$ kg/m^3 (ideal gas) of air at 623.15 K [229] , $d_p = 5\times10^{-5}$ m, free-stream velocity 0.1 m/s (for 3/8" reactor i.d. and assuming bed porosity of 0.4)
Schmidt number	$Sc = \frac{\mu}{D_{AB}\rho_g}$ [228]	**0.829**
Sherwood number Sh	$Sh = 2 + 0.6Re^{\frac{1}{2}}Sc^{\frac{1}{3}}$ (Frössling correlation [228])	**2.16**

Mass transfer coefficient k_c [m/s]	$k_c = \frac{D_{AB}Sh}{d_p}$ [228]	**3.37**
Mears criterion for external diffusion	$\frac{-r_M \rho_b R n}{k_c C_M} < 0.15$ If the condition is satisfied, then no external MTL is present [228]	**3.36 × 10^{-5}** For ρ_b (bed density) 3954 kg/m^3 (catalyst density ρ_c 6590 kg/m^3, bed porosity 0.4), particle radius R = 2.5 × 10^{-5} m, order n = 1, $C_M = C_{Mo}(1-X)$ with initial methane concentration of 0.2025 mol/m^3
Thus, the Mears criterion shows the absence of external mass transfer limitations		
Nusselt number Nu	$Nu = 2 + 0.6Re^{\frac{1}{2}}Pr^{\frac{1}{3}}$ [228]	**2.15** For Prandtl number Pr = 0.683 for air at 623.15 K [229]
Heat transfer coefficient h [kJ/(m^2·s·K)]	$h = \frac{k_t Nu}{d_p}$ [228]	**2.18** For thermal conductivity of air at 623.15 K as 0.03365 W/(m·K) [229]
External temperature gradient criterion	$\left\lvert \frac{-r_M(-\Delta H_{rx})\rho_b R E}{h T^2 R_{gas}} \right\rvert < 0.15$ If the condition is satisfied, then no external HTL are present [228]	**3.18 × 10^{-4}** For the heat of reaction -890 kJ/mol and activation energy E 110 kJ/mol (as reported in Table 4.2)
Thus, the external temperature gradient criterion shows the absence of external HTL		
All the criteria above confirm that the reaction at 350 °C occurs in the kinetic regime and that the ideal PBR mole balance is applicable		

Table B. 3. Example of detailed calculations of criteria to confirm the absence of mass and heat transfer limitations at 350 ˚C in the wet (10 vol%) feed for the Pd-Pt/10Co/ γ-Al_2O_3 catalyst and 5000 ppmv methane concentration.

Parameter	Equation	Value (calculated or experimental)
Reaction rate -r_M, [mol/(s·kg_{cat})]	$-r_M = \frac{F_{Mo}X}{W}$	**1.16×10^{-4}** For initial methane molar flow rate $F_{Mo} = 7.86 \times 10^{-7}$ mol/s, catalyst amount W = 0.34 g, conversion at differential conditions X = 0.05
Methane bulk diffusivity in air at 623.15 K D_{AB} [m^2/s]	$D_{AB} = \frac{1.013 \cdot 10^{-2} T^{1.75} \left[\frac{1}{M_A} + \frac{1}{M_B}\right]^{0.5}}{P\left[\left(\sum \nu_i\right)_A^{\frac{1}{3}} + \left(\sum \nu_i\right)_B^{\frac{1}{3}}\right]^2}$ (Fuller formula [127], [227])	**7.82×10^{-5}** For P =101325 Pa, molecular masses and diffusion volumes for methane and air as 16 g/mol, 29 g/mol, 24.42, and 20.1 [127], [227]
Particle Reynolds number Re_p	$Re = \frac{U\rho_g d_p}{\mu}$ [228]	**0.0772** For dynamic viscosity $\mu = 3.4\times10^{-5}$ Pa·s [226] and density $\rho_g = 0.5247$ kg/m^3 (ideal gas) of air at 623.15 K [229] , $d_p = 5\times10^{-5}$ m, free-stream velocity 0.1 m/s (for 3/8" reactor i.d. and assuming bed porosity of 0.4)
Schmidt number	$Sc = \frac{\mu}{D_{AB}\rho_g}$ [228]	**0.829**
Sherwood number Sh	$Sh = 2 + 0.6Re^{\frac{1}{2}}Sc^{\frac{1}{3}}$ Frössling correlation [228]	**2.16**

Mass transfer coefficient k_c [m/s]	$k_c = \frac{D_{AB}Sh}{d_p}$ [228]	**3.37**
Mears criterion for external diffusion	$\frac{-r_M \rho_b R n}{k_c C_M} < 0.15$ If the condition is satisfied, then no external MTL is present [228]	**3.68 × 10^{-6}** For catalyst density ρ_c = $1/((1/\rho_s)+V_0))$ = 1524.23 kg/m^3 [232]; where ρ_s is solid density = 3890 kg/m^3 and V_0 is pore volume = 0.399 cc/g (bed density ρ_b = 914.537 kg/m^3, (bed porosity 0.4), particle radius R = 2.5 × 10^{-5} m, order n = 1, $C_M = C_{Mo}(1\text{-}X)$ with initial methane concentration of 0.213 mol/m^3
Thus, the Mears criterion shows the absence of external mass transfer limitations		
Knudsen diffusivity [m^2/s]	$D_K = \frac{d_{pore}}{3}\sqrt{\frac{8RT}{\pi M}}$ [127]	**1.30 × 10^{-6}** For methane (molecular mass M 0.016 kg/mol) and catalyst pore diameter d_{pore} = 4.31 nm (Figure A.3.b)
Diffusivity in a pore [m^2/s]	$D_{pore} = \left(\frac{1}{D_{AB}} + \frac{1}{D_K}\right)^{-1}$ [127]	**1.28 × 10^{-6}**
Particle porosity	$\phi_p = \frac{S\rho_c\, d_{Pore}}{4}$ [127]	**0.1971** For catalyst surface area S_{BET} = 120 m^2/g (Figure A.3.a)
Effective diffusivity [m^2/s]	$D_{eff} = \frac{\phi_P D_{pore}}{\tau}$ [127]	**6.47 × 10^{-8}** For tortuosity 3.9

Weisz-Prater criterion for internal MTL	$C_{WP} = \frac{-r_M \rho_c R^2}{D_{eff} C_M}$ If $C_{WP} < 0.6$ for a first-order reaction, then no internal MTL is present [230]	**8.00×10^{-3}** For C_M as the bulk concentration of 0.213 mol/m^3 since the absence of external MTL was proved
Thus, the Weisz-Prater criterion shows the absence of internal mass transfer limitations		
Nusselt number Nu	$Nu = 2 + 0.6Re^{\frac{1}{2}}Pr^{\frac{1}{3}}$ [228]	**2.15** For Prandtl number Pr = 0.683 for air at 623.15 K [229]
Heat transfer coefficient h [kJ/(m^2·s·K)]	$h = \frac{k_t Nu}{d_p}$ [228]	**2.18** For thermal conductivity of air at 623.15 K as 0.03365 W/(m·K) [229]
External temperature gradient criterion	$\left\lvert\frac{-r_M(-\Delta H_{rx})\rho_b RE}{hT^2 R_{gas}}\right\rvert < 0.15$ If the condition is satisfied, then no external HTL are present [228]	**4.44×10^{-5}** For the heat of reaction -890 kJ/mol and activation energy E 133 kJ/mol (as reported in Table 4.2)
Thus, the external temperature gradient criterion shows the absence of external HTL		
Prater number b	$\beta = \frac{-H_{rxn} D_{eff} C_M}{k_{eff} T}$ [127]	**5.62×10^{-7}** For effective thermal conductivity of Al_2O_3 as 0.035 kW/(m·K) [231]
Maximum internal temperature rise [K]	$\Delta T_{max} = \beta T$ [127]	**3.50×10^{-4}** The maximum internal T can be 623.15 K which is the same as 623.15 K surface. The catalyst particle is thus isothermal
Thus, the Prater number shows the absence of internal HTL		
All the criteria above confirm that the reaction at 350 ˚C occurs in the kinetic regime and that the ideal PBR mole balance is applicable		

SECTION B.3: Verification of inexistence of mass and heat transfer limitations at 20 and 80% conversions

Mass transfer limitations are more prominent at conditions when the intrinsic rate is the highest. Hence, the absence of mass and heat transfer limitations was verified for the most susceptible case of highest methane concentration (5000 ppmv), with rate parameters calculated at the corresponding temperatures as illustrated below. Since the kinetic modeling was carried out for conversions ranging from 20% to 80%, the external mass and heat transfer limitations as well as the internal heat transfer limitations have been calculated at these boundary limits, for the above stated feed conditions.

For the γ-Al_2O_3-supported catalyst, an internal effectiveness factor was incorporated to account for the internal mass transfer effects as depicted below:

$$(-r_M) = \eta_1 k_1 C_M + \frac{\eta_2 k_2 C_M}{C_{aq}} \qquad \text{(B.1)}$$

The internal effectiveness factor was estimated based on a first order reaction rate to CH_4 as follows [228]:

$$\eta_1 = \frac{3}{\phi_1^2}\left(\phi_1 \coth\phi_1 - 1\right) \text{ and } \eta_2 = \frac{3}{\phi_2^2}\left(\phi_2 \coth\phi_2 - 1\right); \qquad \text{(B.2)}$$

where, the Thiele modulus (ϕ) was determined as [228]:

$$\phi_1 = \frac{R}{3}\sqrt{\frac{k_{r1}}{D_{eff}}} \text{ and } \phi_2 = \frac{R}{3}\sqrt{\frac{k_{r2}}{D_{eff}}}; \qquad \text{(B.3)}$$

where, R = catalyst particle radius (m) and D_{eff} = effective diffusivity (m^2/s) (though in essence $D_{eff} = m_{fluid}^3\ m_{cat}^{-1}\ s^{-1}$)

Therefore, in Equation B.3, rate constant 'k' should have units of $m_{fluid}^3\ m_{cat}^{-3}\ s^{-1}$ to enable the Thiele modulus to be dimensionless. Thus, the rate constant k_1 and k_2 were re-parameterized as depicted below:

$$K_{r1} = k_1 \rho_c \text{ and } k_{r2} = \left(\frac{k_2}{C_{aq}}\right)\rho_c; \text{ where } \rho_c = \text{ catalyst density } \left(\frac{kg_{cat}}{m_{cat}^3}\right) \qquad \text{(B.4)}$$

The parameters in each of the above definitions is calculated as illustrated in Section B.2. The C_M and C_M/C_{aq} terms were calculated as follows:

$$C_M = \frac{F_{M0}(1 - X_M)}{Q_0} \text{ and } \frac{C_M}{C_{aq}} = \frac{F_{M0}(1 - X_M)}{F_{aq0} + (2 * F_{M0} * X_M)}$$

Table B. 4. Details of calculations to verify inexistence of internal and external mass transfer limitations and ΔT_{max} for the bimetallic catalysts when 5 vol% water is added to the system

Catalyst	Parameter	Unit	Value	
Pd-Pt/10Co/γ-Al_2O_3	X		0.80	0.20
	T	˚C	525	450
	Q_0	m^3/s	3.51×10^{-6}	
	F_{W0}	mol/s	7.81×10^{-6}	
	F_{M0}	mol/s	7.86×10^{-7}	
	k_1	$m^3/kg_{cat}.s$	3.26×10^{-2}	3.13×10^{-3}
	k_2	$mol/kg_{cat}.s$	4.47×10^{-2}	5.76×10^{-3}
	$(-r_M) = k_1C_M + \frac{k_2C_M}{C_{aq}}$	$mol/kg_{cat}.s$	1.27×10^{-3}	6.58×10^{-4}
	C_M (Mears Criterion) $\frac{-r_M\rho_b Rn}{k_cC_M} < 0.15$	-	1.26×10^{-4}	1.92×10^{-5}
	External Temperature Gradient Criteria $\left\lvert\frac{-r_M(-\Delta H_{rx})\rho_b RE}{hT^2R_{gas}}\right\rvert < 0.15$	-	2.59×10^{-4}	1.78×10^{-4}
	β (Prater Number) $= \frac{-H_{rxn}D_{eff}C_M}{k_{eff}T}$		1.05×10^{-7}	4.43×10^{-7}
	$\Delta T_{max} = \beta * T < 0.3$	˚C	8.40×10^{-5}	3.21×10^{-4}
	Internal Effectiveness Factor 1 computed from MATLAB code (η_1)	-	**0.997**	**1.000**
	Internal Effectiveness Factor 2 computed from MATLAB code (η_2)	-	**0.996**	**0.999**
Pd-Pt/10Co/SnO_2	X		0.80	0.20
	T	˚C	445	375
	Q_0	m^3/s	3.51×10^{-6}	
	F_{W0}	mol/s	7.81×10^{-6}	

	F_{M0}	mol/s	7.86×10^{-7}	
	k_1	$m^3/kg_{cat}.s$	2.79×10^{-2}	5.58×10^{-3}
	k_2	$mol/kg_{cat}.s$	1.49×10^{-2}	1.39×10^{-3}
	$(-r_M) = k_1 C_M + \frac{k_2 C_M}{C_{aq}}$	$mol/kg_{cat}.s$	7.35×10^{-4}	5.30×10^{-4}
	C_M (Mears Criterion) $\frac{-r_M \rho_b R n}{k_c C_M} < 0.15$		2.80×10^{-4}	5.67×10^{-5}
	External Temperature Gradient Criteria $\left\lvert \frac{-r_M(-\Delta H_{rx})\rho_b R E}{h T^2 R_{gas}} \right\rvert < 0.15$		6.80×10^{-4}	6.58×10^{-4}

Table B. 5. Details of calculations to verify inexistence of internal and external mass transfer limitations and ΔT_{max} for the bimetallic catalysts when 10 vol% water is added to the system

Catalyst	**Parameter**	**Unit**	**Value**	
Pd-Pt/10Co/γ-Al₂O₃	X		0.80	0.20
	T	˚C	545	450
	Q_0	m³/s	3.51×10^{-6}	
	F_{W0}	mol/s	1.56×10^{-5}	
	F_{M0}	mol/s	7.86×10^{-7}	
	k_1	$m^3/kg_{cat}.s$	5.67×10^{-2}	3.13×10^{-3}
	k_2	$mol/kg_{cat}.s$	7.24×10^{-2}	5.76×10^{-3}
	$(-r_M) = k_1C_M + \frac{k_2C_M}{C_{aq}}$	$mol/kg_{cat}.s$	1.52×10^{-3}	4.39×10^{-4}
	C_M (Mears Criterion) $\frac{-r_M\rho_b Rn}{k_c C_M} < 0.15$	-	1.44×10^{-4}	1.28×10^{-5}
	External Temperature Gradient Criteria $\left\lvert\frac{-r_M(-\Delta H_{rx})\rho_b RE}{hT^2R_{gas}}\right\rvert < 0.15$	-	2.97×10^{-4}	1.11×10^{-4}
	β (Prater Number) = $\frac{-H_{rxn}D_{eff}C_M}{k_{eff}T}$		1.04×10^{-7}	4.43×10^{-7}
	$\Delta T_{max} = \beta * T < 0.3$	˚C	8.51×10^{-5}	3.21×10^{-4}
	Internal Effectiveness Factor 1 computed from MATLAB code (η_1)	-	**0.995**	**1.000**
	Internal Effectiveness Factor 2 computed from MATLAB code (η_2)	-	**0.997**	**1.000**
Pd-Pt/10Co/SnO₂	X		0.80	0.20
	T	˚C	450	375
	Q_0	m³/s	3.51×10^{-6}	
	F_{W0}	mol/s	1.56×10^{-5}	

	F_{M0}	mol/s	7.86×10^{-7}	
	k_1	$m^3/kg_{cat}.s$	3.09×10^{-2}	5.58×10^{-3}
	k_2	$mol/kg_{cat}.s$	1.74×10^{-2}	1.39×10^{-3}
	$(-r_M) = k_1 C_M + \frac{k_2 C_M}{C_{aq}}$	$mol/kg_{cat}.s$	6.86×10^{-4}	4.77×10^{-4}
	C_M (Mears Criterion) $\frac{-r_M \rho_b R n}{k_c C_M} < 0.15$	-	3.48×10^{-4}	1.80×10^{-5}
	External Temperature Gradient Criteria $\left\lvert \frac{-r_M(-\Delta H_{rx})\rho_b R E}{h T^2 R_{gas}} \right\rvert < 0.15$	-	6.08×10^{-4}	5.03×10^{-4}

Table B. 6. Details of calculations to verify absence of internal and external mass transfer limitations and ΔT_{max} for the bimetallic Pd-Pt/Co_3O_4 catalyst

Pd-Pt/Co_3O_4 **(5 vol% runs)**	X		0.80	0.20
	T	˚C	525	450
	F_{W0}	mol/s	7.81×10^{-6}	
	F_{M0}	mol/s	7.86×10^{-7}	
	k_1	$m^3/ kg_{cat}.s$	1.45×10^{-2}	1.21×10^{-3}
	k_2	$mol/kg_{cat}.s$	1.11×10^{-2}	1.43×10^{-3}
	$(-r_M) = k_1 C_M + \frac{k_2 C_M}{C_{aq}}$	$mol/ kg_{cat}.s$	4.15×10^{-4}	1.93×10^{-4}
	C_M (Mears Criterion) $\frac{-r_M \rho_b R n}{k_c C_M} < 0.15$	-	1.38×10^{-4}	1.83×10^{-5}
	External Temperature Gradient Criteria $\left\lvert \frac{-r_M(-\Delta H_{rx})\rho_b R E}{h T^2 R_{gas}} \right\rvert < 0.15$	-	3.53×10^{-4}	2.18×10^{-4}
Pd-Pt/Co_3O_4 **(10 vol% runs)**	X		0.80	0.20
	T	˚C	545	450
	F_{W0}	mol/s	1.56×10^{-5}	
	F_{M0}	mol/s	7.86×10^{-7}	
	k_1	$m^3/ kg_{cat}.s$	2.61×10^{-2}	1.21×10^{-3}
	k_2	$mol/kg_{cat}.s$	1.80×10^{-2}	1.43×10^{-3}

	$(-r_M) = k_1 C_M + \frac{k_2 C_M}{C_{aq}}$	mol/ kg_{cat}.s	5.59×10^{-4}	1.39×10^{-4}
	C_M (Mears Criterion) $\frac{-r_M \rho_b R n}{k_c C_M} < 0.15$	-	2.17×10^{-4}	5.70×10^{-6}
	External Temperature Gradient Criteria $\left\lvert\frac{-r_M(-\Delta H_{rx})\rho_b R E}{h T^2 R_{gas}}\right\rvert < 0.15$	-	4.52×10^{-4}	1.36×10^{-4}

Since the $C_M < 0.15$ and the external temperature gradient < 0.15, external mass and heat transfer limitations can be neglected for the catalysts under consideration. Similarly, the Prater Number and ΔT_{max} values exhibit the absence of internal heat transfer limitations and thus the Pd-Pt/$10Co_3O_4$/γ-Al_2O_3 catalyst particle can be considered isothermal for conversion ranges of interest. Since SnO_2 is non-porous, internal heat transfer limitations do not exist.

SECTION B.4: Additional information for the characterization and kinetic study

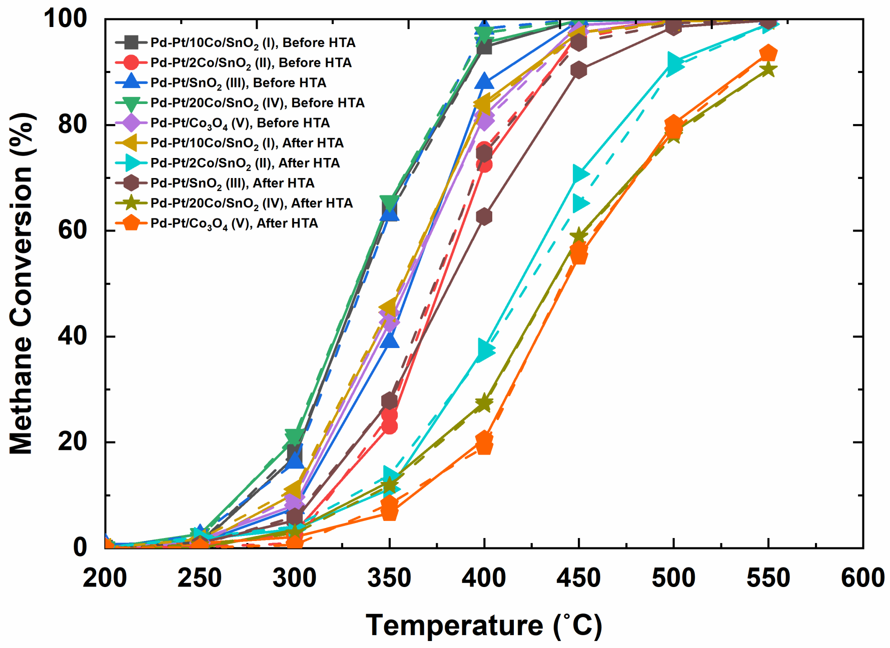

Figure B. 1. IE curves for runs before and after HTA under dry feed conditions for 4000 ppmv methane concentration (solid lines – ignition curves and dashed lines – extinction curves)

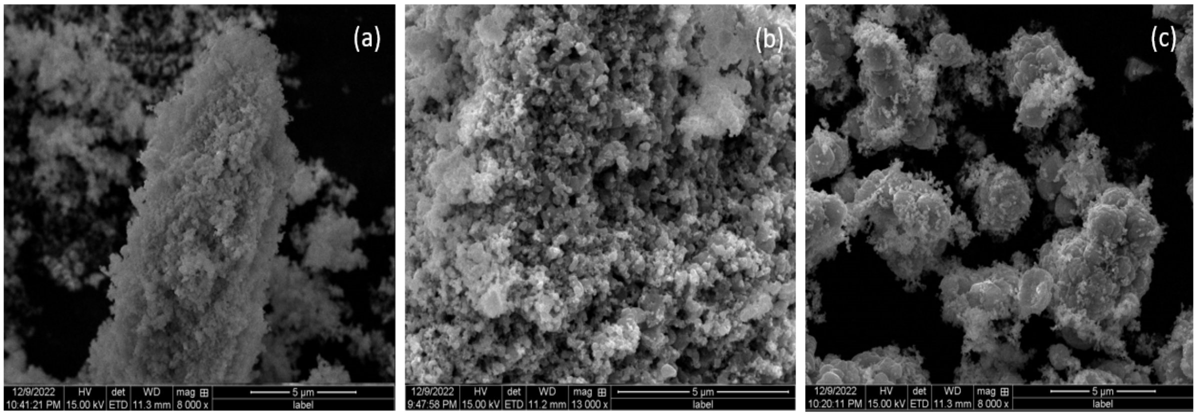

Figure B. 2. Scanning electron micrographs (SEM) for the calcined (a) Pd-Pt/2Co/SnO_2 catalyst; (b) Pd-Pt/10Co/SnO_2 catalyst; and (c) Pd-Pt/20Co/SnO_2 catalyst

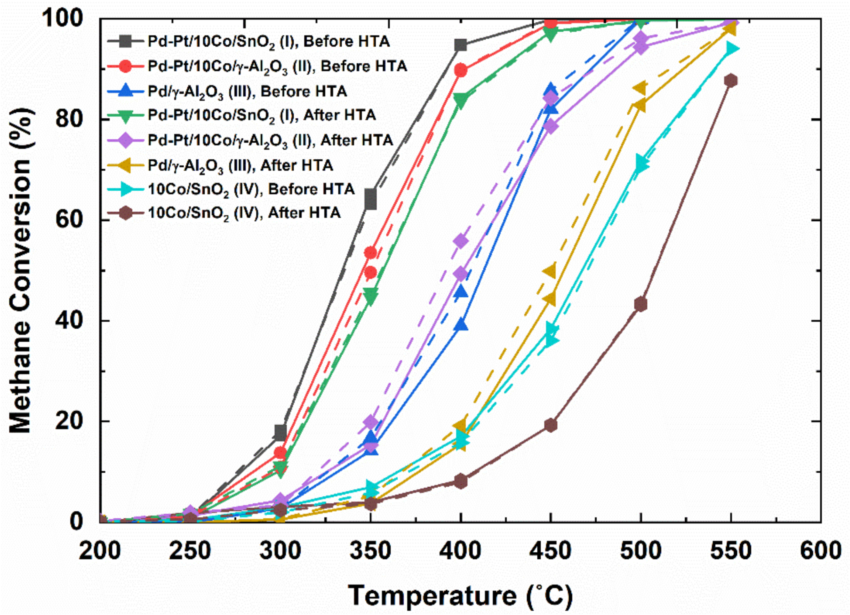

Figure B. 3. IE curves for runs before and after HTA under dry feed conditions for 4000 ppmv methane concentration (solid lines – ignition curves and dashed lines – extinction curves)

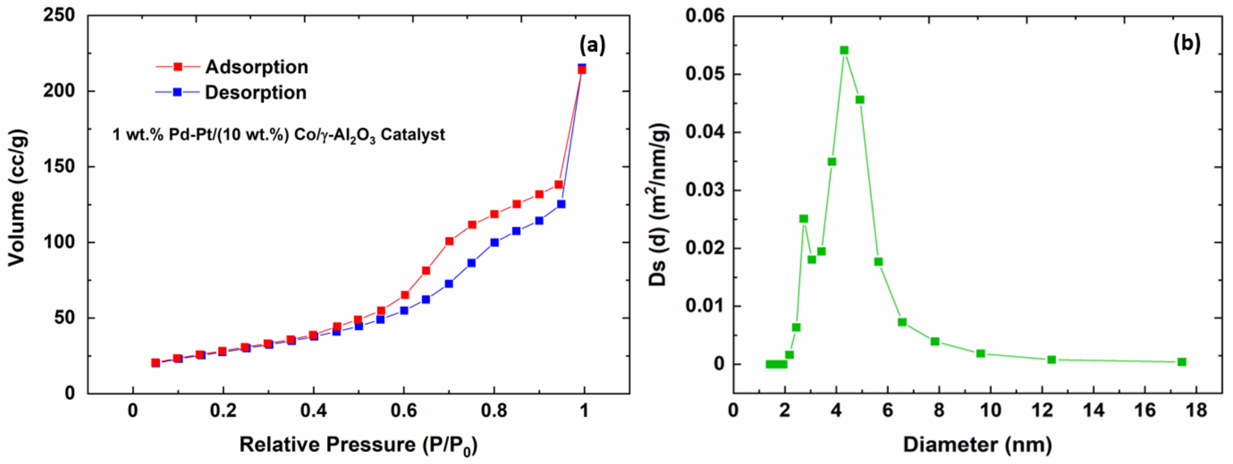

Figure B. 4. (a) BET Isotherm for the hydrothermally aged Pd-Pt/10Co/γ-Al_2O_3 catalyst (BET constant C = 77; Type IV isotherm; BET surface area = 120 m^2/g); (b) Pore size distribution for the hydrothermally aged Pd-Pt/10Co/γ-Al_2O_3 (pore diameter = 4.31 nm)

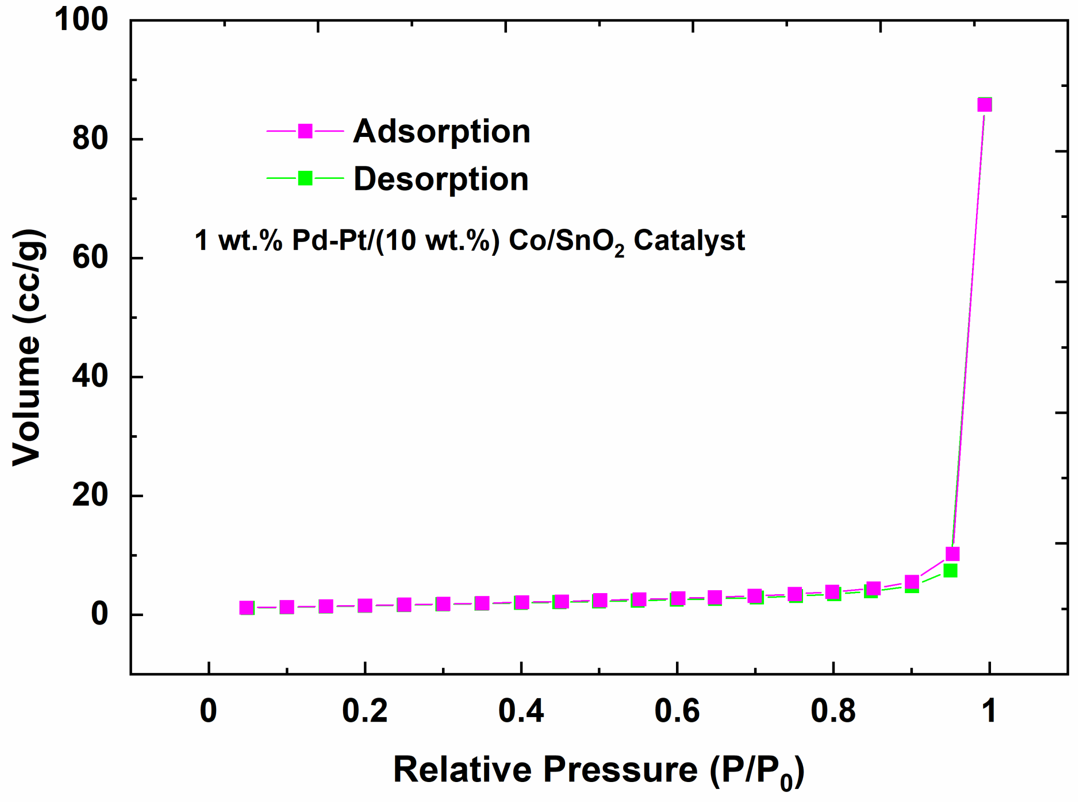

Figure B. 5. BET Isotherms for the hydrothermally aged Pd-Pt/10Co/SnO_2 catalyst (BET constant C = 113; Type II isotherm; BET surface area = 6 m^2/g)

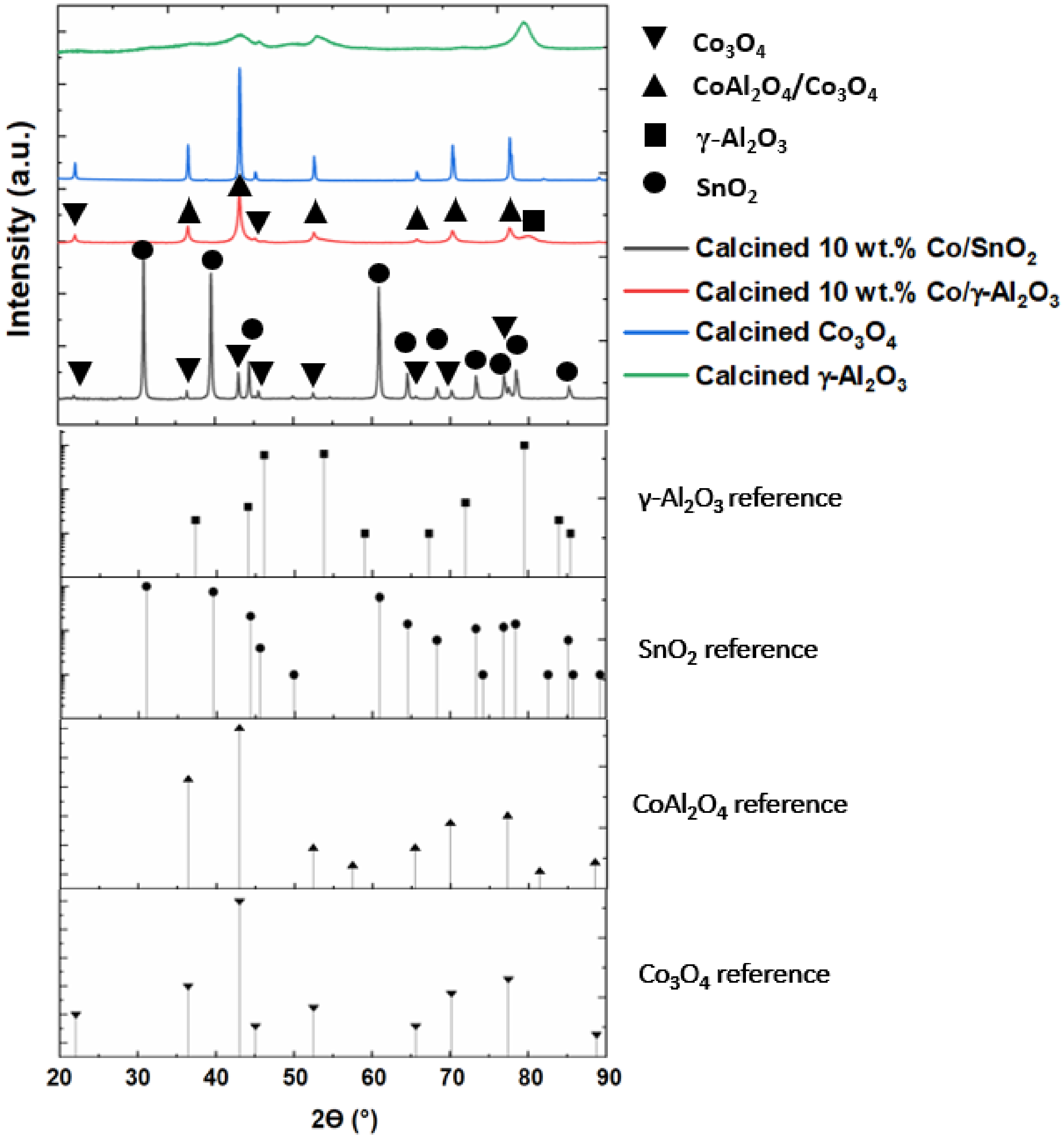

Figure B. 6. XRD profiles of the calcined cobalt oxide impregnated support materials (SnO_2 and γ-Al_2O_3)

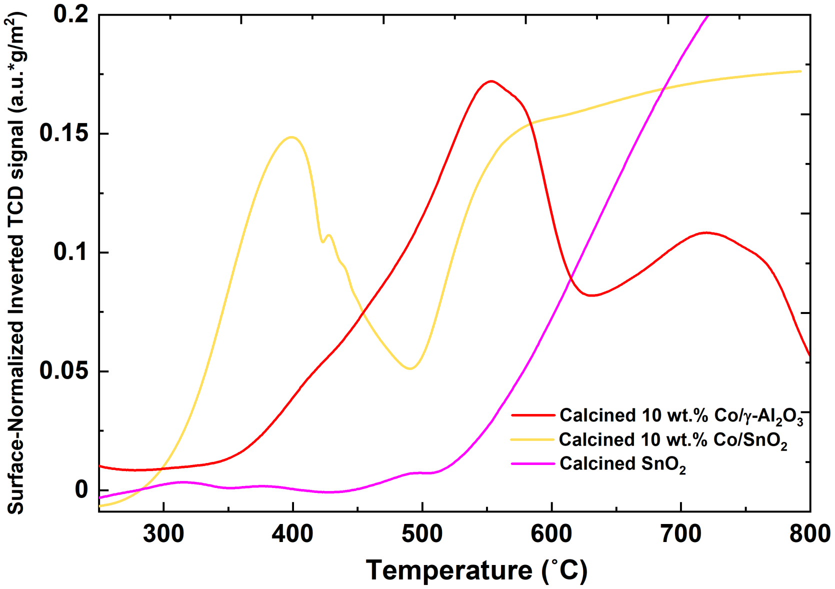

Figure B. 7. TPR curves normalized per sample surface area of the calcined 10Co/S (S = γ-Al₂O₃, SnO₂) samples and SnO₂ support when subjected to 10% H₂/Ar reduction up to 800 ˚C

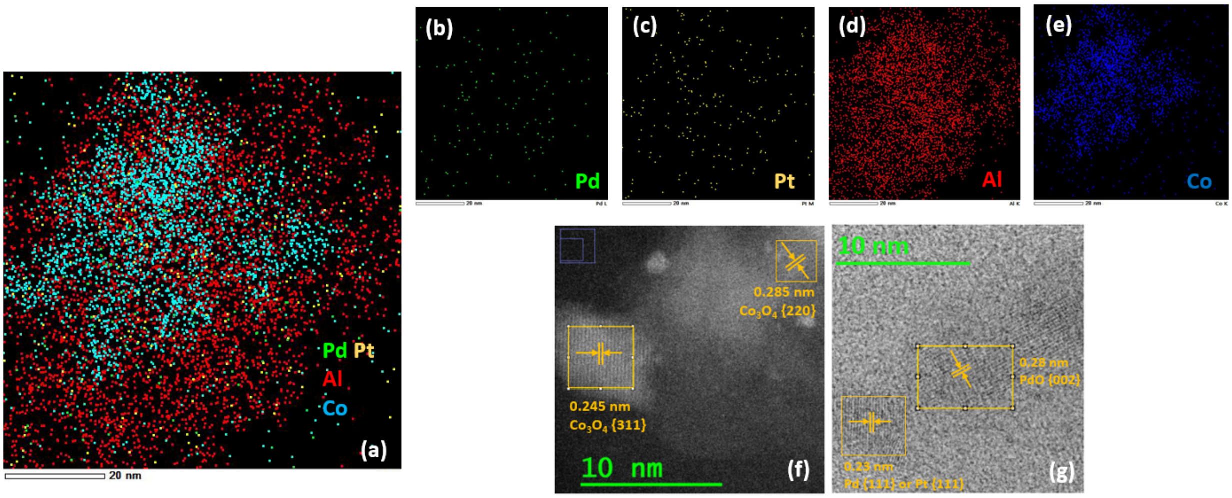

Figure B. 8. Hydrothermally aged Pd-Pt/10Co/γ-Al₂O₃ catalyst: (a)-(e) TEM-EDX analysis showing Pd (green), Pt (yellow), Al (red), and Co (blue) distribution; (f-g) a representation of the Co₃O₄, PdO and PdPt phases

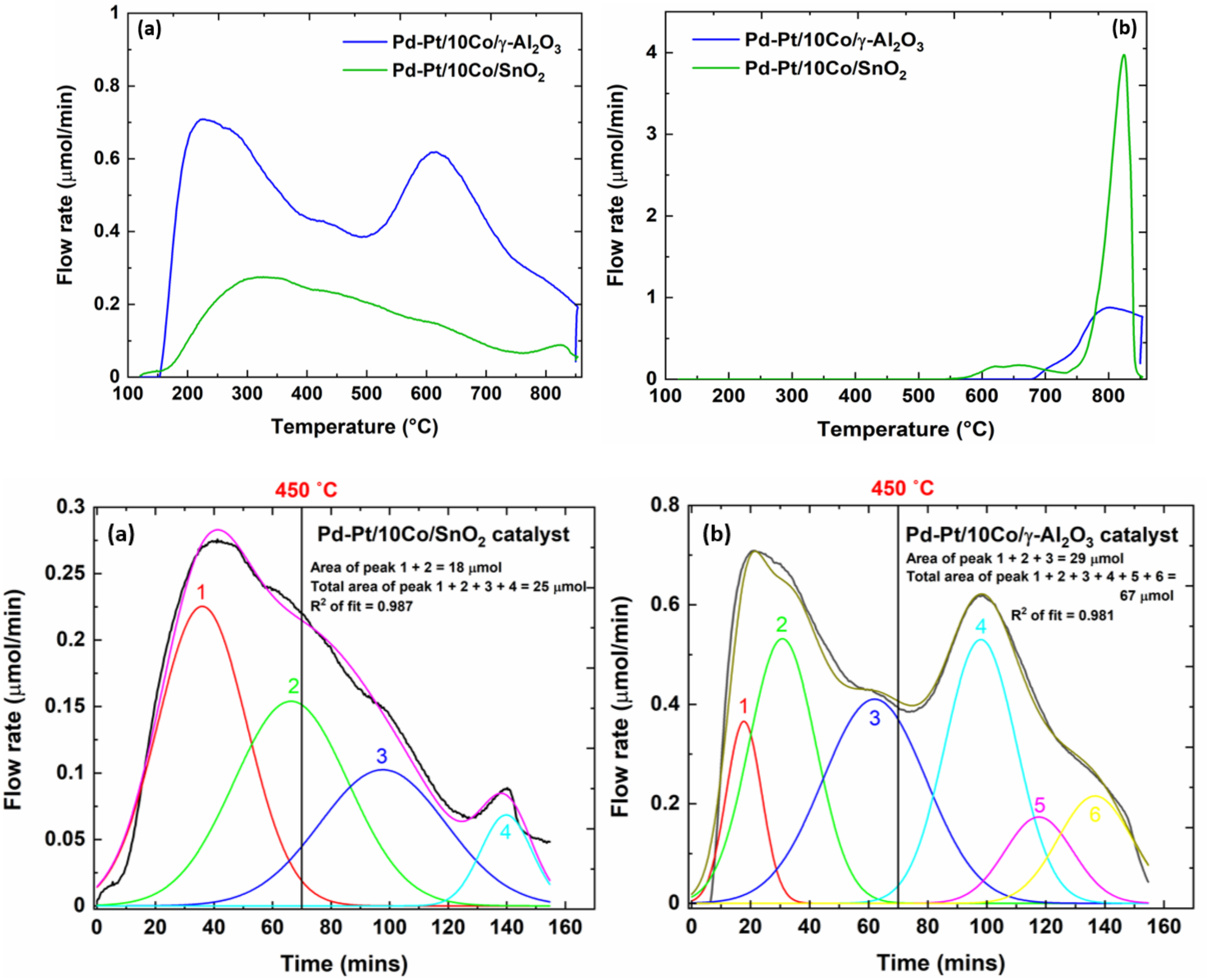

Figure B. 9. (a) Water and; (b) oxygen evolution trends based on TPD studies on the aged Pd-Pt/10Co/S (S = γ-Al_2O_3, SnO_2) catalysts; Deconvoluted peaks for the water evolution trend on the hydrothermally aged (c) Pd-Pt/10Co/SnO_2 catalyst; and (d) Pd-Pt/10Co/γ-Al_2O_3 catalyst

No attempt was made to comprehend the physical meaning of the peaks for each of catalysts in Figure B.9. The aim of the study was only to show a distribution between the water evolved before 450 ˚C and above 450 ˚C because it is known at temperatures above 450 ˚C, Pd is not poisoned by water.

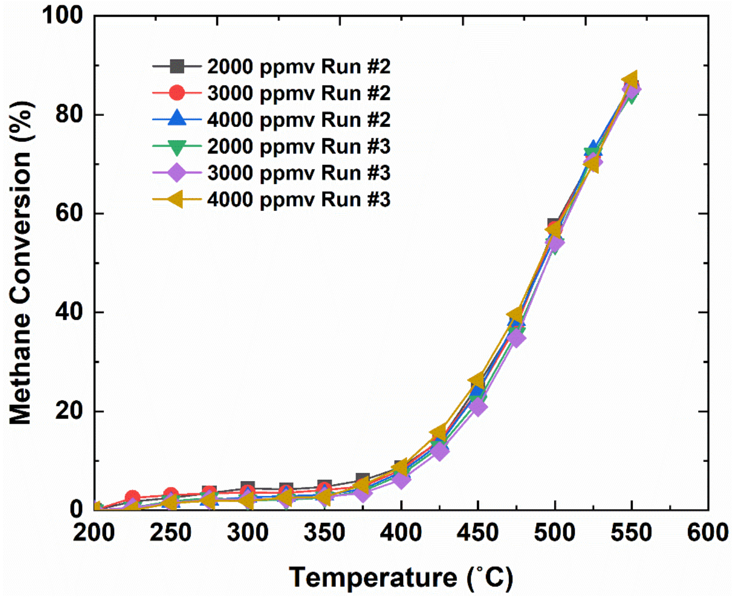

Figure B. 10. Ignition curves for the reproducible runs for the initial methane concentrations of 2000 ppmv, 3000 ppmv, and 4000 ppmv for the Pd-Pt/10Co/γ-Al₂O₃ catalyst under 5 vol% wet feed conditions

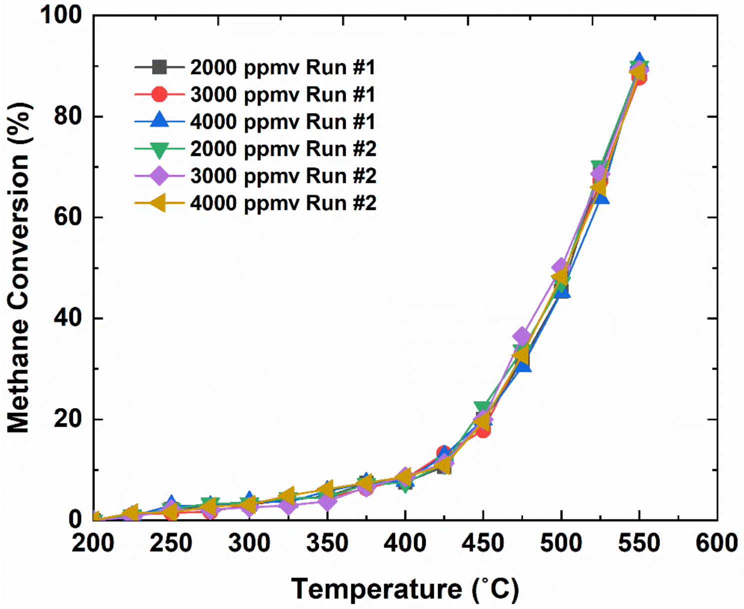

Figure B. 11. Ignition curves for the reproducible runs for the initial methane concentrations of 2000 ppmv, 3000 ppmv, and 4000 ppmv for the Pd-Pt/10Co/γ-Al₂O₃ catalyst under 10 vol% wet feed conditions

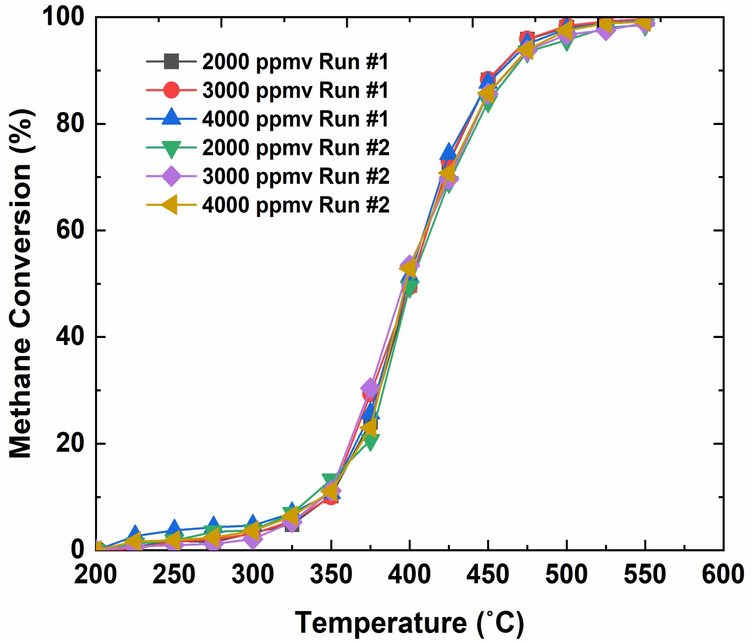

Figure B. 12. Ignition curves for the reproducible runs for the initial methane concentrations of 2000 ppmv, 3000 ppmv, and 4000 ppmv for the Pd-Pt/10Co/SnO_2 catalyst under 5 vol% wet feed conditions

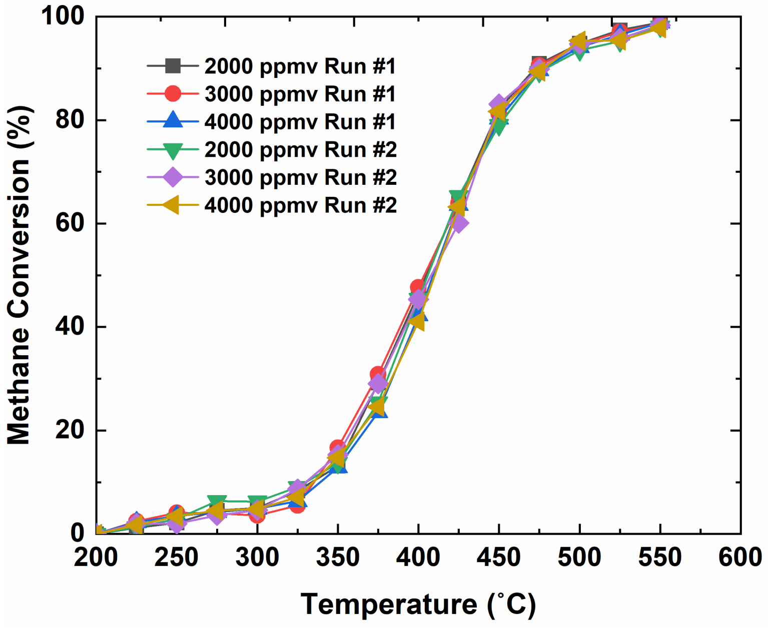

Figure B. 13. Ignition curves for the reproducible runs for the initial methane concentrations of 2000 ppmv, 3000 ppmv, and 4000 ppmv for the Pd-Pt/10Co/SnO_2 catalyst under 10 vol% wet feed conditions

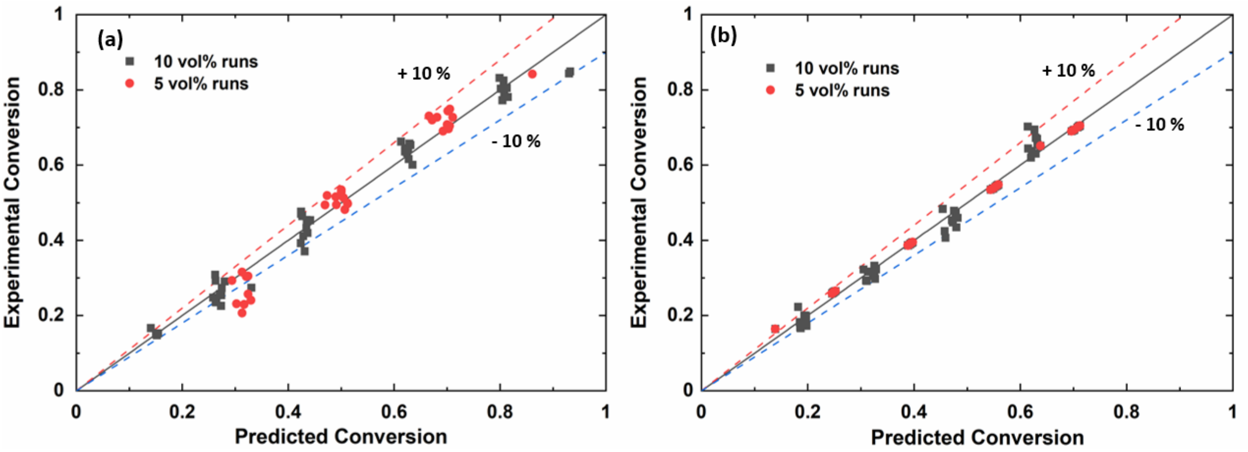

Figure B. 14. Comparison of the predicted and experimental conversion for the combined wet feed condition studies on the aged (a) Pd-Pt/10Co/SnO$_2$ catalyst and (b) Pd-Pt/10Co/γ-Al$_2$O$_3$ catalyst based on Equation 4.1

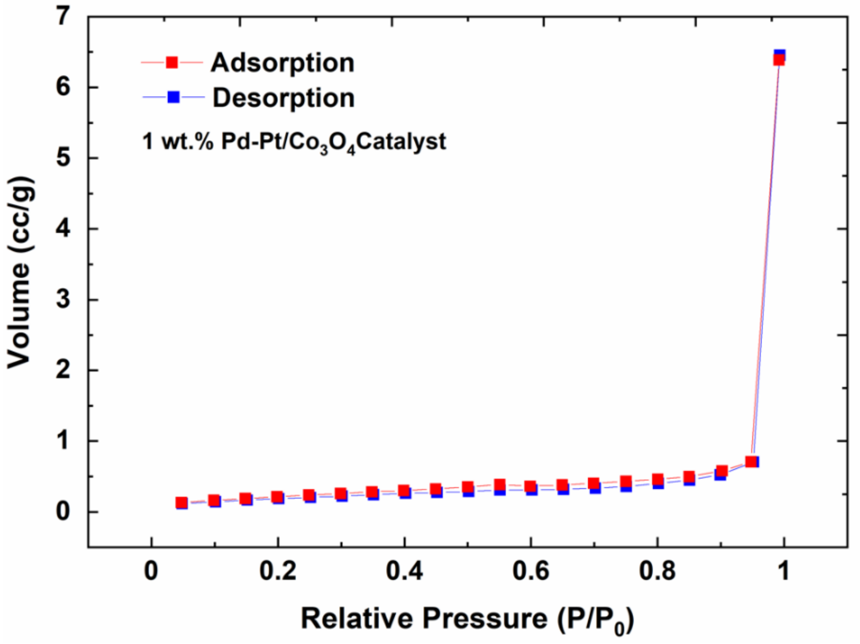

Figure B. 15. BET Isotherms for the hydrothermally aged Pd-Pt/Co$_3$O$_4$ catalyst (BET constant C = 55; Type II isotherm; BET surface area = 9)

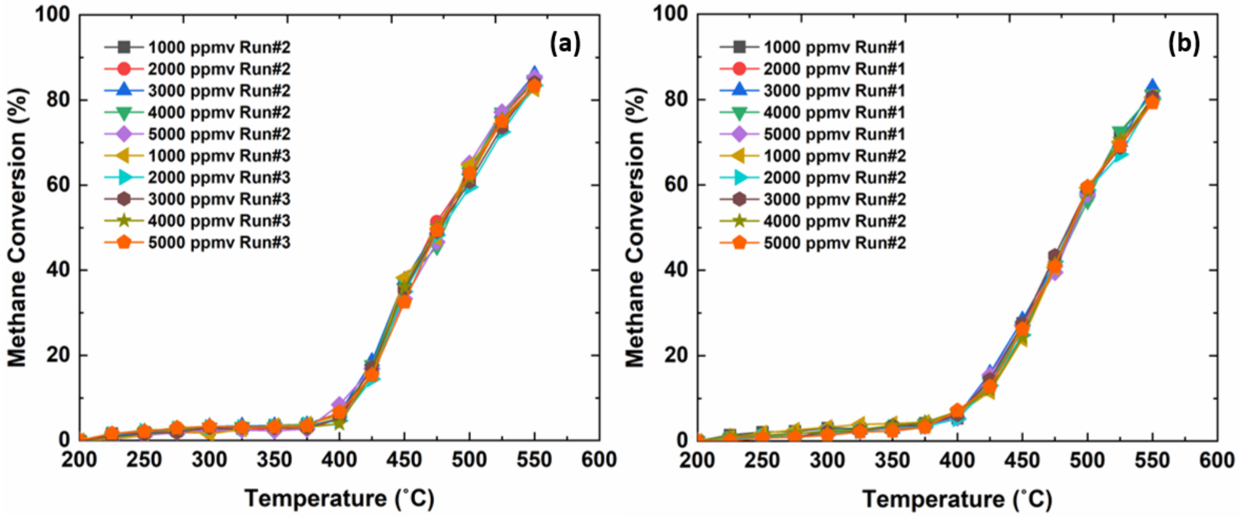

Figure B. 16. Ignition curves for the reproducible runs for all the initial methane concentrations for the aged Pd-Pt/Co_3O_4 catalyst under (a) 5 vol% wet feed conditions and (b) 10 vol% wet feed conditions

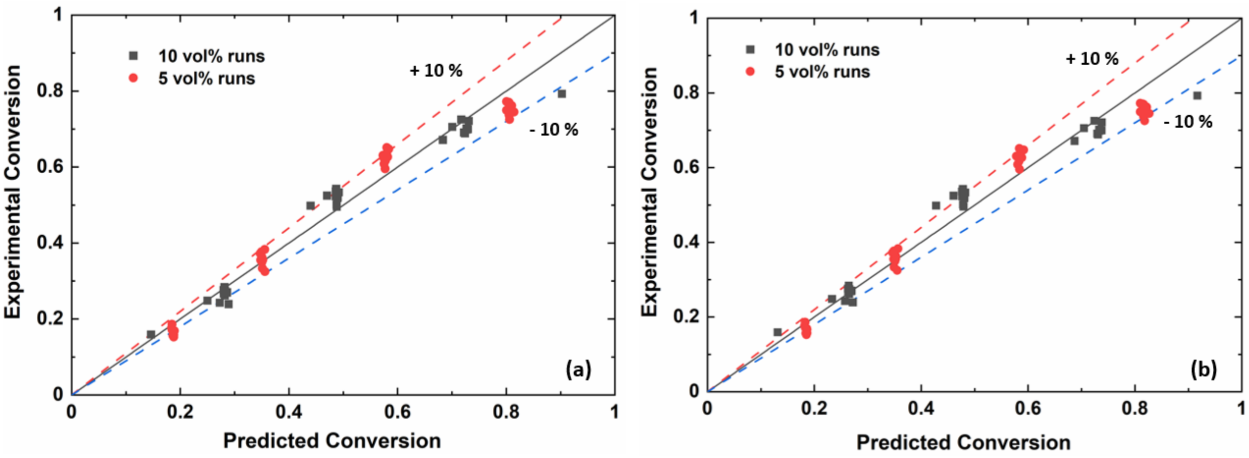

Figure B. 17. Comparison of the predicted and experimental conversion for the combined wet feed condition studies on the aged Pd-Pt/Co_3O_4 catalyst (a) based on Equation 4.1 (b) based on Equation (4.7)-(4.9)

Table B. 7. Estimated kinetic parameters for the Pd-Pt/Co_3O_4 catalyst based on equation (4.1) for the combined modeling under 5 vol% and 10 vol% wet feed conditions for all CH_4 concentrations from the reproducible runs. Rate law (Eq. 4.1): $(-r_M) = k'C_M C_{aq}^n$

Catalyst	Pd-Pt/Co_3O_4
Observed activation energy (kJ mol^{-1})	140 ± 9
Observed pre-exponential factor (mol g_{PGM}^{-1} s^{-1})	(43 ± 10) × 10^5
Observed order with respect to H_2O (-n) in Eq. (4.1)	- 0.42
Objective function value	1 × 10^{-3}

Table B. 8. Estimated kinetic parameters for the Pd-Pt/Co_3O_4 catalyst based on equations (4.7)-(4.9) for the combined modeling under 5 vol% and 10 vol% wet feed conditions for all CH_4 concentrations from the reproducible runs. Rate law (Eq. 4.7): $(-r_M) = k_1 C_M + k_2 C_M C_{aq}^{-1}$

Catalyst	Pd-Pt/Co_3O_4
Observed activation energy 1 (kJ mol^{-1})	159 ± 10
Observed activation energy 2 (kJ mol^{-1})	131
Observed pre-exponential factor 1 (m^3_{fluid} g_{PGM}^{-1} s^{-1})	(37 ± 5) × 10^6
Observed pre-exponential factor 2 (mol g_{PGM}^{-1} s^{-1})	(42 ± 7) × 10^4
Rate constant k_1 @ 426.85 ˚C (m^3 g_{PGM}^{-1} s^{-1})	6.69 × 10^{-4}
Rate constant k_2 @ 426.85 ˚C (mol g_{PGM}^{-1} s^{-1})	5.92 × 10^{-4}
Objective function value	2 × 10^{-3}

Appendix C: MATLAB code for kinetic modeling studies

model1.m

This script file contains the MATLAB code that is utilized to obtain the kinetic parameters for the rate equation with an order ‘n’ to water.

```
function dxdt = model(t,x,k)

%%%%%%%%%%%%%%%%%%%%%%%%%%%%%%%%%%%%%%%%%%%%%%%%%%%%%%%%%%%%

global T P i

T = [452.1      477.1   501.6   526.2   449.9   474.8   499.4   524.1   452.1   476.7   501.1   525.6
        449.7   474.5   498.9   523.6   452.1   476.7   501.4   526.2   452.1   476.7   501.6   526.2
        449.9   474.8   499.4   524.4   451.6   476.7   501.1   525.8   449.2   474     498.7   523.6
        452.6   477.1   501.8   526.5 450.9         475.9   500.6   525.6   451.4   476.4   501.1   525.8
        451.9   476.9   501.4   526.2   451.6   476.7   501.1   525.8   451.6   476.7   501.1   526
        452.1   476.9   501.6   526     451.4   476.2   500.9   525.6   427.3   451.9   476.7   501.1
        525.8   451.1   475.9   500.9   525.8   451.4   476.4   501.1   526]+273.15; % temperature K

P = [1.185485034            1.200791402     1.200791402     1.200791402     1.185485034     1.185485034
        1.246572608     1.246572608     1.155010195     1.185485034     1.185485034     1.200791402
        1.185485034     1.185485034     1.185485034     1.200791402     1.185485034     1.200791402
        1.200791402     1.200791402     1.200791402     1.200791402     1.216028821     1.216028821
        1.170247615     1.170247615     1.185485034     1.216028821     1.200791402     1.185485034
        1.200791402     1.185485034     1.170247615     1.170247615     1.185485034     1.216028821
        1.170247615     1.200791402     1.231335188     1.246572608     1.139703828     1.139703828
        1.155010195     1.155010195     1.124466408     1.139703828     1.155010195     1.155010195
        1.139703828     1.139703828     1.155010195     1.170247615     1.139703828     1.139703828
        1.155010195     1.170247615     1.139703828     1.139703828     1.155010195     1.170247615
        1.139703828     1.139703828     1.155010195     1.170247615     1.139703828     1.155010195
        1.155010195     1.170247615     1.109228989     1.109228989     1.109228989     1.124466408
        1.139703828     1.139703828     1.155010195     1.170247615     1.170247615     1.139703828
        1.155010195     1.155010195     1.170247615]; % pressure bar

Q0 = [3.51E-06     3.51E-06         3.51E-06         3.51E-06         3.51E-06         3.51E-06         3.51E-
06      3.51E-06        3.51E-06        3.51E-06        3.51E-06        3.51E-06        3.51E-06
        3.51E-06        3.51E-06        3.51E-06        3.51E-06        3.51E-06        3.51E-06
        3.51E-06        3.51E-06        3.51E-06        3.51E-06        3.51E-06        3.51E-06
        3.51E-06        3.51E-06        3.51E-06        3.51E-06        3.51E-06        3.51E-06
        3.51E-06        3.51E-06        3.51E-06        3.51E-06        3.51E-06        3.51E-06
        3.51E-06        3.51E-06        3.51E-06        3.51E-06        3.51E-06        3.51E-06
        3.51E-06        3.51E-06        3.51E-06        3.51E-06        3.51E-06        3.51E-06
        3.51E-06        3.51E-06        3.51E-06        3.51E-06        3.51E-06        3.51E-06
        3.51E-06        3.51E-06        3.51E-06        3.51E-06        3.51E-06        3.51E-06
        3.51E-06        3.51E-06        3.51E-06        3.51E-06        3.51E-06        3.51E-06
        3.51E-06        3.51E-06        3.51E-06        3.51E-06        3.51E-06        3.51E-06
        3.51E-06        3.51E-06        3.51E-06        3.51E-06        3.51E-06        3.51E-06
        3.51E-06        3.51E-06]; % total flow rate m3/s (STP)
```

```
FA0 = [0.000000156    0.000000156    0.000000156    0.000000156    0.000000156    0.000000156
       0.000000156    0.000000156    0.000000313    0.000000313    0.000000313    0.000000313
       0.000000313    0.000000313    0.000000313    0.000000313    0.000000468    0.000000468
       0.000000468    0.000000468    0.000000468    0.000000468    0.000000468    0.000000468
       0.000000625    0.000000625    0.000000625    0.000000625    0.000000625    0.000000625
       0.000000625    0.000000625    0.000000786    0.000000786    0.000000786    0.000000786
       0.000000786    0.000000786    0.000000786    0.000000786    0.000000156    0.000000156
       0.000000156    0.000000156    0.000000156    0.000000156    0.000000156    0.000000156
       0.000000313    0.000000313    0.000000313    0.000000313    0.000000313    0.000000313
       0.000000313    0.000000313    0.000000468    0.000000468    0.000000468    0.000000468
       0.000000468    0.000000468    0.000000468    0.000000468    0.000000625    0.000000625
       0.000000625    0.000000625    0.000000625    0.000000625    0.000000625    0.000000625
       0.000000625    0.000000786    0.000000786    0.000000786    0.000000786    0.000000786
       0.000000786    0.000000786    0.000000786];% Initial methane molar rate molCH4/s

FB0 = [0.00001562     0.00001562     0.00001562     0.00001562     0.00001562     0.00001562
       0.00001562     0.00001562     0.00001562     0.00001562     0.00001562     0.00001562
       0.00001562     0.00001562     0.00001562     0.00001562     0.00001562     0.00001562
       0.00001562     0.00001562     0.00001562     0.00001562     0.00001562     0.00001562
       0.00001562     0.00001562     0.00001562     0.00001562     0.00001562     0.00001562
       0.00001562     0.00001562     0.00001562     0.00001562     0.00001562     0.00001562
       0.00001562     0.00001562     0.00001562     0.00001562     0.00000781     0.00000781
       0.00000781     0.00000781     0.00000781     0.00000781     0.00000781     0.00000781
       0.00000781     0.00000781     0.00000781     0.00000781     0.00000781     0.00000781
       0.00000781     0.00000781     0.00000781     0.00000781     0.00000781     0.00000781
       0.00000781     0.00000781     0.00000781     0.00000781     0.00000781     0.00000781
       0.00000781     0.00000781     0.00000781     0.00000781     0.00000781     0.00000781
       0.00000781     0.00000781     0.00000781     0.00000781     0.00000781     0.00000781
       0.00000781     0.00000781     0.00000781]; % water mol/s

Q(i) = Q0(i).*(T(i)./273.15).*(1./P(i)); % scaled volumetric flow rate, m3/s
R = 8.314E-3; %kJ/mol.K

%%%%%%%%%%%%%%%%%%%%%%

k1 = k(1) .* exp(-(k(2)./(R.*T(i)))); % rate constant, mol/s/gcat
dxdt= k1.*((1-X)./Q(i)).*(((FB0(i)+(2.*FA0(i).*X))./Q(i)).^k(3));


%%%%%%%%%%%%%%%%%%%%%%%%%%%%%%%%%%%%%%%%%%%%%%%%%%
end
```

model2.m

This script file contains the MATLAB code that is utilized to obtain the kinetic parameters for the rate equation with additive contributions from two different active sites.

```
function dxdt = model(t,x,k)

%%%%%%%%%%%%%%%%%%%%%%%%%%%%%%%%%%%%%%%%%%%%%%%%%%%%%%%%%%%%%%%%%%%%%%%%%%%%%%%%%%%%%%%%%%%%%%%%%%%%

global T P i

T = [452.1      477.1   501.6   526.2   449.9   474.8   499.4   524.1   452.1   476.7   501.1   525.6
        449.7   474.5   498.9   523.6   452.1   476.7   501.4   526.2   452.1   476.7   501.6   526.2
        449.9   474.8   499.4   524.4   451.6   476.7   501.1   525.8   449.2   474     498.7   523.6
        452.6   477.1   501.8   526.5   450.9   475.9   500.6   525.6   451.4   476.4   501.1   525.8
        451.9   476.9   501.4   526.2   451.6   476.7   501.1   525.8   451.6   476.7   501.1   526
        452.1   476.9   501.6   526     451.4   476.2   500.9   525.6   427.3   451.9   476.7   501.1
        525.8   451.1   475.9   500.9   525.8   451.4   476.4   501.1   526]+273.15; % temperature K

P = [1.185485034        1.200791402     1.200791402     1.200791402     1.185485034     1.185485034
        1.246572608     1.246572608     1.155010195     1.185485034     1.185485034     1.200791402
        1.185485034     1.185485034     1.185485034     1.200791402     1.185485034     1.200791402
        1.200791402     1.200791402     1.200791402     1.200791402     1.216028821     1.216028821
        1.170247615     1.170247615     1.185485034     1.216028821     1.200791402     1.185485034
        1.200791402     1.185485034     1.170247615     1.170247615     1.185485034     1.216028821
        1.170247615     1.200791402     1.231335188     1.246572608     1.139703828     1.139703828
        1.155010195     1.155010195     1.124466408     1.139703828     1.155010195     1.155010195
        1.139703828     1.139703828     1.155010195     1.170247615     1.139703828     1.139703828
        1.155010195     1.170247615     1.139703828     1.139703828     1.155010195     1.170247615
        1.139703828     1.139703828     1.155010195     1.170247615     1.139703828     1.155010195
        1.155010195     1.170247615     1.109228989     1.109228989     1.109228989     1.124466408
        1.139703828     1.139703828     1.155010195     1.170247615     1.170247615     1.139703828
        1.155010195     1.155010195     1.170247615]; % pressure bar

Q0 = [3.51E-06     3.51E-06        3.51E-06         3.51E-06         3.51E-06         3.51E-06         3.51E-
06      3.51E-06        3.51E-06        3.51E-06        3.51E-06        3.51E-06        3.51E-06
        3.51E-06        3.51E-06        3.51E-06        3.51E-06        3.51E-06        3.51E-06
        3.51E-06        3.51E-06        3.51E-06        3.51E-06        3.51E-06        3.51E-06
        3.51E-06        3.51E-06        3.51E-06        3.51E-06        3.51E-06        3.51E-06
        3.51E-06        3.51E-06        3.51E-06        3.51E-06        3.51E-06        3.51E-06
        3.51E-06        3.51E-06        3.51E-06        3.51E-06        3.51E-06        3.51E-06
        3.51E-06        3.51E-06        3.51E-06        3.51E-06        3.51E-06        3.51E-06
        3.51E-06        3.51E-06        3.51E-06        3.51E-06        3.51E-06        3.51E-06
        3.51E-06        3.51E-06        3.51E-06        3.51E-06        3.51E-06        3.51E-06
        3.51E-06        3.51E-06        3.51E-06        3.51E-06        3.51E-06        3.51E-06
        3.51E-06        3.51E-06        3.51E-06        3.51E-06        3.51E-06        3.51E-06
        3.51E-06        3.51E-06        3.51E-06        3.51E-06        3.51E-06        3.51E-06
        3.51E-06        3.51E-06]; % total flow rate m3/s (STP)

FA0 = [0.000000156      0.000000156     0.000000156     0.000000156     0.000000156     0.000000156
        0.000000156     0.000000156     0.000000313     0.000000313     0.000000313     0.000000313
        0.000000313     0.000000313     0.000000313     0.000000313     0.000000468     0.000000468
        0.000000468     0.000000468     0.000000468     0.000000468     0.000000468     0.000000468
        0.000000625     0.000000625     0.000000625     0.000000625     0.000000625     0.000000625
```

```
          0.000000625   0.000000625   0.000000786   0.000000786   0.000000786   0.000000786
          0.000000786   0.000000786   0.000000786   0.000000786  0.000000156   0.000000156
          0.000000156   0.000000156   0.000000156   0.000000156   0.000000156   0.000000156
          0.000000313   0.000000313   0.000000313   0.000000313   0.000000313   0.000000313
          0.000000313   0.000000313   0.000000468   0.000000468   0.000000468   0.000000468
          0.000000468   0.000000468   0.000000468   0.000000468   0.000000625   0.000000625
          0.000000625   0.000000625   0.000000625   0.000000625   0.000000625   0.000000625
          0.000000625   0.000000786   0.000000786   0.000000786   0.000000786   0.000000786
          0.000000786   0.000000786   0.000000786];% Initial methane molar rate molCH4/s

FB0 = [0.00001562     0.00001562    0.00001562    0.00001562    0.00001562    0.00001562
          0.00001562    0.00001562    0.00001562    0.00001562    0.00001562    0.00001562
          0.00001562    0.00001562    0.00001562    0.00001562    0.00001562    0.00001562
          0.00001562    0.00001562    0.00001562    0.00001562    0.00001562    0.00001562
          0.00001562    0.00001562    0.00001562    0.00001562    0.00001562    0.00001562
          0.00001562    0.00001562    0.00001562    0.00001562    0.00001562    0.00001562
          0.00001562    0.00001562    0.00001562    0.00001562    0.00000781    0.00000781
          0.00000781    0.00000781    0.00000781    0.00000781    0.00000781    0.00000781
          0.00000781    0.00000781    0.00000781    0.00000781    0.00000781    0.00000781
          0.00000781    0.00000781    0.00000781    0.00000781    0.00000781    0.00000781
          0.00000781    0.00000781    0.00000781    0.00000781    0.00000781    0.00000781
          0.00000781    0.00000781    0.00000781    0.00000781    0.00000781    0.00000781
          0.00000781    0.00000781    0.00000781    0.00000781    0.00000781    0.00000781
          0.00000781    0.00000781    0.00000781]; % water mol/s

Q(i) = Q0(i).*(T(i)./273.15).*(1./P(i)); % scaled volumetric flow rate, m3/s
R = 8.314E-3; %kJ/molK

%%%%%%%%%%%%%%%%%%%%%%%%%%%%%%%%%%%%%

X = x(1);
epsilon = 0.4; % bed voidage
db = 0.9145; % bed density, gcat/cm3
denp = 1524.23; % catalyst particle density, kg/m3
dp = 5e-05; % particle diameter, m
tf = 3.9; % tortuosity factor
Sbet = 120; % BET surface area of aged catalyst, m2/g
dpore = 4.31E-09; % diameter, m
k1 = k(1).*exp(-k(2)./(R.*T(i))); % rate constant, m3/s/gcat
k2 = k(3).*exp(-131./(R.*T(i))); % rate constant, mol/s/gcat (fixed Ea2 = 140 kJ/mol)

%%%%%%%%%%%% effectiveness factor calculations
kr1 = k1*1000; % rate constant; % rate constant 1, m3/kgcat/s
kr2 = k2*1000*Q(i)/(FB0(i)+2*FB0(i)*X); % rate constant 2, m3/kgcat/s
Dk = 12.125*dpore*(T(i))^0.5; % Knudson diffusion, m2/s
Dab = (1.013E-02*(T(i)^1.75)*(((1/16)+(1/29))^0.5))/(101325*(((24.42)^0.33)+((20.1)^0.33)^2)); % diffusivity of
CH4 in Air, m2/s; Fuller equation
Dpore = (1/Dk+1/Dab)^-1;  % pore diffusivity, m2/s
Op = Sbet*denp*dpore/4; % particle porosity
Deff = Op*Dpore/tf; % effective diffusivity, m2/s
thi1 = (dp/6)*sqrt(kr1*denp/Deff); % Thiele modulus 1
eta1 = 3/thi1^2*(thi1*coth(thi1)-1); % internal effectiveness factor 1
thi2 = (dp/6)*sqrt(kr2*denp/Deff); % Thiele modulus 2
eta2 = 3/thi2^2*(thi2*coth(thi2)-1); % internal effectiveness factor 2

dxdt= ((eta1).*((k1.*(1-X))./Q(i))) + ((eta2).*((k2.*(1-X))./(FB0(i)+(2*FA0(i).*X))));
```

```
%%%%%%%%%%%%%%%%%%%%%%%%%%%%%%%%%%%%%%%%%%%%%%%%%
end
```

x_exp.m

This script file contains the experimental conversions obtained from the 5 vol% and 10 vol% wet feed conditions runs.

```
function u = x_exp(s)
% This file contains the experimental conversion for 5 vol% and 10 vol% wet conditions
A = [19.98621655 32.27525871    47.22039266    67.0096686     16.65554359    31.67142139
         44.78570716    63.03607304    19.99975479    31.54709409    45.3626398     69.437325
         16.8666435     29.20103876    42.46622305    64.42274713    17.82559282    33.24643594
         47.89135907    67.24201069    17.26995553    30.53493874    43.45493848    65.4639423
         18.22713675    29.33371397    40.65545344    61.98683659    19.91780253    30.50034736
         45.19655926    63.74400805    22.2907421     32.24089482    48.3695583     70.22735881
         19.09543808    29.73751136    45.98564211    67.99668535    23.30913018    39.71348168
         58.70313281    72.83976897    24.34431225    38.16613922    58.59948556    73.38354915
         25.28963998    37.82335193    57.64429569    71.66826072    22.01782141    35.83674541
         53.79888187    72.12608253    24.01480181    37.25555865    56.90952669    71.82396246
         20.88429001    34.80581268    54.12245853    70.43080441    23.97492518    38.41412592
         55.29653448    72.83719324    15.79611718    26.34617038    39.61946351    56.77909612
         69.96995245    24.36329016    37.49928139    56.09697905    72.50466523    21.40100739
         35.35645533    53.66954225    72.63632334]/100;
u = A(s);
```

Obj. m

This script file contains the ODE solver that solves model1.m and model2.m for given k parameters and produces the objective function

```
function obj = Obj(k)
%%%%%%%%%%%%%%%%%%%%%%%%%%%%%%%%%%%%%%%%%%%%%%%%%%
global r i
for i = 1:81
tspan=[0 0.34];% 0.34g of supported Pd-Pt catalyst (or 0.12g of supported Pd catalyst)
x0= 1E-90;
[t,x]= ode45(@(t,x)model(t,x,k),tspan,x0);
r(i)= x(end,:); % predicted
end
x_obs = x_exp(1:81);% experimental
obj = sum (( r-x_obs).^2)/81;
end
```

run.m

This script file contains the Pattern Search algorithm optimizer that optimizes the k parameters

```
%% This m-file uses the Pattern Search Algorithm to do the optimization.
%The ans of this file is the optimized k vector.
%FVAL is the value of the objective function calculated using the optimized k.
%This answer can be saved and plotted by typing delta(ans).
%%%%%%%%%%%%%%%%%%%%%%%%%%%%%%%%%%%%%%%%%%%%%%%%%%%%%%%%%%%%%%
%%%%%%
tic;
tt = cputime;
objectiveFunction = @Obj; % @scr_opt;

%%
%Bounds
% LB = [1E+2 80 -0.6]; % for model1.m
% UB = [1E+6 200 -0.5]; % for model1.m
LB = [1E+2 80 1E+2]; % for model2.m
UB = [1E+6 200 1E+5]; % for model2.m
%Start with default options
options = psoptimset;

% X0=[[1E+3 150 0.55]]; % for model1.m
X0=[[2E+3 150 1E+3]]; % for model2.m

%%
%Inequality constraints
Aineq = [];
Bineq = [];
%Equality Constraints
Aeq = [];
Beq = [];
%ConstraintFunction = @simple_constraint;
%Start with default options
options = psoptimset;
%%Modify some parameters
options = psoptimset(options,'InitialMeshSize' ,50);
options = psoptimset(options,'TolMesh' ,1e-15);
options = psoptimset(options,'TolX' ,1e-15);
options = psoptimset(options,'TolBind' ,1e-15);
options = psoptimset(options,'TolFun' ,1e-15);
options = psoptimset(options,'MeshRotate' ,'off');
options = psoptimset(options,'PollMethod' ,'GPSPositiveBasis2N');
options = psoptimset(options,'CacheTol' ,1e-20);
options = psoptimset(options,'MeshAccelerator' ,'ON');
options = psoptimset(options,'CompletePoll' ,'ON');
options = psoptimset(options,'PollingOrder' ,'Random');
options = psoptimset(options,'SearchMethod' ,@GPSPositiveBasis2N);
options = psoptimset(options,'CompleteSearch' ,'on');
options = psoptimset(options,'MaxFunEvals' ,8000000000);
options = psoptimset(options,'MaxIter' ,10000000000);
options = psoptimset(options,'Display' ,'iter');
options = psoptimset(options,'UseParallel' ,true);
options = psoptimset(options,'PlotFcns' ,@psplotbestf);
```

```
options = psoptimset(options,'Cache' ,'on');

%%%%% PATTERNSEARCH
[X,FVAL,EXITFLAG,OUTPUT] = patternsearch(@Obj,X0,Aineq,Bineq,Aeq,Beq,LB,UB,options);
X
FVAL
```

delta.m

This script file is used to compare the experimental data to the predicted conversion by plotting the results

```
function com2 = delta(k)

global r i
for i=1:81
tspan=[0 0.34];% 0.34g of supported Pd-Pt catalyst (or 0.12g of supported Pd catalyst)
x0= 0;
[t,x]= ode45(@(t,x)model(t,x,k),tspan,x0);
r(i)=x(end,:); % predicted
end
x_obs =x_exp(1:81);% experimental
obj = sum (( r-x_obs ).^2)/81;
figure
scatter (x_obs, r,'green','filled')
hold on
hline.Color='b';
hline= refline(1,0);
precisionT = 4;
precisionObj=6;
precisionk=6;
axis square
box on
axis ([0 1 0 1])
ylabel('Predicted conversion')
xlabel('Experimental conversion')
title('Additive model all wet runs');
temp=['Additive model all wet runs','.tiff'];
saveas(gca,temp);

%%%%%%%%%%%%%%
filename =['All wet runs additive model','.xlsx'];
sheet = 1;
xlRange = 'A1';
A = {'All wet runs additive model'};
xlswrite(filename,A,sheet,xlRange)
xlRange = 'A2';
A = {'Experimental Conversion'};
xlswrite(filename,A,sheet,xlRange)
xlRange = 'B2';
A = {'Predicted Conversion'};
xlswrite(filename,A,sheet,xlRange)
xlRange = 'A4';
```

```
xlswrite(filename,(x_obs)',sheet,xlRange)
xlRange = 'B4';
xlswrite(filename,r',sheet,xlRange)
xlRange = 'H2';
xlswrite(filename,k,sheet,xlRange)
xlRange = 'H3';
xlswrite(filename,obj,sheet,xlRange)

end
```